2005

Preparation and Properties of the Mn-Oxide Thin Films by Spray Pyrolysis Technique

Islam, Abu Kalam Md. Faridul

University of Rajshahi

PREPARATION AND PROPERTIES OF THE Mn-OXIDE THIN FILMS BY SPRAY PYROLYSIS TECHNIQUE

Abu Kalam Md. Faridul Islam

A Thesis Submitted for the Degree of Doctor of Philosophy to the Department of Applied Physics & Electronics, University of Rajshahi, Rajshahi-6205 Bangladesh.

Department of Applied Physics
& Electronics, University of
Rajshahi, Rajshahi-6205
Bangladesh.

APRIL-2005

DEDICATED
TO
MY PARENTS

CIRTIFICATE

The thesis entitled "**PREPARATION AND PROPERTIES OF THE Mn-OXIDE THIN FILMS BY SPRAY PYROLYSIS TECHNIQUE**" submitted by Abu Kalam Md. Farid ul Islam embodies the results of research carried out by him under our direct supervision and guidance. We certify that this work has not been presented for any degree or prize elsewhere.

(Dr. M. Khairul Alam Khan)
Professor
Department of Applied Physics & Electronics
University of Rajshahi, Rajshahi-6205
Bangladesh.

(Md. Rezaul. Islam)
Associate Professor
Department of Applied Physics & Electronics
University of Rajshahi, Rajshahi-6205
Bangladesh.

PREFACE

This thesis is based on experimental work carried out at the Department of Applied Physics & Electronics, University of Rajshahi, Bangladesh, during the period 1999-2004 under the supervision of Dr. M. Khairul Alam Khan and Md. Rezaul Islam. The subject is the preparation and properties of MnO_2 thin films by spray pyrolysis technique. The following three papers are included in the thesis:

1. A.K.M. Farid ul Islam R. Islam and K.A. Khan, Effects of deposition variables on spray-deposited MnO_2 thin films prepared from $Mn(C_2H_3O_2)_2.4H_2O$., J. Renewable Energy, (in press), 2005.

2. A.K.M. Farid ul Islam, R. Islam and K.A. Khan, Studies on the Seebeck effect in semiconducting MnO_2 thin films. J. Mater. Sci. Vol.16, Issue 4, 2005, p.203.

3. A.K.M. Farid ul Islam R. Islam and K.A. Khan, Effects of deposition variables on spray-deposited MnO_2 thin films prepared from $Mn(C_2H_3O_2)_2.4H_2O$ for Applications in Selective Surface. Proceeding in 9th Asia Pacific Physics Conference, Hanoi, Vietnam– October 25-31, 2004.

ABSTRACT

Oxides of manganese in particular undoped manganese dioxide (MnO_2) thin films of thickness ranges 85 – 380 nm have been prepared onto glass substrate at a deposition rate of 6.7 nm/min by a simple spray pyrolysis technique under various deposition conditions. The effects of different deposition variables on structural, electrical and optical properties of the films have been studied in detail. These studies show that various deposition parameters have remarkable effects on spray deposited MnO_2 thin films.

X-ray diffraction and Transmission Electron Microscopy studies show that MnO_2 thin films are homogeneous and polycrystalline in structure.

The virgin films are shown highly resistive whereas annealed films exhibit a reasonable conduction. Electrical conductivity has been measured as a function of temperature ranging from 303 to 413K and its conductivity exhibits an anomaly at a temperature 323K. The decrease in resistivity with increasing temperature indicates that the samples are semiconducting in nature.

The heat-treatment of the MnO_2 samples at different ambient have remarkable effects on the electrical transport properties. The annealing was carried out in vacuum for 2 hours at a constant temperature of 473K. During annealing oxygen chemisorption-desorption mechanism is found to play an important role in controlling the electronic properties of the films.

A thickness effect of activation energy is observed in MnO_2 films. The effect shows that the activation energy above anomaly is inversely proportional to the thickness whereas its value is directly proportional below the anomaly temperature.

Variation of electrical conductivity with thickness is observed in MnO_2 films. It is observed that the conductivity increases with thickness and attains a constant value $\approx 6.5\ \Omega^{-1}\text{-m}^{-1}$ at 220 nm. Above this thickness value, the electrical conductivity is approximately thickness independent, which is agreed well with the Fuchs-Sondheimer theory.

Aging effect is studied for consecutive 15 days at various thicknesses of MnO_2 films. This study shows that the conductivity decreases sharply with time and its fall in conductivity is more pronounced in films of lower thickness than the higher one.

The Hall effect study shows that the MnO_2 film is an n-type semiconductor and its band gap is found approximately 0.27eV. The carrier concentration is increased with increasing temperature as well as with increasing thickness. Various grain boundary and energy band parameters have been calculated by using conventional extrinsic semiconductor theory and grain boundary trapping models. The samples are

shown non-degenerate and the Hall mobility is found to be modulated by the grain boundary potential barrier height via the samples temperature.

Thermoelectric power (TEP) of **MnO_2** films has been measured from room temperature up to 403K with reference to pure lead (**Pb**). The thickness and temperature dependence of its related parameters have been studied in detail. This study shows that **MnO_2** sample is an n-type semiconductor. The Fermi level is determined using a non-degenerate semiconducting model. The carrier scattering index, activation energy and temperature co-efficient of the activation energy have been calculated at different range of thickness as well as of temperature. It is interesting to note that the Fermi level is found to be pinned near the conduction band edge with the increase of temperature. The calculated value of the scattering index is $\approx$ -1.5, which indicates that ionized impurity scattering is dominant in the **MnO_2** films.

The optical study was carried out in the wavelength range $0.3 < \lambda < 2.5$ μm using Perkin-Elmer Lambda-19 double beam spectrophotometer at room temperature. This study shows a transition of indirect allowed type with a band gap of E_g = 0.26eV. A similar study of band gap in electrical measurements of **MnO_2** films does give a value of 0.27eV, which is an excellent agreement with the reported value of band gap by other workers.

The calculation of the electron affinity and work function are done for the polycrystalline **MnO_2** samples. It may be explained from the calculation that the bonds between manganese and oxygen are considered as the principal bond and within the limits of native and foreign impurity content, **MnO_2** is more covalent than ionic.

Integrated luminous and solar transmittances as well as reflectance of **MnO_2** films are calculated from the optical data. It is observed that the values of the integrated luminous and solar transmittance are increased up to 593K with deposition temperatures and then their values are decreased monotonously. Similar behavior is also observed for the case of integrated luminous and solar reflectance. The integrated luminous and solar transmittances are decreased with increasing film thicknesses, whereas their values for reflectance are increased with increasing film thicknesses. Higher order of transmittance and lower values of reflectance suggest that this material is a potential candidate for the application in selective surface devices.

ACKNOWLEDGEMENTS

At first I express very much gratefulness to the Almighty Allaha, who gives me the strength and energy to fulfill this research work.

I would like to express my profound gratitude to my supervisor **Dr. M. Khairul Alam Khan**, Professor, and my co-supervisor **Md. Rezaul Islam**, Associate Professor, Department of Applied Physics & Electronics, University of Rajshahi, Rajshahi, for the continuous support and for being always open to discussions. I also thank them for giving me the freedom to do my research work with an appreciable confidence in my work. Due to their constant guidance and inspiring collaboration, I have very much benefited from their knowledge and experience.

I would like to thank to Professor MD. Mozaffor Hossain, chairman and Professor M.A. Sobhan, former chairman of this department for providing necessary facilities to carry out this research work.

I am very grateful to Mr. A. Latif Talukder, principle Instrument Enginner, for his help to do the optical study. I also express my thanks to Mr. Ayub Ali, caretaker of Thin Film laboratory and all other official stuffs of this department.

I would like to express my thanks to all my teachers of the Department of Applied Physics and Electronics for their different kinds of helps and valuable successions. Specially, I express my gratefulness to Dr. Mamunur Rashid Talukder and Syed Mustafizur Rahman, who always inspired me and help me in difficult moments during this work.

Specially thanks are dedicated to Dr. Yoshiyuki Yamamoto, Assistant Professor, Magnetic Materials Lab., School of Material Science, Japan Advanced Institute of Science and Technology, 1-1, Asahidai, Tatsunokuchi, Ishikawa 923-1292, Japan, for his kind help in doing the XRD, TEM and ED studies of the samples. At the same time, I would like to thanks Dr. Syed Anisul Haque, Associate Professor, Department of Applied Physics & Electronics, University of Rajshahi, Rajshahi, who helps me to contact with Dr. Yoshiyuki Yamamoto.

I would also like to thanks the Ministry of Education for granting me study leave during the period of my research work.

I gratefully acknowledged my sponsor U.G.C. for awarding me an M.Phill fellowship to carry out this research work.

I am very grateful to all my teachers, colleagues and stuffs of Carmichael College, Rangpur and Govt. Begum Rokeya College, Rangpur.

I want to thank my teacher Dr. Arun Kumar Basak, Professor, Dept. of Physics, University of Rajshahi, Rajshahi, Md. Abdul Jalil Mia, ex-assistant Prof. Dept. of Physics, Carmichael College, Rangpur and my friend A.K.M. Fazlul Haque, Assistant Professor, Dept. of Physics, University of Rajshahi, Rajshahi, who always inspired and encouraged me to complete this research work.

I also wish to express heartfelt thanks to all my friends and students, who have always encouraged me to complete this work.

I owe to express my deep gratitude and love to my family and acknowledge their unconditional trust and multifaceted support through all these years. Thanks are also given to all my relatives who are always appreciating me to doing this work.

Last, but not least, I am very grateful to my wife for her encouragement and sacrifices during the period of my research work.

The Author

CONTENTS

Chapter 1
Introduction

INTRODUCTION

1.1 OVERVIEW

Experimental work on thin films has been continued in different parts of the world for successful applications of their properties in scientific, engineering and industrial purposes. The increasing demands for microelectronics and micro structural components in different branches of science and technology have greatly expanded the sphere of thin film research [1, 2].

During the last three decades a great deal of research works has been carried out on the thin films of metals, semiconductors, insulators and cermets (granular metal) materials [3]. Sufficient time has also been utilized to search for other new coating materials relevant to electrooptical properties. These include the spectrally selective coating, transparent conducting coating, solar absorbing coating, heating elements, antistatic coating on instrument panels, and electrical contact in liquid crystal, electrochromic and electroluminescent display, smart window coating, photochromic and thermochromic coating etc [4]. According to design and structure of the devices, these coating may be either a single or multilayer on a suitable neutral substrate or may be a layer forming composite structure with the substrate [4]. Among the above varieties of coatings, transparent conducting oxide thin films have initially figured prominently for their application in solar cells [5] and recently their utility in the different branches of science and technology [6] has been extended so much that they have become the subject matter of study and research with great interest.

1.2 APPLICATION AREAS OF THIN FILM

Thin films are widely used in today's technology, and their applications are expected to be even more widespread in the future. It is not possible to give an exhaustive survey over thin film applications, but a list of them is given below [7, 8].

Thin film property category	Typical applications
Optical	• reflective/ antireflective coatings; • interference filters • decoration (color, luster) • compact disks (CD), • spacecraft temperature control • solar absorbing coatings
Electrical	• conductors • insulators (resistors, capacitors, etc,) • semiconductor devices • solar cells • microelectronic devices • super-conductors
Magnetic	• memory disks
Chemical	• barriers to diffusion or alloying • protection against oxidation or corrosion • gas/liquid sensors
Mechanical	•Tribological (wear-resistance) coatings • hard coating for cutting tools • adhesion • lubrication • micromechanics
Decorative	• costume jewelry • watch bezels and bands • eyeglass frames

1.3 CHARACTERISTICS OF THIN FILM

Thin film means a layer of coating of a material onto another material (called, substrate), which is non-reactive except for sufficient adhesion. The properties of thin film change appreciably when it is cooled to a very low temperature or heated to a higher temperature (above room temperature). In general, a number of factors are determined the physical properties of thin films [9]. They are the followings:

(i) **The nature of substrate:** It may be non-crystalline, crystalline or glass and films characteristics may be different for each substrate.

(ii) **The temperature of the substrate during deposition of films:** At low temperature polycrystalline films with high densities of structural imperfections are formed on both vitreous and crystalline substrate, but a high temperature oriented single-crystal films are formed on crystalline substrates.

(iii) **Deposition conditions:** The properties of thin films strongly depend on the deposition conditions, such as substrate temperature, carrier air pressure, solution concentration, spray rate, spray outlet to substrate distance, etc.

(iv) **The annealing temperature:** The freshly deposited films, i.e. virgin films seem to be associated with the formation of highly unstable phases along with innumerable defects and imperfections, i.e. vacancies, interstitials, impurities, grain boundaries, dislocations. Such films are also under strained conditions due to the associated compressive or tensile stresses induced by the deposition or growth conditions. On annealing i.e. keeping the film for a long time at a constant temperature, some of these defects will diffuse out with time and the crystallites or grains tend to assume a minimum potential energy configuration. This leads to the stabilization of the film.

(v) **Annealing cycle:** Annealing cycle, however, also plays an important role for the surface mobility of the atoms at the temperature of the substrate during deposition.

1.4 CHARACTERISTICS OF MnO_2

Manganese dioxide, a gray to black in color, occurs in ores such as pyrolusite [10]. It is an element of group IV in the periodic table. Manganese dioxide is a low band gap [11, 12], high optical constant semiconductor. It has also ferroelectric properties [11, 12].

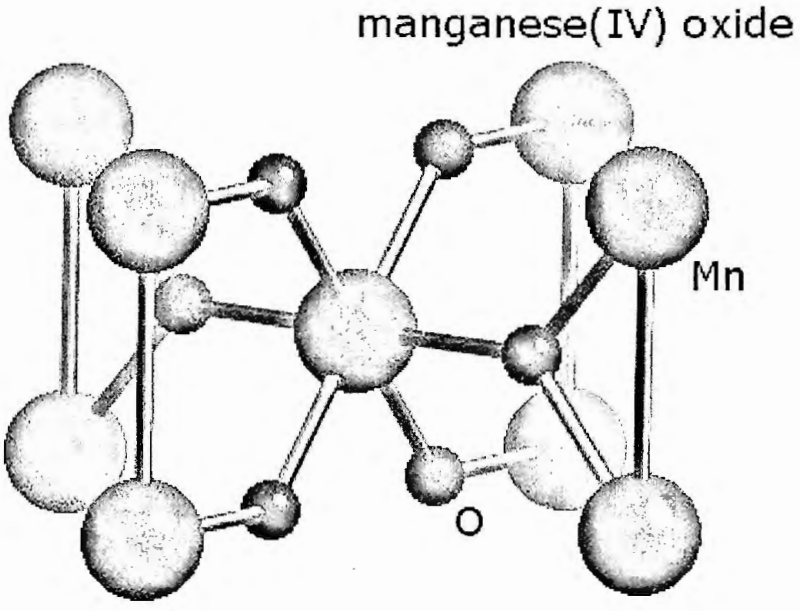

Figure 1: *Crystal Structure of MnO_2.*

[*Reproduced from Reference 10, Chemistry: Web Elements Periodic Table: Manganese: compound data, URL:* http://www.webelements.com/Mn/]

Each $\mathbf{Mn^{4+}}$ ion is connected to two oxygen ions situated at a distance of about 0.17 nm from it [11]. Thus **O-Mn-O** forms a basis of the body-centered tetragonal structure of $\mathbf{MnO_2}$, as shown in Figure 1 [10, 11]. The corner $\mathbf{Mn^{4+}}$ ions have the oxygen linkage along one of the diagonals of the square face, whereas the central $\mathbf{Mn^{4+}}$ ions have a linkage with two oxygen ions along the other diagonal [11]. The conductivity in $\mathbf{MnO_2}$ essentially arises from the controlled valance mechanism [11].

1.5 REVIEW OF EARLIER WORKS

Manganese dioxide has been prepared by many workers in a numbers of techniques. Some of those are briefly presented here.

In 1914 Honda and Sone [13] investigated the variation of the magnetic susceptibilities of pyrolusite ($\mathbf{MnO_2}$) within the temperature range 87 to 826K. The value of the mass susceptibility is reported about 38×10^{-6}.

Sawer and Tower [14] in 1930 recorded the dielectric hysteresis loop of pyrolusite ($\mathbf{MnO_2}$) at different temperatures. Their result indicates that these samples possess spontaneous polarisation, i.e. polarisation that persists even when the applied electric field is zero.

Blechstein [15] in 1938 studied the dielectric constant of $\mathbf{MnO_2}$. It reports that $\mathbf{MnO_2}$ exhibits a very high dielectric constant of the order of 10^5.

In 1950 Hipple [16] studied the temperature dependence of the dielectric constant of $\mathbf{MnO_2}$. It suggests that above 323K this material transforms ferroelectric state to a non-ferroelectric state and this transition is due to a change in the crystal structure or due to a chemical transformation.

Verwey [17] in 1951 studied the frequency dependence of the d.c. and a.c. conductivity of $\mathbf{MnO_2}$. This study shows that there is a slight increase in conductivity with the increase in applied frequency. Volger [18] and Koops [19] performed the similar study in 1951.

In 1953 Mansfield *et al* [20] and Goucher, *et al* [21] investigated the crystal structure of pyrolusite ($\mathbf{MnO_2}$). Their result signifies that the sample is a polycrystalline structure with highly reflecting microcrystalline faces.

In 1954 Sasaki and Kojima [22] measured the electrical resistivity of $\mathbf{MnO_2}$ samples prepared by a technique of pressing pellets out of ground $\mathbf{MnO_2}$ powder. Their reported value of resistivity varies from 30 to 300 ohm-cm.

Lidiard [23] in 1954 investigated the temperature dependence of magnetic susceptibility of pyrolusite ($\mathbf{MnO_2}$). It reports that $\mathbf{MnO_2}$ (rutile) has anti-ferromagnetic behavior.

In 1956 Glicksman and Moorehouse [24] measured the electrical resistivity of $\mathbf{MnO_2}$ samples prepared by a technique of pressing pellets out of ground $\mathbf{MnO_2}$ powder. Their reported value of resistivity ranges from 30 to 300 ohm-cm.

In 1957 Megaw [25] investigated the temperature dependence of dielectric properties of $\mathbf{MnO_2}$. It is reported that the values of dielectric constant are

increased with temperature up to 323K (this temperature varies slightly from sample to sample) and then their values are decreased.

Das [26] studied the Hall effect of $\mathbf{MnO_2}$ in 1958. It reports that $\mathbf{MnO_2}$ is an n-type semiconductor and the Hall mobility is of the order of 10×10^4 $m^2V^{-1}S^{-1}$.

In 1959 Bhide *et al* [27] studied the dielectric hysteresis in pyrolusite ($\mathbf{MnO_2}$). Their result indicates that these samples exhibit a very high dielectric constant and its value is of the order of 10^5. It also reports that at a particular temperature (about 323K) the dielectric constant has a maximum value.

In 1959 Chevillot and Brenet [28] studied the influence of foreign ions on the $\mathbf{MnO_2}$ semiconductor and the temperature dependence of the electrical conductivity. This study suggests that β-$\mathbf{MnO_2}$ is an intrinsic semiconductor with a band gap of 0.26eV.

In 1960 Brenet [29] measured the electrical resistivity of $\mathbf{MnO_2}$ samples prepared by a technique of pressing pellets out of ground $\mathbf{MnO_2}$ powder. The reported value of resistivity ranges from 30 to 300 ohm-cm.

Bhide and Damel [11] in 1960 studied the effects of the temperature, frequency and voltage on the electrical conductivity, dielectric constant and loss factor for pyrolusite ($\mathbf{MnO_2}$). Their study suggests that this sample is an n-type semiconductor and there is an anomaly in conductivity at about 323K. This behavior indicates that the sample becomes ferroelectric below 323K. Their report also indicates that $\mathbf{MnO_2}$ has a rutile body centered tetragonal structure with the lattice constants: a = 4.865 Å, c = 3.824 Å, respectively and each Mn^{4+} ion is connected to two oxygen ions situated at a distance of about 1.7 Å.

In 1960 Vosburgh and Delap [30] studied the discharging mechanism of electrodeposited $\mathbf{MnO_2}$ electrode in the cell containing $(NH_4)_2SO_4$ electrolyte.

Bhide and Dani [12] in 1960 studied the electrical conductivity in oxides of manganese and its related compounds. Their result indicates that $\mathbf{MnO_2}$ is an n-type semiconductor and has a rutile structure with the Mn^{4+} ions on a body centered tetragonal lattice. This study also reports that the value of activation energy ranges from 0.1 to 0.2eV and this sample has ferroelectric behavior with a Curie temperature of about 323K. They also determine that the values of Hall constant, carrier concentration and Hall mobility are - $0.15cm^3$/Coul., $4\times10^{19}/cm^3$ and 1.2 $cm^2V^{-1}S^{-1}$, respectively.

In 1964 Wiley and Knight [31] studied the electrical properties of $\mathbf{MnO_2}$ prepared by pyrolytic decomposition of chemically pure $Mn(NO_3)_2$. They reported that the resistivity of the samples is about 0.1 ohm-cm.

Cash and Clark [32] in 1966 prepared the conductive **MnO_2** films by reactive sputtering technique. Their report indicates that the composition of the manganese oxides depends on the percentage of oxygen in sputtering gas.

In 1966 Valletta *et al* [33] prepared the **MnO_2** film by the pyrolysis of chemically pure $Mn(NO_3)_2$. Their result indicates that substrate temperature, concentration of the manganous nitrate solution and spray rate have remarkable effects on the properties of **MnO_2** film.

Valletta and Pliskin [34] in 1967 reported that the reactive sputtering is a desirable method for the preparation of conductive **MnO_2** films. Their result indicates that the conductivity and oxide nature of the manganese strongly depend on the substrate temperature.

In 1970 Klose [35] studied the electrical properties of **MnO_2** prepared by the pyrolysis of $Mn(NO_3)_2$. The reported value of resistivity varies from 0.23 to 115 ohm-cm and **MnO_2** is an n-type semiconductor with a band gap of 0.37eV. This study suggests that the Hall mobility depends on the resistivity and the ionized impurity scattering is dominant in **MnO_2**.

Kozawa [36] in 1987 studied the effect of **MnO_2** as an electrode in Lithium-**MnO_2** cells containing CF_x or C_2F in the cathode. It is noted that the cell property depends on the discharging behavior of each component (MnO_2, C_2F or CF_x).

In 1987 Goncharov *et al* [37] investigated the density and strength of rolled manganese dioxide electrodes in alkaline cell.

In 1988 Rophoul *et al* [38] studied the kinetices of the catalytic decomposition of hydrogen peroxide solution by Manganese dioxide samples. Their investigation suggests that the catalytic decomposition of hydrogen peroxide increases by the Ga and Mo doped MnO_2.

In 1989 Kuwabara *et al* [39] investigated the effects of **MnO_2** as an electrode in a solid electrolyte cell. Their result indicates that the discharge reaction mechanism of the manganese dioxide cathode in electrolyte cell is similar to that in dry cell.

Takahara [40] in 1989 studied the dielectric property of the Manganese oxide additive mixed sintering ceramic. Their report indicates that the influence of internal electrode material on the sintering of mixed sintering ceramics and the addition of **MnO_2** improve their dielectric properties.

In 1989 Chiba *et al* [41] investigated the physicochemical properties of activated chemical manganese dioxide and its discharge characteristics in $ZnCl_2$ type dry cells. Their result indicates that the charging and discharging of this cell depend on the properties of MnO_2.

Nohma *et al* [42] in 1989 studied the effect of **MnO_2** as an electrode in flat shaped manganese dioxide-lithium secondary battery. Their investigation suggests that the heat-treatment of MnO_2 with the LiOH at about 648K improves the battery performance.

In 1990 Raj *et al* [43] studied the characteristic of electrolytic MnO_2-base oxygen electrodes in alkaline cell.

Jarvis [44] in 1990 studied the Mg/MnO_2 battery performance to increase the water content of the electrode.

In 1990 Lampart *et al* [45] investigated the oxygen-regeneration of discharged manganese dioxide electrode in alkaline cell.

Susana *et al* [46] in 1992 studied the electrochromic properties of **MnO_2** prepared by electrochemical deposition and thermal evaporation techniques, respectively.

In 1993 Erlandsson *et al* [47] studied the electrochromic properties of manganese oxide thin films prepared by electron beam deposition technique. Their result indicates that the best electrochromic efficiency of the film offers in the borate electrolyte.

Mallick and Khan [48] in 1994 studied the pressure effect on the electrical properties of **MnO_2** thin films prepared by thermal evaporation technique. It is reported that there is an anomaly in conductivity at temperature near 323K. Their result indicates that the samples are n-type semiconductors and its activation energy is of the order of 0.1 to 0.3eV. Their aging effect study indicates that the decrease in conductivity may be due to adsorption or absorption of gases or other impurities.

In 1994 Fau *et al* [49] studied the electrical properties of sputtered **MnO_2** thin films. Their result indicates that the properties of the films depend on the percentage of oxygen in sputtering gas and the substrate temperature.

In 1997 Gassa *et al* [50] studied the impedance effect in electrodeposited manganese oxide films onto Pt substrate in borate buffers. It is reported that the films are n-type semiconductors.

Tanakaa and Tsujib [51] in 1998 prepared **MnO_2** by pyrolysis from a mixture of manganese carbonate and potassium tert-butoxide at 603K.

In 1998 Xu *et al* [52] studied the preparation and properties of amorphous **MnO_2** formed by sol-gel technique. Their result suggests that this material is a good candidate as cathode for the application in lithium batteries.

Gorgulho [53] in 1998 studied the electrical property of **MnO_2**. It reports that manganese dioxide is an n-type semiconductor.

In 1998 Poinsignon [54] studied the chemical-structural disorder, electronic properties and electrochemical activity of **MnO_2**, respectively.

In 2000 Gal *et al* [55] studied the Lithium insertion into **γ-MnO_2** compounds. Their report indicates that **γ-MnO_2** compound may be good candidate for the application in Li-metal rechargeable batteries as a cathode.

Lvov *et al* [56] in 2000 prepared the nanostructure films of manganese oxide by alternate-layer adsorption technique.

In 2001 Guo *et al* [57] prepared single crystal **β-MnO_2** films onto MgO substrate by plasma-assisted molecular beam epitaxy technique.

Long *et al* [58] in 2001 prepared highly porous and nanostructure thin films of manganese oxide by sol-gel-derived technique and studied their electrochemical and electrochromic properties.

In 2001 Chigane *et al* [59] studied the preparation and properties of manganese oxide thin films by electrolysis/chemical deposition. Their result indicates that the samples are electrochromic in nature.

Juline *et al* [60] in 2001studied the structural defects in **γ-MnO_2** thin films by Raman spectroscopy.

In 2002 Wang and Lie [61] studied the selected-control hydrothermal synthesis of **α-** and **β-MnO_2** single crystal nanowires. Their XRD and TEM studies indicate that the structure of **β-MnO_2** is a pure tetragonal phase [space group: $P4_2/mnm$ (136)] with lattice constants: a = 4.3999 Å and c = 2.8740 Å, respectively.

In 2003 Unuma *et al* [62] prepared **MnO_2** thin films onto glass substrates from aqueous solutions in a temperature ranges from 313 to 333K by a modified chemical bath deposition technique. Their report indicates that the composition of the starting solution, deposition temperature and the compatibility of the substrates to the film have remarkable effects on the film properties.

Mingdeng *et al* [63] in 2005 studied the synthesis of single-crystal **MnO_2** nanowires by a soft chemical process. Their XRD and TEM studies suggest that the structure of **β-MnO_2** is polymorphic in structure and has a pure tetragonal phase with lattice constants: a = 0.4399 nm, c = 0.2874 nm, respectively.

1.6 THE AIM OF THE PRESENT WORK

Research and development on thin films have led to the conclusion that different classes of materials are of particular interest for different applications. In recent years manganese dioxide has a variety of applications, particularly as an electrode in electrochemical and electrochromic batteries, in fuel cells as well as in energy efficient devices applications. Manganese dioxide is a low band gap, high optical constant semiconductor that exhibits ferroelectric properties.

Literature reports indicate that thin films of manganese dioxide have been produced by a number of techniques by many researchers. Most of the reports address themselves to the electrochromic, electrochemical and spectroscopic performance of the films, emphasizing the inter-relation between the substrate materials, film structure and their performance in catalytic and rechargeable battery oriented applications. Although there have been a number of investigation on the electrical, optical, electrochemical and electrochromic properties of the films, but no systematic study appears to have been done on electrical, thermoelectric, Hall effect, optical properties and also on structural studies at varying deposition conditions. Moreover, there is a considerable lack of understanding concerning the surface properties of the oxides in different applications oriented measuring techniques. Different microstructures caused by different deposition conditions could be the probable reasons to the lacks in understanding. Hence there is a need to study how varying deposition conditions affect the physical properties of manganese dioxide films to assess its usefulness in the energy efficient devices applications.

In the light of the previous results and the existing problems it is necessary to select materials that can be deposited by a simple and easy method to yield relatively better transparent conducting films. Furthermore, among the various film deposition methods, chemical spray pyrolysis method is indigenous, simple and inexpensive. The above mentioned causes stimulate the author to deposit $\mathbf{MnO_2}$ thin films by spray pyrolysis technique.

To utilize these films successfully it is essential to characterize the sample and to study of their different properties. The following studies have been carried out and reported in this thesis:

A Production of MnO_2 thin films by spray pyrolysis technique,

B Characterization of MnO_2 samples by X-ray diffraction,

C Characterization of MnO_2 samples by Transmission Electron Microscopy,

D Effect of deposition variables on film thickness and film resistivity;

E Effect of films thickness on resistivity and activation energy;

F Heat-treatment of the as-deposited films;

G Aging effect;

H Hall effect studies;

I Studies on the Thermo electrical effect;

J Optical studies;

K Electron affinity and work function calculation for MnO_2 thin films;

L Selective surface studies.

Chapter 2

Theoritical Aspect of Thin Film

Deposition of films by vacuum and non-vacuum techniques yield films of different nature but the basic principles of condensation and nucleation of the films from its vapor phase (in the initial film growth stage) are the same. Chemical spray deposition method is a non-vacuum technique. To deposit a good quality film, one should have a thorough knowledge of the principles that are associated with this method. In this chapter, a brief description of nucleation and film growth aspects are presented and then it includes the methods of analysis of various properties of semiconducting thin films.

2.1 OVERVIEW OF VARIOUS THIN FILM DEPOSITION TECHNOLOGIES

The different technologies for thin-film depositions are tabulated in Table 2.1[64]. Only a detail description of spray pyrolysis technique is included in this chapter.

Table 2.1

EVAPORATION METHODS	
Vacuum Evaporation	
Conventional vacuum evaporation	Molecular-beam epitaxy (MBE)
Electron-beam evaporation	Reactive evaporation
GLOW-DISCHARGE PROCESSES	
Sputtering	**Plasma Process**
Diode sputtering	Plasma –enhanced CVD
Reactive sputtering	Plasma oxidation
Bias sputtering (ion plating)	Plasma anodization
Magnetron sputtering	Plasma polymerization
Ion beam sputtering	Plasma nitridation
Ion beam sputter deposition	Plasma reduction
Reactive ion platting	Microwave ECR plasma CVD
Cluster beam deposition (CBD)	Cathodic arc deposition
GAS-PHASE CHEMICAL PROCESSES	
Chemical Vapor Deposition (CVD)	**Thermal Formation Processes**
CVD epitaxy	Thermal oxidation
Atmospheric-pressure CVD (APCVD)	Thermal nitridation
Low-pressure CVD (LPCVD)	Thermal polymerization
Metalorgainc CVD (MOCVD)	
Photo-enhanced CVD (PHCVD)	
Laser-induced CVD	
Electron-enhanced CVD	Ion implantation
LIQUID-PHASE CHEMICAL TECHNIQUES	
Electro Process	**Mechanical Techniques**
Electroplating	Spray pyrolysis
Electroless plating	Spray-on techniques
Electrolytic anodization	Spin-on techniques
Chemical reduction plating	
Chemical displacement plating	
Electrophoretic deposition	Liquid phase epitaxy

2.2 THEORETICAL CONSIDERATION OF CHEMICAL SPRY TECHNIQUE

Spray Pyrolysis [65, 66] which is the main area of this work, involving spraying of an ionic solution, usually aqueous, containing soluble salts of the constituent atoms of the desired compounds onto heated substrate. Hydrolysis and pyrolysis are the main chemical reactions normally involved in this technique. There is a bit of difference between spray pyrolysis (SP) and chemical vapor deposition (CVD). In spray pyrolysis technique, the chemicals are vaporized and are reacted on the hot substrate surface after reaching on it [67], but in chemical vapor deposition, vaporization takes place before reaching the substrate surface. In SP technique there are two sections. One of it produces spray particles and in other section, the pyrolysis reaction takes place and this section is known as reactor zone.

To discuss this method, it is needed to consider first the chemistry, the thermodynamics and possible chemical kinetics that are the essential features of the chemical spray method. Some of the relevant usefulness of these studies is briefly described below.

2.2.1 Chemistry of the Method

Spray Pyrolysis method can be defined as a material synthesis, in which the constituents of the vapor phase react to form a solid film at some surface, thus the occurrence of chemical reaction is an essential characteristic of the pyrolysis method.

To understand this process, it is needed to know, which chemical reactions occur in the reactor and to what extent. Furthermore, the effects of process variables such as temperature, pressure, solution concentration and flow rates on these reactions can be understood. The nature and extent of chemical reactions can be deduced if one knows the composition of the solid and vapor phases in pyrolysis system. The composition of the solid product can be analyzed after the deposition but that of the vapor phase must be determined in situ at the particular reaction condition.

2.2.2 Chemical Reaction

The types of reaction in chemical methods to form a solid film are as follows:

(a) Pyrolysis;

(b) Hydrolysis;

(c) Oxidation;

(d) Reduction;

(e) Synthesis;

(f) Disproportion;

(g) Carbide and Nitride formation;

(h) Combined reaction, etc.

Among these reactions, the first four types are very important and have role in spray pyrolysis method [64, 68].

The thermal decomposition of a compound to yield a deposit of the stable residue is called pyrolysis and the chemical decomposition that is caused by the action of water is called hydrolysis. Hydrolysis and pyrolysis reactions are involved in the formation of MnO_2 thin films by the pyrolytic method. Hydrolysis reaction occurs first in preparing aqueous ionic solution of starting material and the pyrolysis reaction takes place onto the glass substrate as a MnO_2 thin film. During the MnO_2 film deposition by spray pyrolysis technique the probable reaction that occurs under non-equilibrium conditions is:

$$Mn(C_2H_3O_2)_2.4H_2O + H_2O \overset{heat}{\leftrightarrow} MnO_2 + 2CH_3COOH + 3H_2O + H_2 \quad (2.1)$$

2.2.3 Reactor System

The reactor is an important part of a pyrolytic deposition system. Its design and equipments should be adequate enough to accomplish the following functions [68, 72]:

(a) Supply heat to the reaction site, namely substrate material being coated and control of this temperature.

(b) Remove the by-product exhaust gasses from the deposition zone and safely dispose of them.

The quality of the film depends on the degree of fulfillment of the above mentioned functions and to meet these requirements one should give attention to avoid the complexity in the construction of the reactor.

The geometry and construction material of the reactor are selected by physical and chemical characteristics of the entire system and by the process

parameters. For the chemical spray deposition method usually three types of rectors are found:

(i) Low temperature reactor system whose temperature is kept < 773K at normal pressure.

(ii) High temperature reactors whose operating temperature > 773K at normal pressure.

(iii) Low pressure reactors.

Low pressure reactors are generally hot-wall type but the low temperature or high temperature reactor may be either of hot wall or cold wall type.

It is expected that a fully developed thermal field exists in hot-wall reactors because of the fact that low gas velocities are employed there. These types of reactors are generally tubular in form. In the cold-wall reactors the situation are more complex [64, 68].

Hot-wall reactors are used in the case of system where the deposition reaction is exothermic in nature, since the high wall temperature minimizes or even presents undesirable deposition on the reactor walls. In the case of endothermic reaction cold-wall reactors are more useful [64, 68].

2.2.4 Transport Phenomena in the Reactor

Transport phenomena in fluids are related to the nature of the fluid flow. The following parameters affect the nature of gas flow in reactor [64, 68]:

(i) Velocity of flow;

(ii) Temperature and temperature distribution in the system;

(iii) Pressure in the system;

(iv) Geometry of the system, and

(v) Gas or vapor characteristics.

For following two basic reasons the study of transport phenomena is important [68]:

(a) The requirement of thickness can be fulfilled only when equal amount of the reactants are delivered onto the substrate in the system.

(b) The requirement of high chemical efficiency to achieve satisfactory growth rates and utilization of input chemicals; this means that sufficient amounts of reactants must be delivered to the film growth surfaces.

All the above points should be brought under consideration at the time of designing the reactor.

2.2.5 Thermodynamics of Pyrolytic Deposition

The main functions of thermodynamics in relation to chemical spray method are to predict the feasibility of the process under some specified conditions and to provide quantitative information about the process. Properly performed thermodynamic calculations give the theoretically obtainable amount of a deposit under specific experimental conditions, such as the temperature, pressure in the reactor and the input concentrations of the reactants [64, 68]. Thus, thermodynamics can be used as a guide line for establishing general process parameters. Initial step of a chemical spray deposition process is to perform the necessary thermodynamic calculations to obtain the general conditions. In order to perform the calculations, one needs reliable thermodynamic data. The most useful data are free energy of formation of all vapor and condensed constituents of the system. G_f^0 is the standard free energy of formation of a compound and $\Delta G_f^0 = 0$ for all elements in their standard state. The free energy of some chemical reaction (ΔG_f^0) can be calculated if (ΔG_f^0) values are known [68].

$$\Delta G_f^0 = \sum \Delta G_f^0 \text{ products} - \sum \Delta G_f^0 \text{ reactants} \qquad (2.2)$$

In chemical spray deposition, one usually deals with a multicomponent and multiphase system. Most often, there are only two phases, the vapor and solid; although more than one condensed phase may be present. There are several ways for computing thermodynamic equilibrium in multicomponent system. Most important method is the optimization method.

2.2.6 Optimization Method

Consider a system in which a chemical reaction proceeds to some degree of completion [68] ε:

$$(1-\varepsilon)\ (\text{Reactants}) \rightarrow \varepsilon\ (\text{Products}) \qquad (2.3)$$

If one plots the free energy of the system versus ε, one sees that the energy curve has a minimum at some value of ε. This value of ε is the equilibrium concentration of reactants and products. The equation describing the free energy (G) of the whole system consisting of 'm' gaseous spices and 's' solid phases is [68]

$$G = \sum_{i=n_i}^{m} \left(n_i^g \Delta G_{fig}^0 + RT \ln P + 2T \ln \frac{n_{ig}}{N_g}\right) + \sum_{i=1}^{s} n_i^s \Delta G_{fis}^0, \qquad (2.4)$$

where n_i^g and n_i^s are the number of moles of gaseous and solid species, respectively, N_g is the total number of moles of gaseous species, P is the total pressure, ΔG_{fig}^0 and ΔG_{fis}^0 are the free energies for the formation of gaseous and solid species, respectively. The objective of optimization calculations is to determine the set of n_i which minimizes G. The set of n_i represents the equilibrium composition of the system.

2.2.7 Kinetics of the Method

The situation in spray pyrolysis reaction might differ from the prediction of thermodynamical equilibrium calculations. The deposition reaction is almost always a heterogeneous reaction [68]. The sequence of events in the usual heterogeneous processes can be described as follows:

(a) Diffusion of reactants to the surface;

(b) Adsorption of reactants at the surface;

(c) Surface events, such as chemical reaction, surface motion, lattice incorporation, etc.

(d) Desortption of products from the surface;

(e) Diffusion of the products away from the surface.

The application of kinetics in film deposition process has been explained by Eversteijn [69]. Some of the factors that cause deviation from equilibrium are:

(i) Temperature dependence of deposition rate: for a given substrate the nature of the rate controlling step changes with temperature. The rate controlling steps are:

(a) Adsorption of reactants on the substrate surface;

(b) Diffusion of reactants and products to and from the substrate surface, respectively.

The rate of deposition (r) is exponentially dependent on the temperature (T) as given by **Arrhenius** rate equation:

$$\mathbf{r = a \exp\left(-\frac{\Delta E}{k_B T}\right)}, \qquad (2.5)$$

where ΔE is the activation energy for the process and 'a' is the frequency factor.

(ii) Dependence of the deposition rate on substrate orientation:

It is well known that the deposition rate can strongly depend on the crystallographic orientation of the substrate [70, 71].

There are several fundamental reasons for the observed differences, among them are:

(1) Densities and geometric arrangements of surface sites;

(2) The number and nature of surface bonds;

(3) The composition of various crystallographic surfaces;

(4) The number and nature of surface features, such as steps, kinks, ledges, vacancies, etc.

All of these factors can influence on deposition by affecting adsorption, desorption, surface mobility, reactivity, etc [68].

It is important to keep in mind that while thermodynamics specifies what ought to happen in the reactor, the kinetics determine what actually will happen in the reactor.

2.3 FILM GROWTH ASPECTS

The properties of thin film strongly depend on their structure. Therefore, it is important to know the factors that govern the structure of the film. When spray particles reach to the substrate surface, then following processes can take place [64, 72]:

(a) Impingement (deposition) onto the substrate surface;

(b) Reflection of impinging atoms;

(c) Desorption (evaporation) from the substrate surface.

The schematic figure of the above processes is shown in Figure 2.1

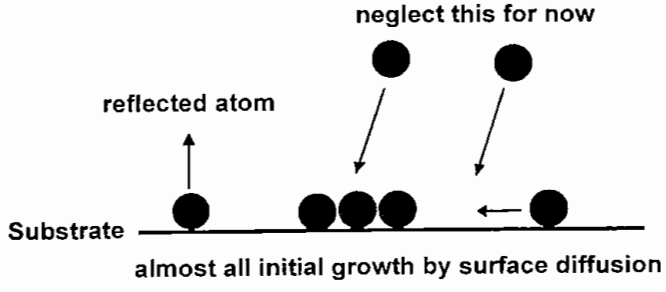

Figure 2.1: *Initial stage of the film growth onto substrate. [Reproduced from reference 72, M. Ohring, in "The Materials Science of Thin films", Academic Press, New York, 1992.]*

After impingement of the spray particles onto substrate surface, the following steps take place to form film:

1. Thermal accommodation:

In this stage the impinging atoms lose enough energy thermally to stay on the substrate surface. It is a very fast process, i.e. around 10^{-14} seconds [68, 76].

2. Binding:

When the atoms are stay on the substrate surface due to the thermal accommodation, then the atoms are bounded. There are two types of surface bonds take place [64, 72]:

(a) Physisorption (physical adsorption) bonds: which are Van der Waals type and it is weak bonds;

(b) Chemisorption (chemical adsorption) bonds: which are chemical bonds and these are strong bonds.

3. Surface Diffusion:

In this stage atoms are adsorbed to form clusters. Clusters are stable. It is the primary stage of nucleation. Two processes can take place in the cluster formation [64, 72]:

(1) Clusters have a condensation energy per unit volume which is lower than the desorption rate.

(ii) Clusters have a higher surface energy than individual atoms.

4. Nucleation:

The stable clusters are called nuclei and the process of formation nuclei is called nucleation. In order to explain the nucleation, there are two types of models such as

(a) Capillarity Model (heterogeneous nucleation);

(b) Atomistic or Statistical nucleation model.

The modern theory of nucleation is based upon the atomistic nucleation concept [68], which states that not all surfaces have equal bonding characteristics. Those with strong bonds are particularly favorable nucleation sites. When nuclei reach a certain size, it becomes energetically more favorable for them to grow than to reevaporate. The growing nuclei come into contact to form island stage.

5. Island Growth:

To explain the island growth stage there are three models, such as

(a) According to Volmer-Weber [73] model to form three dimensional islands, films atoms are more strongly bond to each other than to substrate as shown in Figure 2.2. In this model diffusion takes place slowly.

Island growth (Volmer-Weber)

Figure 2.2: *Volmer-Weber model to form three dimensional island.*

[Reproduced from reference 72, M. Ohring, in "The Materials Science of Thin films", Academic Press, New York, 1992.]

(b) According to Frank-van der Merwe model to form three dimensional islands, film atoms are more strongly bound to substrate than to each other as shown in Figure 2.3.

Island growth (Frank-van der Merwe)

Figure 2.3: *Frank-van der Merwe model to form three dimensional island.*

[Reproduced from reference 72, M. Ohring, in "The Materials Science of Thin films", Academic Press, New York, 1992.]

(c) According to Stranski-Krastanov model to form three dimensional islands are growth layer by layer and finally form three dimensional islands, as shown in Figure 2.4.

Island growth (Stranski-Krastanov)

Figure 2.4: *Stranski-Krastanov model to form three dimensional island.*

[Reproduced from reference 72, M. Ohring, in "The Materials Science of Thin films", Academic Press, New York, 1992.]

6. Island Coalescence:

The formed islands coalesce with the neighbour ones, which are known as island coalescence. Three mechanisms can take place in the coalescence stage [64, 72],

(a) In the Ostwald ripening mechanism- the atoms are adsorbed by the small islands more readily than larger islands;

(b) In the sintering mechanism- the neighbour islands are coalesce to reduce the surface energy; and

(c) In the cluster migration mechanism- the smaller clusters move randomly and some of them are absorbed by the larger clusters to increase their radius and height. All these mechanisms are shown in Figure 2.5.

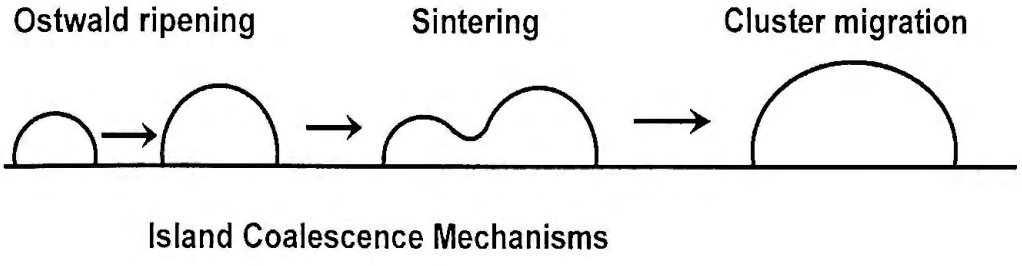

Figure 2.5: *Three mechanisms in the island coalescence stage.*

[Reproduced from reference 72, M. Ohring, in "The Materials Science of Thin film", Academic Press, New York, 1992.]

7. Channel Stage:

As the coalescence continues with deposition there will be a resultant network of the film with channels in between as shown Figure 2.6. These channels may remain void and soon some secondary nuclei start to grow within their void space in the channel [64, 72].

Figure 2.6: *Channel stages.*

[Reproduced from reference 72, M. Ohring, in "The Materials Science of Thin films", Academic Press, New York, 1992.]

With further deposition these nuclei will increase in size along with the film thickness in addition to form of new islands and eventually join to the main islands or aggregate thus bridging the gaps.

8. Continuous Film Growth Stage:

When all the gaps of the channel stage are completely bridged by the secondary nuclei, films will be continuous, as shown in Figure 2.7.

Figure 2.7: *Continuous film stage.*

[Reproduced from reference 72, M. Ohring, in "The Materials Science of Thin films", Academic Press, New York, 1992.]

However, it often happens that some void space may still remain unbridged. In an ideal continuous film there should not be any gap in the aggregate mass. Such a stage in a film can be obtained only when the film has attained certain average film thickness [3]. The minimum film thickness for continuous stage is dependent on the nature of the deposits, modes of deposition, deposition parameters etc [3].

2.3.1 Polycrystalline and Amorphous Thin Films

The films deposited by spray pyrolysis are generally polycrystalline or amorphous in structure [74]. Lower temperature and higher gas phase concentration are actually favorable in forming polycrystalline film. In these situation the rate of arrival of the aerosol (spray particles) at the surface is high, but the surface mobility of adsorbed atoms is low [74]. A large number of differently oriented nuclei are formed, after coalesce between them the films that are obtained possess grains of different orientation. Further decrease in temperature and increase in supersaturation result in even more nuclei and consequently in finer grained films are deposited. When crystallization is completely stopped formation of amorphous film is favored [74].

2.3.2 The Incorporation of Defects during Film Growth

When the islands during the initial stages of thin film growth are still quite small, they are observed to be perfect single crystal [75]. A large number of defects are incorporated in the film during their recrystallization process at the early stage of film formation [75]. The defects that are usually encountered in spray deposited films are lattice vacancies, stoichiometric excess and grain boundary. Another type of defect namely surface roughness which stems from the quality of the sprayer is especially important in the use of spray deposited films. The properties of the film are strongly affected due to surface roughness if the film thickness is low. The most frequently encountered defects in evaporated films are dislocations, which are less important in chemical spray deposited films.

2.3.3 The Grain Boundaries

In polycrystalline thin film, the grain size and the boundary regions markedly depend on the deposition variables such as [68]

(i) The film thickness;

(ii) Substrate temperature;

(iii) Annealing temperature and

(iv) The deposition rate.

Thus the numbers of such boundaries are controllable parameters. The variation of crystallite size with the parameters mentioned above are shown schematically [76] in Figure 2.8. From this figure the dependence of grain size on film thickness is that the larger grains are expected as the new grains are nucleated on the top of the old ones after a certain film thickness has been reached. Another possibility of getting larger grain sizes are expected for increasing substrate or annealing temperature because of an increase in surface mobility. Thus allowance is made to the film to decrease its total energy by growing large grains and thereby decreasing its grain-boundary area. Annealing at temperatures higher than the deposition temperature increases the grain size but the growth effect is significantly different from that obtained by using the same temperature during deposition [77]. The dependence of grain size on deposition rate is less obvious but can be understood on the basis that film atoms just impinged on the surface. Although they may possess a large surface mobility become buried under subsequent layer at high deposition rates before much diffusion can take place [76]. In order for this effect to operate, however, a certain minimum rate must be expected.

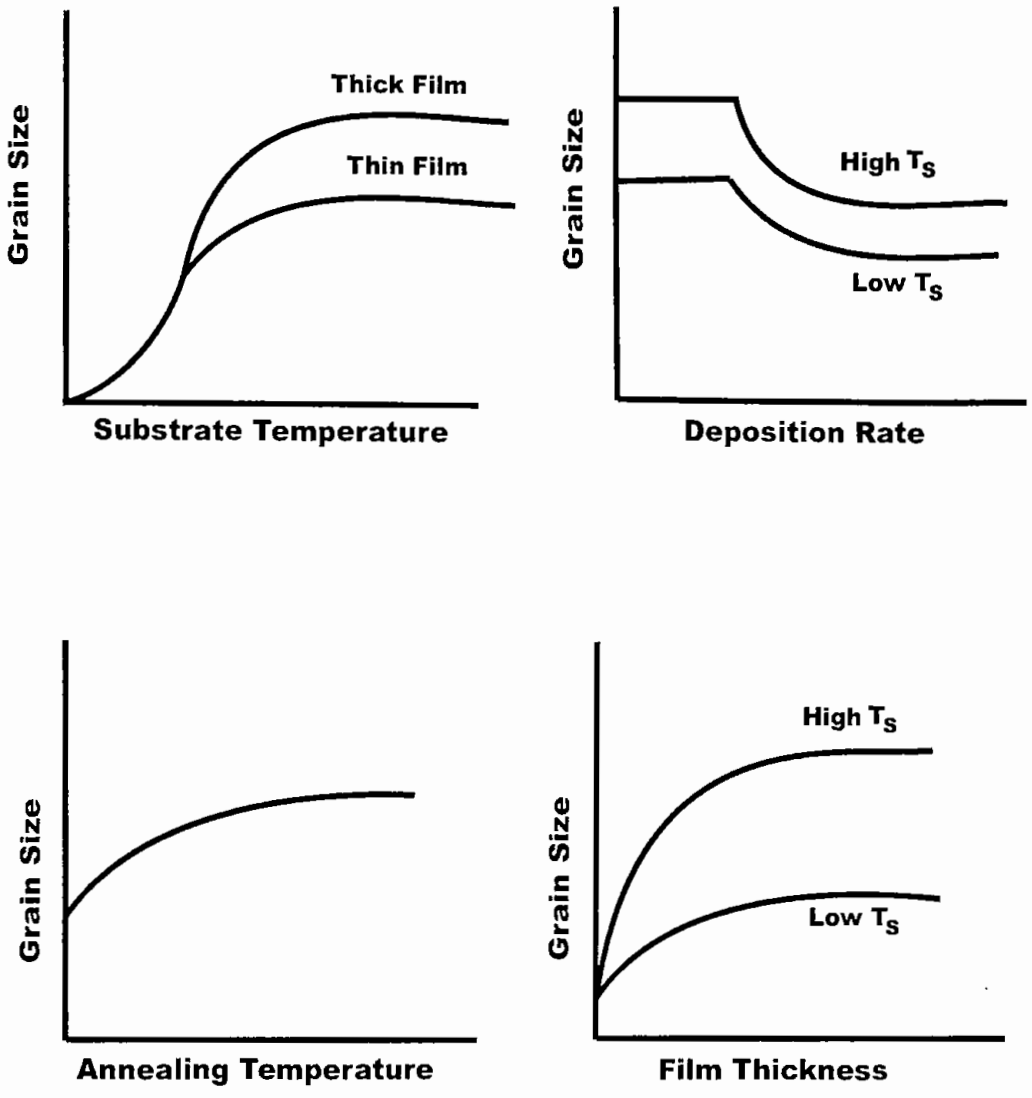

Figure 2.8: *Dependence of grain size on substrate temperature, deposition rate, annealed temperature and film thickness.*

[Reproduced from reference 72, M. Ohring, in "The Materials Science of Thin Films", Academic Press, New York, 1992.]

Rather than this threshold rate, grain size is limited by temperature alone and above it the grain size is decreased more and more for higher and higher rate. The rate of deposition does not significantly affect the grain size except at very high deposition rate.

Statistical methods are generally employed for analyzing the electrical and optical properties of semiconducting materials.

2.4 MEASUREMENT OF FILM THICKNESS

Film thickness plays an important role on the properties of thin film and thus it is one of the most significant film parameter. Therefore, the thickness should be measured with great care as far as possible to have an accurate value. The thickness may be measured either by monitoring the rate of deposition or after the film is taken out of the deposition chamber. The latter type is appropriate for the spray deposition technique because it is operated in open atmosphere. There are many techniques for measuring film thickness, such as Microbalance technique, Crystal oscillatory, Photometric, Ellipsometry, Optical interference, etc.

2.4.1 Method Adopted for the Present Work

Optical interference method is one of the film thicknesses measuring methods by which the thickness of the thin film can be determined accurately. In this method two reflecting surfaces are brought into close proximity to produce interference fringes.

Weiner [78] was the first to use interference fringes for the measurement of film thickness. Latter on using Fizeau fringes, Tolansky [79] developed this method (interferometric method) to a remarkable degree and is now accepted as a standard method.

For the experimental setup a low power microscope, a monochromatic source of light, a glass plate and an interferometer are required. To see the Fizeau fringes of equal thickness in a multiple beam interferometer a thin absorbing film on a glass substrate with an auxiliary reflecting coating on the film surface is required. For a transparent film with a very smooth surface no such auxiliary coating is necessary [80].

The film whose thickness is to be measured is required to form a step on a glass substrate and over it another plane glass plate (Fizeau plate) is placed. This type of interferometer is shown in Figure 2.9(a). When the interferometer is illuminated with a parallel monochromatic beam of light (sodium light) at normal incidence, a fringe system [as shown in Figure 2.9(b)] is produced and is viewed with a low power microscope.

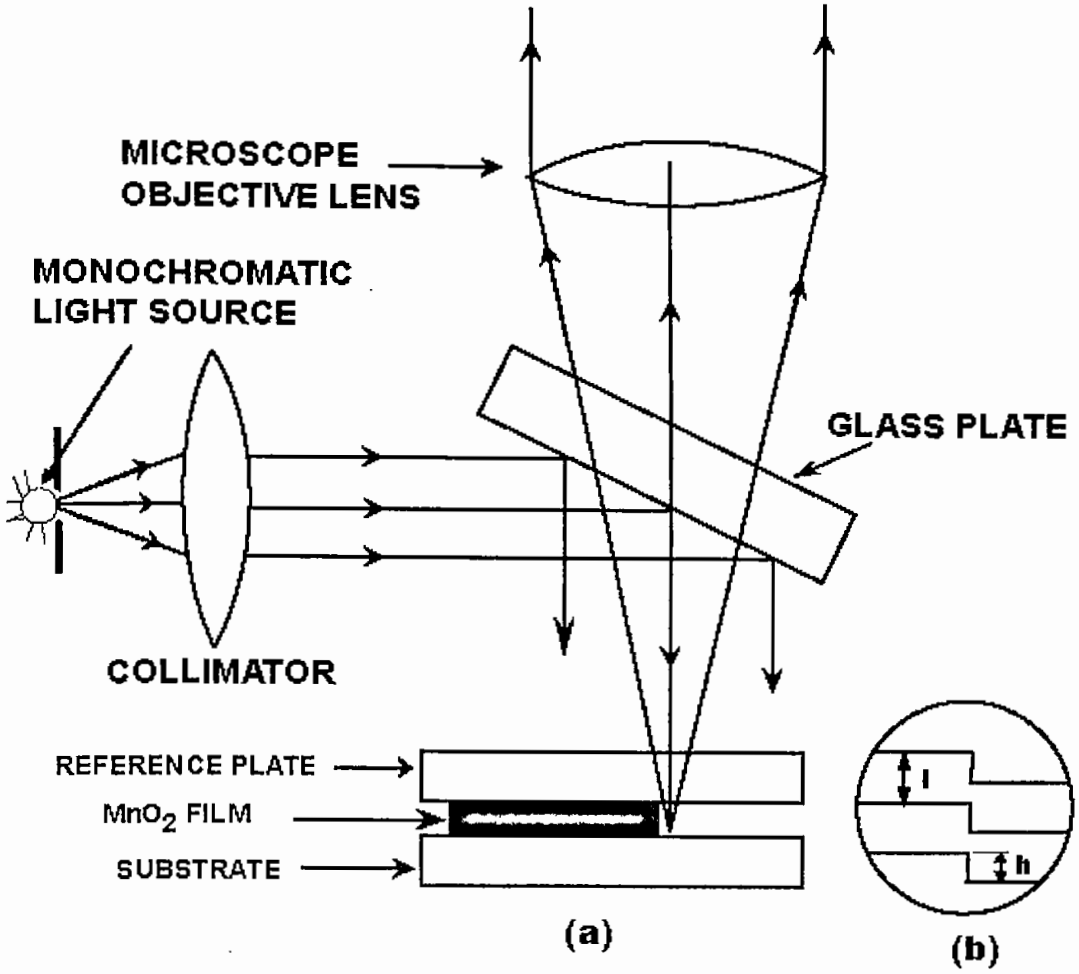

Figure 2.9: *(a) Enlarge view of the interferometric arrangement for the measurement of film thickness;*
(b) The fringe pattern with step height 'h' and fringe spacing 'I'.
[Reproduced from reference 8, K.L. Chopra, in "Thin Film Phenomena" Published by McGraw-Hill Book Company, New York, 1969.]

Dark fringes are also observed against a white background. The displacement 'h' of the fringe system across the film-substrate step is then measured to calculate the film thickness (t), using the relation.

$$t = \frac{\text{step height}}{\text{fringe spacing}} \times \frac{\lambda}{2} = \frac{h}{I} \times \frac{\lambda}{2} \qquad (2.6)$$

where λ is the wavelength of the monochromatic light (Sodium light). In this method, thickness from 3 nm to 2,000 nm can be measured with an accuracy of ± 5 nm .

2.5 STRUCTURAL ANALYSIS OF THIN FILMS

The techniques employed for structural analysis of thin films may be classified under two groups, one dealing primarily with the "surface" structure and the other with "volume and surface" structure [8]. This arbitrary classification is obviously meaningless for ultra thin films. The two groups consist of the following techniques [8].

(a) Optical interference, light-figure reflectograms, low-energy electron diffraction (LEED), field-emission and field-ion microscopy, sputter-ion microscopy, electron-reflection diffraction and electron microscopy.

(b) X-ray microscopy or topography, X-ray diffraction (XRD), transmission electron diffraction and Transmission electron microscopy (TEM).

The following two methods are generally used to study the structural analysis of the thin films.

2.5.1 X-ray Diffraction (XRD) Study

The X-ray diffraction (XRD) provides substantial information on the crystal structure. XRD is one of the oldest and effective tools for the determination of the atomic arrangement in a crystal; X-rays are the electromagnetic waves and its wavelength ≈ 0.1nm. The wavelength of an X-ray is thus of the same order of magnitude as the lattice constant of crystals.

When X-rays are incident on a crystal surface, they are reflected from it. The reflection obeys the following Bragg's law

$$\mathbf{2d\sin\theta = n\lambda}, \tag{2.7}$$

where d is the distance between crystal plane; θ is the X-ray incident angle; λ is the wavelength of the X-ray and n is a positive integer. Bragg's law also suggests that the diffraction is only possible when $\lambda < 2d$.

2.5.2 Transmission Electron Microscopy (TEM) Study

The specific crystal structure was determined by the Electron Diffraction. The ring pattern of Electron Diffraction indicates the structure of the films. The interplanar distances (d_{hkl}) of the crystalline phase are calculated by means of the following expression [81]:

$$\mathbf{d_{hkl} = \frac{\lambda L}{R}}, \tag{2.8}$$

where λ is the electron wavelength, L is the effective camera length of the TEM and R is the radius of the rings of diffraction pattern.

2.6 RESISTIVITY OF SEMICONDUCTOR

Van-der-Pauw technique [82] is one of the standard and widely used techniques for the measurement of resistivity of thin film.

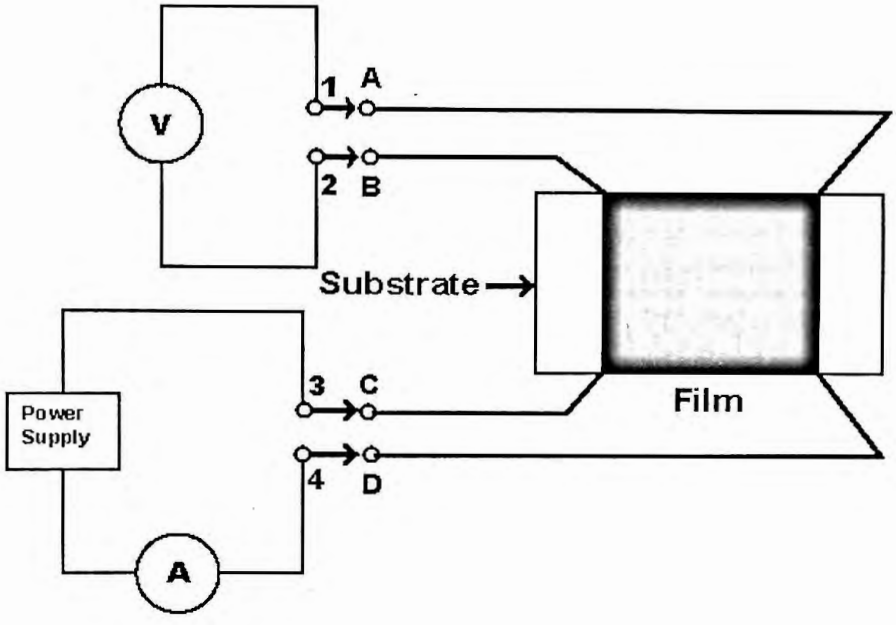

Figure 2.10: *Schematic diagram for the measurement of film resistivity; 1, 2, 3 & 4 are meter terminals and A, B, C & D are the film terminals; Arrows indicates commutator switches.*

Figure 2.10 shows the van-der-Pauw's specimen with four small contacts A, B, C and D in order; 1, 2, 3, and 4 indicate the terminals of the electrometer for the measurement of voltage and currents, respectively. The sample should not need to be of the shape as shown in figure. This method is applicable for any arbitrary shape of uniform sheet of material with four contacts applied to the periphery. Through commutative switches the connections are made between the film and the meter terminals.

If a dc current I_{AB} entering the specimen through the contact A and leaving it through the contacts B, produces a potential difference V_{CD} between the contacts D and C then $R_{AB,CD}$ can be expressed as

$$R_{AB,CD} = \frac{V_{CD}}{I_{AB}}.$$

Similarly,

$$R_{BC,DA} = \frac{V_{DA}}{I_{BC}},$$

$$R_{BD,AC} = \frac{V_{AC}}{I_{BD}}$$

and $$R_{CD,AB} = \frac{V_{AB}}{I_{CD}}.$$

Using the reciprocal theorem Van-der-Pauw showed that

$$\rho = 4.543\, t \times \left(\frac{R_{AB,CD} + R_{BC,DA}}{2}\right) \times \int\left(\frac{R_{AB,CD}}{R_{BC,DA}}\right) \ \Omega\text{-cm} \qquad (2.9)$$

where t is the film thickness and expressed in cm. The correction factor $\int$ has been calculated by Van-der-Pauw and is equal to unity, when

$R_{AB,CD} \cong R_{BC,DA}$, then Equation 2.9 can be written as

$$\rho = 2.266\, t \times (R_{AB,CD} + R_{BC,DA}) \ \Omega\text{-cm} \qquad (2.10)$$

If σ be the conductivity of the film, then

$$\sigma = \frac{1}{\rho} \ (\Omega\text{-cm})^{-1} \qquad (2.11)$$

2.7 THE ACTIVATION ENERGY

The activation energy (E_a) measures the thermal or other form of energy required to raise the electrons from the donor levels to the conduction band or to accept electrons by the acceptor levels from the valance band for n-type and p-type materials, respectively. The activation energy, which is related to the electron transport process in the material, can be expressed by a conventional **Arrhenius** type relation

$$\sigma = \sigma_0 \exp\left(-\frac{E_a}{2k_B T}\right), \qquad (2.12)$$

where σ_0 is a constant and σ is the electrical conductivity at TK. k_B is the Boltzmann constant and T is the absolute temperature. The above equation can be written as

$$\ln \sigma = -\frac{E_a}{2k_B T} + \ln \sigma_0 \qquad (2.13)$$

Equation 2.13 is equivalent to straight line equation **y = mx + c**. So that from the graph of lnσ vs. 1/T, E_a can be determined from the slope of the straight line using the following relation

$$E_a = -\left(\frac{\ln \sigma}{1/T}\right) \times 2k_B \qquad (2.14)$$

Activation energy also varies considerably with the film thickness, thicker films having lower and eventually a constant value [83, 84] approaching to that of the bulk semiconductor. It may be mentioned here that band gap measured by optical and other methods often differs slightly in magnitude from the thermal ones. This is due to the fact that in the latter case the mobility of the charge carriers is generally assumed to be independent of temperature which is not necessarily so [3].

2.8 SHEET RESISTANCE

The resistance (R) of a thin film is directly proportional to the resistivity (ρ) and inversely proportional to the thickness (t) and we can write for a rectangular film of length (L) and width (W).

$$R = \left(\frac{\rho}{t}\right) \times \left(\frac{L}{W}\right) = R_S \times \left(\frac{L}{W}\right),$$

where R_S is known as the sheet resistance and expressed in ohms per square. Hence

$$R_S = \frac{\rho}{t} \text{ Ohm per square.} \qquad (2.15)$$

The ratio (L/W) is called the number of squares. The number of "squares" is a pure number has no dimension. This parameter is widely used for comparing films; particularly those of the same material are deposited under similar conditions.

2.9 TEMPERATURE COEFFICIENTS OF RESISTANCE

The temperature coefficients of resistance (T.C.R) play an important role for film characterization. The resistivity of any metal and semiconductor are temperature dependent. According to the law of Ghosh and Deb [85] the relation between resistivity and temperature is given by

$$\rho_T = \rho_0 \left(1 + \alpha T + \beta T^2 + ...\right) \tag{2.16}$$

where ρ_0 is a constant and ρ_T is the resistivity at T K. α is the temperature coefficient of resistance (T.C.R.) and β is a constant. Generally $\alpha >> \beta$ at low temperature, and we can write from first approximation

$$\rho_T = \rho_0 \left(1 + \alpha T\right) \tag{2.17}$$

At temperatures T_2 and T_1 Equation 2.17 can be written as

$$\rho_{T2} = \rho_0 \left(1 + \alpha T_2\right) \text{ and}$$

$$\rho_{T1} = \rho_0 \left(1 + \alpha T_1\right)$$

Using these two equations we can be written as

$$\alpha = \frac{\left(\rho_{T2} - \rho_{T1}\right)}{\rho_{T1}\left(T_2 - T_1\right)} \tag{2.18}$$

Generally, ρ_{T1} is the resistivity at room temperature and ρ_{T2} is the resistivity at temperature T_2.

2.10 THE HALL CONSTANT, ELECTRICAL CONDUCTIVITY AND MOBILITY

When a magnetic field is applied at right angle to the direction of current in a conductor, Hall effect [86] is produced as shown in Figure 2.11. In the presence of a magnetic field, a magnetic force e**B** acts on the electrons having on average velocity v due to the current I. The force acts in the direction perpendicular to both **B** and v causes the electron to deflect (for n-type materials) towards the surface of one side of the conductor. As a result, an additional electric field $\mathbf{E_H}$ is produced. Under equilibrium condition, the sideways force on the moving carriers due to this field just balances that arising from the magnetic field.

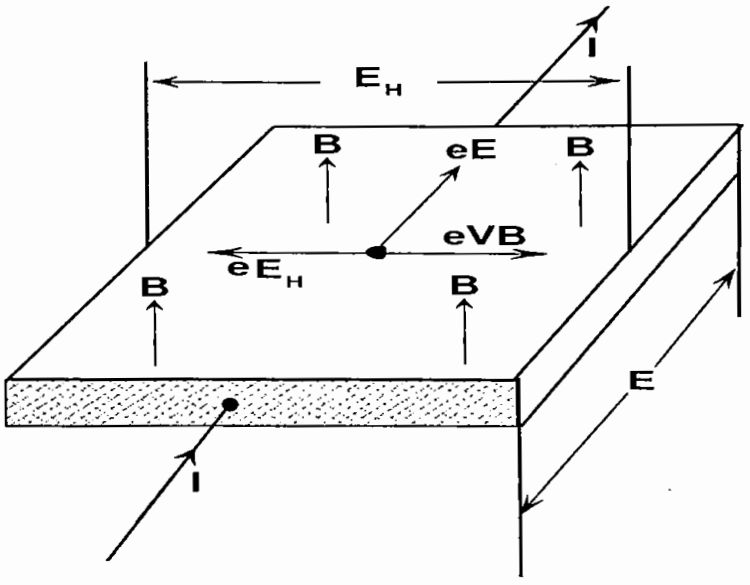

Figure 2.11: *The forces acting on a current carrier in a conductor placed in a magnetic field leading to the observable Hall field E_H.*

The magnitude of the transverse Hall field E_H, is found by equating the sideways forces

$$\mathbf{eE_H = e\,v\,B}, \tag{2.19}$$

expressing v in terms of current density J and the conduction electron density n from the relation

$$\mathbf{J = n\,e\,v},$$

we have,

$$\mathbf{E_H = \left(\frac{1}{ne}\right)JB = R_H JB}, \tag{2.20}$$

where the Hall constant

$$\mathbf{R_H = \pm\frac{1}{nec}}, \tag{2.21}$$

gives the carrier concentration (n) directly and here c is the velocity of light. R_H will be negative for n-type semiconductor and positive for p-type semiconductor, respectively. We know that

$$\mathbf{E_H = \frac{V_H}{W}}, \text{ and } \mathbf{J = \frac{I}{Wt}},$$

where V_H is generated Hall voltage and W, t are the sample width and thickness, respectively. Therefore, Equation 2.20 becomes

$$\mathbf{R_H = \pm\frac{1}{ne} = \pm\left(\frac{V_H t}{IB}\right)\times 10^8} \text{ (cm}^3\text{/ Coulomb)} \tag{2.22}$$

where V_H, I, B and t are expressed in volt, ampere, gauss and cm, respectively. In Equation 2.22, e is the magnitude of charge carrier and the algebraic sign of the Hall voltage V_H indicates whether the carriers are holes or electrons. This treatment of Hall effect is very simple and is applied for specimens with a constant energy surface.

When the charge carrier is moving in an electric field E with the average velocity v then the Hall mobility μ_H is defined as the velocity of charge carrier per unit electric field, i.e.

$$\mu_H = \frac{\mathbf{v}}{\mathbf{E}} \tag{2.23}$$

Combining this equation with the Ohm's law, $\sigma = \frac{\mathbf{J}}{\mathbf{E}}$ and $\mathbf{J} = \mathbf{nev}$, the expression for conductivity is

$$\sigma = \mathbf{n}\,\mathbf{e}\,\mu_H$$

or, $$\mu_H = |\mathbf{R}_H|\,\sigma \tag{2.24}$$

where R_H and σ are expressed in cm^3/coulomb, Ω^{-1}-cm^{-1}, respectively.

Due to thermal energies the electrons and holes in a semiconductor are set to rapid random motion and collide among themselves. If τ is the average time between such collisions then the rate of change of velocity is $\frac{\mathbf{v}}{\tau}$. In steady state condition this rate of change must be equal to the acceleration due to the field $\frac{\mathbf{eE}}{\mathbf{m}^*}$, where $\mathbf{m}^*$ is the effective mass of the charge carrier. Therefore

$$\frac{\mathbf{eE}}{\mathbf{m}^*} = \frac{\mathbf{v}}{\tau} = \frac{\mu_H \mathbf{E}}{\tau}$$

or, $$\mu_H = \frac{\mathbf{e}\tau}{\mathbf{m}^*} \text{ and } \sigma = \frac{\mathbf{ne}^2\tau}{\mathbf{m}^*} \tag{2.25}$$

In this expression τ is assumed to be free from the electron's velocity for simplicity.

For semiconductor with spherical constant energy surfaces it is found that over a considerable range of energy [87]

$$\tau = \mathbf{aE}^{-r}, \tag{2.26}$$

where r is a constant and may vary with temperature. The value of r is generally derived from the observed variation of mobility with temperature and is dependent on the scattering processes. Therefore, it is a fundamental problem in semiconductor physics to determine the exact nature of the dependence of τ on energy of the electrons.

2.11 VARIATION OF CARRIER CONCENTRATION WITH TEMPERATURE

The concentration of electrons or holes or both in a semiconductor can be obtained from the knowledge of the densities of available band as well as the Fermi-Dirac distribution function [88]. The expression for the Fermi energy is then obtained from these carrier concentrations. Semiconductors may be intrinsic or extrinsic.

2.11.1 For Intrinsic Semiconductor

Using Fermi-Dirac distribution the total number of electrons per unit volume or electron density (n) in the conduction band can be expressed as [88]

$$n = n_0 \exp\left[\frac{E_F - E_C}{k_B T}\right], \tag{2.27}$$

where,

$$n_0 = 2\left[\frac{2\pi m_e^* k_B T}{h^2}\right]^{\frac{3}{2}}$$

is the possible states in the conduction band, m_e^* is electron effective mass, E_c is the energy level at the bottom of the conduction band i. e. at the conduction band edge and E_F is the Fermi energy level, k_B and T are Boltzmann constant and absolute temperature, respectively.

Similarly, hole density (p) in the valence band can be expressed as

$$p = p_0 \exp\left[\frac{E_F - E_v}{k_B T}\right], \tag{2.28}$$

where,

$$p_0 = 2\left[\frac{2\pi m_h^* k_B T}{h^2}\right]^{\frac{3}{2}}$$

is the possible states in the valence band, m_h^* is the effective mass of the hole and E_v is energy level at the top of the valence band i.e. at the valence edge.

2.11.2 For Extrinsic Semiconductor

Due to the presence of various types defects such as imperfections, disorders, impurities, etc. in semiconductor, new energy states are created in the band gap region as a result of which there may be a large change in their

conductivities with thermal excitation [3]. These energy states result in the formation of some discrete energy levels in the forbidden energy band gap and these levels can now donate electrons to the conduction band or accept them from valence band when sufficiently excited, thermally or otherwise, leading to an increase in the conductivities [3]. The corresponding states are respectively called donor, acceptor levels. The donor level will be below the conduction band edge but close to it and the acceptor level will be above the valence band edge but also close to it. In such semiconductor the electron density (n) in the conduction band can be expressed as [88]

$$n = (n_0 N_d)^{\frac{1}{2}} \exp(-\frac{E_d}{2k_B T}), \tag{2.29}$$

where E_d is the donor ionization energy, N_d is the donor density, and

$$n_0 = 2\left[\frac{2\pi m_e^* k_B T}{h^2}\right]^{\frac{3}{2}}$$

Similarly, the hole density (p) in the valence band can be expressed as [88]

$$p = (n_0 N_A)^{\frac{1}{2}} \exp(-\frac{E_A}{2k_B T}), \tag{2.30}$$

where E_A is the acceptor ionization energy, N_A is the acceptor density, and

$$n_0 = 2\left[\frac{2\pi m_h^* k_B T}{h^2}\right]^{\frac{3}{2}}$$

The variation of electron concentration n (or hole concentration p) with temperature in extrinsic semiconductor is considered in the following manner. If the donor centers are partially ionized so that $n < N_D$ (or $p < N_A$), where N_D and N_A is the donor density and the acceptor density, respectively. When $N_D > n >> N_A$, then the semiconductor becomes uncompensated semiconductor.

2.12 THOMSON COFFICIENT AND THERMOELECTRIC POWER

It has been seen that even in the absence of current, there must be an electric field if a temperature gradient is present in a conductor. This indicates the elementary concept of thermoelectric effect in conductors. Phenomenologically one may define the Thomson coefficient as the coefficient of proportionality related to the electric field and the temperature gradient as follows:

$$E_X = -T_h\left(\frac{\delta T}{\delta X}\right) \tag{2.31}$$

Practically, this effect arises as a result of increased energy of electrons at the hot end of the martial causing a diffusion of electrons towards the cold end. The charge imbalance due to diffusion sets up an electric field (Seebeck e.m.f.) in the material and this field strongly opposes further flow of charge in this direction. A quantity commonly used to describe the effect is thermoelectric power Q_{ML}. This refers to two materials denoted by 'L' and 'M'.

If we have a circuit containing two junctions at A and B as shown in Figure 2.12 at temperatures T_2 and T_1, the material is being open at point C which is assumed to be at temperature T_0, then the open circuit voltage V_0 at C is given by

$$V_0 = \int_{T_1}^{T_2} Q_{ML}(T)dT$$

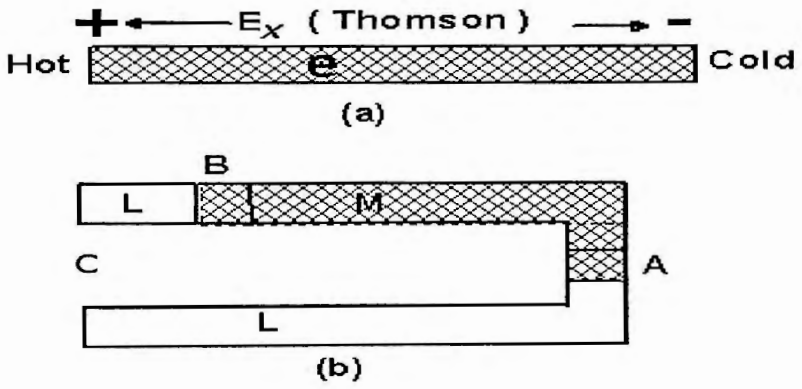

Figure 2.12: *Origin of thermopower in semiconductor, A and B are two junctions in two types of materials L and M.*

If $T_2 = T_1 + \Delta T$, where ΔT is small temperature variation, we have

$$V_0 = Q_{ML}\Delta T$$

or,
$$Q_{ML} = \frac{V_0}{\Delta T} \qquad (2.32)$$

where Q_{ML} is the thermoelectric power of the material 'M' with respect to material 'L' and indicates specific thermoelectric power.

2.12.1 Absolute Thermoelectric Power

If T_h (M), T_h (L) are the Thomson coefficients for the two materials then from thermodynamical argument [87] we have

$$T_h(M) - T_h(L) = T\frac{dQ_{ML}}{dT} \tag{2.33}$$

If the material L is one for which $T_h(L) = 0$ (usually lead, **Pb**), the thermoelectric power of other material relative to this material can be expressed as $Q_{ML} = Q_M = Q$, then Q is sometimes called the absolute thermoelectric power. In this case Equation 2.33 can be written as

$$T_h(M) = T\left(\frac{dQ}{dT}\right) \tag{2.34}$$

2.13 THE POSITION OF FERMI LEVEL

For a non-degenerate n-type crystalline semiconductor with spherical constant energy surface under thermal equilibrium the thermoelectric power is given by [89]

$$Q = -\frac{k_B}{e}\left(\frac{E_C - E_F}{k_B T} + A\right) \tag{2.35}$$

Here A is a constant that depends on the nature of the scattering process. When the energy is measured with reference to the bottom of the conduction band the Equation 2.35 reduces to

$$Q = -\frac{k_B}{e}\left(A + \frac{E_F}{k_B T}\right) \tag{2.36}$$

where E_F is the position of the Fermi level in the band gap. Harry *et al* [90] have pointed out that, $A = \frac{5}{2} - r$, where r is the scattering index.

According to Mott and Davis [89] for limited temperature range, the Fermi energy is

$$E_C - E_F = E_0 - \gamma T \tag{2.37}$$

where E_0 is the low temperature limit of $(E_C - E_F)$ and corresponds to the activation energy equivalent to the band gap, and γ is the temperature coefficient of activation energy. Substituting Equation 2.37 into 2.35

$$Q = -\frac{E_0}{eT} + \left(\frac{\gamma}{e} - \frac{Ak_B}{e}\right) \tag{2.38}$$

Now, the Peltier Coefficient, $\pi = QT$, can be expressed as

$$\pi = -\frac{E_0}{e} + \left(\frac{\gamma}{e} - \frac{Ak_B}{e}\right)T \tag{2.39}$$

From Equation 2.39 the plot of π versus T yields a straight line. From its slope γ is obtained. Using the value of γ in Equation 2.38, the value of E_0 can be calculated. From the knowledge of γ and E_0 the value of Fermi energy, $(E_C - E_F)$ can be obtained from Equation 2.37.

2.14 DEGENERATE AND NON-DEGENERATE SEMICONDUCTOR

In most of the semiconductors the Fermi-level lies in about $2k_BT$ below the bottom of the conduction band edge. In that case, the electrons in conduction band follow closely Boltzmann statistics and the electron gas is said to be non-degenerate.

In some cases of an n-type semiconductor, when the Fermi-level enters into the conduction band or goes close to the band edge from the mid gap, then the electron gas becomes degenerate.

When the temperature increases from absolute zero, the donors begin to ionize and the lower energy states in the bottom of the conduction band become completely occupied due to its low density of states. The position of the Fermi-level related to the bottom of the conduction band is given by [91]

$$E_F = \left(\frac{h^2}{8m_e^*}\right)\left(\frac{3n}{\pi}\right)^{\frac{2}{3}}, \tag{2.40}$$

where n is the density of electrons in the conduction band, m_e^* is the effective mass of the electron.

If $E_F << k_BT$ and $E_g >> k_BT$, then the electron gas becomes non-degenerate [92]. It is also observed that 10^{24} or 10^{25} carriers/m^3 is an absolute upper limit to the carrier concentration in a non-degenerate semiconductor [93].

2.15 EFFECTIVE MASS OF ELECTRONS

In extrinsic polycrystalline semiconductors the electrical conductivity is mainly controlled by impurity level. In that case, the carrier concentration n is a function of temperature, which is given by [88]

$$n = (n_0 N_d)^{\frac{1}{2}} \exp\left(-\frac{E_d}{2 k_B T}\right) \tag{2.41}$$

where E_d is the donor ionization energy, N_d is the donor density, and

$$n_0 = 2\left(\frac{m_e^* k_B T}{2\pi\hbar^2}\right)^{\frac{3}{2}}$$

The plot of $\ln(nT^{-3/4})$ versus $1/T$ gives E_d. Using the value of E_d and considering hydrogenic model for the impurity, the effective electron mass m_e^* can be obtained from the relation.

$$E_d = \frac{e^4 m_e^*}{2\,(4\pi\varepsilon\varepsilon_0\hbar)^2}, \tag{2.42}$$

where ε is the dielectric constant of the material. The position of the Fermi level E_F can be determined from the following relation [88]

$$E_F = -\frac{1}{2}E_d + \frac{1}{2}(k_B T)\ln\left[\frac{N_d h^3}{2\left(2\pi m_e^* k_B T\right)^{\frac{3}{2}}}\right] \tag{2.43}$$

2.16 DIFFERENT SCATTERING MODES IN SEMICONDUCTOR

When the charge carriers move in a real crystal, they suffer numerous collisions among themselves as well as with the lattice phonons, impurities and imperfections resulting in a phenomenon known as scattering [3]. There are several processes by which charge carriers may be scattered and these are also affected the semiconducting parameters [3]. It has tactically been assumed that

(i) The mean collision or relaxation time of electrons (or carriers) is constant,

(ii) These collisions do not involve any change of the energy of electrons (or carriers), and

(iii) The probability of the final state of electrons (or carriers) is dependent of the initial state.

These assumptions need not be true for the carriers in many semiconductors. The scattering agents (i.e. scatters) of the charge carriers are primarily

(a) lattice vibrations,

(b) ionized impurities,

(c) natural impurities such as defects, vacancies, interstitials etc.

(d) dislocations,

(e) grain boundaries,

(f) phonon drag, etc.

Even though the effects of some these are seen in bulk single crystals, these will be more predominant in polycrystalline materials and more so in thin films. The above different scattering modes that in turn affect the mobility are briefly described below:

2.16.1 Lattice Scattering

It is due to the thermal vibrations of the crystal lattice, thus giving rise to longitudinal as well as transverse waves.

There two types of lattice scattering viz.

(i) phonon or acoustic and

(ii) optical and intervalley types.

(i) Phonon or Acoustic mode of Scattering:

When a semiconductor is exposed to thermal energy, the crystal lattice, which is otherwise considered to be at rest, starts vibrating. As a result, the lattice potential field is deformed due to the superposition of longitudinal phonon (acoustic) waves having a wavelength of the order of sound waves ($\approx \times 10^5$ cm/sec). The deformation arises due to the contraction or dilation of the unit volume of the crystal lattice by the thermal vibration of the lattice. In such scattering the mobility is given by the relation [94].

$$\mu = \left(\frac{2\sqrt{2\pi}}{3}\right).\frac{\hbar^4.C_{11}}{E_{1(n)}^2.m^{*5/2}.k_B^{3/2}}T^{3/2}, \tag{2.44}$$

i.e., $\mu \propto T^{3/2}$ (2.45)

Thus for phonon scattering mobility, μ follows $T^{3/2}$ law.

(ii) Optical and Intervalley modes of scattering:

An additional mode of scattering arises from the optical vibration caused by the interaction of electromagnetic (optical) waves with polar semiconductors

such as oxides, sulphides, etc. having dipole moment or from collision where the momentum of an electron changes from one valley to another by means of absorption or emission of phonon of proper energy and momentum in multi-valley semiconductor. The scattering mechanism in both optical and intervalley is similar and can be treated from the perturbation [95, 96] and intermediate [97, 98] theories. In this mode scattering mobility follows $e^{1/T}$ law.

2.16.2 Impurity Scattering

Impurity scattering is important in impure and nonstoichiometric semiconductors in which ionized and neutral atoms are present. Both of them may scatter under specific conditions.

(i) Ionized impurity scattering:

In many cases especially at low temperatures mobility follows an entirely different trend. This behavior is assumed to be the scattering of carriers by ionized impurity centers [99]. A theoretical treatment has been made by Conwell and Weisskopf [100] about the contribution of these ionized impurities to the scattering process assuming a Rutherford type of scattering and in the present case the scattering of charge carriers say electrons by the Coulombic field of ionized impurity atoms. In a semiconductor there may be a sufficient number of ionized impurity atoms, which will scatter the charge carriers moving past by them. Rutherford scattering relation Conwell-Weisskopf mobility takes the form [101]

$$\mu_i = \frac{2^{7/2}\varepsilon^2(k_B T)^{-3/2}}{\pi^{3/4}\left[m^{(N)1/2}(eZ)^3 N_i\right]}\left[\frac{1}{\ln\left[1+\left(\frac{3\varepsilon k_B T}{e^2 N_i^{1/3}}\right)\right]}\right] \tag{2.46}$$

where $m^{(N)}$ is the density of states effective mass, N_i is the density of ionized impurities of charge eZ. This has been modified by other workers by introducing a shielding factor. The above relation leads to

$$\mu_i \propto T^{-3/2} \tag{2.47}$$

Therefore in the ionized impurity scattering mode, the mobility follows $T^{-3/2}$ law.

2.16.3 Neutral Impurity Scattering

In this type of scattering, the scattering of charge carriers by neutral impurities is quite similar to the scattering of electron by hydrogen atoms. This type of scattering gives rise to relation [102]

$$\mu_n \approx \frac{T^{-1/2}}{7.6} \times 10^{22} N_n, \tag{2.48}$$

where N_n is the density of the neutral impurities. In this case mobility becomes proportional to $T^{-1/2}$.

2.16.4 Scattering at Dislocation

Distortions of crystalline lattice cause scattering of electrons and holes. Dexter and Seitz [103] have discussed this form of scattering theoretically.
It has negligible contribution unless the dislocation density is in excess of 10^{24} m^{-3} when the density is of the order of 10^{17} m^{-3} scattering should be comparable to lattice scattering at room temperature. Dislocation may be regarded as charge cylinder in the path of an electron and causes scattering. The relaxation time τ_d for the process is given by

$$\tau_d = \frac{3}{8RNv} \tag{2.49}$$

Where N is dislocation density and R is the radius of the dislocation line and v is the velocity of the electron. At room temperature this type of scattering is not important but at low temperature it may be important. For spray–deposited samples dislocations are less important.

2.16.5 Scattering by Grain Boundaries

Grain boundary scattering is very important for polycrystalline samples either in bulk or thin film form. From the theories of grain [104-106] boundary potential, it is known that the boundary regions are characterized by a potential barrier of height E_μ and density of traps θ_t. These two quantities are related by

$$E_\mu = \frac{e^2 \theta_t^2}{(8 \varepsilon_0 \varepsilon n)}, \tag{2.50}$$

where n is the carrier concentration, the barrier height is also dependent on the grain size. However, according to the nature of this barrier height the carrier transport that depends upon the scattering process in the sample may be influenced by all or any of the following mechanisms:

(a) Thermionic emission of carriers over the barrier,

(b) Quantum mechanical tunneling,

(c) Barrier reflection mechanism.

Petriz [107] suggested that due to the presence grain boundaries between crystallites, potential barrier heights would be generated across these grain boundaries and the relation between the mobility of the charge carriers and the barrier height will be given by the expression

$$\mu = \frac{M}{N.k_B.T} \exp\left[-\frac{E_\mu}{k_B T}\right] \tag{2.51}$$

where E_μ is the barrier height potential, M is a parameter depending on the nature of the barrier and N is the number of crystallites per unit length. Hence the above expression can be written as

$$\mu \propto \frac{\exp(-1/T)}{T}. \tag{2.52}$$

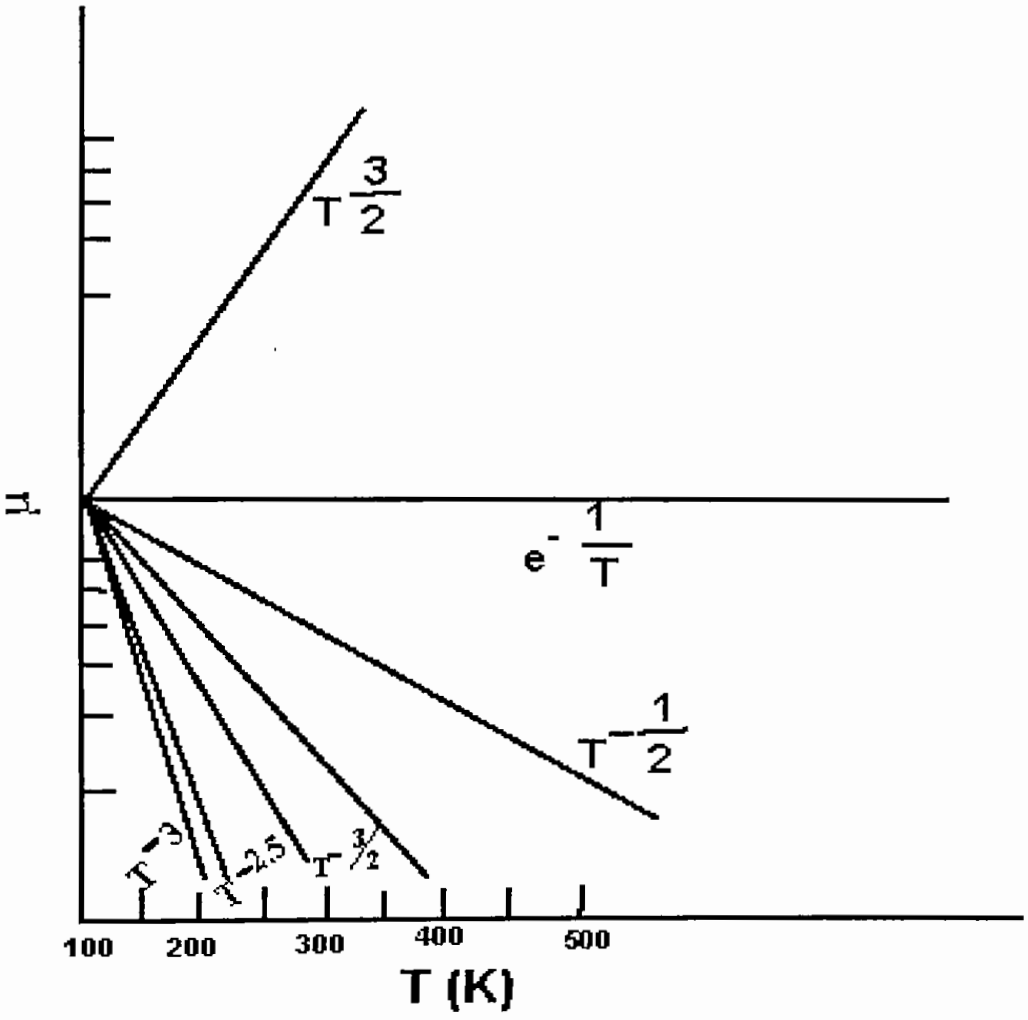

Figure 2.13: *Mobility vs. temperature graphs (log-log scale) for different theoretical modes of scattering.*

[Reproduced from Reference 3, A. Goswami, in "Thin Film Fundamentals", New Age Int. (P) Ltd. Publishers, New Delhi, 1996.]

Thus from the above discussion for the different scattering modes, it is observed that the mobility of charge carriers is a function of temperature and can be expressed in general form [3]

$$\mu \propto T^{X} \tag{2.53}$$

where the magnitude and sign of X is determined the mode of scattering of the charge carriers.

Even though it is not possible to estimate quantitatively the contribution of each factor, a qualitative idea can be obtained from the nature of the graph μ vs. T and comparing the theoretical graphs for different modes of scattering. Figure 2.13 shows the nature of theoretical graphs for different modes of scattering without taking into account their absolute magnitude [108].

It is seen that the slopes of these curves vary with the modes of scattering. A decrease in the mobility with the increase of temperature corresponds to the $T^{-3/2}$ law for ionization scattering process for charge carriers. A nearly constant graph or one with a slight downward slope suggests respectively the effects of neutral impurities and grain boundaries. A deviation from the theoretical graph may be caused by the presence of several modes of scattering of the charge carriers either at the same or different temperature regions. Feature some of them may be predominant at one region to the exclusion of the others and μ vs. T graph may also show a maximum at a certain temperature region. These features are more often observed in semiconducing films and because of the presence disorders, imperfections, etc. the effects will predominant in the polycrystalline films [3].

2.17 OPTICAL STUDIES

The optical behaviors of a semiconductor are investigated in term of the three phenomena namely transmission, reflection and absorption. Therefore, it is necessary to study the ultraviolet (**UV**), visible and infrared (**IR**) characteristics of the material.

2.17.1 Inter Band Optical Transition and the Band Gap

When photon energy is incident on a material, the valence electron absorbs energy from incident photon and is excited. When incident energy exceeds threshold value, the electron may make a transition to the conduction band under suitable conditions. If this transition occurs between the bands at the same value

of the wave vector, the transition is considered as vertical and is allowed. Non-vertical transitions are normally forbidden. For the simple case shown in Figure 2.14 the minimum absorption of radiation occurs at $h\nu = E_g$ and it would intensify for all $h\upsilon > E_g$, where E_g is called the absorption edge or optical band gap. During the process of this type of transitions no phonon is involved for the conservation of energy except the creation of an electron and a hole and is termed as direct absorption process. The electronic transitions between the valance and the conduction bands can be direct or indirect. In both cases it can be allowed as permitted by the transition probability (p) or forbidden where no such probability exists. The transition probability is related by the following relation [109-111]

$$\alpha = A\left(h\nu - E_g\right)^p, \tag{2.54}$$

where α is the absorption coefficient of the film, E_g is the energy band of the film and A, p are constants. p has discrete values like 1/2, 3/2, 2, or more depending on whether the transition is direct or indirect and allowed or forbidden. p = 1/2 for direct allowed transition and 3/2 for the direct forbidden transition.

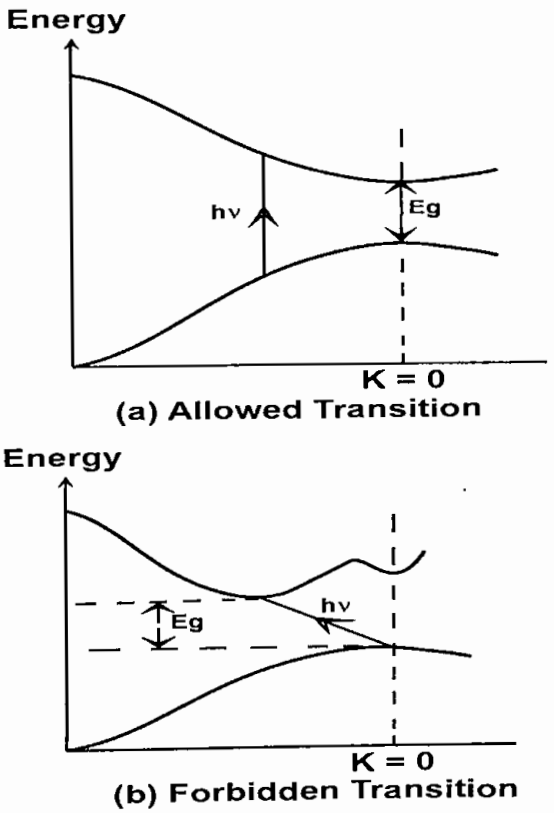

Figure 2.14: *Optical transition in semiconductor; (a) Allowed transition, (b) Forbidden transition.*

. Therefore, the plot of $(\alpha h\nu)^p$ vs. hν would be provided the value of E_g and the type of transition takes place in the semiconductors.

2.17.2 Refractive Index of Transparent Films

Figure 2.15 represents a thin film with a complex refractive index $n = n_f - ik_0$, bounded by transparent media with refractive indices n_a and n_g, where n_a is the refractive index of air, n_g is that of glass substrate, n_f is the real part of the film's refractive index (n) and k_0 is the extinction coefficient. Assuming unit amplitude for the incident light and in the case of normal incidence the amplitude of the transmitted wave is given by [112]

$$A = \frac{t_1 t_2 \exp\left(-\frac{2\pi i \eta t}{\lambda}\right)}{\left[1 + r_1 r_2 \exp\left(\frac{-4\pi i \eta t}{\lambda}\right)\right]} \tag{2.55}$$

where t_1, t_2, r_1 and r_2 are the transmission and reflection coefficients at the front and rear faces, respectively.

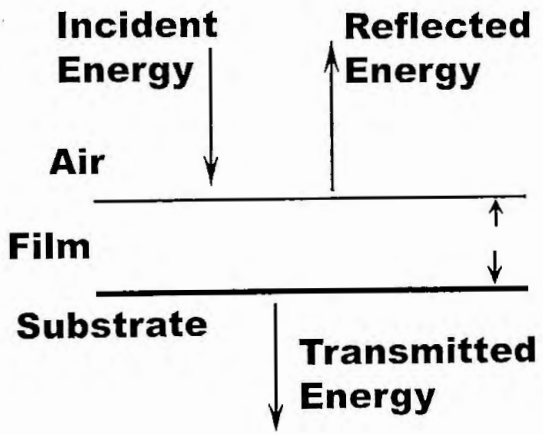

Figure 2.15: *Incident energy, Reflected energy and Transmitted energy of light when incident on a material.*

The transmission of the layer is given by

$$T = \frac{n_g}{n_a}|A|^2 \tag{2.56}$$

For transparent film (weak absorption) with

$k_0^2 << (n_f - n_a)^2$ and $k_0^2 << (n_f - n_g)^2$,

then the expression for T is given by

$$T = \frac{(16\, n_a n_g n_f^2\, k)}{\left[C_1^2 + C_2^2\, k^2 + 2C_1C_2\, k \cos\left(\frac{4\pi n_f t}{\lambda}\right)\right]} \tag{2.57}$$

where $C_1 = (n_f + n_a)(n_g + n_f)$;

$C_2 = (n_f - n_a)(n_g - n_f)$ and

$k = \exp\left(-\frac{4\pi k_0 t}{\lambda}\right) = \exp(-\alpha t)$.

Generally outside the region of fundamental absorption ($h\upsilon > E_g$) or of the free carrier absorption (at higher wavelength), the dispersion of n_f and k_0 is not very large. The maxima and minima of T in Equation 2.57 occur for,

$$\frac{4\pi n_f t}{\lambda} = m\pi, \tag{2.58}$$

where m is the order number. Using Equation 2.58 in 2.57 for transparent film on a non-absorbing substrate, we obtain [113]

$$n_f = \left[N + \left(N^2 - n_a^2 n_g^2\right)^{1/2}\right]^{1/2}, \tag{2.59}$$

where

$$N = \frac{\left(n_a^2 + n_g^2\right)}{2} + \frac{2\, n_a\, n_g (T_{max} - T_{min})}{T_{max}\, T_{min}}$$

T_{max} and T_{min} are the maximum and minimum transmittance of the film.

2.18 ELETRON AFFINITY AND WORK FUNCTION CALCULATION FOR THIN FILM

To obtain the highest performance from an electrode in electrochromic cell and photoelectrochemical cell, the conduction band discontinuity ($\Delta E_c = \chi_s - \chi_{os}$) should be zero [114], where χ_s and χ_{os} are the electron affinities of the base semiconductor and the oxide semiconductor, respectively. To get optimum device performance, the work function of the oxide semiconductor should be less than or equal to the electron affinity of the base semiconductor. Therefore to use MnO_2 thin film as electrodes, its work function is to be known.

According to Sanderson electronegativity principle [115], when two or more atoms initially different in electronegativity combine chemically, they adjust to have the same intermediate electronegativity within the compound. This intermediate electronegativity is given by the geometric mean of the individual electronegativity of the component atoms. That is, the geometric mean of n numbers is obtained by multiplying all of the numbers together and taking the n^{th} root of the product. According to this principle, the electronegativity of A_xB_y compound can be written as

$$E_n(A_xB_y)=\left[(E_A)^x \times (E_B)^y\right]^{\frac{1}{n}} \tag{2.60}$$

where E_A and E_B are the electronegativities of A and B atoms, respectively [115], E_n is the electronegativity of A_xB_y and x, y are the number of atoms of A and B, respectively.

Semiconductors are generally covalent in nature, but it is an established fact that no bond is purely covalent or purely ionic in character but always a mixture. From the electronegativity concept the percentage of the ionic character, y of the bond between the constituent atoms can be obtained by using Sanderson's electronegativity values [115] in Pauling's empirical relation [116]

$$\textbf{\% ionic character} = [1 - \exp(-0.25\{E_A - E_B\}^2)] \times 100\% \tag{2.61}$$

Electron affinity and work function are defined as the energy required to remove an electron from the bottom of the conduction band E_c, and from the Fermi level E_F, to a position just outside the surface of the material (vacuum level), respectively. In the absence of straightforward method of determining the electron affinity of the bulk semiconductor, an indirect and empirical method [117] is used to determine the electronegativity of the atoms. In the case of semiconductor the relation between bulk electronegativity E_n corresponds to the intrinsic Fermi level E_F with respect to the vacuum level is [118]

$$E_F \approx E_n = \chi + E_g/2 \tag{2.62}$$

where χ is the electron affinity and E_g is the optical band gap between the conduction band and valance band. The position of E_F in a bulk semiconductor is determined by the regular crystallographic structure of the intrinsic material, the electronegativity can be assumed a constant parameter, and the effect of a change in the impurity contents possible in the bulk material may be accounted for by a net change in the electron affinity of the sample. The work function W of the samples is obtained using the following relation [118]

$$W = \chi - E_F. \tag{2.63}$$

2.19 SELECTIVE SURFACE STUDIES

The most fundamental radiative property is that all objects emit electromagnetic radiation. The radiation that impinges on us under daily life conditions is a combination of a radiation emitted by different sources. The amount and the wavelength range of this radiation are determined by the absolute temperature and the nature of the surface of the object.

Figure 2.16(a) shows the solar radiation that falls on the earth surface, being passed through the atmosphere at normal incidence, air mass 1 (AMI)[119].

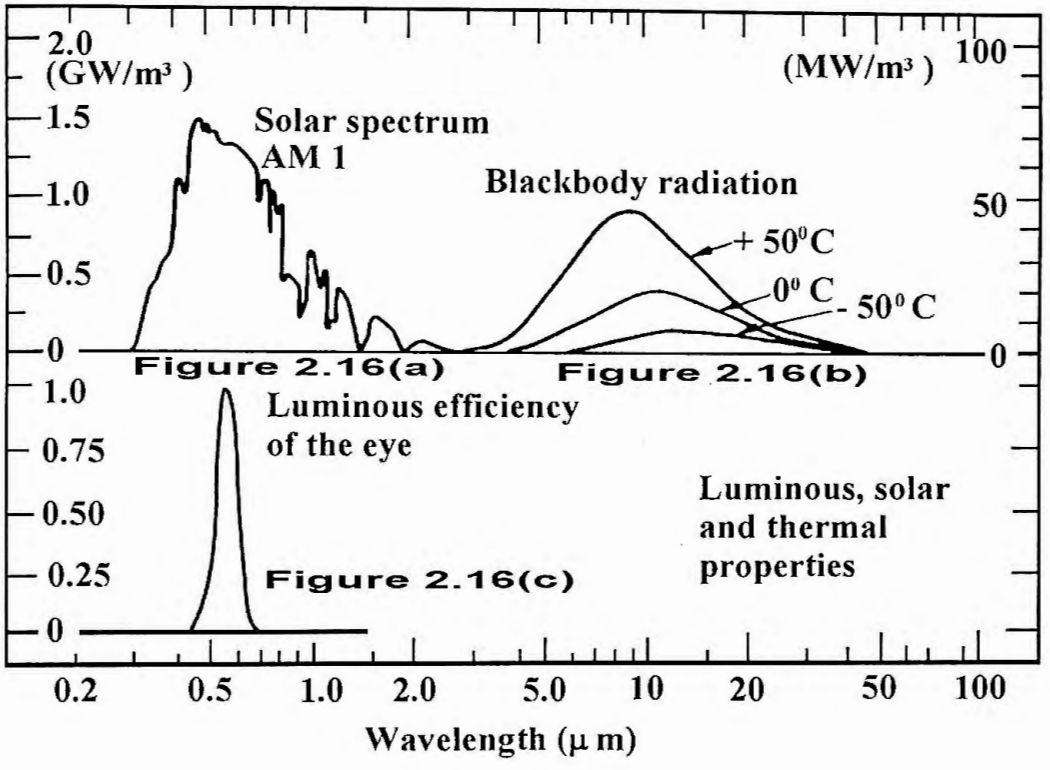

Figure 2.16(a): *Solar spectrum for radiation that passed through the atmosphere at normal incidence;*

Figure 2.16(b): *Black body radiation from surfaces at three different temperatures;*

Figure 2.16(c): *Luminous efficiency of the eye when adapted for daylight.*

[Reproduced from Reference 121, M.K.A. Khan, Ph.D. Thesis, University of Rajshahi, Rajshahi, Bangladesh, 1989.]

The spectrum is similar to that of blackbody radiation from a surface at 6000K which has been attenuated by the absorption in the atmosphere. The absorption is mainly due to the presence of carbon dioxide, water vapor and ozone. The spectrum of solar radiation AM2, AM3 etc., which falls on the earth surface at different angles, is qualitatively similar to AM1 but they are more

attenuated because of their longer travel through the atmosphere. The solar radiation is very intense and is mainly located in the $0.3<\lambda< 2.5$ μm wavelength range.

Figure 2.16(b) shows spectra for blackbody radiation at three different temperatures [120]. The vertical scale shows the radiated power per unit area and wavelength interval and the horizontal scale shows the wavelength. The spectra indicate that at rising temperature the total amount of radiation increases and the peak wavelength moves towards shorter wavelength. It is well-known from the Stefan-Boltzmann law that the total radiation power P can be expressed by the following equation.

$$P = \sigma T^4 \quad W\,m^{-2}$$

where, $\sigma = 5.67 \times 10^8\ Wm^{-2}\ K^{-4}$ and T = absolute temperature of the blackbody.

One can obtain the peak wavelength by Wien's displacement law from the following equation

$$\lambda_0 T = 2.898 \times 10^{-3}\ Km$$

where λ_0 denotes peak wavelength. If the object is not a perfect blackbody, the radiated power from that object can be obtained by multiplying the blackbody value with the emission function $E(\lambda)$. The values of $E(\lambda)$ lie in the interval $0< E(\lambda) <1$, depending on the nature of the surface of the object. For a perfect blackbody one has $E(\lambda) =1$.

It is seen from Figure 2.16(b) that for the shown temperatures the radiation is confined almost totally to the wavelength range $3<\lambda< 100$ μm. Comparing Figure 2.16(a) and 2.16(b), it is seen that for ambient temperatures there is practically no overlap between solar and blackbody spectra.

Figure 2.16(c) shows the spectral sensitivity of the human eye [122, 123]. The human eye is sensitive only in the $0.4 <\lambda< 0.7$ μm range. Hence only the shorter parts of the solar spectra are observed as a visible light.

It is very important to note that about half of the energy of the solar radiation that reaches the earth surface consists of wavelengths longer than 0.7 μm.

The infrared part of the solar radiation that contributes to the heating of the object has no effect on the illumination as seen by the human eye. Hence for energy efficiency and solar applications, it is of great importance to know the surface properties of the materials.

For example, one can have selective surfaces with properties entirely different for visible and near-infrared solar radiation.

For selective surface it is of great interest to know how much of the impinging solar radiation that is transmitted or reflected and how it is perceived by an observer. This is done by introducing integrated solar and luminous properties by

$$T_{sol(lum)} = \frac{\int d\lambda \Phi_{sol(lum)}(\lambda) T(\lambda)}{\int d\lambda \Phi_{sol(lum)}(\lambda)} \tag{2.64}$$

and analogous relations for $R_{sol\,(lum)}$. Here Φ_{sol} is the spectral solar irradiance [124] and Φ_{lum} denotes the luminous efficiency [125] of the eye.

Chapter 3
Experimental Details

This chapter includes the design and construction of the film deposition equipments of spray pyrolysis process and illustrates in details the preparation of MnO_2 samples onto glass substrate. A detail discussion about every experimental setup with appropriate method adopted throughout the course of the work for the analysis of the structural, electrical and optical properties have been presented.

3.1 INTRODUCTION

Spray pyrolysis is well known as one of the simplest, least expensive and indigenous one. By this technique, a large area of thin film can be prepared in relatively short time. The variety of properties of the deposited material can be varied easily with precise control over all the associated parameters. However, a number of difficulties arise in controlling the process variables for its extreme simplicity. Experimental arrangements have been put forward by many workers [66, 126-133] to promote ease of preparation and to overcome difficulties, which were often encountered at the time of film deposition.

Pyrolysis process [134, 135] is chemical spray deposition process, which contains two sections. In one section of the apparatus, an aerosol is produced from the working solution and simultaneously carried to the other section where the pyrolysis reaction takes place and is known as reactor zone. The common defects that are usually noticed in the films prepared by this process are the surface roughness and thickness inhomogeneities. Therefore, the role of the deposition apparatus is very important in preparing defect free highly conducting films.

3.2 TROUBLE WITH THE CONVENTIONAL PNEUMATIC SPRAY SYSTEM

The spray particles those are produced from the exit nozzle during the time of spraying become of different sizes. They do not depend on the fineness of the spray nozzle. It is an inherent property of a pneumatic spray gun. The size of the droplets also depends on the cone angle covered by the spray particles [136, 137]. Aerosol droplets behave differently depending on their size [67]. This creates problem in the film deposition process. The chemical reaction that takes place in the vapor phase is a fundamental mechanism of this process. Droplets of different sizes take different time to reach at the same site of the substrate. Beside this, at a constant substrate temperature they take different fraction of time to complete their vaporization and reaction. As a result, unwanted interaction between the

reacted and unreacted species may take place at the substrate surface. These undesired factors create problem to obtain a film of uniform in structure and homogeneous in composition.

To obtain uniform film, it should be assured that the fineness and uniformity of the spray particles. In order to achieve this, it should be given equal importance in making a fine spray nozzle and at the same time arrangement should be kept to filter the spray particles so that a very fine and uniform droplets may be supplied from the output to the reactor zone. Keeping these points in view, a new apparatus for the spray system is described here.

3.3 DESIGN OF A NEW SPRAY DEPOSITION APPARATUS

The spray deposited apparatus furnishes a number of functions. These are the production of aerosol and their filtration for uniformity, transport of them to the reactor section and formation of films. The different stages of the apparatus required for these purposes are described below:

3.3.1 The Spray Nozzle and its Modification

In the chemical spray method, the characteristic of the spray nozzle plays a very important role for the thin film deposition. The different characteristics of the spray nozzle are:

(i) The spray rate that determines the amount of liquid sprayed during a given interval of time under any ejection condition,

(ii) The size of the droplets,

(iii) Cone angle of spray that determines the total coverage of the spray i.e. degree of mixing of the spraying liquid with the surrounding atmosphere. Among these spray rate and size of the droplets have significant effect on the property of the deposited film.

In a conventional compressed air sprayer, the spray nozzle consists of two capillary glass tube fitted at right angle to each other as shown in Figure 3.1(a). When a high speed compressed air is allowed to pass through the upper tube A in a direction tangential to the mouth of the lower tube B, some air in the upper part of it (tube B)is pushed forward by the air current. As a result, a partial vacuum (or air gap) is created at the upper end of the tube B whose lower end is kept immersed in the spray liquid.

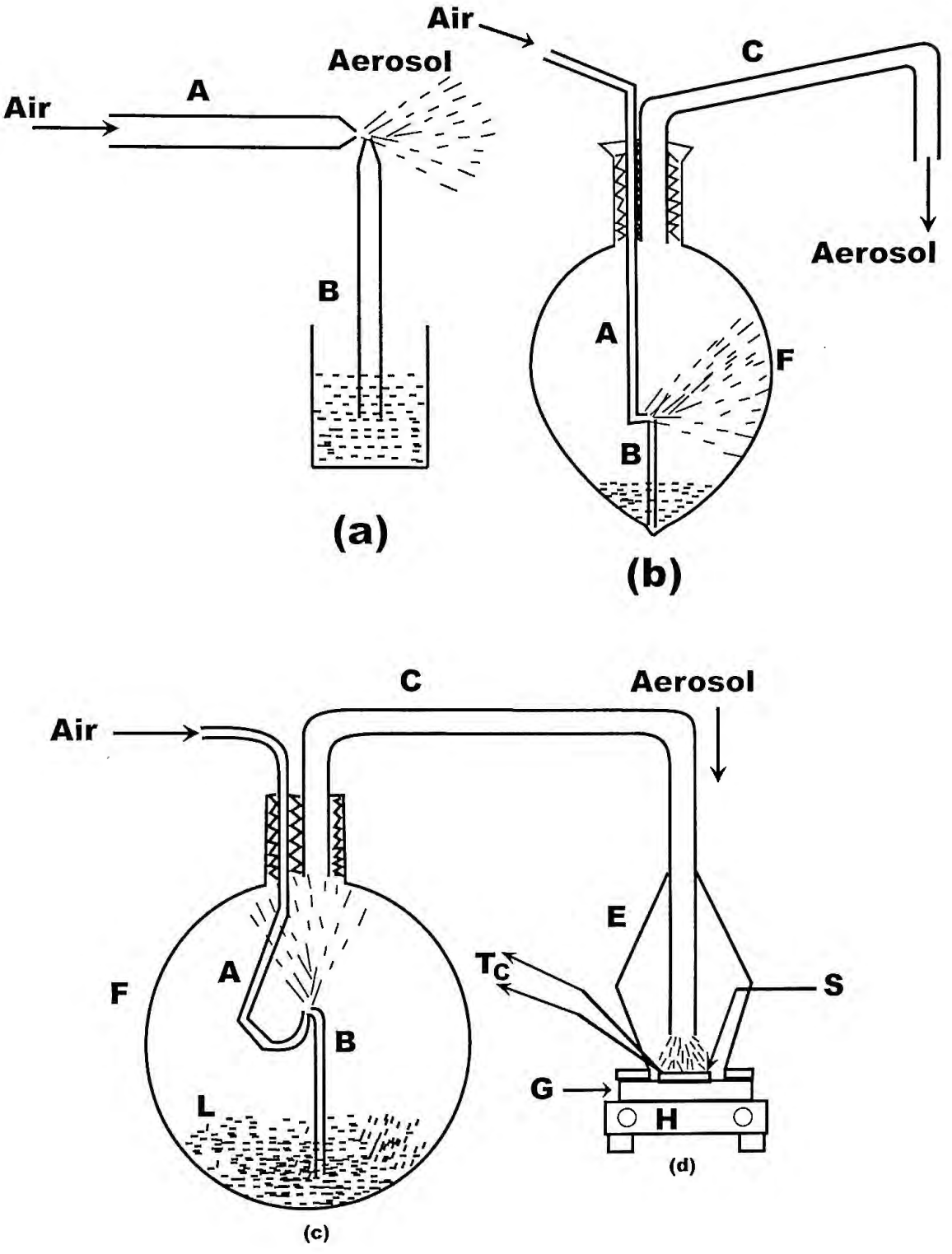

Figure 3.1: *(a) Conventional Pneumatic Spry gun; (b) the modified spray system, which was use early worker in our laboratory; (c) and (d) are author's modified spray system and reactor, respectively.*

To fill up this air gap, liquid is ejected up through the tube B and by the action of the compressed air this liquid emerges from the tube B as fine spray particles (aerosol)

This type of spray guns has been directly used by many of the earlier workers for deposition of thin films of various materials [66, 126-130]. However, the problem of nonuniformity of droplet size remains with this type of spray guns.

Considering this aspect, Islam and Hakim [135] have made a simple modification on the conventional spray gun system in our laboratory in a way as shown in Figure 3.1(b). In this setup, larger droplets and heavier precipitates are discouraged to reach the substrate. Here the spray gun has been kept in a large capacity (1500ml) round bottom glass container F in the bottom of which there is a little protuberance and at the top of it an outlet, a bent pipe C is connected. The protuberance is blown there because a very small amount of fresh liquid (not more than 10 ml) can then be used at each run for a single sprayer without wastage. In the flux the spray particles sprayed horizontally, hence spray rate is low. To increase spray rate there are two ways:

(i) Using a number of nozzles in a single container,

(ii) Using a number of spray nozzles in separate containers and the outlet pipe from each of the container are finally combined to a single outlet pipe whose open end is fitted to the reactor inlet.

To overcome this complexity, the author modified the shape of the spray nozzle, which is shown in Figure 3.1(c). In this modified system, the spray particles are sprayed vertically and hence maximum amount of spray particles are come out through the outlet pipe, which increased the spray rate.

When the aerosol is produced in the flask, they mixed with the surrounding atmosphere and form a cloud of the spray particles. Then this cloud of spray particles in the confined space of the flask are carried out by the carrier gas through the outlet pipe C and during this time they are automatically separated into heavier and lighter droplets due to the action of vertical air current and gravitational effects. In this process the larger droplets would be coalesced in the flask or in the conduit pipe C and ultimately drop down in the flask to be fed back. On the other hand, very light and relativity smaller droplet will be carried by the same incoming carrier air to the reactor zone. This is how a virtual filtration process acts in the spray system and produces almost uniform and very small droplet size at the outlet of the sprayer. Therefore, this system is economic in many respects.

The facilities with this arrangement are as follows:

(i) The solution flow rate can be controlled to a better accuracy by suitable design of the spray nozzle and adjusting the airflow rate. In the present work, the solution flow rate was maintained constant to 0.80 ml/min in preparing $\mathbf{MnO_2}$ thin films. This rate is about (50-100) times less than that used by the earlier workers [66, 126-130, 134].

(ii) Due to this lower flow rate, the time of deposition is increased which provides a better thickness control and larger grain size [70] of the film.

(iii) Extra loss of working solution which was apparent in conventional setup [66, 126-130, 134] can be reduced sufficiently by setting the flow rate to its required lower limit.

(iv) Very fine droplets that are supplied to the reactor section may be vaporized easily without any extra pre-heating furnace [66], which saves excess power consumption.

3.3.2 The Design of the Reactor

The reactor is an essential part of the spray deposition apparatus. The completion of the chemical reaction occurred here to form solid film. It is batch type reactor, which is shown in the Figure 3.1(d). It consists of the following components:

(i) a stainless steel enclosure E having a Pyrex glass jacket inside;

(ii) a heater H on which a thick stainless steel block susceptor G is placed;

(iii) a chromel-alumel thermocouple $\mathbf{T_C}$ used to monitor the substrate temperature.

Substrate is placed on the susceptor block and the thermocouple is kept in contract with the substrate. The heater is controlled with an electronic power controller circuit to obtain different required temperatures. For the rapid expulsion of the byproduct gases there are openings at the side and at the top of the reactor. The double cone shape of the reactor wall E has dual action. It helps focusing the incoming aerosol towards the substrate and provides a chimney action to the exhaust gas upwards.

This type of reactor system plays an intermediate role between the hot-wall and cold-wall type reactors. Endothermic chemical reaction occurs for the formation of $\mathbf{MnO_2}$ thin film and therefore a hot–wall reactor should be adequate. Since the incoming aerosol is cold and if the reactor wall is cold one, it will cause a sudden fall of substrate temperature and give a tremendous thermal shock to the

heated substrate. As a result, the glass substrate may be cracked at once. Furthermore, the reaction process would be distributed due to this rapid fall of substrate temperature and will give an unexpected result. To overcome these difficulties the temperature of the reactor wall should be maintained at a level much higher to the room temperature but lower to that of the optimum temperature for the decomposition temperature. This temperature is maintained automatically here by the metallic enclosure E placed over the heater H, and thus it provides a pre-heating action easily to the input aerosol.

3.3.3 The Heater

The heater H is an ordinary round shaped hot plate having a heating coil of 2 KW nichrome wire. It is placed on an insulated horizontal platform. The top of the plate is covered by a piece of asbestos sheet with a small rectangular opening at the center where a mica sheet is attached. A thick stainless steel or graphite plate G is placed on this mica sheet. It serves as heat susceptor. Substrate that is placed on this susceptor plate has a uniform temperature throughout the substrate surface. To avoid the chemical corrosion, another mica sheet is placed between the susceptor block and the substrate. An electronic power supply unit is connected with the heater power line to supply proper heat to the substrate.

3.3.4 The Fume Chamber

It is a large box provided with a slanting top. The top and the side walls of it are made of glass. There is a chimney at the top of the box. An exhaust fan with regulated power supply unit is fitted at the mouth of the chimney. At the front face of the chamber some air tight doors are provided. The chamber has purging facilities also. The spray system and the reactor are kept inside the fume chamber at the time of film deposition because it establishes safety film deposition atmosphere and checks air current disturbances at the deposition site. These two points are very important for pyrolysis process where deposition is carried out in open atmosphere.

3.3.5 The Carrier Gas

The carrier gas takes an important role in spray pyrolysis technique. In some cases, carrier gas takes active part in chemical reaction for the formation of the film, in the other cases it remains inactive with deposition material but serves

only to transport the spray particles to the reactor section. For the deposition of an oxide film air or oxygen may be used so as to supply oxygen needed for the reaction. Other gases like nitrogen, argon, helium may be used to serve this purpose. In the present work dry compresses air has been used as carrier gas. The pressure of the gas can be varied by adjusting the outlet valve of the air compressor and should maintain constant according to the requirement of the spray rate during the deposition run. The standard pressure for the spray system has been found to be 1.39×10^5 Pa.

3.3.6 The Air Compressor

It is a reservoir type of electrical air compressor. A rotary pump in its suction mode draws atmospheric air and keeps it reserve in a large capacity air tank. To keep the outlet pressure constant there is a bypass valve through which excess air can pass out. The air is forced to pass through a silica gel column in order to make it dry before passing it into the sprayer. A pressure gauge is fitted at the end of the delivery tube with a control valve. This records the carrier gas pressure for the sprayer.

3.3.7 Selection of the Spray Solution

3.3.7.1 Source Compound

There are several numbers of source compounds, which are found available. Among then the most suitable one is selected in order to fulfill a number of essential requirements. It should be a stable compound at room temperature, it should not oxidize in air or in the presence of water at room temperature, its decomposition temperature should not be very high (not >737K). The decomposition reaction leading to the formation of solid film should be thermodynamically favorable so that the residue of the reactant will not be left behind in the deposition material and the products of the decomposition reaction other than the desired one should be volatile so that they can easily escape from the deposition chamber. On the basis of these criteria, manganese acetate compound [$Mn(C_2H_3O_2)_2.4H_2O$] is selected for the preparation of **MnO_2** thin films.

3.3.7.2 Solvent

Different types of solvents may be used to prepare ionic solution, for a single source compound. Among them, the most suitable one is chosen so that it

can permit a high aerosol flow rate in connection with the concentration and viscosity of this solvent. The spray system that is used in the present experiment has a spray nozzle of capillary bore type. The ejection of spray liquid through the spray nozzle depends on the solution concentration. Higher solution concentration causes to reduce the spray rate because it has to pass through a partial vacuum path. So the concentration of the solution prepared by the solvent should be such that it could at least be drawn by the nozzle. Preference is given in selecting a solvent that is not easily inflammable to avoid sudden combustion in the reactor. The most commonly used solvent is water, which facilitates the hydrolysis action. Besides this, water and methanol or water and ethyl alcohol may be used. In this experiment, water is used as a solvent because there is no possibility of occur any accident with it in the reactor and it acts as a powerful oxidizing agent.

3.3.7.3 Preparation of the Ionic Solution for MnO_2 Film

The ionic solution is prepared by dissolving a soluble salt of the anion (metal) in water. Different quantity of source compound [$Mn(C_2H_3O_2)_2.4H_2O$], reagent grade are used to obtain different molar concentration. The optimum solution concentration has been found to be 0.8 M.

3.4 SUBSTRATE CLEANING

The cleanliness of the substrate surface exerts decisive influence on film growth and adhesion. A thoroughly cleaned substrate is a pre-requisite for the preparation of films with reproducible properties. The choice of cleaning techniques depends on the nature of the substrate, the type of contamination and the degree of cleanliness required. Residues from manufacturing and packaging, lint, fingerprints, oil and airborne particulate matters are examples of frequently encountered contaminants. For the deposition of polycrystalline films generally, glass, quartz, plastic and ceramic substrates are used. In this work, the ordinary microscope slides glass is used as substrate. For its cleaning, the following procedure was adopted by the author in the laboratory.

At first, the substrates are immersed in a luke warm aqueous solution of sodium carbonate in an ultrasonic cleaner for the removal of gross contaminations. After this, these are wasted in a stream of cold water and again dip in to dilute nitric acid for several minute. Then they are transferred into chromic acid [a mixture of Potassium dichromate in Sulfuric acid] for several

days. Taking them out from the Chromic acid, the traces of impurities that are loosely in contact with the substrate are eliminated by treating with cold water. Finally rinsing with deionized water for several times they are made dry by blowing hot air. Subsequent contamination was avoided by storing the substrate in desiccators. Cleanliness was tasted by carrying out the water-break cleaning test [138]. During the whole process the substrates were always held by slide holding forceps.

3.5 PATTERN OF THE SAMPLE AND PREPARATION OF MASK

In order to study the various properties of thin films, specific shape and size of films are necessary. The most commonly used methods of pattering thin films are:

(i) Physical masking,
(ii) Photoresist,
(iii) Inverse photoresist and
(iv) Inverse metal masking.

In the work, Physical masking has been used by author. These are suitably shaped apertures through which deposition is made to have a desired pattern of the film. Specially for the chemical spray deposition system, the material for the masks should be selected in such a way that it remained inert to the chemicals used for the deposition. Mica and stainless steel is a suitable masking material for this process because of their chemical inertness and capacity for high temperature tolerance. The film uniformity strongly depends on the dimension of mask. Hence, the mask should be as thin as possible. In the pyrolysis process, it is assumed that the chemical reaction takes place in the vapor phase at the substrate surface or in its close vicinity. So the effect of mask dimension on the uniformity of film thickness is very important and should be taken into account. This problem can be properly solved by preparing mask using single layer mica sheet.

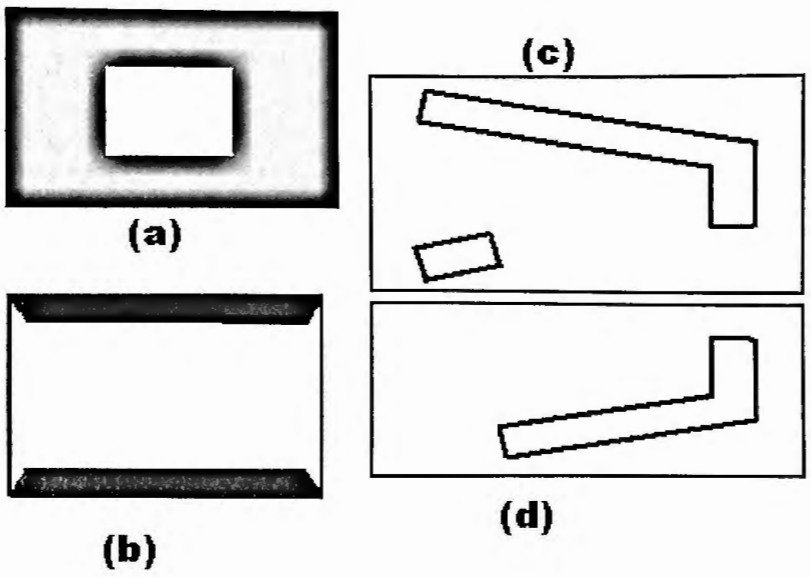

***Figure 3.2**: Pattern of mask used in film deposition; (a) Mica mask to deposit the sample for electrical, optical and Hall effect measurement; (b) A stainless steel frame to hold the mask and the substrate intimately in contact; (c) Mask to deposit Pb-film for thermopower reference contact; (d) Mask to deposit the MnO_2 sample for thermopower measurement.*

The measurement of resistively and Hall co-efficient of the samples van-der-Pauw method [82] was followed. In order to do this, it is necessary to deposit the sample of such a pattern that can take the shape of van-der-Pauw specimen and this can done by a suitable mask (mica) as shown in Figure 3.2(a). To keep this mask in contact with the substrate surface, a stainless steel frame is cut in the shape in Figure 3.2(b). This frame can hold the mask with substrate surface by giving suitable pressure. Other type of mask is shown in Figure in 3.2 (c) and (d) for the study of thermoelectric power of the samples. Figure 3.2(c) illustrate the mask made of stainless steel or aluminum sheet and is used to deposit metal film (**Pb**) as to form a junction with $\mathbf{MnO_2}$ films. **Pb** film was deposited by vacuum evaporation method. Figure 3.2(d) shows the mask, made of mica for the deposition of $\mathbf{MnO_2}$ films. A great care was taken in preparing mask with a thin mica sheet because of its brittle nature. Only fresh cleaved mica sheet was to avoid cleaning procedure and mask was cut by a sharp knife to have sharp edge, which became favorable in measuring film thickness by optical interference method.

3.6 FILM DEPOSITION PARAMETERS

In the chemical spray deposition technique the structure, composition and other characteristics of the deposited films depend on a number of process variables [deposition parameters]. The variable quantities such as the substrate temperature, solution and gas flow rate, deposition time, quality of the substrate material, size of atomized particles, solution concentration, and substrate to spray outlet distance, etc. are affected on the film properties. It is obvious that the substrate temperature is the most important deposition parameter and it is controlled with great care.

For the deposition of $\mathbf{MnO_2}$ thin film, all the above mentioned parameters except

(i) Substrate temperature (T_S);
(ii) Deposition time (t_d);
(iii) Solution concentration (C);
(iv) Spray rate (S_r)
(v) Spray outlet to substrate distance (d_s) and
(vi) Carrier air pressure (P_a).

were kept at their optimum vales. To study the effect of any one of these six parameters on the film properties the remaining other were kept constant.

Air current disturbances become another parameter, which creates problem to get uniformity of thickness and homogeneity of the film.

3.7 FILM DEPOSITION

Before starting deposition, the whole setup is thoroughly cleaned. Solution of $Mn(C_2H_3O_2)_2.4H_2O$ is taken in the flask F [Figure 3.1c]. A clean substrate with suitable mask is placed on the heat susceptor of the heater H. A Chromel-alumel thermocouple is put in contact with the substrate surface on which film is to be deposited. Before supplying the compressed air, the heater is kept on for some time to attain the substrate and the reactor wall E at the requisite temperature. The substrate temperature, T_s is raised to a level which is several degree higher than that of the required substrate temperature because at the onset of deposition the substrate temperature is dropped down somewhat.

As soon as the compressed air is passed through the tube A at a constant pressure of 1.39×10^5 Pa, a fine aerosol in the form of cloud is produced in the

flask. This aerosol is carried by the incoming air current to the reactor zone. On reaching the hot substrate surface $\mathbf{MnO_2}$ is formed by the pyrolytic action and deposits on the substrate surface. Films of $\mathbf{MnO_2}$ with appreciable thickness (≈ 200 nm) were obtained at substrate temperature, T_s = 593K in a deposition time of 30 min.

3.8 FILM THICKNESS CONTROL

In the present spray deposition process, it is found that the required film thickness may be obtained by controlling the deposition time (t_d) provided that the other parameters are kept constant. A longer deposition time yields a thicker film. Therefore, deposition time is the only thickness controlling factor in this process. Direct and in situ control of thickness, t is a difficult task because the deposition is carried out in normal atmosphere. In order to control the film thickness, a calibration chart is prepared, by plotting a graph t_d vs. t. The charts should be prepared at different constant substrate temperatures and priority is given for a particular experimental sample using the same solution and deposition variables. The rate of deposition is low and the reaction rate [the film formation for $\mathbf{MnO_2}$] is slow in the present setup. Therefore, the thickness may be controlled easily.

3.9 EVAPORATION OF METAL FILM (Pb) FOR CONTACT

For the study of thermoelectric power of $\mathbf{MnO_2}$ thin film, a reference material is required with respect to which thermopower is measured. In this experiment pure metallic lead (**Pb**) was used as a reference contact material, which has been thermally evaporated on a requisite substrate in a high vacuum coating unit at a pressure of 1.33×10^{-3} Pa. Molybdenum boat was used as a resistive heating element for the evaporation of **Pb**.

3.10 OPTIMIZATION OF THE DEPOSITION PROCESS

To obtain the optimum condition of the film deposition process, it is essential to select at first the requirements with respect to which the process should be optimized. The optimization process is very lengthy because there are a number of process variables. The basic requirement was to get a film of high transparency as well as high electrical conductivity.

For the process of optimization following set of films have been deposited:

(i) The first set of films was deposited at various substrate temperatures, T_s keeping all other deposition parameters constant at an arbitrary level. From this set of films, the optimum substrate temperature T_s was selected with respect to the best conducting and transparent films.

(ii) After obtaining the optimum value of T_s, second set of films were deposited by varying the substrate to spray outlet distance, d_s using the optimized T_s and other parameters were kept constant to the arbitrary level as they were in the first set. From this second set of films the optimum distance d_s was selected corresponding to the best film.

(iii) Fixing the distance d_s and substrate temperature T_s, a third set of films were deposited by varying the pressure of the carrier gas P_a. From this set, optimum carrier air pressure P_a was selected.

(iv) Keeping T_s, d_s and P_a as fixed, fourth set of films were deposited by taking spray rate S_r as variable parameters. From this set, optimum spray rate S_r was selected.

(v) The fifth set of films were deposited keeping T_s, d_s, P_a and S_r at their optimum values. In this case, the solution concentration C was varied for selecting the optimum concentration of the working solution.

Thus in all cases the optimum values of parameters [T_s, d_s, P_a, S_r and C] were selected for deposition of films that exhibit good conductivity and high transparency.

The resulting optimization is undoubtedly a tentative one because the process variables are in some degree mutually interdependent. It is found that the optimum values of the variables for **MnO_2** thin film are as

T_s = 593K,
Deposition rate = 6.7 nm/min;
d_s = 0.05 m;
$p_a = 1.39 \times 10^5$ Pa;
S_r = 0.8 ml/min and
C = 0.8M [molar].

3.11 LEAD ATTACHMENT TO THE FILM

Electrical measurements are performed by attaching leads to the films. Two methods are generally employed for this purpose:

(i) Solid phase bonding and

(ii) Alloy bonding.

The solid phase bonds are formed by thermocompression and ultrasonic means; on the other hand, the alloy bonds are formed by soldering. The soldering material is selected in such a way that it could provide an ohmic contact with the films.

In the present work, silver paint (leading silver D-200) is used. One end of a fine copper wire is attached to the film by using a little amount of silver paint on it. It is done carefully to avoid dry or poor contact. To obtain tight contact, a slight pressure was applied at the contact points.

3.12 MEASUREMENT OF FILM THICKNESS

Film thickness plays an important role on the electrical and optical properties of thin film and thus it is one of the most significant film parameters. Almost electrical parameters except the Hall mobility need for their evaluations the value of film thickness. Therefore, the thickness should be measured with a great care as far as possible to have an accurate value. The thickness may be measured either by monitoring the rate of deposition or after the film is taken out of the deposition chamber. The latter type is appropriate for the spray deposition technique because it is operated in open atmosphere. Optical interference method is one of the film thicknesses measuring method by which the thickness of the thin film can be determined accurately, a detail of this method has been already discussed in chapter two.

3.13 RESISTIVITY, SHEET RESISTANCE & T.C.R. MEASUREMENT

Van-der-Pauw technique [82] is one of the standard and widely used techniques for the measurement of resistivity of thin film. The theory of this technique has been discussed in chapter two. To measure resistivity, varying temperature the following experimental setup was adopted. Figure 3.3 shows the experimental setup of the van-der-Pauw's specimen with four small contacts A, B, C and D. in order and the points 1, 2, 3 and 4 indicate the terminals of the

electrometer for the measurement of voltage and currents, respectively. The voltage and current of the samples were measured for different temperatures. To vary the sample temperature, it was placed on a special designed heater.

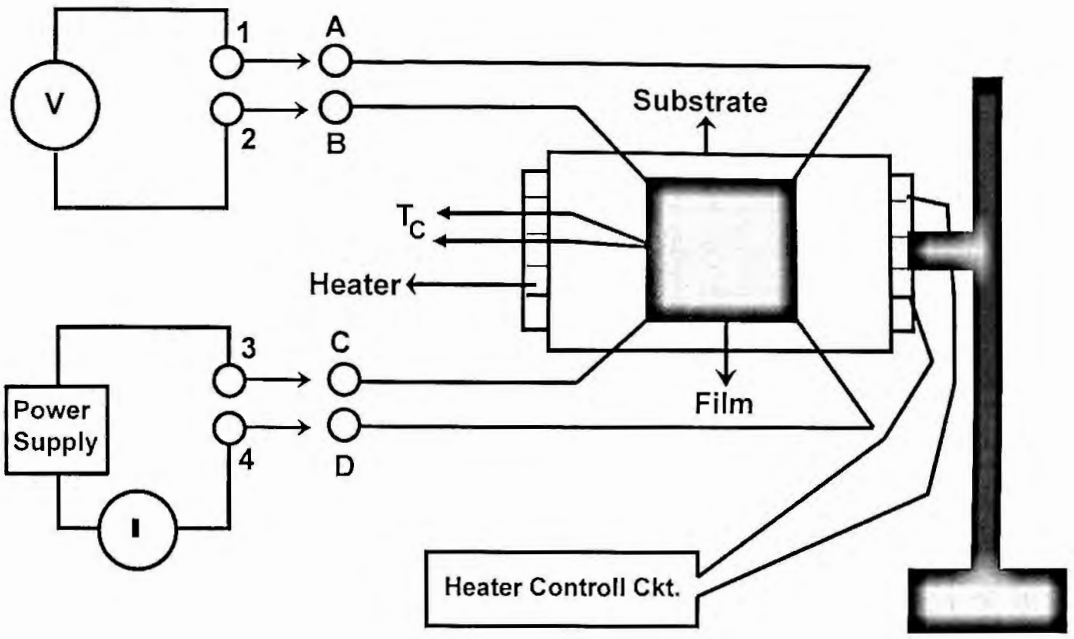

Figure 3.3: *Experimental setup for the measurement of film resistivity; 1, 2, 3& 4 are meter terminals and A, B, C & D are the film terminals; Arrows indicates commutator switches. V and I represent the voltmeter and ammeter, respectively; T_C is the thermocouple, which is used to measure film temperature.*

A dc 15 V is applied as a bias voltage across the film and the corresponding voltage and current were recorded. Using these data in Equations 2.10, 2.11, 2.15 and 2.18, the resistivity, conductivity, sheet resistance and T.C.R, of the films were calculated for a particular temperature, respectively.

Similar procedure was done for the $\mathbf{MnO_2}$ films of different substrate temperatures as well as different thicknesses.

3.14 HEAT TREATMENT OF THE AS-DEPOSITED FILMS

The as-deposited films show the high resistivity. For this reason, all samples were annealed.

For the heat-treatment, experiments a set of as-deposited undoped MnO_2 thin films of thickness about 180 nm were deposited onto glass substrate at

various substrate temperatures, viz. 563, 573, 583, 593, 603 and 613K, respectively. Heat-treatments were performed in four steps as described below. The heating and cooling rate was about 10 K-min^{-1} for each sample. A flat nichrome wire strip heater covered with mica sheet was used to heat the samples. The maximum heating temperature was 413K for all samples. The temperature was measured by a digital thermometer.

The first step of heat-treatment operation was carried out on as-deposited samples in air. After completing the first step of the heating and cooling cycle in air, the second step was performed on the sample in a similar manner. The variation of resistivity with temperature and the Hall voltage were measured using van-der-Pauw's four-probe method.

Then the sample was placed in the vacuum of the order of 1.33×10^{-3} Pa and the sample was heat-treated at a constant temperature 473K during one hour. Then the sample was taken out from the vacuum chamber and the third heating-cooling cycle was performed in air.

Again the sample was placed in the vacuum chamber for the heat-treated during 1 hour at a constant temperature 473K. The sample was then removed from the vacuum chamber. The fourth heating-cooling cycle was performed in air. The electrical resistivity and the Hall voltage were measured simultaneously during the heat-treatment in air only.

3.15 AGING EFFECT MEASURMENT

Aging effect has been studied for consecutive 15 days of $\mathbf{MnO_2}$ films at various thicknesses. The resistivity of the $\mathbf{MnO_2}$ films were measured using the technique, as described in section 3.13.

3.16 MEASUREMENT OF HALL EFFECT

Hall effect studies were carried out by van-der-Pauw [82] technique. The magnetic field used for the study of Hall effect was provided by an electromagnet designed and produced by Newport Instruments Ltd. England. Here a special designed heater is mounted on one end of an aluminum foil and the film was mounted on the other end of that aluminum foil. Aluminum foil is used because it is non-magnetic and high heat conducting material. At first, the special designed heater heats the foil and then the film is heated slowly. The temperature of the film was measured by the chromel-alumel thermocouple. Figure 3.4 shows the

experimental setup to measure Hall effect of the van-der-Pauw's specimen with four small contacts A, B, C and D. in order 1, 2, 3 and 4 indicate the terminals of the electrometer for the measurement of voltage and currents.

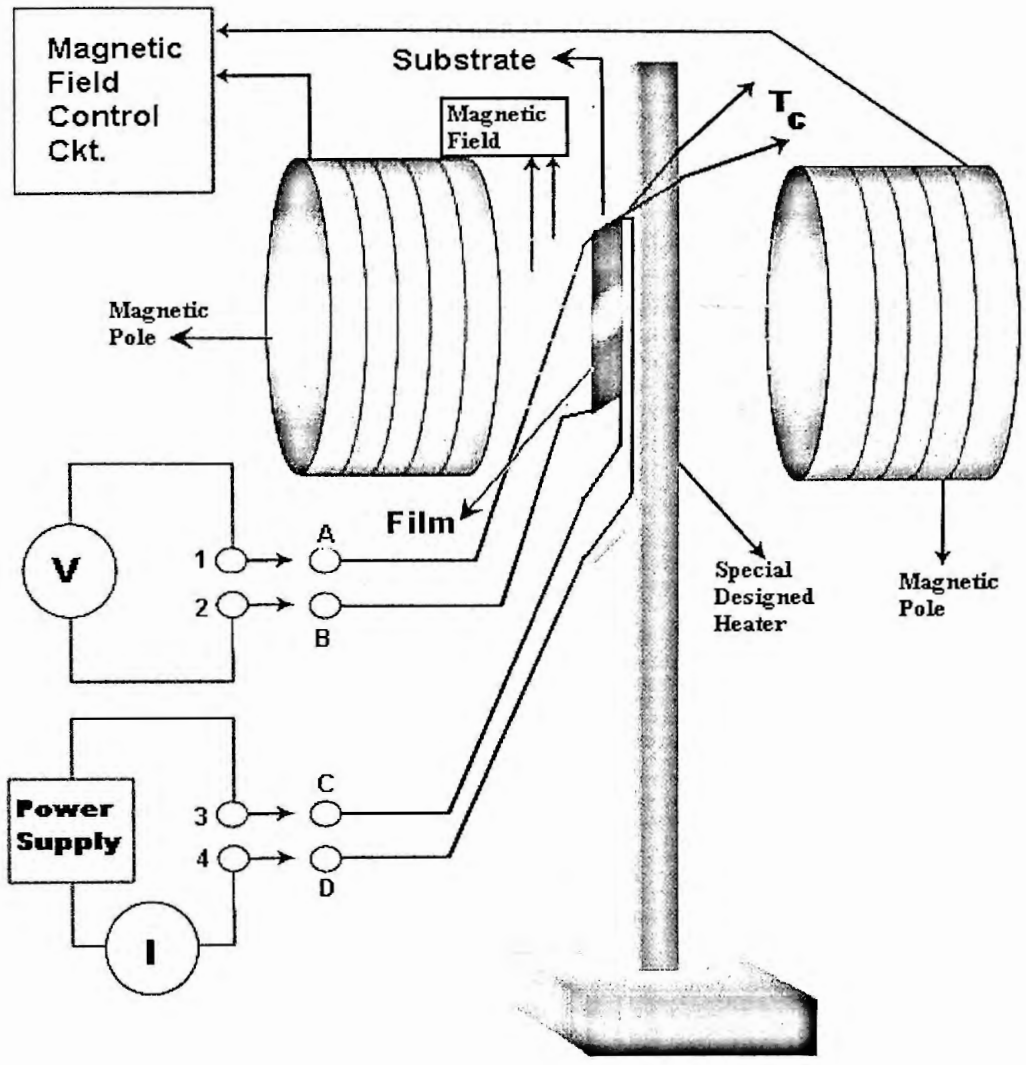

Figure 3.4: *Experimental setup for the measurement of Hall voltage; 1, 2, 3& 4 are meter terminals and A, B, C & D are the film terminals; Arrows indicates commutator switches. V and I represent the voltmeter and ammeter, respectively; T_C is the thermocouple, which is used to measure film temperature.*

A dc 15 V is applied as a bias voltage across the film and the corresponding voltage and current were recorded without magnetic field and applying magnetic field, respectively. In the present work, the magnetic field was varied between 4.75

to 7.22 KGS. The current and voltage were measured by a digital multimeter (model, DL-711) and digital electrometer (Keithley, 614), respectively. The corresponding Hall voltage was recorded for different temperatures.

3.17 MEASUREMENT OF THERMOELECTRIC POWER [TEP]

For the measurement of thermoelectric power of MnO_2 thin films, the experimental set up is shown in the Figure 3.5.

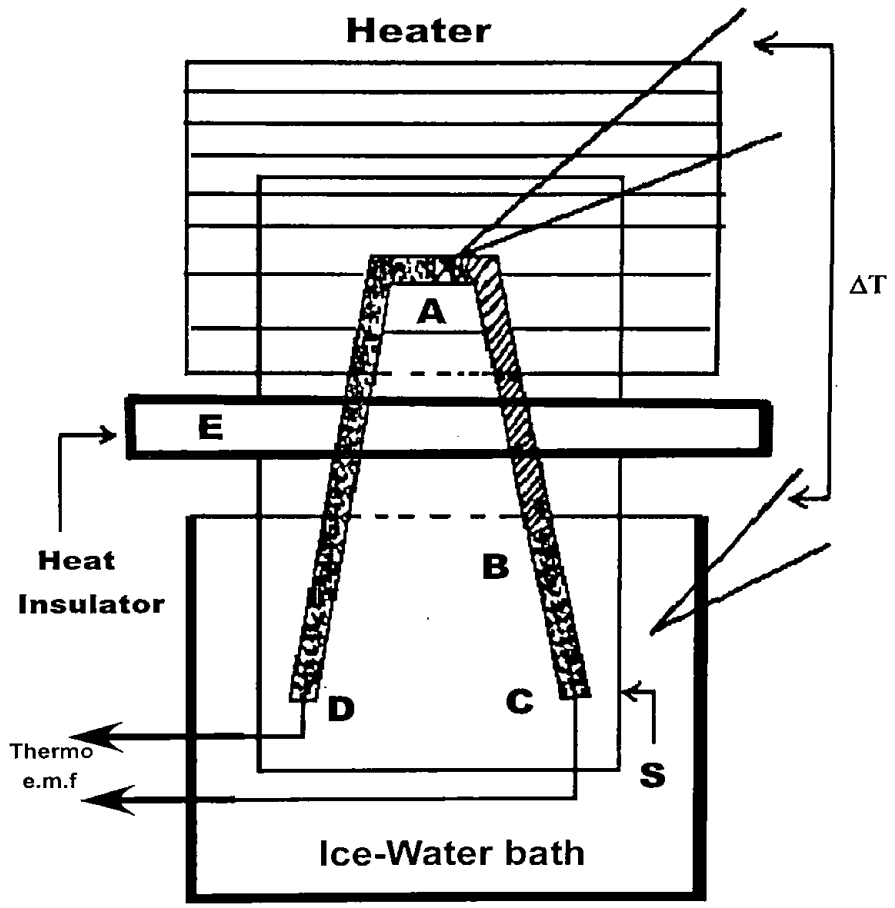

Figure 3.5: *Schematic diagram of thermopower measuring apparatus, AB-MnO_2 film; AD and BC- lead films, S- substrate, E- heat insulating barrier, ΔT is the temperature difference between hot and cold ends.*

The cold junction B was immersed into an ice-water bath of constant [273K] temperature. The temperature of the hot junction was measured using a chromel–alumel thermocouple attached to the sample. The generated thermo e.m.f was recorded using a digital voltmeter. The hot and cold junctions were kept thermally isolated by inserting an insulated barrier, E between the junctions to

minimize heat radiation from the hot to cold end. The immersed portion of the sample was kept electrically insulated to remove any leakage of e.m.f. between D and C due to contact with the ice water. The whole apparatus was kept in a suitable enclosure to minimize air current disturbances.

The temperature of the hot junction was raised slowly from room temperature and at regular intervals of 10K, the thermo e.m.f was noted up to the highest temperature of 413K. All the samples were annealed in vacuum before using for any measurement. This was necessary because the as-deposited samples were of very high resistivity. Using this process, e.m.f. was measured for different films of different thicknesses.

3.18 MEASUREMENT OF OPTICAL SPECTRA

Optical spectra has been measured in wavelength ranges $0.3 < \lambda < 2.5$ μm using a Perkin-Elmer lambda-19 double beam spectrophotometer for both the as-deposited and annealed $\mathbf{MnO_2}$ films.

A sample with substrate was placed in the spectrometer. Optical transmission [in percentage] of the film for normal incidence was obtained from a graph that was automatically plotted against wavelengths during the period of spectral transmission. Similarly, the optical reflectance of that sample was measured. The optical spectra were measured for different thicknesses as well as different deposition temperatures of $\mathbf{MnO_2}$ samples.

Optical absorptions of these samples were calculated from the transmission data at different wavelengths. Since the samples were highly transparent in the visible region of the spectra, the reflection coefficients for the normal incidence were taken negligible in consideration. The value of the reflective index of the film was calculated from the transmission data. From these optical data the band gap of the films were also determined.

3.19 ELECTRON AFFINITY AND WORK FUNCTION CALCULATION FOR MnO_2

According to Sanderson electronegativity principle [115], when two or more atoms initially different in electronegativity combine chemically, they adjust to have the same intermediate electronegativity within the compound. This intermediate electronegativity is given by the geometric mean of the individual electronegativity of the component atoms. That is, the geometric mean of n numbers is obtained by multiplying all of the numbers together and taking the n^{th} root of the product. According to this principle, the electronegativity of $\mathbf{MnO_2}$ can be written as

$$\mathbf{E_n\,(MnO_2) = \left[E_{Mn} \times (E_O)^2\right]^{\frac{1}{3}}},$$

where E_{Mn} and E_O are the electrornegativities of manganese and oxygen atoms, respectively. E_n is the electronegativity of $\mathbf{MnO_2}$.

From the electronegativity concept the percentage of the ionic character, y of the bond between manganese and oxygen can be obtained by using Sanderson's electronegativity values [115] in Pauling's empirical relation [116]

$$\mathbf{\%\ ionic\ character = [1 - exp\ (-0.25\{E_{Mn} - E_O\}^2)]\ x\ 100\%}$$

In the absence of straightforward method of determining the electron affinity of the bulk semiconductor, an indirect and empirical method [117] is used to determine the electronegativity of the atoms. In the case of semiconductor the relation between bulk electronegativity E_n corresponds to the intrinsic Fermi level E_F with respect to the vacuum level is

$$\mathbf{E_F \approx E_n = \chi + E_g/2} \qquad (3.1)$$

where χ is the electron affinity and E_g is the optical band gap between the conduction band and valance band. The work function W is obtained using the following relation [118]

$$\mathbf{W = \chi - E_F}. \qquad (3.2)$$

Using the optical data of $\mathbf{MnO_2}$ thin film the band gap E_g is obtained from the plot of $(khv)^{1/2}$ vs. hv. The position of the Fermi level E_F is obtained from the

thermoelectric data for $\mathbf{MnO_2}$ thin film and the carrier concentration n is determined from the Hall effect experiment. From graphs of the variation of E_g and E_F with the carrier concentration n, taking the value of E_n, the electron affinity χ of different $\mathbf{MnO_2}$ samples is determined using Equation 3.1. Using the values of χ and taking values of E_F from the E_F vs. n graph, different values of the work function (W) for $\mathbf{MnO_2}$ films are calculated using the Equation 3.2.

3.20 STUDIES FOR SELECTIVE SURFACE

To determine the selective surface properties of $\mathbf{MnO_2}$ thin films, the integrated values of %T and %R for some particular wavelengths were determined from the optical data using computer program and then their average values were calculated. The integrated luminous transmittance as well as reflectance were obtained using standard luminous efficiency function for photooptic vision [124] as specified CIE (Commission International de I'Éclairage). The integrated solar transmittances as well as reflectance were obtained according to the tabulated AM2 irradiance spectrum [125].

These calculations were done for $\mathbf{MnO_2}$ films of different thicknesses as well as of different substrate temperatures.

Chapter 4

Results & Discussions

In this chapter the results and discussions of the various experimental studies on MnO_2 thin films have been presented and discussed step by step.

4.1 STRUCTURAL STUDIES

4.1.1 XRD Study of MnO_2 Thin Films

The X-ray diffraction of **MnO_2** samples were done using a diffractometer, model **MACSCIENCE M18XHF-SRA, Japan,** courtesy by Y. Yamamoto [140].

The samples of **MnO_2** were prepared at constant spray rate = 0.8 ml /min, solution concentration = 0.8 M, spray outlet to substrate distance = 0.05m and carrier air pressure = 1.38×10^5 Pa and the deposition rate = 6.7 nm/min, respectively.

X-ray diffractograms of all the samples were recorded using monochromatic CuK_α radiation (λ = 1.541838 Å), scanning speed 1degree/min, starting from 20^0 and ending at$100^0$to ensure the information of the single phase nature of the sintered product. Peak intensities are recorded corresponding to their 2θ values.

The X-ray diffractogram of **MnO_2** samples of different deposition temperatures and thicknesses are shown in Figures 4.1 to 4.6, respectively. From these diffractogram, the **MnO_2** films, which are deposited at 593K, have remarkable peaks and others have no peaks. Figure 4.3 and Figure 4.6, respectively show such two samples, which are deposited at 593K of thicknesses 200 nm and 380 nm, respectively.

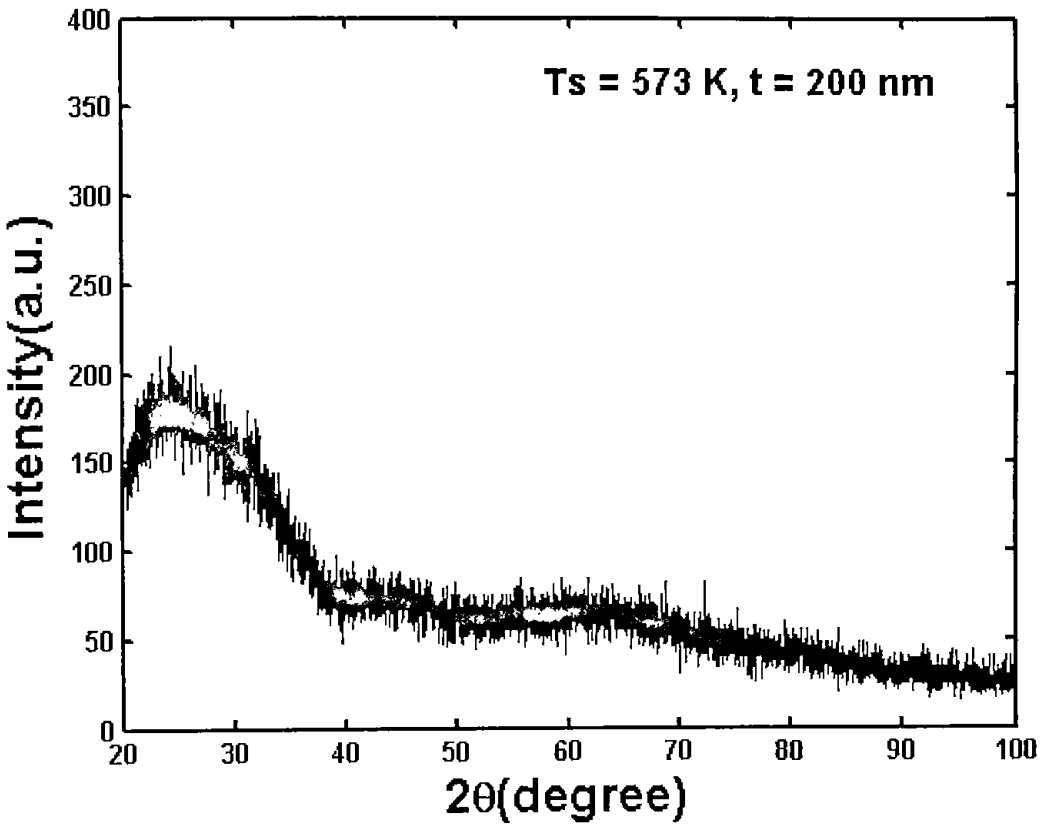

Figure 4.1: *XRD pattern of MnO_2 film of thickness 200nm and substrate temperature 573K.*

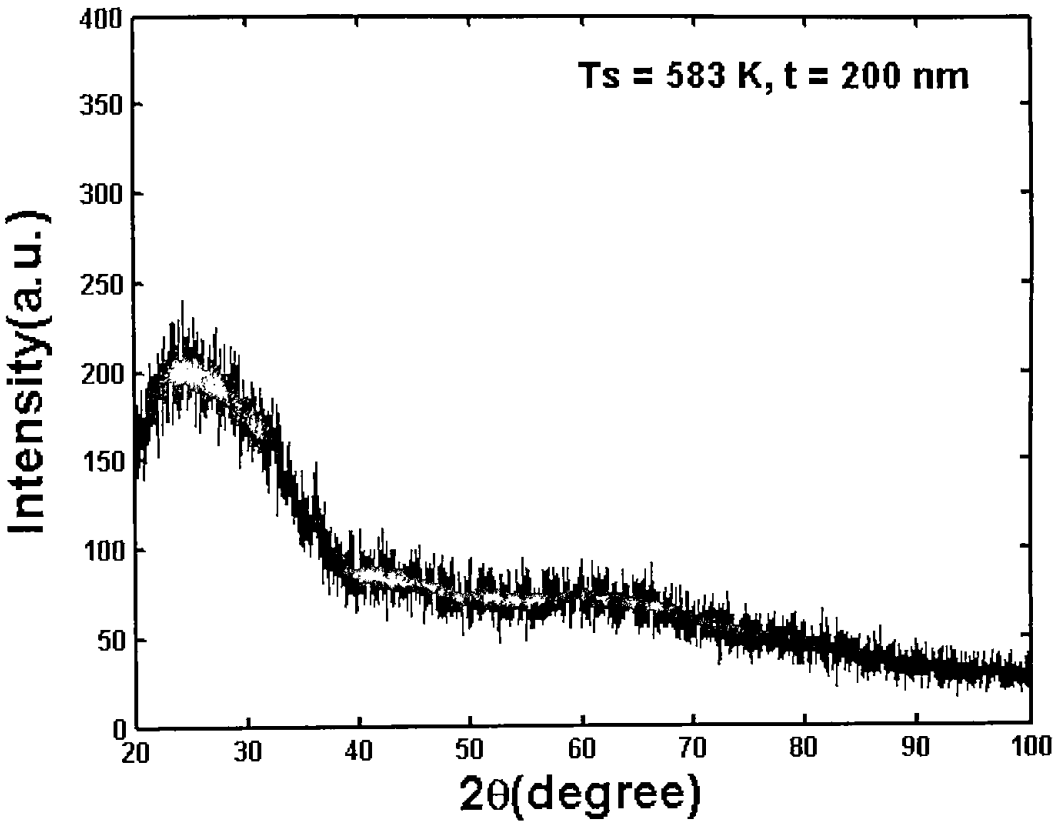

Figure 4.2: *XRD pattern of MnO_2 film of thickness 200nm and substrate temperature 583K.*

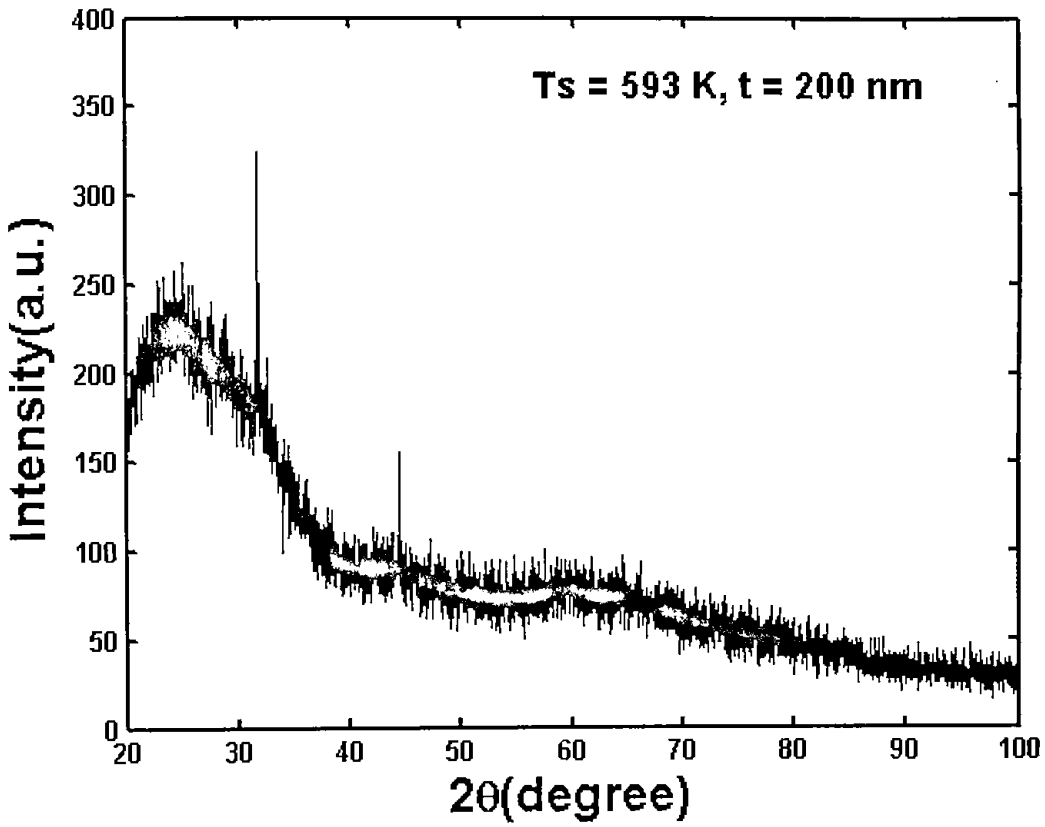

Figure 4.3: *XRD pattern of MnO_2 film of thickness 200nm and substrate temperature 593K.*

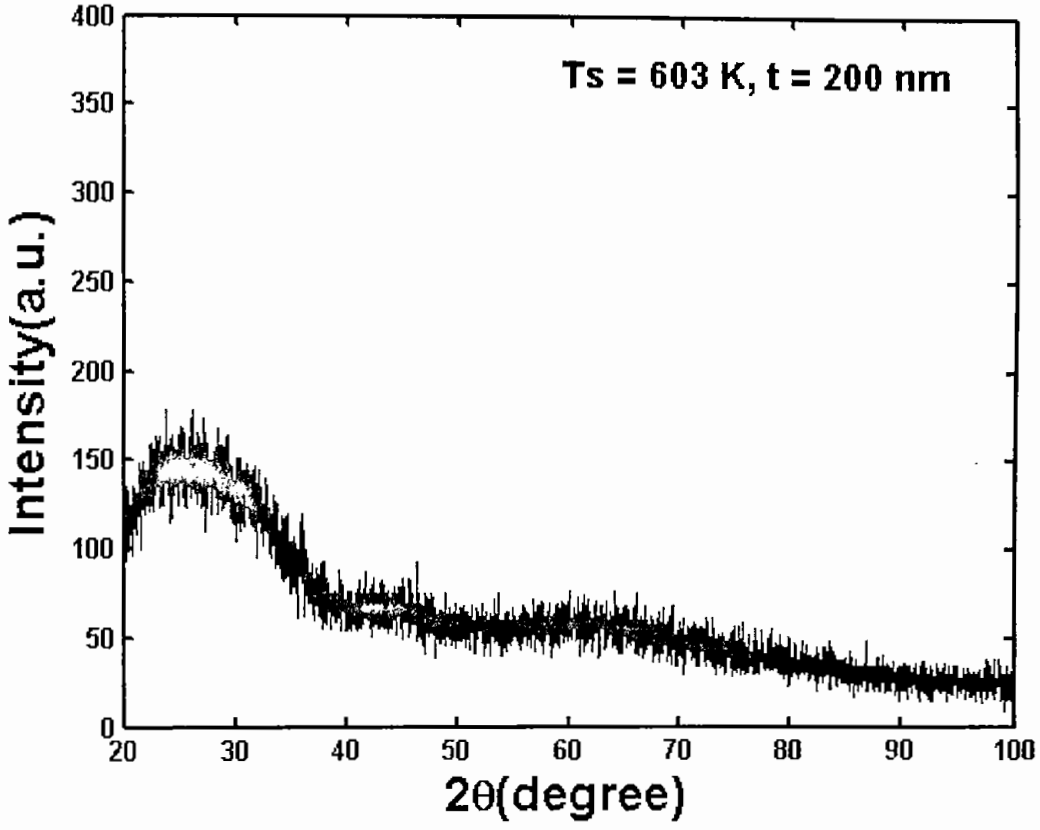

Figure 4.4: *XRD pattern of MnO_2 film of thickness 200nm and substrate temperature 603K.*

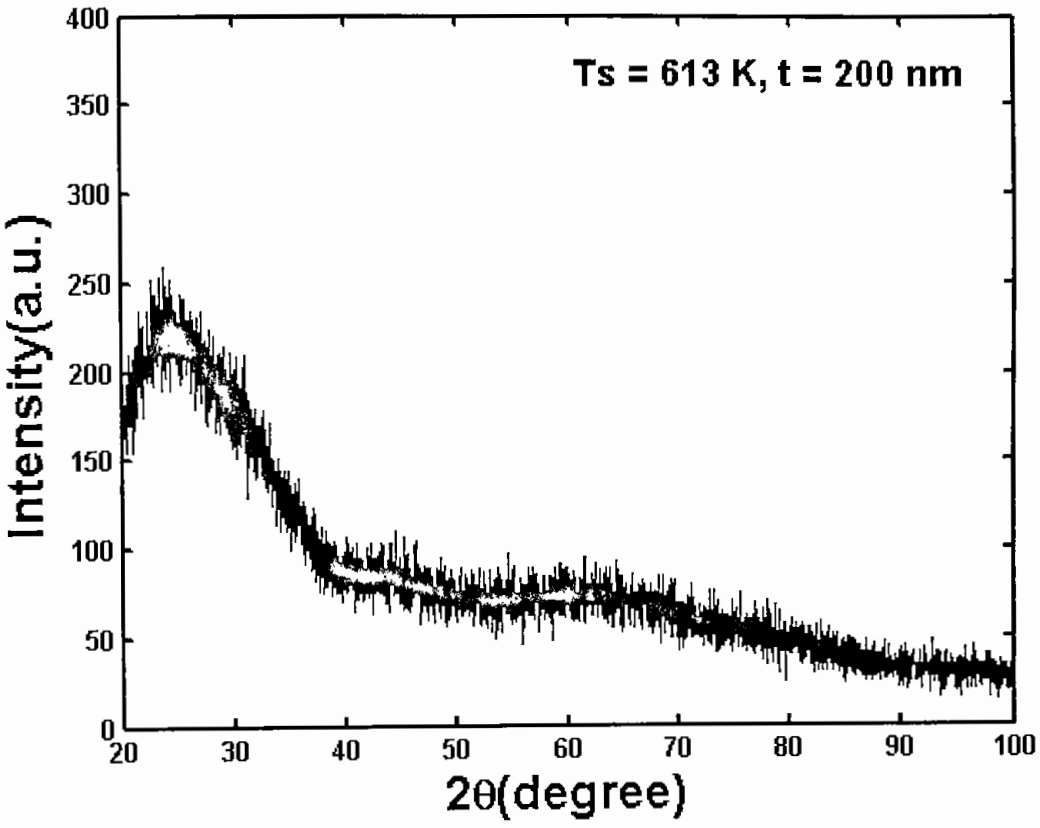

Figure 4.5: *XRD pattern of MnO_2 film of thickness 200nm and substrate temperature 613K.*

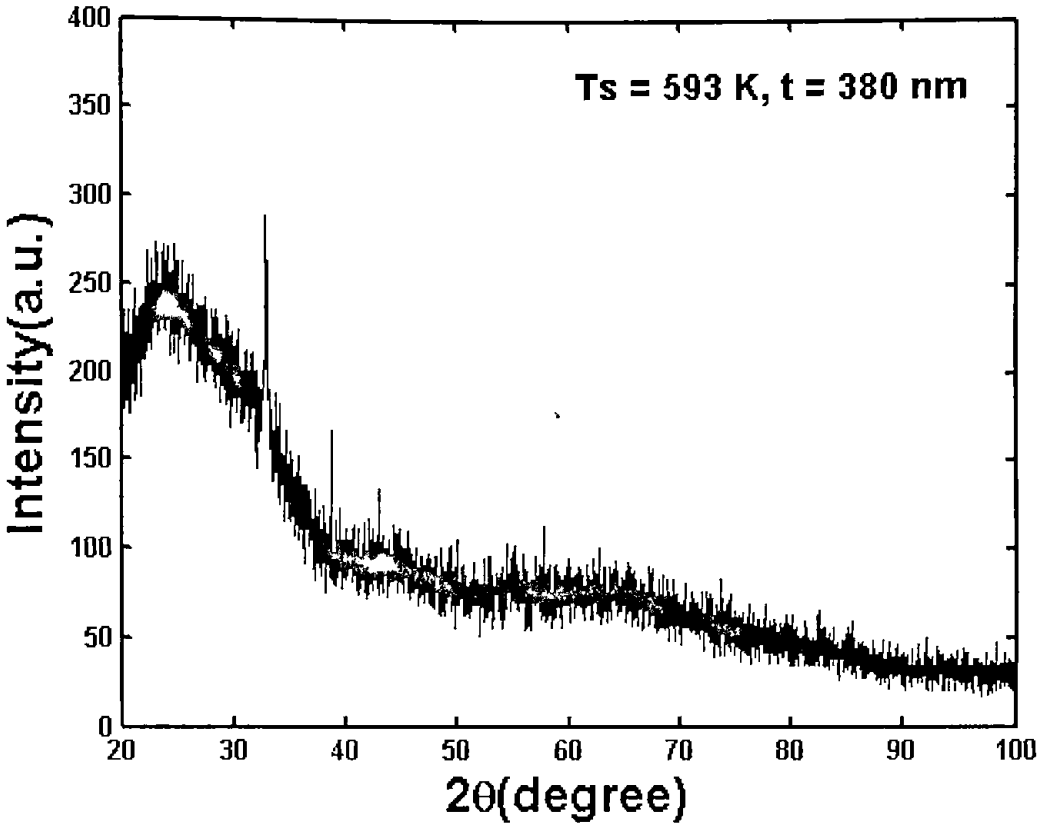

Figure 4.6: *XRD pattern of MnO_2 film of thickness 380nm and substrate temperature 593K.*

Using these data of diffractogram the d_{hkl} (interplanar distance) values and their corresponding <hkl> values are calculated using computer program "PowderCell for Windows v.2.3". The d_{hkl} values and their corresponding <hkl> values from the standard JCPDS Card# 24-0735 [141] and the calculated d_{hkl} values of these two samples are tabulated in Table 4.1 and Table 4.2, respectively. Using these data the calculated lattice parameters of the **MnO_2** are: a = 4.3985 Å and c = 2.8750 Å.

Table-4.1

Plane#	d_{hkl} (calculated) in Å	d_{hkl} (JCPDS Card# 24-0735) Å	hkl
1	3.1076	3.1100	110
2	2.4018	2.4070	101
3	2.1969	2.1990	200
4	2.1087	2.1100	111
5	1.9681	1.9681	210
6	1.6202	1.6234	211
7	1.5570	1.5554	220
8	1.4370	1.4370	002
9	1.3909	1.3912	310
10	1.3609	1.3677	221
11	-	1.3061	301
12	1.3033	1.3045	112
13	1.2534	1.2524	311
14	1.2184	1.2192	320
15	1.2016	1.2029	202
16	1.1605	1.1604	212
17	1.1229	1.1232	321
18	-	1.1000	400
19	-	1.0679	410
20	1.0560	1.0556	222
21	1.0367	1.0370	330
22	-	0.9998	312
23	-	0.9838	420
24	-	0.9360	103
25	-	0.8734	402
26	-	0.8629	510
27	-	0.8614	213
28	-	0.8567	412
29	-	0.8110	332

[Reproduced from reference 141, JCPDS Card# 24-0735].

Table-4.2

Plane#	d_{hkl} (calculated) in Å	d_{hkl} (JCPDS Card# 24-0735) Å	hkl
1	3.1066	3.1100	110
2	2.4011	2.4070	101
3	2.1965	2.1990	200
4	2.1081	2.1100	111
5	1.9681	1.9681	210
6	1.6231	1.6234	211
7	1.5560	1.5554	220
8	1.4380	1.4370	002
9	1.3910	1.3912	310
10	1.3690	1.3677	221
11	-	1.3061	301
12	1.3035	1.3045	112
13	1.2513	1.2524	311
14	1.2186	1.2192	320
15	1.2023	1.2029	202
16	1.1606	1.1604	212
17	1.1224	1.1232	321
18	-	1.1000	400
19	-	1.0679	410
20	1.0561	1.0556	222
21	1.0365	1.0370	330
22	-	0.9998	312
23	-	0.9838	420
24	-	0.9360	103
25	-	0.8734	402
26	-	0.8629	510
27	-	0.8614	213
28	-	0.8567	412
29	-	0.8110	332

[Reproduced from reference 141, JCPDS Card# 24-0735].

There are 18 d_{hkl} (interplanar distance) values identified in author's study. Their relative d_{hkl} magnitude may be compared with the 29 d_{hkl} magnitude of JCPDS Card# 24-0735 [141]. In comparison, it is found that author's 18 d_{hkl} do agree closely in values, with 18 d_{hkl} values of the JCPDS Card and their corresponding planes are <110>, <101>, <200>, <111>, <210>, <211>, <220>, <002>, <310>, <221>, <112>, <311>, <320>, <202>, <212>, <321>, <222>, <330>, respectively.

4.1.2 Electron Microscopy Study of MnO_2 Thin Film

Transmission Electron Microscopy was used to characterize the microstructure of **MnO_2** thin films. Electron energy of 300KeV and the value of the electron wavelength 0.00196875 nm and effective camera length 1 m are used in this study. Figure 4.7(a) and 4.7(b) show the TEM image of the **MnO_2** thin films of thicknesses 200 nm and 380 nm, respectively.

Figure 4.7 (a): *TEM image of MnO_2 film of thickness 200nm deposited at a substrate temperature 593K.*

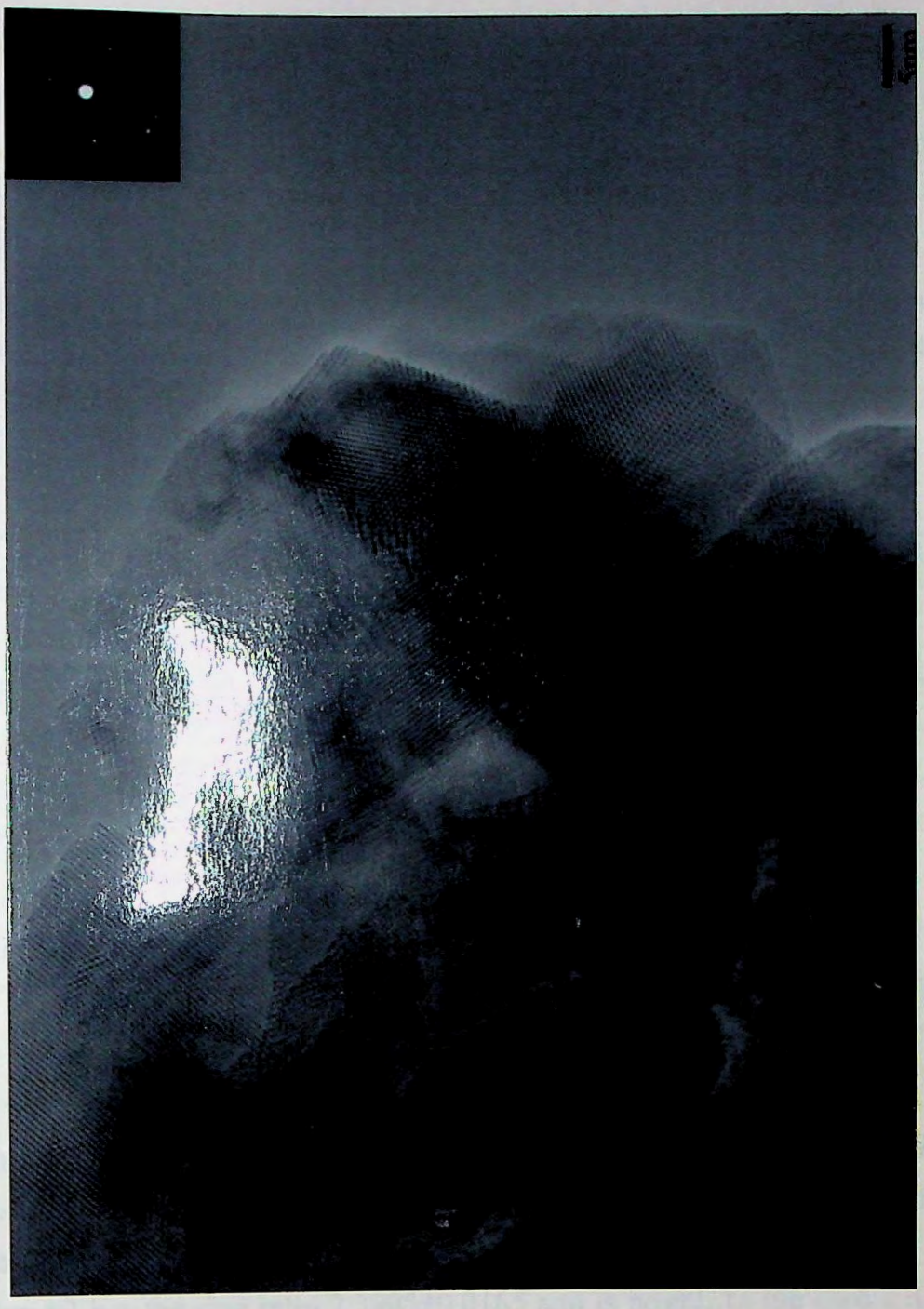

Figure 4.7(b): *TEM image of MnO_2 film of thickness 380nm deposited at a substrate temperature 593K.*

The specific crystal planes were determined by the Electron diffractogram. Figures 4.8(a) and 4.8(b) show the electron diffraction pattern of $\mathbf{MnO_2}$ thin films of thicknesses 200 nm and 380 nm, respectively. The interplanar distances (d_{hkl}) of the crystalline phase were calculated by means of the following expression [81]:

$$\mathbf{d_{hkl} = \frac{\lambda L}{R}} \; ;$$

where λ is the electron wavelength at 300KeV, i.e. 0.00196875 nm, L is the effective camera length of the TEM and R is the radius of the rings from the electron diffraction pattern. For analysis, the ring diameters of the studied diffractogram were measured and their relative ratios were calculated using the above equation.

Table 4.3 shows the calculated data from an electron diffraction pattern of 200 nm thick MnO_2 film and data from the standard JCPDS Card# 24-0735 [141]. Six rings are identified in the diffractogram; they are designated with the <hkl> indices in Figure 4.8(a).

Table: 4.3

Data from Diffraction Pattern			Data from JCPDS Card # 24-0735		
Ring#	**Ring ratio**	**Remarks on ring intensity**	**Lattice Ratio**	**Relative intensity**	**hkl**
1	3.0985±0.0115	weak	3.1100	100	110
2	2.3905±0.0165	bright	2.4070	55	101
3	2.0921±0.0179	weak	2.1100	16	111
4	1.6093±0.0141	bright	1.6234	55	211
5	1.5440±0.0114	weak	1.5554	14	220
6	1.2776±0.0269	bright	1.3045	20	112

[Reproduced from reference 141, JCPDS Card# 24-0735].

In the card's result, plane <110> has lattice parameter ratio 3.1100 and the corresponding relative intensity is 100. Comparing this result with the result (3.0985+0.0115) of ring #1 in the diffraction pattern, it is seen that the ring #1 may correspond to the plane <110>.

Ring #2 has the ring ratio 2.3905±0.0165 and is bright. In the card's data, plane <101> has the relative intensity 55 and the lattice ratio is 2.4070. Comparing these results with the result of ring #2, the plane <101> may correspond to ring #2.

Now considering ring #3, it is seen that it is weak and its ring ratio is 2.0921±0.0179. Comparing this result with the card's data, plane <111> has the relative intensity 16 and the corresponding lattice ratio is 2.1100. Thus the plane <111> may correspond to ring #3.

The 4th bright ring has the ring ratio 1.6093±0.0141. Comparing its brightness and ring ratio with the intensity and lattice ratio of the plane <211>, respectively, it is seen that the plane <211> may correspond to ring #4.

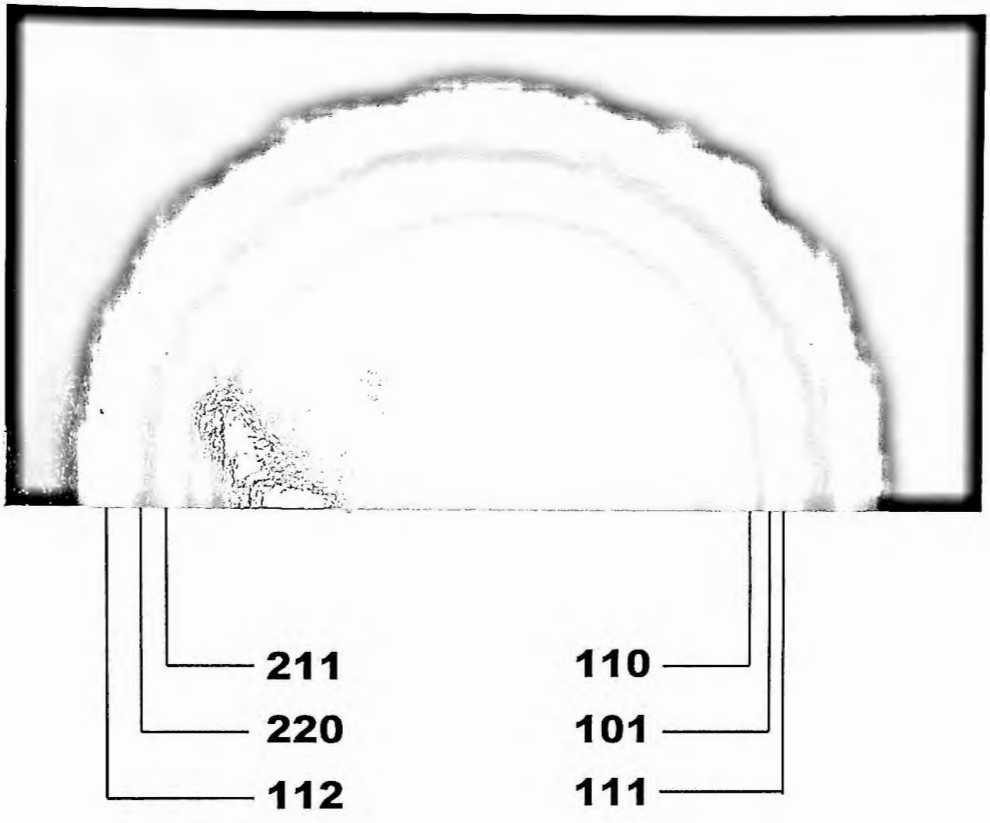

Figure 4.8 (a): *Electron Diffraction pattern of MnO_2 film of thickness 200nm deposited at a substrate temperature 593K.*

The 5th ring has weak intensity and the corresponding lattice ratio is 1.5440±0.0114. Comparing its intensity and the ring ratio with the intensity and lattice ratio of the plane <220>, respectively, it is seen that the plane <220> may correspond to ring #5.

The 6th ring has bright intensity and the corresponding lattice ratio is 1.2776±0.0269. Comparing its intensity and the ring ratio with the intensity and lattice ratio of the plane <112>, respectively, it is seen that the plane <112> may correspond to ring #6.

Table 4.4 shows the calculated data from an electron diffraction pattern of 380 nm thick **MnO_2** film and data from the standard JCPDS Card # 24-0735.

Six rings are identified in the diffractogram; they are designated with the <hkl> indices in Figure 4.8(b).

Table: 4.4

Data from Diffraction Pattern			Data from JCPDS Card # 24-0735		
Ring#	**Ring ratio**	**Remarks on ring intensity**	**Lattice Ratio**	**Relative intensity**	**hkl**
1	3.0875±0.0225	weak	3.1100	100	110
2	2.3965±0.0105	bright	2.4070	55	101
3	2.1090±0.0010	weak	2.1100	16	111
4	1.6202±0.0032	bright	1.6234	55	211
5	1.5462±0.0092	weak	1.5554	20	220
6	1.2856±0.0178	bright	1.3045	20	112

[Reproduced from reference 141, JCPDS Card# 24-0735].

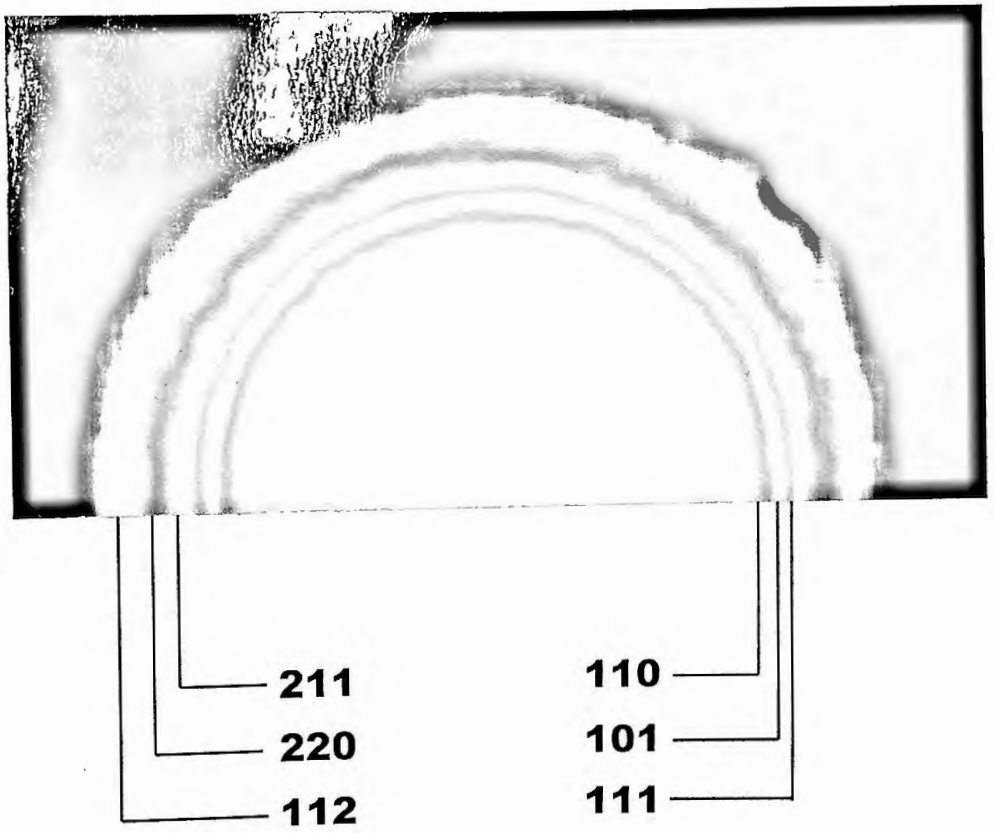

Figure 4.8(b): *Electron Diffraction pattern of MnO_2 film of thickness 380nm deposited at a substrate temperature 593K.*

In the card's result, plane <110> has lattice parameter ratio 3.1100 and the corresponding relative intensity is 100. Comparing this result with the result of ring #1 in the diffraction pattern, it is seen that the ring #1 may correspond to the plane <110>.

Ring #2 has the ring ratio 2.3965±0.0105 and is bright. In the card's data, plane <101> has the relative intensity 55 and the lattice ratio is 2.4070. Comparing these results with the result of ring #2, the plane <101> may correspond to ring #2.

Ring #3, it is seen that it is weak and its ring ratio is 2.1090±0.0010. Comparing this result with the card's data, plane <111> has the relative intensity 16 and the corresponding lattice ratio is 2.1100, thus the plane <111> may correspond to ring #3.

The 4th bright ring has the ring ratio 1.6202±0.0032. Comparing its brightness and ring ratio with the intensity and lattice ratio of the plane <211>, respectively, it is seen that the plane <211> may correspond to ring #4.

The 5th ring has weak intensity and the corresponding lattice ratio is 1.5462±0.0092. Comparing its intensity and the ring ratio with the intensity and lattice ratio of the plane <220>, respectively, it is seen that the plane <220> may correspond to ring #5.

The 6th ring has bright intensity and the corresponding lattice ratio is 1.2856±0.0178. Comparing its intensity and the ring ratio with the intensity and lattice ratio of the plane <112>, respectively, it is seen that the plane <112> may correspond to ring #6.

It is therefore, evident from the XRD and Electron Diffraction studies that **MnO_2** films prepared by spray pyrolysis are polycrystalline in structure which is well agreed with the reports by the other workers [11, 12, 61, 63].

4.2 EFFECT OF SUBSTRATE TEMPERATURE ON THICKNESS AND RESISTIVITY

The substrate temperature (T_s) is the most important parameter in the pyrolysis process. Figure 4.9(a) and 4.9(b) show the dependency of thickness and resistivity, respectively, with T_s in the ranges of 563 to 623K for a MnO_2 film prepared at a fixed spray rate 0.8 ml/min, solution concentration 0.8M, and carrier air pressure 1.38 x 10^5 Pa. Below 563K no stable film but a brawn powdery deposit was found.

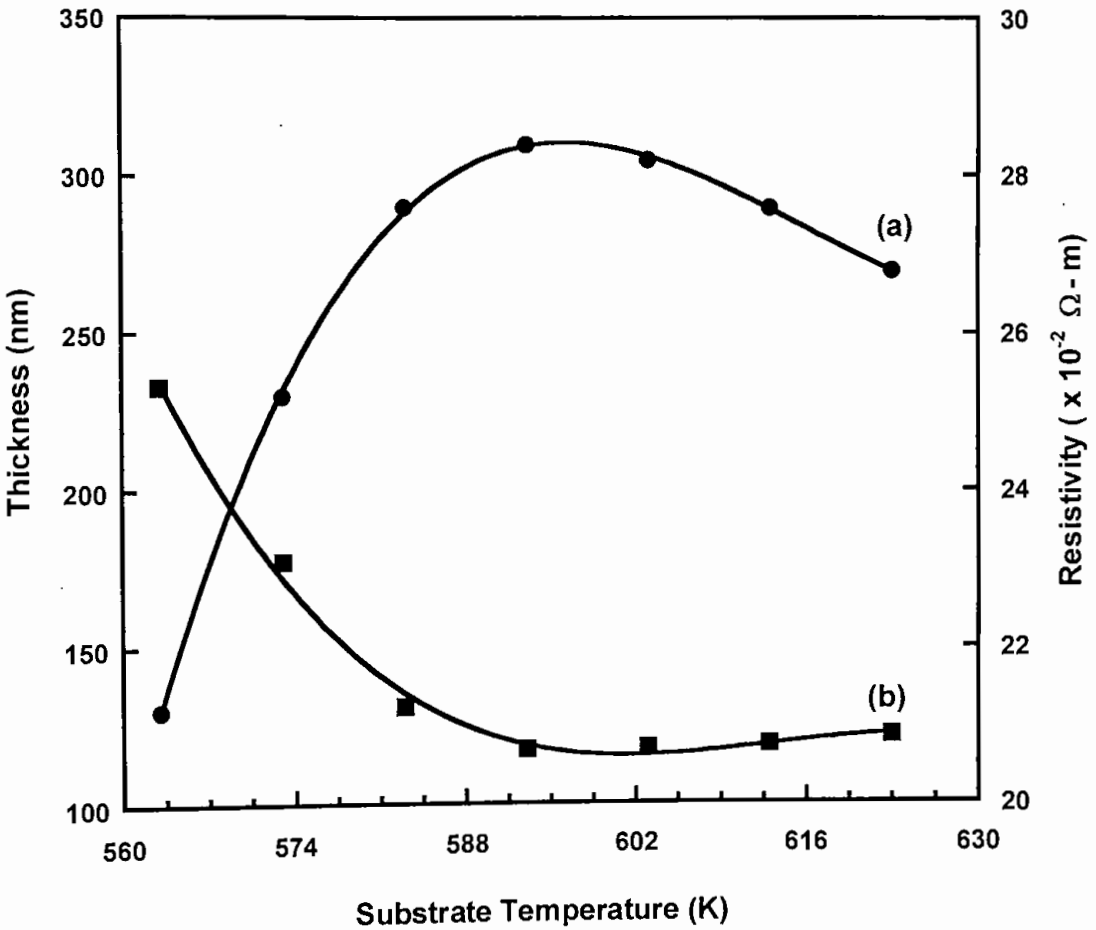

Figure 4.9: *Variation of (a) thickness (b) resistivity with substrate temperature, respectively.*

This can occur because thermal decomposition of manganese acetate needs a particular temperature. It is noted in Figure 4.9(a) that the film thickness is increased up to T_s = 593K and then its value falls with T_s. Generally, at lower

substrate temperatures diffusely scattering films are obtained. On the other hand, at higher substrate temperatures yield continuous and homogeneous films. At low temperatures, if the pyrolytic reactions have not been completed, some by-products or intermediate compounds will be trapped as impurities in the film. Film growth is controlled by gas and droplet dynamics [128]. As the substrate temperature increases wetting decreases, splitting, bouncing and the lateral mobility of the droplets increase. Laterally moving droplets in which the reaction proceeds more slowly have the opportunity to be swept away by the lateral wind. Thus at higher substrate temperatures re-evaporation of anionic species may occur which reduces the film thickness.

Figure 4.9(b) is a plot of resistivity vs. substrate temperature for a MnO_2 film of thickness 200 nm. It indicates the fall in resistivity with substrate temperature until it attains a minimum resistivity at T_s = 593K and beyond this range its resistivity goes slowly up. It is, therefore, significant that substrate temperature plays a vital role in obtaining conductive films. The optimum thickness as well as minimum resistivity are obtained at substrate temperature T_s = 593K and the author is used T_s = 593K in all deposition of MnO_2 films.

The substrate temperature has also a remarkable effect on the film growth rate. The growth rate t/t_d, where t_d denotes the deposition time, a plot of the variation of growth rate $\ln(t/t_d)$ with inverse substrate temperature T_s is shown in Figure 4.9(c).

The curve has a part of linear growth as well as a portion of flat growth region. The linear growth portion has a slope of activation energy of about 0.25eV. The flat region indicates a temperature independent character at higher temperature. This phenomena indicates that in the lower temperature region the surface reaction in the decomposition of $Mn(C_2H_3O_2)_2.4H_2O$ is dominated by two factors, the temperature T_s and the rate of reactant supply. On the other hand, at the higher temperature region the rate is so fast that the film growth rate becomes mostly dependent on the rate of reactant supply, which was kept constant in the present study.

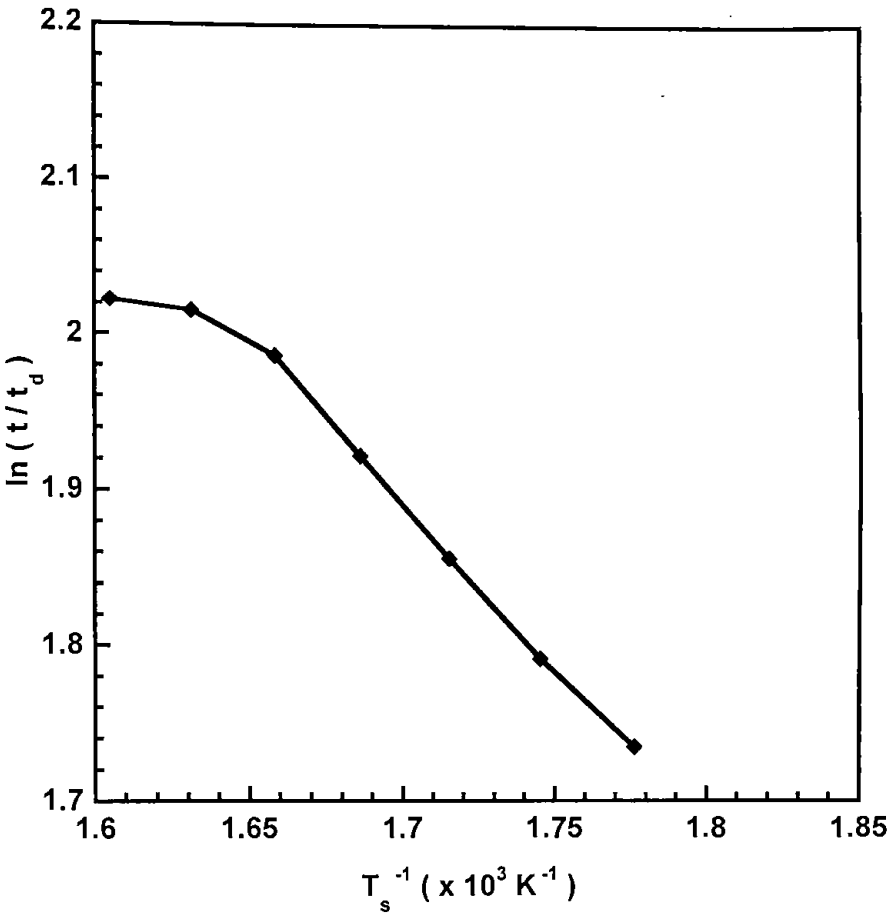

Figure 4.9(c): *The variation of growth rate $ln(t/t_d)$ with inverse substrate temperature T_s.*

4.3 EFFECT OF DEPOSITION TIME ON FILM THICKNESS

The dependence of film thickness on the deposition time is shown in the Figure 4.10. From the figure it is observed that, the film thickness increases with increasing deposition time. It is also observed that the variation of film thickness with deposition time is not exactly linear. This may naturally happen because at the starting of the spray, a portion of the aerosol can not reach at the substrate for its non-uniform distribution in the reaction chamber. This results in a lower deposition rate. From this result, the average deposition rate 6.7 nm/min is obtained.

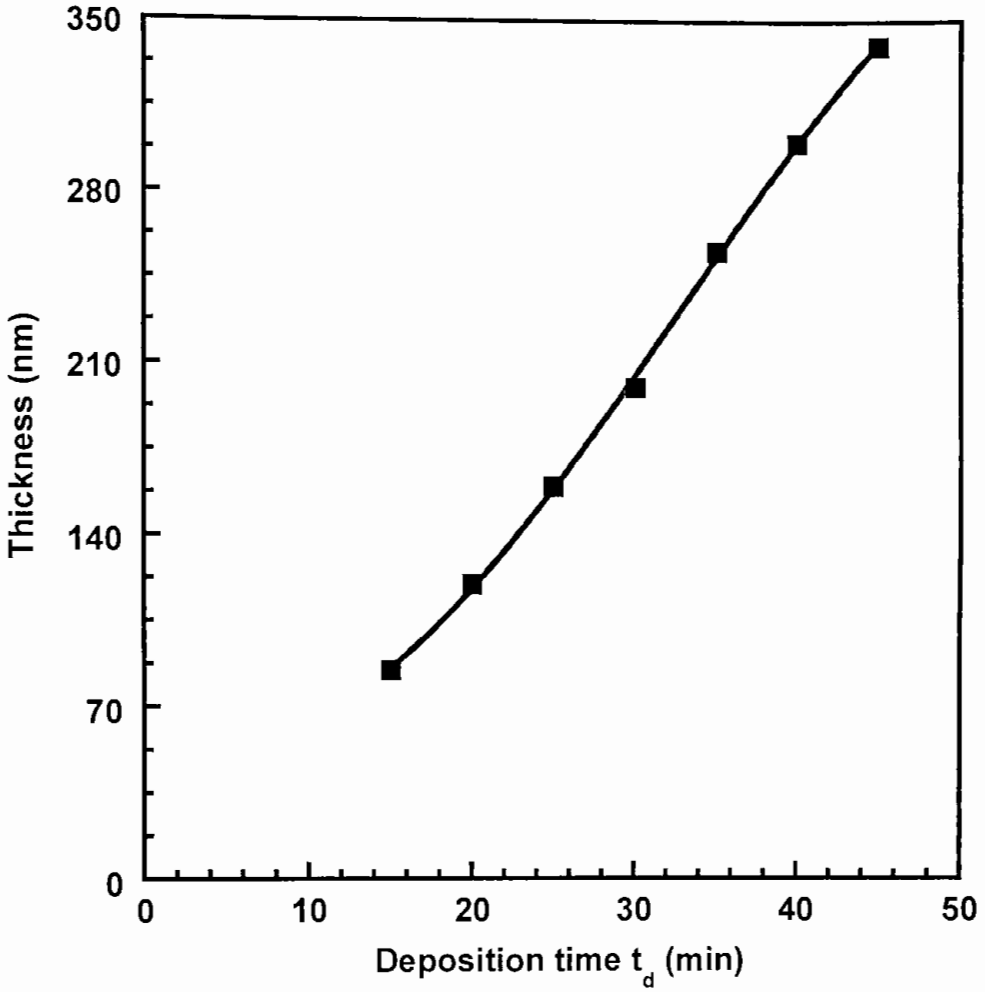

Figure 4.10: *Variation of thickness with deposition time.*

After deposition to a certain thickness of the film a steady state of the process is attained, and it becomes energetically favorable for the rest of the film to grow easily on the initial deposited layer and thus the thickness of the film increases linearly with time.

4.4 EFFECT OF SPRY OUTLET TO SUBSTRATE DISTANCE ON FILM THICKNESS AND RESISTIVITY

The effect of the distance (d_s) between the substrate and the spray outlet on thickness and resistivity are shown in the Figure 4.11(a) and 4.11(b), respectively.

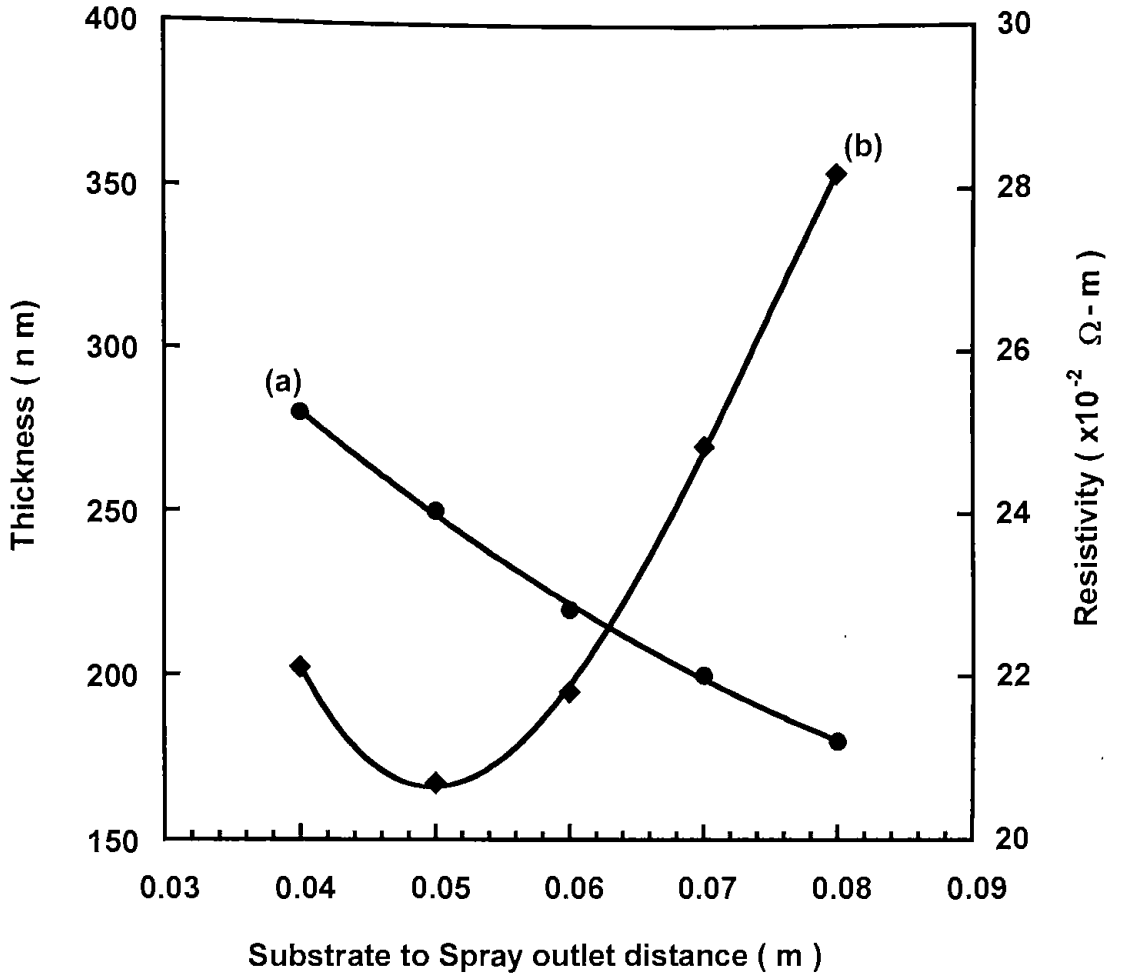

Figure 4.11: *Variation of (a) thickness (b) resistivity with spray outlet to substrate distance, respectively.*

It shows that the film thickness is a function of the d_s at a constant substrate temperature. From the figure it is observed that the film thickness decreases with increasing d_s. At higher distance the decrease in thickness is more pronounced. At small d_s, the maximum amount of vapor molecules, which come out from the nozzle, can strike the substrate directly before getting the scope of distributing in the reaction chamber. As the outlet to the substrate distance increases, the vapor molecules get sufficient space to distribute laterally in the reaction chamber. As a result a smaller quantity of the aerosol can reach onto the substrate and cause a decrease in deposition rate. At sufficiently large d_s ($d_s \approx 0.1$m), the substrate remains deprived of any coating even after a long time spraying. This is obviously due to the vaporization of the aerosol before reaching the substrate. Again from Figure 4.11(b), it shows that the resistivity of the film decreases with increasing d_s

up to 0.05 m and then it increases with increasing d_s. Since at lower d_s, maximum amount of aerosol are reached to the substrate surface. Due to the constant deposition temperature the reaction rate remains constant. Therefore some unreact species may present on the film, which are increased the film thicknesses. These unreacted species caused barrier to the carrier conduction, hence the resistivity of the samples may be increased. From Figure 4.11(b) it is shown that the optimum distance is at 0.05 m.

4.5 EFFECT OF SPRAY RATE ON THICKNESS AND RESISTIVITY

Figure 4.12(a) and 4.12(b) show the variation of film thickness and resistivity with spray rate (S_r), respectively, for a $\mathbf{MnO_2}$ film that was deposited at a fixed substrate temperature 593K, solution concentration 0.8M and carrier air pressure 1.38×10^5 Pa. It is noted that film thickness linearly increases with S_r, and its value saturates at S_r of 0.8 ml/min. Figure 4.12(b) is a plot of resistivity vs. spray rate for a $\mathbf{MnO_2}$ film of thickness 200 nm. It is seen that the fall in resistivity is observed up to spray rate at 0.8 ml /min after this value resistivity is increased with higher spray rate. Therefore, from these plots the minimum resistive film is obtained at a spray rate S_r of 0.8 ml/ min. The film thickness increases with spray rate may be attributed to the structural characteristics of the films. The resistivity decreases with the increase in film thickness. This is due to an improvement of the crystalline and grain size of the film.

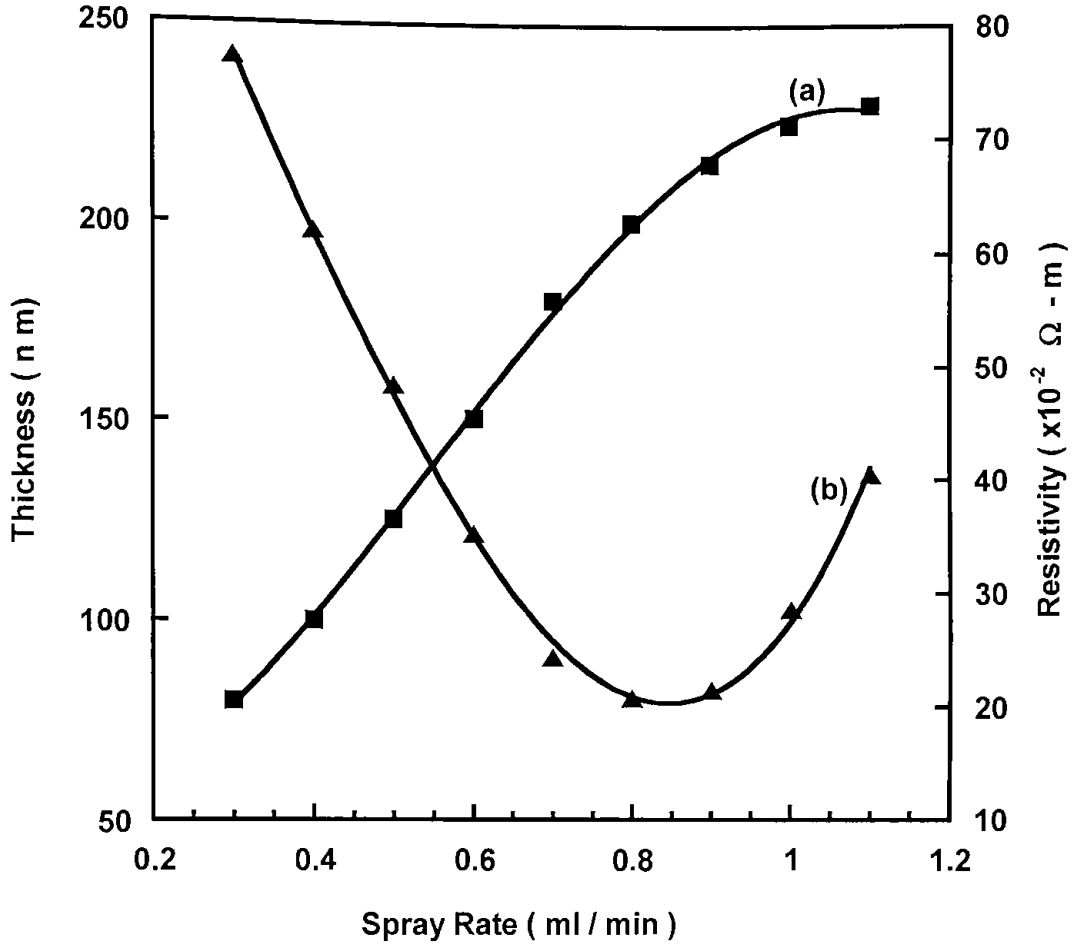

Figure 4.12: *Variation of (a) thickness (b) resistivity with spray rate, respectively.*

4.6 EFFECT OF SOLUTION CONCENTRATION ON FILM THICKNESS AND RESISTIVITY

The variation of film thickness and resistivity of MnO_2 film deposited at the substrate temperature T_s = 593K as a function of solution concentration are shown in Figure 4.13(a) and 4.13(b), respectively. Figure 4.13(a) shows increase of thickness with concentration and its saturation is attained within 0.7M to 0.9M and the author used the concentration of 0.8M in all depositions. This is quit natural, of course up to a certain maximum limit, since an increasing supply of the reactant should increase the product accordingly.

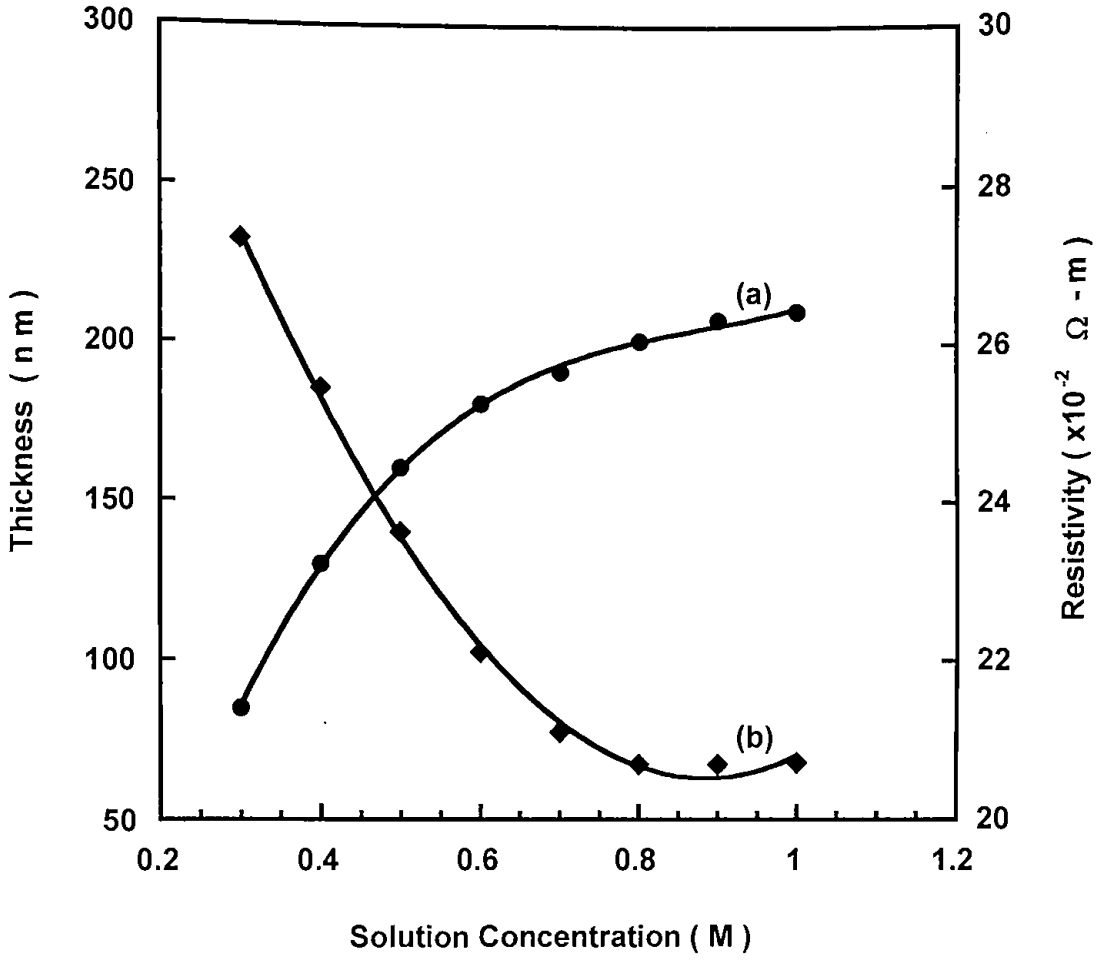

Figure 4.13: *Variation of (a) thickness (b) resistivity with solution concentration, respectively.*

Figure 4.13(b) represents a plot of resistivity vs. solution concentration for MnO_2 film of thickness 200 nm. It indicates a fall in resistivity with increasing solution concentration and it attains a minimum resistivity at concentration of 0.8M. Higher solution concentration reduces the spray rate, which is reduced the film thickness. Thus at higher solution concentration the resistivity of the film may increased. Obviously, to optimize the deposition process, working solution concentration was maintained of 0.8M in all deposition.

4.7 EFFECT OF CARRIER AIR PRESSURE ON THICKNESS AND RESISTIVITY

Compressed air was used as a carrier gas. The dependency of film thickness and resistivity of the MnO_2 film prepared at T_s = 593K, as a function of carrier air pressure are shown in Figure 4.14(a) and 4.14(b), respectively.

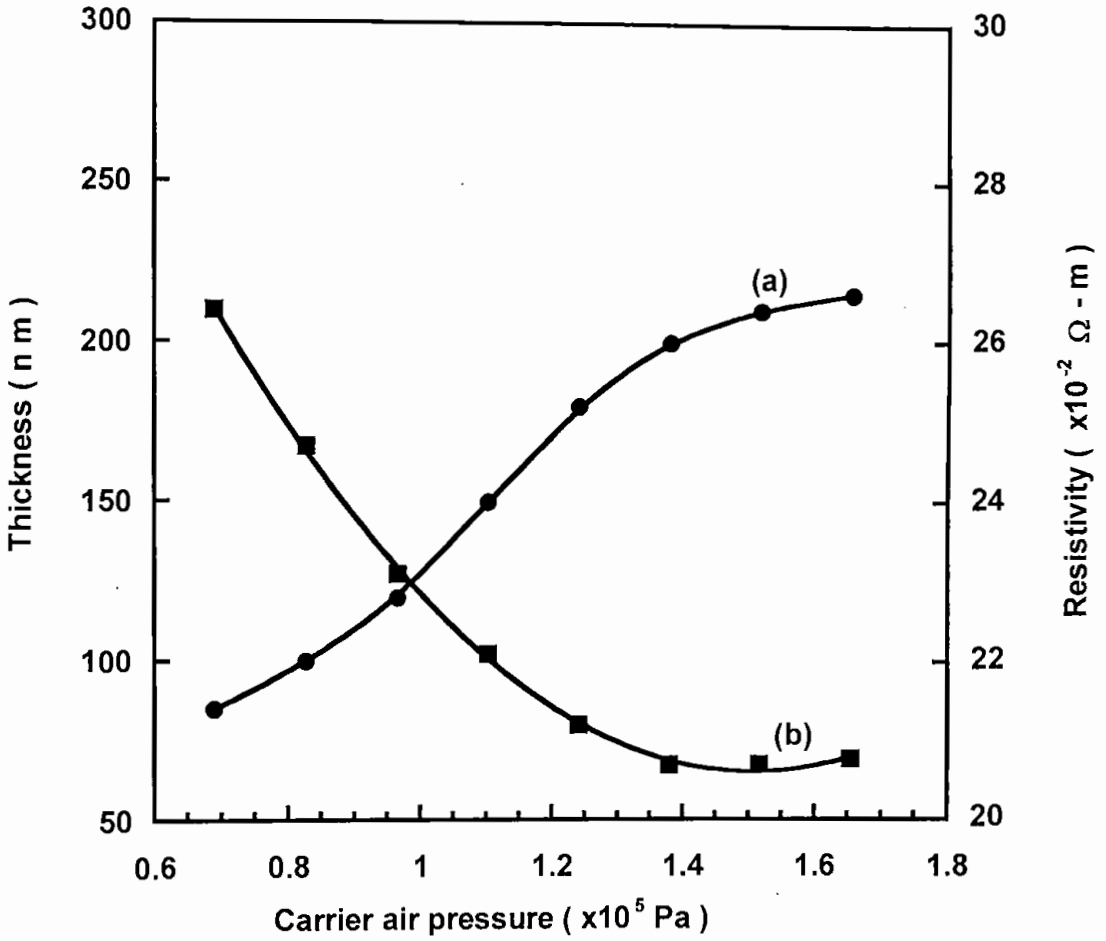

Figure 4.14: *Variation of (a) thickness (b) resistivity with carrier air pressure, respectively.*

Figure 4.14(a) shows the variation of film thickness with carrier air pressure. From this plot it is observed that the thickness is increased with P_a upto 1.38×10^5 Pa and above this carrier air pressure the thickness remains approximately constant. The decrease in resistivity with increasing carrier air pressure in Figure 4.14(b) of a 200 nm MnO_2 film, shows a minimum resistivity at carrier air pressure 1.38×10^5 Pa. At higher carrier air pressure bouncing and lateral mobility of the incoming

droplets are increased which reduced the film thickness. Thus at higher carrier air pressure the film resistivity is increased. Therefore, the author used the 1.38×10^5 Pa pressure in all deposition of MnO_2 films.

4.8 EFFECT OF THE HEAT-TREATMENT

Variation of resistivity with temperature for a typical undoped virgin MnO_2 film of thicknesses 180 nm is shown in Figure 4.15. The sample is undoped in the sense that no intentional doping has been used during deposition, but various crystal defects and impurities from the starting material may be present in the film. As observed in the figure, the heating and cooling cycles are almost irreversible in the investigated temperature range.

During the first step of heat-treatment, a virgin sample shows a sharp decrease in resistivity in the investigated temperature range. This type of behavior was observed for all samples, irrespective of their deposition temperatures. In Figure 4.15, AB shows the first heating cycle, BC represents the fall of resistivity due to first heat-treatment in air at a constant temperature 473K during 1 hour. CD represents the first cooling cycle in air. In the cooling cycle, it is observed that the resistivity increases with decreasing temperature, but does not follow the heating cycle AB.

In the second step of heat-treatment in air, the heating cycle is shown by DE, which shows that the resistivity gradually fall with temperature in the investigated temperature range. The cooling cycle is shown by EF; the resistivity does not change remarkably. FG represents the fall of resistivity when the sample is heat-treated in the vacuum chamber at 473K for an hour.

The third step of heat-treatment on this vacuum annealed film was subsequently carried out in air. GH shows the variation of resistivity during heating the sample. It still decreases slowly up to 403K and then tends to increase slightly but not noticeably. The cooling cycle HI at the beginning follows partially the heating cycle GH. This cycle is thus somewhat reversible. The drop in resistivity in GH is relatively smaller than that in DE. IJ shows the drop of resistivity due to second vacuum heat-treatment. Finally, JK shows the variation of resistivity of the fourth heating cycle in air and this variation is not remarkable.

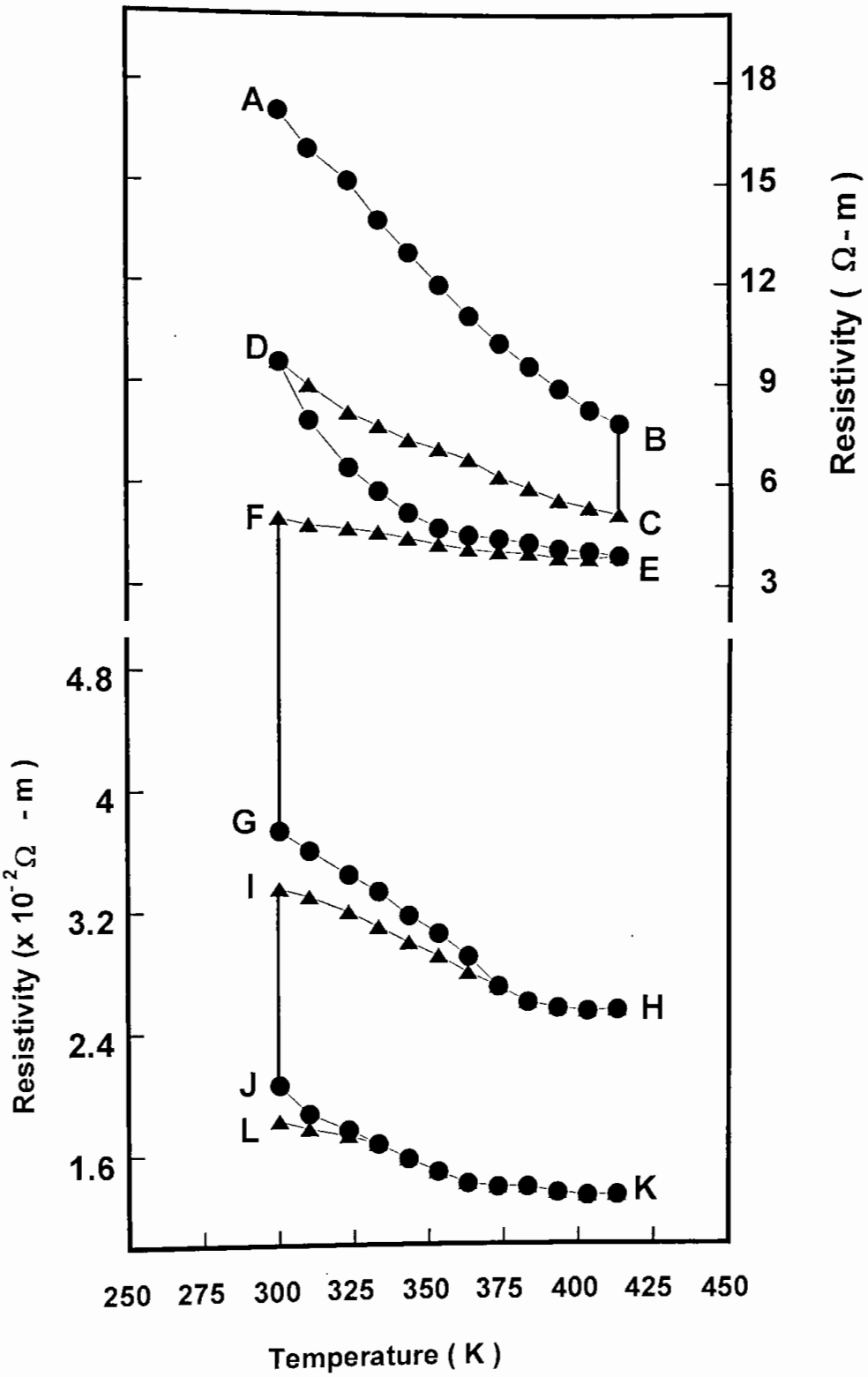

Figure 4.15: *Variation of resistivity with temperature of MnO_2 film of thickness 180 nm deposited at 593K. FG and IJ represent the drop in resistivity during the first and second vacuum heat-treatment, respectively.*

The reverse cycle of cooling, KL mostly follows the heating cycle JK except in the last portion. Thus, this cycle is almost reversible. During the variation of resistivity the Hall mobility and carrier concentration were also found to vary with temperature. All films were shown such behavior during heat-treatment.

It is known that pyrolytically deposited films with deposition temperature > 523K are polycrystalline in structure [142, 143]. From XRD and TEM studies, it is seen that MnO_2 samples are polycrystalline and homogeneous in structure. At the time of film deposition air has been used as carrier gas, it is quite likely that a large number of oxygen molecules are chemisorbed in the film at the grain boundary and on the surface during deposition, because these molecules do not have time to leave the sample at the end of deposition, due to rapid cooling effect. During the first heating cycle, these molecules are escaped from the film and the resistivity falls rapidly.

A similar observation is also noted in films of **ZnO** [74, 131, 144, 145]. The detailed explanation of the nature of chemisorption-desorption mechanism is the following. It may be mentioned that the principal chemisorption species in **MnO_2** is $2O_2^{1-}$ at room temperature and as the temperature of the sample rises, the chemisorbed $2O_2^{1-}$ desorbed from the sample surface donating electrons to **MnO_2** ($O_2 + 2e \rightarrow 2O_2^{1-}$, or $\frac{1}{2}O_2 + 2e = O^{2-}$) and hence the conductivity rises rapidly. The effect of successive heat-treatment on the films is briefly tabulated in Table 4.5.

Table: 4.5

Substrate Temp. (K)	Resistivity in ($\times 10^{-2}$) Ω-m		Increase in resistivity (%)	Hall mobility ($\times 10^4$ $m^2V^{-1}S^{-1}$)		Increase in mobility (%)	Carrier concentration ($\times 10^{25}$ m^{-3})		Increase in Concen-tration (order)
	Virgin state	After heat-treatment		Virgin state	After heat-treatment		Virgin state	After heat-treatment	
563	25.32	0.0244	99.90	0.23	0.97	321.74	0.032	3.95	10^2
583	21.25	0.0215	99.81	0.33	1.035	213.64	0.046	4.55	10^2
593	20.69	0.0171	99.92	0.47	1.057	124.89	0.058	4.63	10^2
613	20.76	0.0181	99.91	0.51	1.046	105.10	0.052	4.47	10^2

The resistivity of the sample is drastically decreased due to heat-treatment. The Hall mobility in the virgin sample was relatively difficult to measure, values

given in Table 4.5 are the results of several observations, but may still be approximate. A large change in Hall mobility occurs in films deposited at lower substrate temperature. In all cases, mobility was found to increase due to heat-treatment. The carrier concentration also increased due to heat-treatment. In the fourth step of heat-treatment the nature of the variation of resistivity, Hall mobility and carrier concentration with temperature is almost flat, which indicates that desorbable oxygen is exhausted from the sample and the film is relatively stable towards heat-treatment.

In fact, in a polycrystalline oxide semiconductor, oxygen chemisorption and desorption may both occur at all temperatures when heat-treated in vacuum or in air. Which process is dominant is determined by their respective rates that are functions of the ambient temperature and relative concentrations of the chemisorption species available in the ambient and in the chemisorption sites [146]. Thus, up to the third heat-treatment, the gross decrease in resistivity in the film is due to the oxygen desorption process, which lowers the grain-boundary barrier heights and enhance the mobility and carrier concentration. If the crystal is now caused to lose oxygen by heat-treatment the ions escape as neutral molecules (O_2) leaving two electrons per atom behind. Then one electron can easily ionize into the conduction band [147]. Thus the conductivity of the films may easily increase due to the heat-treatment. The fourth step of heat-treatment shows the samples are relatively stable. Therefore, all the samples are heat-treated in vacuum of the order of 1.33×10^{-3} Pa during two hours at a constant temperature 473K.

4.9 EFFECT OF SPRAY RATE ON HALL MOBILITY AND CARRIER CONCENTRATION

Figure 4.16(a) shows the variation of the Hall mobility with the spray rate for annealed films. The maximum Hall mobility is shown at the spray rate of 0.8 ml /min. Above and below this spray rate the Hall mobility decreases.

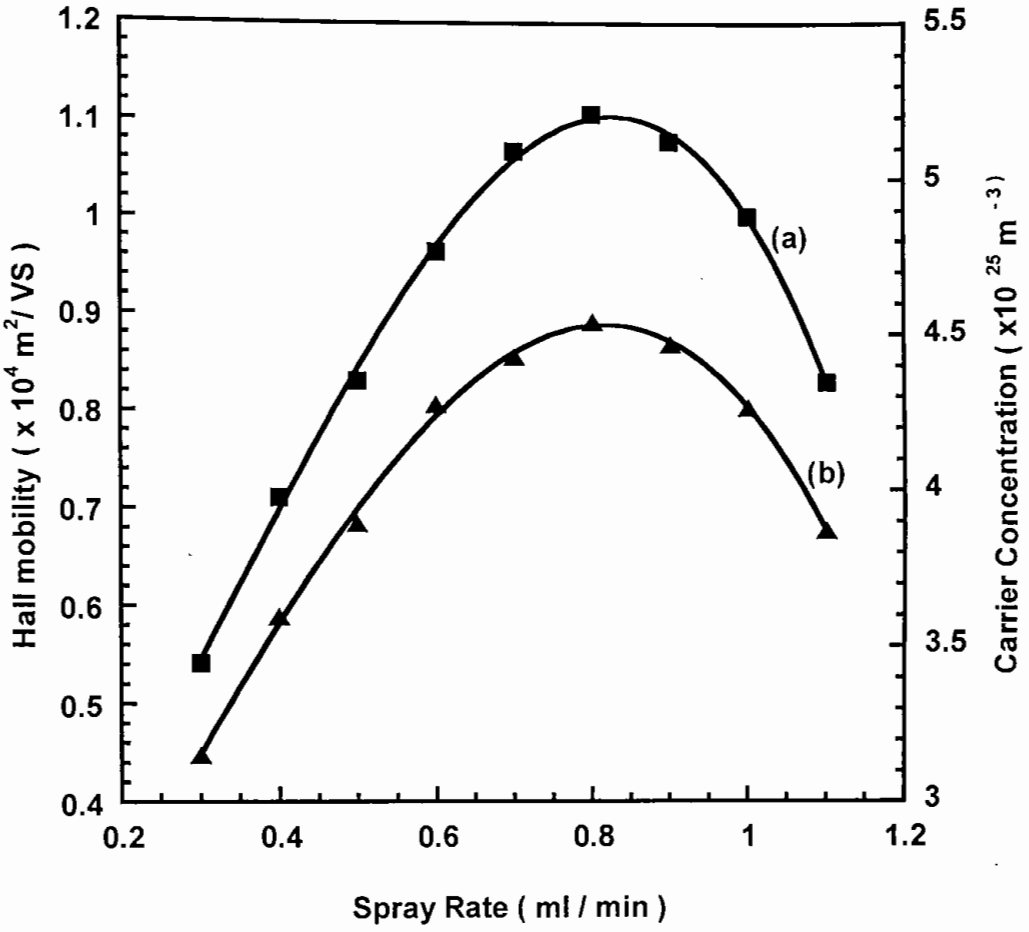

Figure 4.16: *Variation of (a) Hall mobility (b) carrier concentration with spray rate, respectively.*

At lower spray the decrease in Hall mobility is probably due to the increase in the grain boundary barrier heights and at higher spray rate poorer films are produced due to the presence of unreacted species of the starting materials [131, 148].

Figure 4.16(b) shows the variation of the carrier concentration with the spray rate. The maximum carrier concentration is shown at the spray rate 0.8 ml/min. Above and below this spray rate carrier concentration decreases. At lower spray rate the decrease in carrier concentration is perhaps due to the relatively better stoichiomtry of the films at this spray rate, which in turn may increase the resistivity. At higher spray rate the carrier concentration decreases is probably due

to the increase in the grain boundary barrier heights for the presence of unreacted species of the starting materials [131, 148].

4.10 EFFECT OF SOLUTION CONCENTRATION ON HALL MOBILITY AND CARRIER CONCENTRATION

Figure 4.17(a) shows the variation of the Hall mobility with the solution concentration for annealed films.

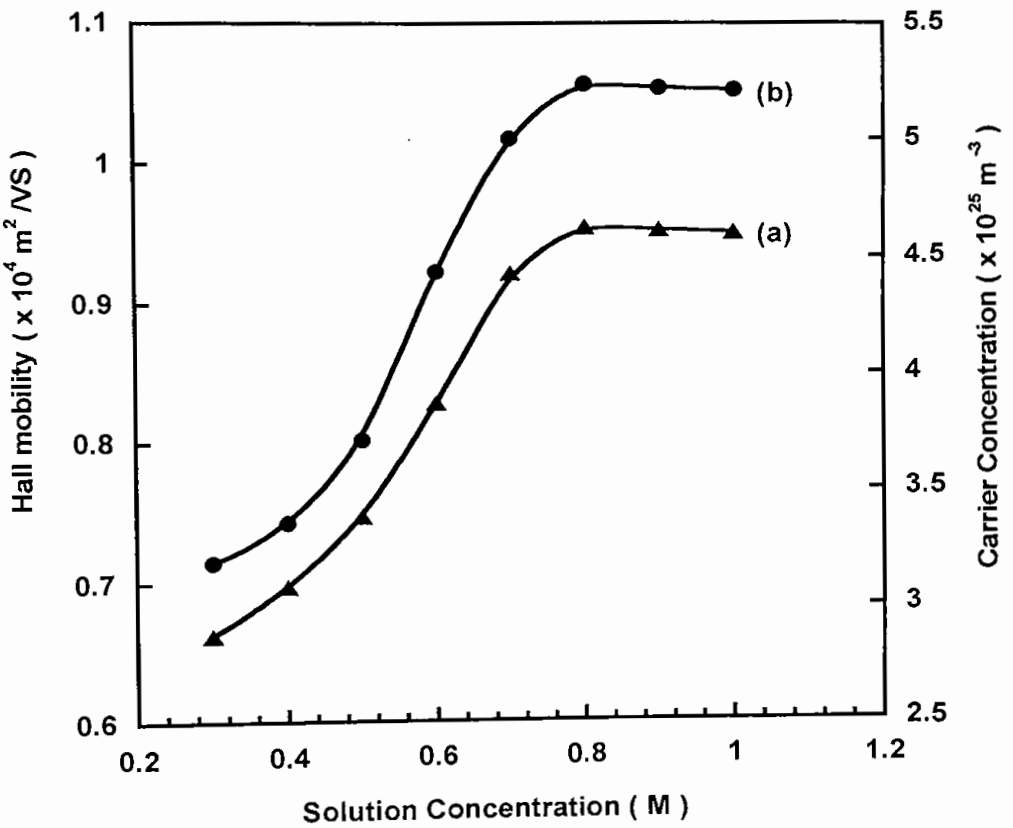

Figure 4.17: *Variation of (a) Hall mobility (b) carrier concentration with solution concentration, respectively.*

From this graph it is shown that Hall mobility increases up to 0.8M and then it becomes approximately saturated. At higher solution concentration the spray rate is reduced. At lower spray the decrease in Hall mobility is probably due to the increase in the grain boundary barrier heights [131, 148].

Figure 4.17(b) shows the variation of the carrier concentration with the solution concentration. From this graph it is shown that the carrier concentration increases up to 0.8M and then it becomes approximately saturated.

4.11 VARIATION OF CONDUCTIVITY WITH TEMPERATURE

Figure 4.18 represents the lnσ versus T^{-1} curves for annealed MnO_2 films of thicknesses 100, 120, 160 and 200nm, respectively. It is observed that the conductivity increases with temperature indicating semiconducting behavior, similar behavior also observed for as-deposited films. It is, however, interesting to point out that this behavior is not linear over the entire range of temperature.

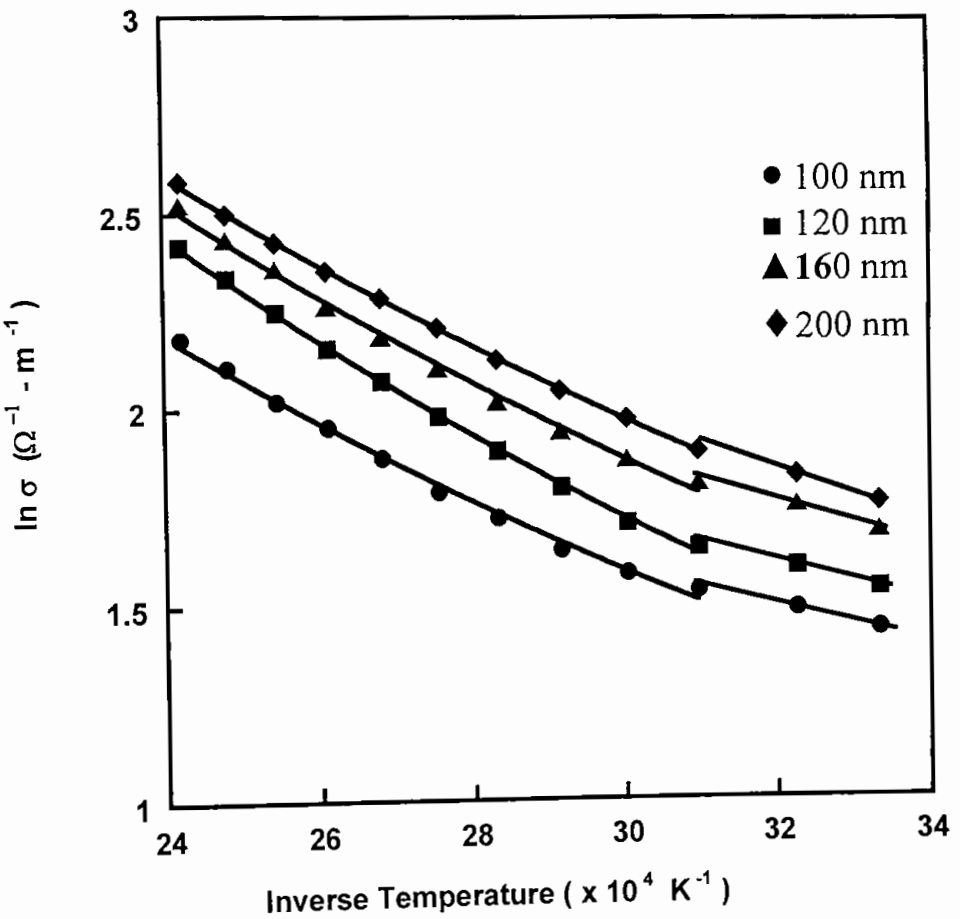

Figure 4.18: *lnσ vs T^{1} curves for annealed MnO_2 films of different thicknesses.*

It is also seen that there is an anomaly in conductivity in the lnσ versus T^{-1} curves at a particular temperature and this temperature is observed at 323K. The anomaly in conductivity of author's work is noted both in as-deposited and annealed films, which is well agreed in reports of other workers [11, 12, 48]. This result suggests that MnO_2 becomes ferroelectric below the anomaly temperature. The evaluated value of the activation energy of the above four annealed MnO_2 films in Figure 4.18 are tabulated in a Table-4.6.

Table 4.6

Thickness (nm)	Activation energy below the anomaly (eV)	Activation energy above the anomaly (eV)
100	0.1390	0.2413
120	0.2510	0.2240
160	0.2612	0.2110
200	0.2711	0.2010

It is seen that the activation energy for the four MnO_2 films are fairly low and is of the order of 0.13 to 0.27 eV. This value of activation energy is well agreed with the other workers [11, 12, 28, 48]. The increase of activation energy with decreasing film thickness above the anomaly temperature can be understood from island structure theory based on tunneling of charged carries between islands separated by a short distance [149].

4.12 SIZE EFFECT

Variation of electrical conductivity (σ) with thickness (t) of MnO_2 films is shown in Figure 4.19. It is observed that the conductivity increases with thickness and attains a constant value $\approx 6.5\ \Omega^{-1}\text{-m}^{-1}$ at 220 nm. Since the conductivity does not depend on film thickness in the range 220 to 320 nm, the current density should be uniform and therefore, the calculated values are considered to give the volume conductivity but not the surface conductivity in this thickness range. The thickness dependence of conductivity is well in conformity with Fuchs-Sondheimer theory [150, 151]. The conductivity decreases sharply below 160 nm, which is probably due to the discontinuous structure of the film.

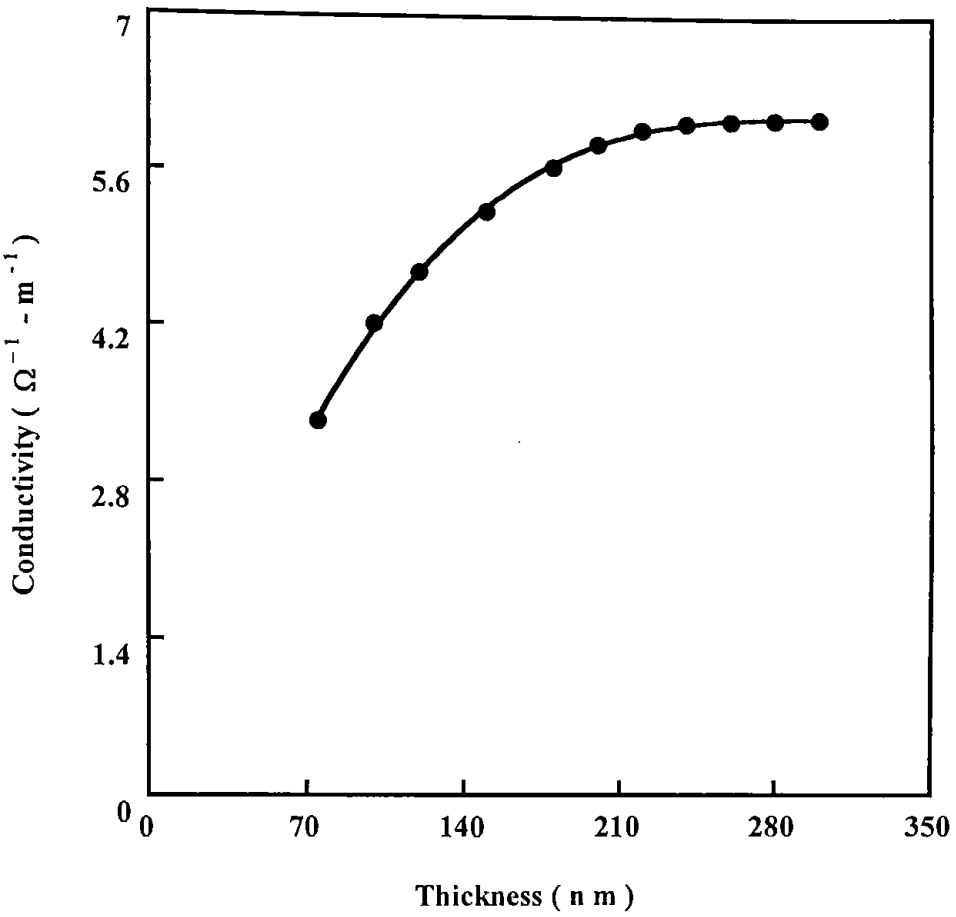

Figure 4.19: *Variation of electrical conductivity with thickness of MnO_2 films.*

4.13 AGING EFFECT

The natural aging at room temperature for annealed **MnO_2** films of thicknesses 100, 160, 200 and 280 nm, respectively, was investigated and the data for electrical conductivity versus time are shown in Figure 4.20. It is observed that in all films, the electrical conductivity decreases with time and the conductivity decreases in the thinner film more rapidly than in the thicker one. For higher thicknesses films it remains almost constant after a certain time. This decrease in conductivity can be interpreted in terms of oxygen absorption.

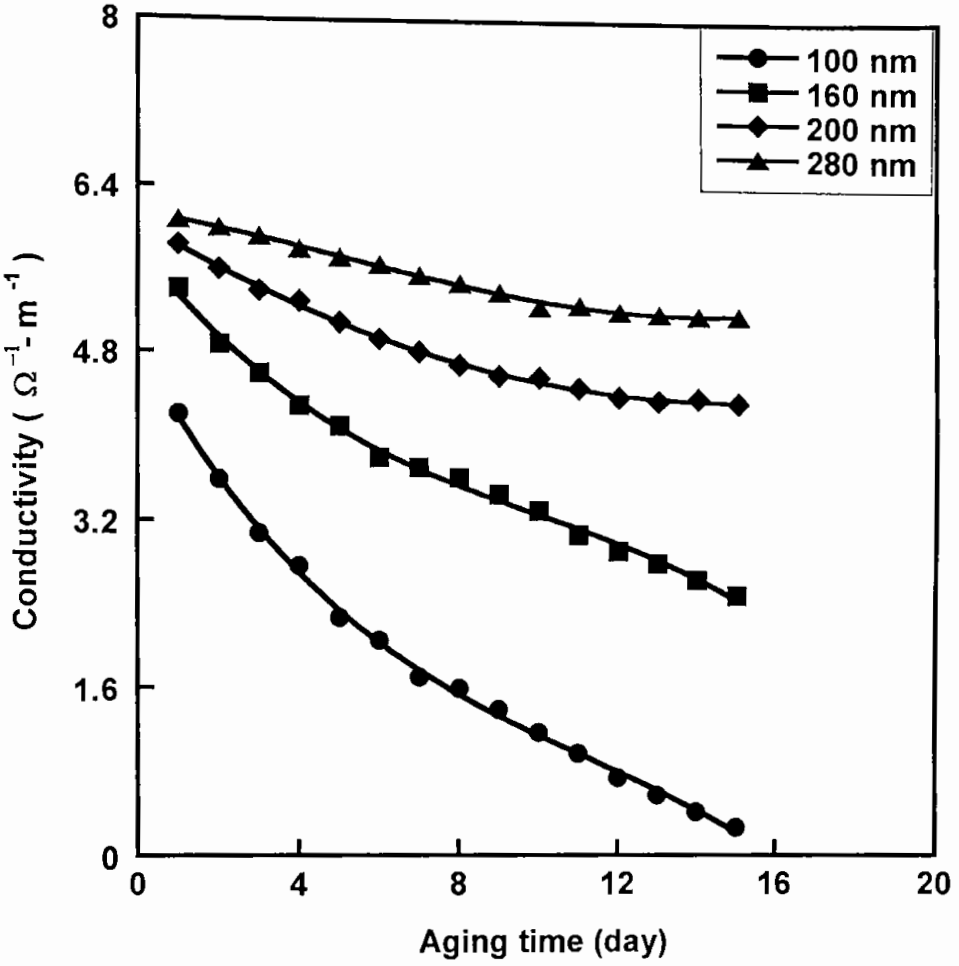

Figure 4.20: *Variation of electrical conductivity with aging time of different thicknesses MnO_2 films.*

Oxygen molecular ions (O_2^-) are chemisorbed and incorporated at the grain boundaries and on the surface of the film producing potential barrier for the conduction electrons. This hinders the electrical transports and raises the resistivity [131, 132].

4.14 HALL EFFECT STUDY

Hall Effect studies were carried out by van-der-Pauw [82] technique. The variation of Hall voltage with temperature for different thicknesses annealed MnO_2 thin films are shown in Figure 4.21.

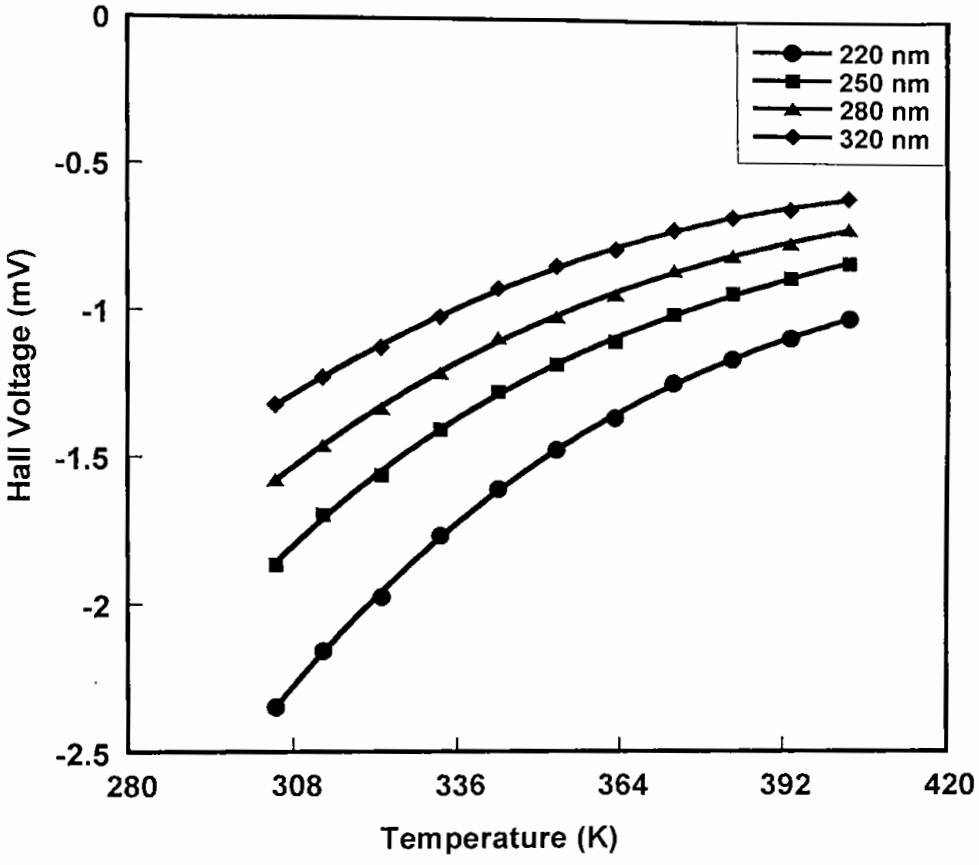

Figure 4.21: *Variation of Hall voltage with temperature of annealed MnO_2 films.*

From this study, the negative sign of the Hall voltage indicates that the MnO_2 samples are n-type semiconductors. In as-deposited films, however, it was very difficult to observe any appreciable Hall voltage.

4.14.1 Effect of Film Thickness on the Carrier Concentration and Mobility

Figure 4.22 shows the thickness dependence of Hall mobility (μ_H) and Carrier concentration (n) of annealed MnO_2 films.

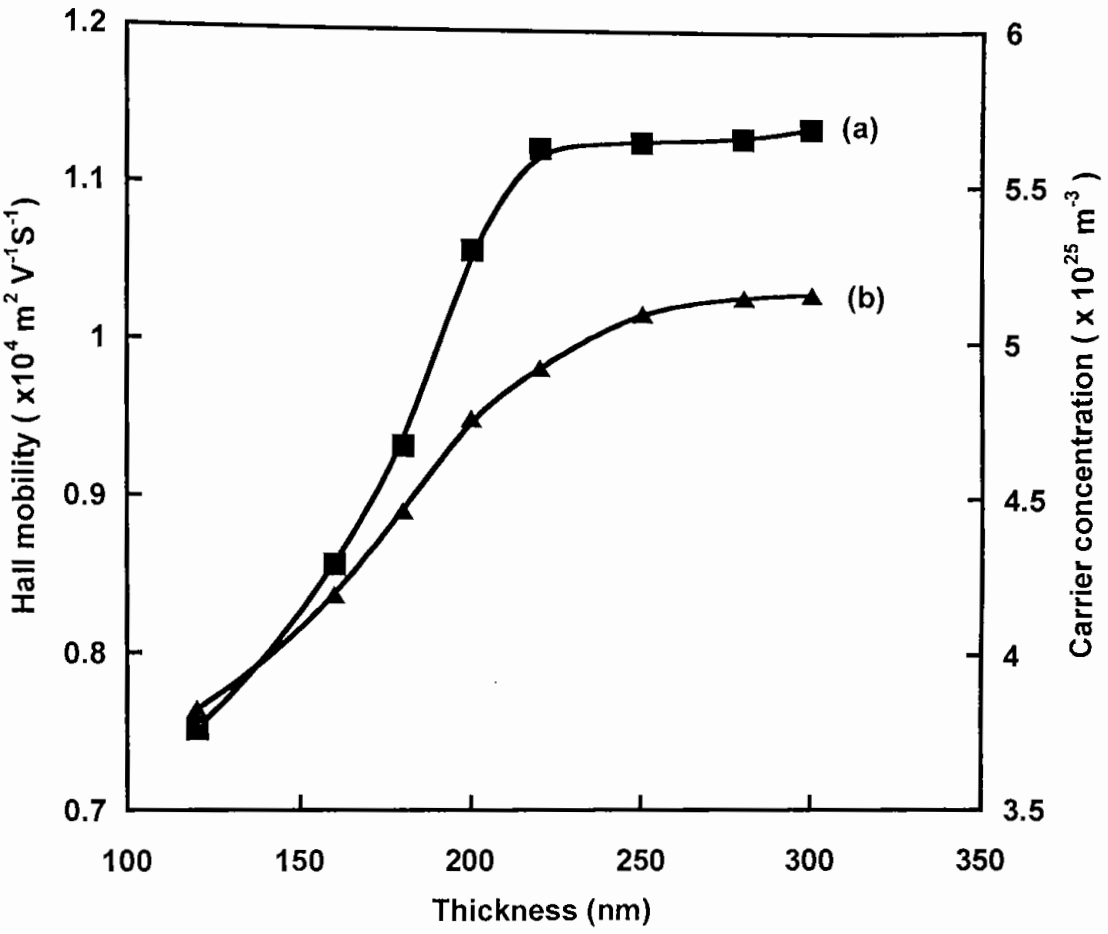

Figure 4.22: *Variation of (a) Hall mobility and (b) Carrier Concentration with film thickness, respectively.*

From this figure it is shown that the Hall mobility and carrier concentration both increases with increasing thickness upto 220 nm and above this thickness their values remain approximately constant. In the lower range of film thickness n and μ_H are very sensitive to the film thickness, but in the higher range of thickness, the dependency is rather feeble. This behavior may be attributed to the increases in grain size of the film with the increases in film thickness [152].

4.14.2. Donor Ionization Energy

Although the MnO_2 thin films are undoped and polycrystalline in structure. In undoped films the oxygen vacancies and the interstitial chlorine ions (incorporated in the film from the working solution) may be act as an impurity in the films [74, 153]. Electrical conductivity in such a film is mainly controlled by the impurity level. The carrier concentration (n) shows a temperature dependence, which can be represented by a conventional expression [88]

$$n = (n_0 N_d)^{\frac{1}{2}} \exp\left(\frac{-E_d}{2 k_B T}\right), \tag{4.1}$$

where E_d is the donor ionization energy N_d is the donor density, and

$$n_0 = 2\left(\frac{m_e^* k_B T}{2\pi\hbar^2}\right)^{\frac{3}{2}}.$$

By plotting $\ln(nT^{-3/4})$ against 1/T, E_d can be calculated. Figure 4.23 shows these plots and the calculated values are given in Table 4.7.

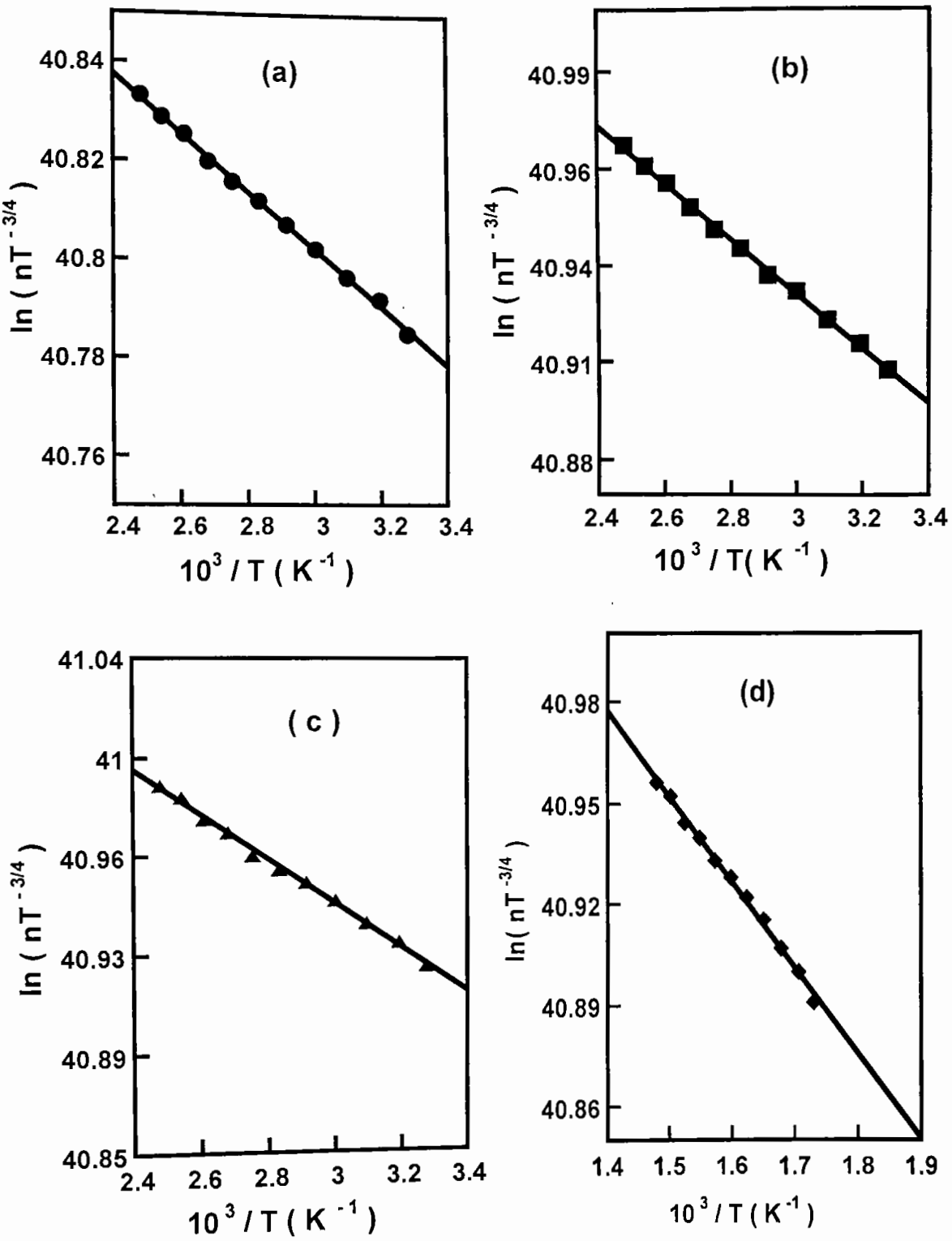

Figure 4.23: *ln ($nT^{-3/4}$) vs. T^{-1} curves for different deposited temperatures MnO_2 samples of thickness 200 nm [(●) 563K, (◆) 583K, (▲) 593K, (■) 613K] .*

Table 4.7

Substrate temperature in K	Resistivity in ($\times 10^{-2}$ Ω-m)	Carrier concentration, n ($\times 10^{25}$ m^{-3})	Donor ionization energy, E_d in eV	Fermi level, E_F in eV	Donor density, N_d ($\times 10^{25}$ m^{-3})	Effective mass, m_e^*/m_e	TCR (10^{-3} K^{-1})
563	0.0244	3.95	0.127	0.104	3.98	0.299	-9.09
583	0.0215	4.55	0.121	0.093	4.95	0.285	-9.45
593	0.0171	4.63	0.114	0.083	5.09	0.269	-6.58
613	0.0181	4.47	0.122	0.094	4.54	0.287	-6.91

The calculated values of the donor density N_d using Equation 4.1 also tabulated in Table 4.7. The donor levels are shallow and are mainly due to the native defects, such as interstitial manganese and oxygen vacancies. Considering a hydrogenic model for the impurities, the density of states effective mass m_e^* can be calculated in such a material using the relation

$$E_d = \frac{e^4 m_e^*}{2 (4\pi\varepsilon\varepsilon_0 \hbar)^2}, \tag{4.2}$$

where the ε is the dielectric constant of the medium MnO_2 and can be taken as $\varepsilon = 10^4$ [154]. Calculated values of m_e^*/m_e are given in Table 4.7. The position of the Fermi level E_F can be determined from the following relation [88]

$$E_F = -\frac{1}{2}E_d + \frac{1}{2}(k_B T)\ln\left[\frac{N_d h^3}{2(2\pi m_e^* k_B T)^{\frac{3}{2}}}\right] \tag{4.3}$$

Calculated value of E_F with reference to the conduction band edge E_c are also given in Table 4.7. It is noted that the Fermi level in all samples lies above the donor level. The donor density (N_d) is greater than the carrier concentration (n) for MnO_2 samples, which is the characteristic for an uncompensated semiconductor [74]. In updoped films the oxygen vacancies and the interstitial chlorine ions (incorporated in the film from the working solution) may act as the major sources of donors [74, 153].

4.14.3 Grain Boundary Effect

Petritz [107] suggests that due to the presence grain boundaries between crystallites, potential barrier heights would be generated across these grain boundaries and the mobility (μ_H) of the charge carriers is some function of temperature (T) depending on the mode of scattering. A qualitative estimate of scattering effects prevailing in a semiconductor can be made from the slope of mobility graphs ($\log\mu_H$ vs. logT) since all scattering processes are expected to follow $\mu_H \propto T^X$, where the value of X characteristics the scattering process. Figure 4.24 shows such plots.

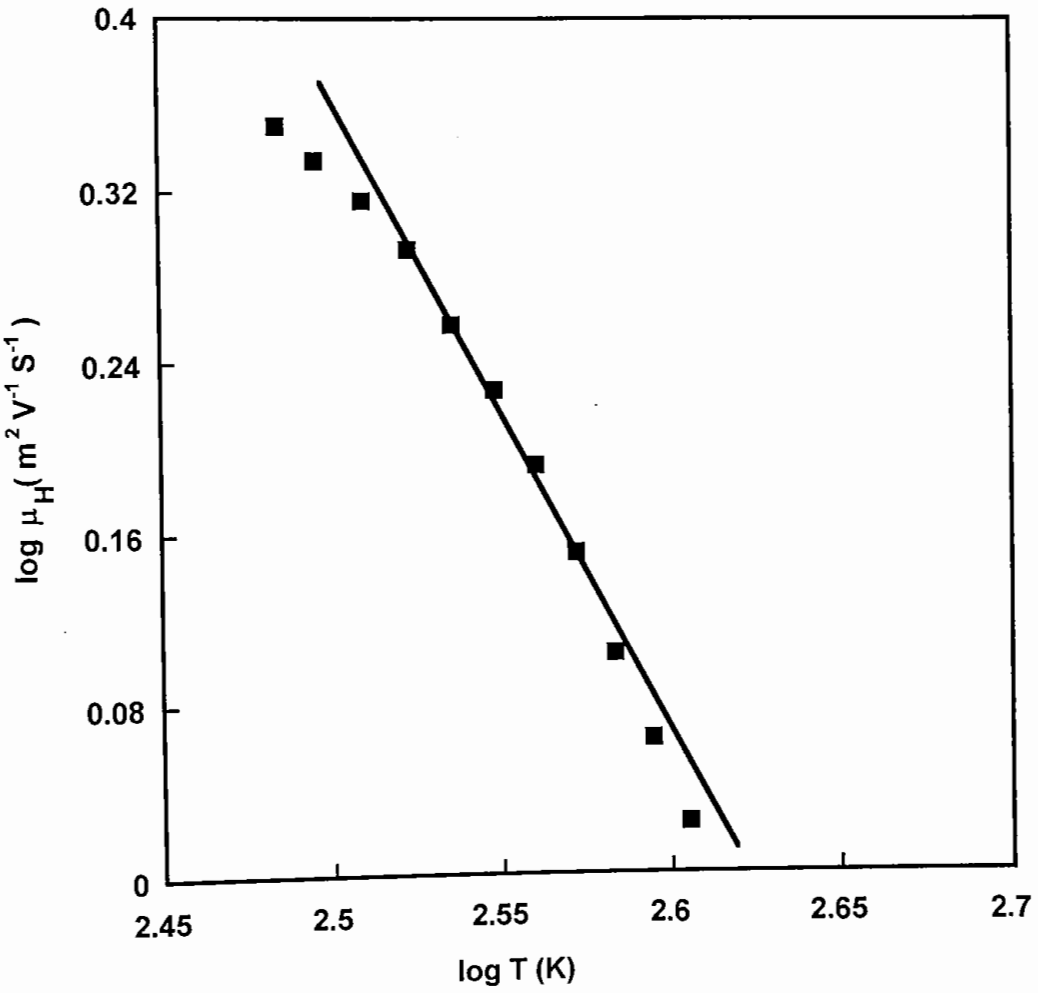

Figure 4.24: *logT versus* $\log\mu_H$ *graph for* MnO_2 *thin film of thickness 200 nm.*

From this plot, the slope of the straight line the value of X is obtained approximately -1.5. This value of X is corresponding to the ionized impurity

scattering [100]. Therefore, the Hall effect measurement shows that the ionized impurity scattering of the charge carriers is dominant in MnO_2 films.

4.14.4 Grain- Boundary Parameters

It is known that in polycrystalline films, the electrical properties are largely controlled by the grain boundary effects. Grain boundary trapping models [155, 156] state that when the trapping states in the grain boundary region are occupied, they create a depletion region in the grain and a potential barrier at the interface. Under this condition, if the grain size (l) is larger than twice the Debye screening length (L_D) then the measured mobility (μ_H) is thermally activated with the activation energy (ϕ_b), which is the barrier height at the grain boundary [155]. In an extrinsic non-degenerate samples, thermally activated mobility can be accounted by [156]

$$\mu = \mu_0 T^{-\frac{1}{2}} \exp\left(\frac{-\phi_b}{k_B T}\right), \tag{4.4}$$

where

$$\mu_0 = \frac{e l}{\left(8 \pi m_e^* k_B\right)^{\frac{1}{2}}} \tag{4.5}$$

is a constant which depends on the grain size (l). In author's sample, the carrier concentrations are of the order of $\sim 10^{25}$ m^{-3} and the position of the Fermi level indicates that the samples are non degenerate. Plotting ln ($\mu T^{1/2}$) as a function of 1/T, gives the value of ϕ_b. Figure 4.25 shows such plots, where it is seen that the mobility is thermally activated in the investigated temperature range. Calculated values of ϕ_b are given in Table 4.8.

Table 4.8

Substrate temperature (K)	Hall mobility μ ($x10^4$ $m^2V^{-1}S^{-1}$)	Grain boundary barrier height ϕ_b (eV)	Estimated grain size l (Å)	Debye screening length L_D (Å)	Mean free path L (Å)
563	0.97	0.063	140.82	6.83	0.461
583	1.035	0.058	151.57	6.81	0.482
593	1.057	0.052	160.03	6.99	0.478
613	1.046	0.057	172.23	6.91	0.486

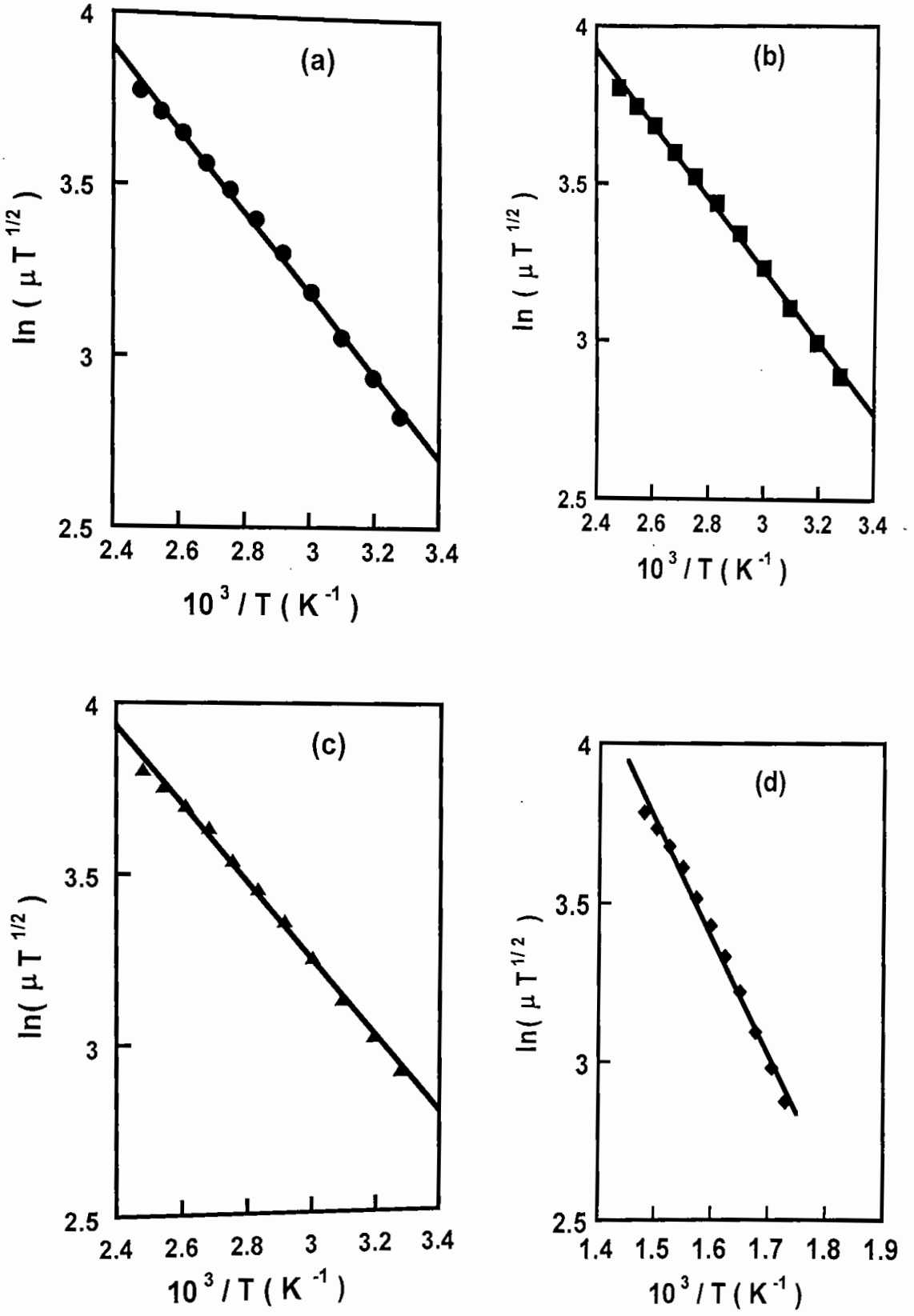

Figure 4.25: *ln($\mu T^{1/2}$) vs. 1/T curves for MnO_2 thin film of different substrate temperature [(●) 563K, (◆) 583K, (▲) 593K, (■) 613K], respectively.*

4.14.5 Grain Size Estimation

The grain size (l) may be calculated from Equation 4.5 if one takes the values of μ and ϕ_b at room temperature. This procedure is not entirely correct, since Equation 4.4 is strictly valid when the mobility is limited mainly by the grain boundaries. An improved value of the μ_0 can be obtained by using μ_g in place of μ in Equation 4.4, where the approximation is based on **Mattiessen's rule**,

$$\frac{1}{\mu} = \frac{1}{\mu_g} + \frac{1}{\mu_s}, \tag{4.6}$$

here μ_g is the grain boundary limited mobility and μ_s is the corresponding mobility if the sample is a single crystal and has the same structure as the film.

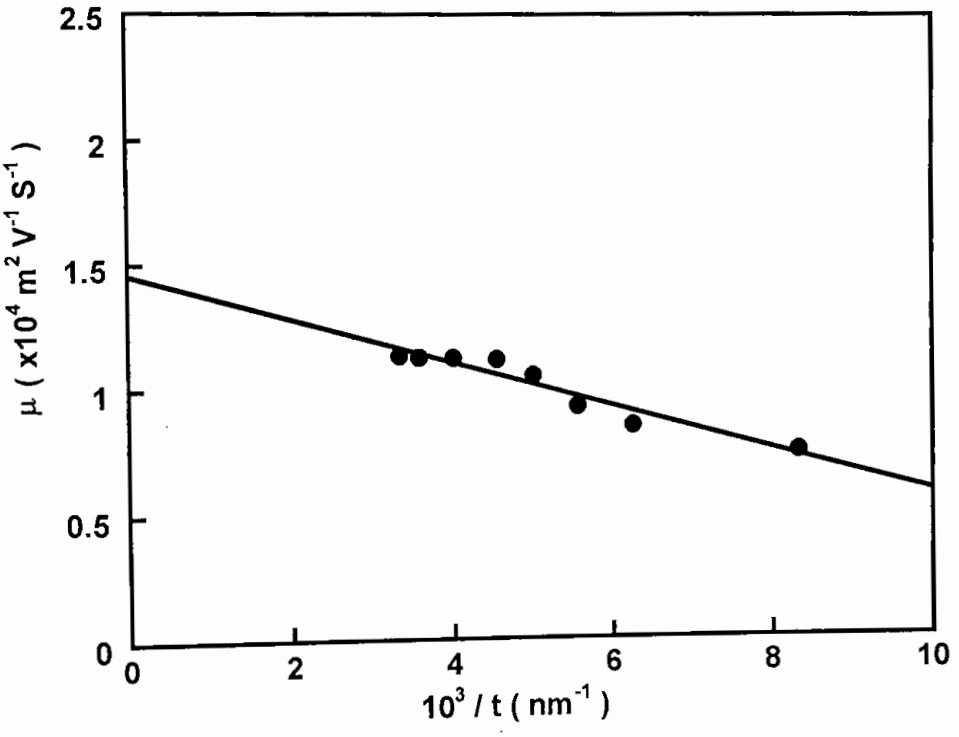

Figure 4.26: *Variation of μ with 1/t of MnO_2 film deposited at 593K.*

The bulk value of μ may be taken for μ_s. The value of μ_s is obtained from the intercept in an μ versus 1/t plot, where t is the film thickness. Such a plot is shown in Figure 4.26 and the calculated value of grain size is tabulated in Table 4.8. From the calculated values, it is shown that a higher deposition temperature favors the formation of larger grains.

4.14.6 Debye Screening Length

The Debye screening length can be calculated from a hydrogenic model of the possible donor centers. The pertinent expression is [88]

$$\frac{1}{L_D^2} = \frac{4n^{\frac{1}{3}}}{a_0}, \tag{4.7}$$

where n is the uniform carrier concentration and a_0 is the Bohr radius for the donor centers, given by

$$a_0 = \frac{4\pi\varepsilon\varepsilon_0 \hbar^2}{m_e^* e^2}. \tag{4.8}$$

From Equations 4.7 and 4.8, we obtained

$$L_D = \left(\frac{h}{2e}\right)\left(\frac{\varepsilon\varepsilon_0}{\pi m_e^* n^{1/3}}\right)^{\frac{1}{2}}. \tag{4.9}$$

Calculated value of L_D obtained from Equation 4.9 is given in the Table 4.8. It can be noticed that the condition $2L_D < l$ appropriate for a grain boundary trapping model is obeyed here. Thus the author's approach of analyzing the data using the grain boundary trapping model for the thermal activation of mobility is valid.

Oxygen chemisorption-desorption process in the polycrystalline **MnO_2** thin films are important due to their power to control their electronic transport properties. When these films are deposited by a spray pyrolysis process in air, oxygen molecules from the atmosphere are chemisorbed in the grain boundaries and also on the surface of the film during the deposition. This produces very high resistivity of the film in the virgin state. When these films are heat-treated in vacuum, desorption takes place, which drastically increases the electrical conductivity, Hall mobility and carrier concentration as well. The effect of successive heat-treatment on the samples is briefly given in Table 4.5. Hall mobility is controlled by the grain boundary potential barrier heights, which are modulated by the heat-treatment effects. In all author's samples, the possible donor levels are shallow and are situated at various depths in the band gap. Fermi level lies near the donor level, but is at 1.8 to 2.6 k_BT below the conduction band edge at room temperature. The samples are thus safely considered to be non-degenerate.

4.15 THERMOELECTRIC POWER (TEP)

The thermoelectric power measurement of MnO_2 films was carried out by the integral method [139] in the temperature ranges 300 to 450K by taking pure metallic lead (**Pb**) as reference metal. Thermoelectric power (TEP) is the most sensitive quantity to any change or distortion of the Fermi-surface in the material; a measurement of TEP would be a useful option for investigating the electronic conduction process in such a sample.

Figure 4.27 shows the value of thermo e.m.f. at different temperatures for four samples of thickness 160, 200, 220 and 250 nm, respectively.

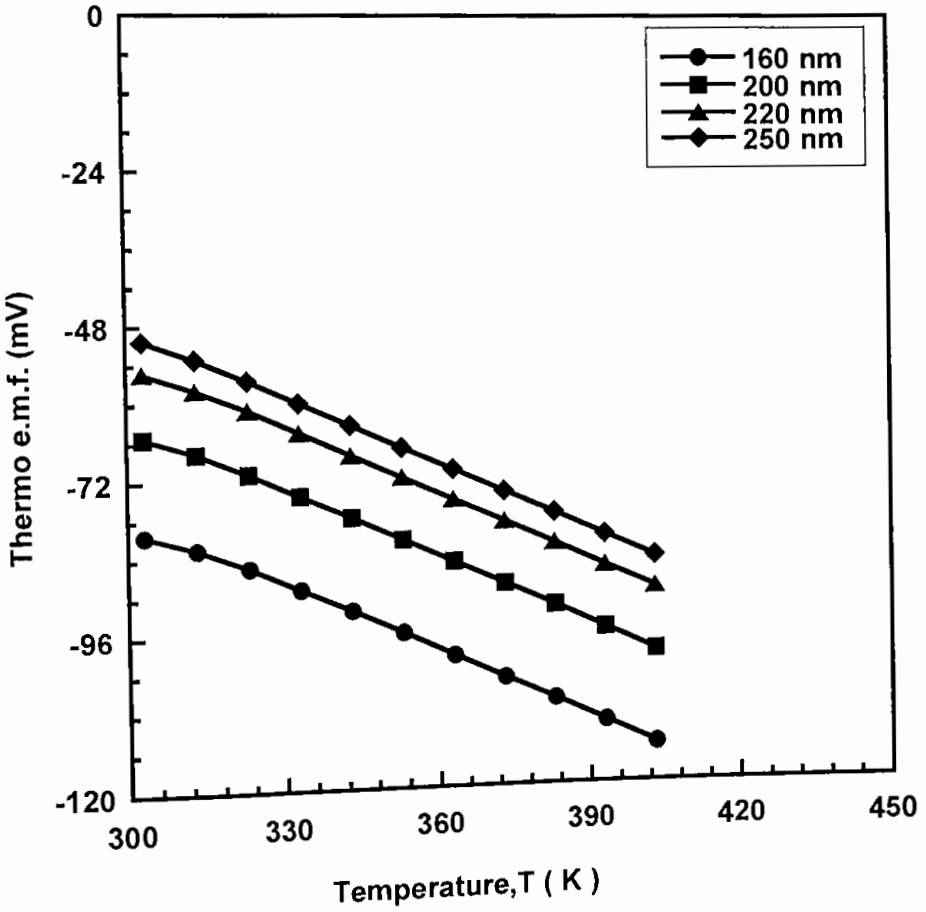

Figure 4.27: *Variation of thermo e.m.f. with temperature of different thicknesses MnO_2 thin films.*

It is observed that the thermo e.m.f. is negative with respect to lead (**Pb**). The negative sign of the thermo e.m.f. indicates that the current carriers of the MnO_2 films are electron. Therefore, MnO_2 films are n-type semiconductor in nature, which is well agreed with the Hall effect measurement. The plots indicate a linear decrease in thermo e.m.f. with increasing temperature. Figure 4.28 shows the variation of the corresponding thermoelectric power (Q), with inverse temperature, 1/T.

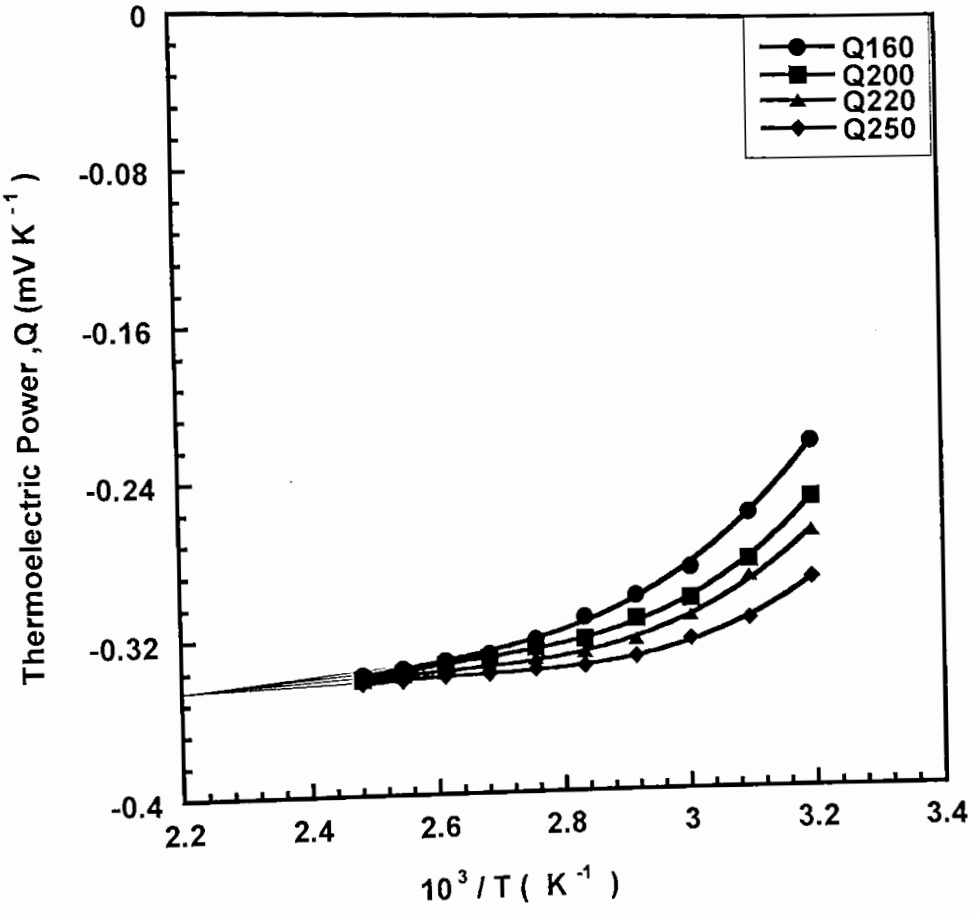

Figure 4.28: *Variation of thermoelectric power with inverse temperature of different thicknesses MnO_2 thin films.*

It is observed from this figure that the thermoelectric power decreases continuously with increasing temperature and saturates at higher temperature region. The rate of change of Q with temperature is higher for films of higher thickness than that of lower ones. At a fixed temperature, the variation of thermo power with film thickness is shown in Figure 4.29. This figure represents the

variation of thermo power of MnO_2 films as a function of thickness at three different temperatures of 313, 333 and 413K, respectively. It indicates that at lower temperature it has thickness dependence while it is thickness independent in higher temperature.

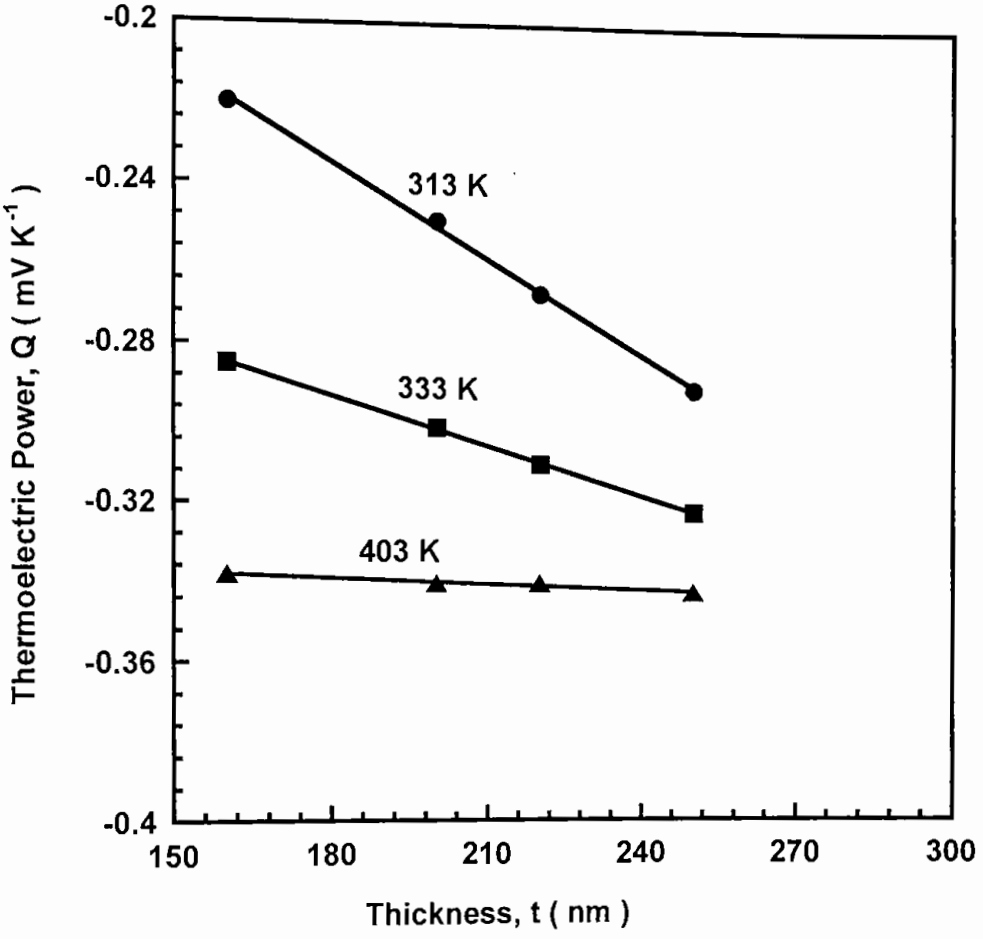

Figure 4.29: *Variation of thermoelectric power with thickness at different temperature of MnO_2 thin films.*

The author's sample of Hall effect measurement yields the carrier concentration (n) of MnO_2 films of the order of 4.7×10^{25} to 8.4×10^{25} m^{-3} and it is of n-type carrier. Therefore, it is logical to analyze the thermoelectric power data to employ a non-degenerate model. For a non-degenerate n-type crystalline semiconductor with spherical constant energy surface under thermal equilibrium, the thermoelectric power is given by [89]

$$Q = -\frac{k_B}{e}\left(\frac{E_c - E_F}{k_B T} + A\right) \tag{4.10}$$

Where k_B is the Boltzmann constant and E_c is the energy of conduction band edge; A is a constant that depends on the nature of the scattering process. Normally, for a material like a Fermi glass, A runs between 2 and 4. If energy is measured with respect to the bottom of the conduction band, then Equation 4.10 reduces to

$$Q = -\frac{k_B}{e}\left(A - \frac{E_F}{k_B T}\right) \tag{4.11}$$

where E_F is the position of Fermi level in the band gap. Harry *et al.* [90] have pointed out that A = (5/2) - r, where r corresponds to the scattering index and is equal to - 0.5 for piezoelectric scattering and - 1.5 for ionized impurity scattering. Thus A=3 for piezoelectric scattering and 4 for ionized impurity scattering. From Equation 4.10, it is clear that A corresponds to a value of the thermopower at infinite temperature limit.

From Figure 4.28 the extrapolated tangent at the higher temperature region of the curves approximately gives a common intercept at the ordinate from which the value of A has been obtained as 4.003. This value corresponds to the scattering index ≈ - 1.5 and is an indication that ionized impurity scattering is dominant in these MnO_2 films. Similar observation is also observed from the Hall effect measurement. This is a signature of ionized impurity scattering, which is well verified by other workers [35].

In all of the author's samples it has been found that (E_c-E_F) varies with temperature (T), and it can be assumed that for a limited temperature range [89].

$$E_c - E_F = E_0 - \gamma T \tag{4.12}$$

where E_0 is the low-temperature limit of (E_c-E_F) and corresponds to the activation energy equivalent to the band gap, γ is the temperature coefficient of activation energy. Putting Equation 4.12 into Equation 4.10

$$Q = -\frac{E_0}{eT} + \left(\frac{\gamma}{e} - \frac{Ak_B}{e}\right) \tag{4.13}$$

Now, the Peltier coefficient $\pi = QT$, is given by

$$\pi = -\frac{E_0}{e} + \left(\frac{\gamma}{e} - \frac{Ak_B}{e}\right)T \tag{4.14}$$

This equation shows that a π versus T plot should yield a straight line and the value of γ can be obtained from its slope. Figure 4.30 shows such plots and it is observed that the slopes at room and higher temperature regions are different.

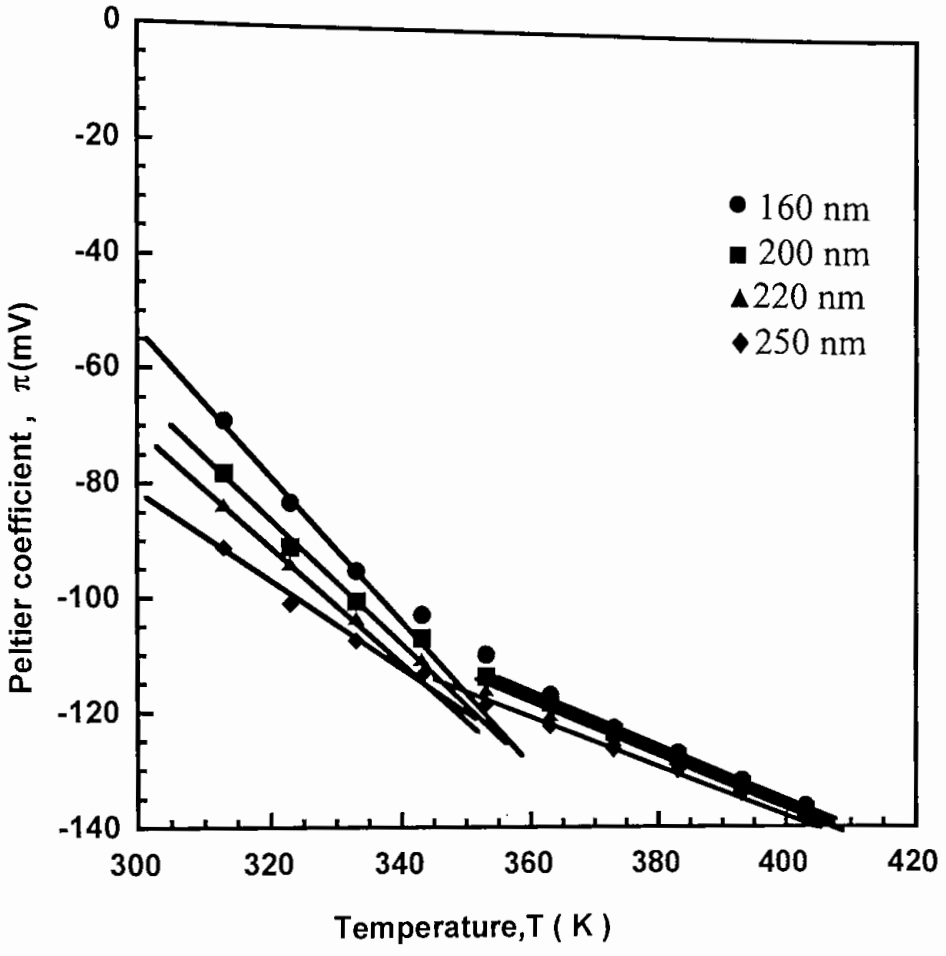

Figure 4.30: *Variation of Peltier coefficient with temperature of different thicknesses MnO_2 thin films.*

Both slops have been determined and using A = 4.0, various values of γ were calculated for films of different thicknesses. These values of γ are plotted as a function of thickness in Figure 4.31. It shows that at higher temperatures, γ is almost thickness independent, while in the room- temperature limit; it shows strong thickness dependence.

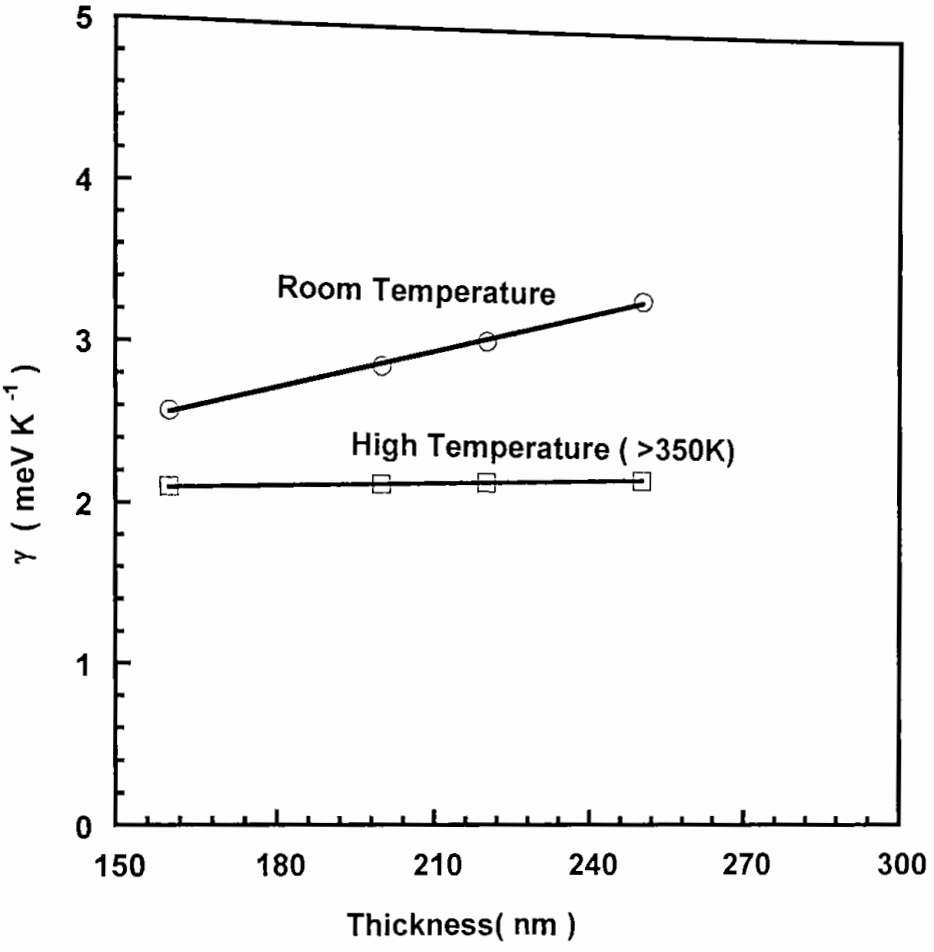

Figure 4.31: *Variation of temperature coefficient of activation energy γ as a function of thickness of MnO_2 thin films at room temperature and high temperature (above 350K).*

Using these values of γ at room temperature, the values of E_0 for the different film thickness may be calculated from Equation 4.14 and the values of $(E_c - E_F)$ from Equation 4.12. The variation of E_0 and of $(E_c - E_F)$ at room temperature as a function of inverse film thickness, 1/t, is shown in Figure 4.32. In this figure it is observed that E_0 has fair thickness dependence and its bulk value corresponding to 1/t = 0, is 0.27eV. This value agrees well with the band gap of **MnO_2** samples (0.28 and 0.26 eV, respectively) as reported previously [11, 12, 28, 48, 157]. In extrinsic samples, the variation of E_0 with film thickness is obvious which is calculated from Equation 4.12; is some type of thermal activation energy and

depends on the detailed variations of the pattern of conduction and valance edges with the structure of the film, including various defects. This is not necessarily a vertical transition.

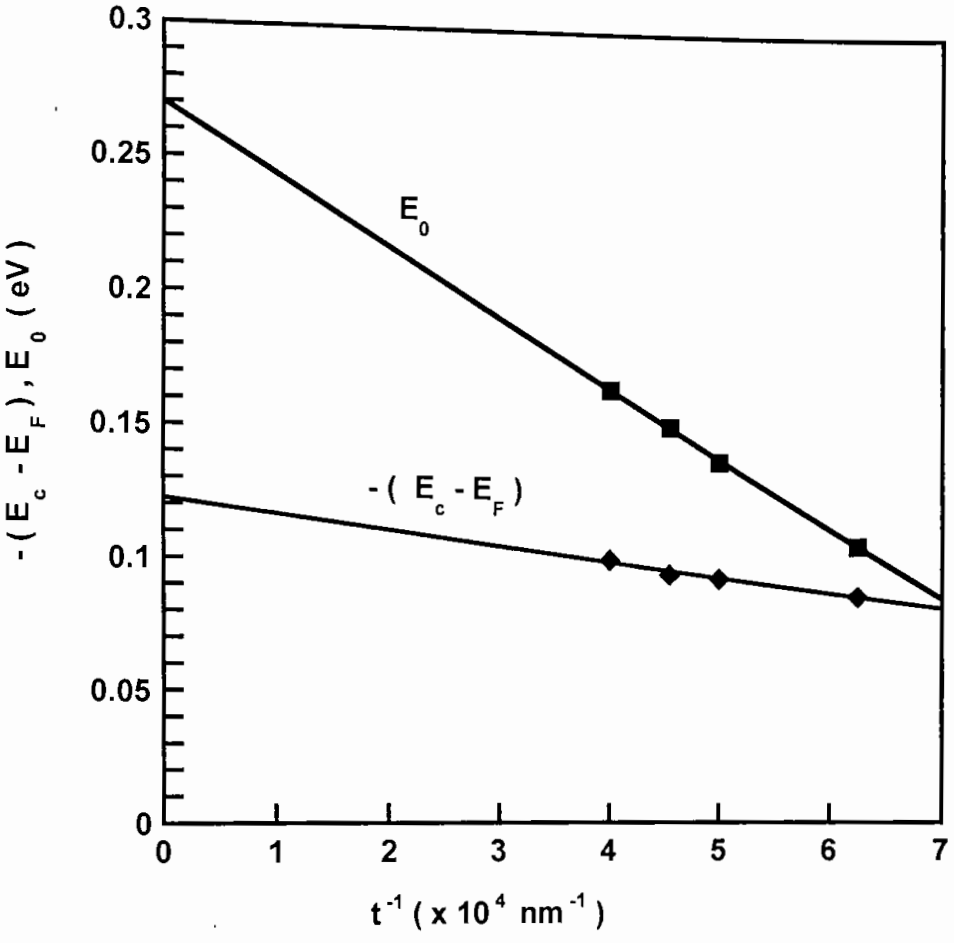

Figure 4.32: *The variation of E_0 and Fermi energy – $(E_C - E_F)$ with inverse of thickness, respectively.*

But the optical band gap E_g corresponds to the optical absorption at some frequency and involves mostly vertical transitions between the bands. Thus the variation of E_g with thickness is not as straightforward as for E_0. In this case, of course, carrier concentration plays an important role.

In the high-temperature region, the thermo power saturates for all the samples (Figure 4.28 and 4.29), it suggests that the Fermi-levels in these films are pinned near the band edge at higher temperature. This is now shown in Figure 4.33 where

this pinning can be clearly observed. The gradual decrease of thermo power with temperature also is shown in Figure 4.28. In thin film samples when the material behaves like a Fermi-glass, this type of variation is usual [89]. We obtain some idea about this variation by differentiating Equation 4.10 with respect to temperature, which yields,

$$\frac{dQ}{dT} = -\frac{k_B}{e}\left[\frac{d(E_c - E_F)}{k_B T dT} - \left(\frac{E_c - E_F}{k_B T^2}\right) + \frac{dA}{dT}\right] \tag{4.15}$$

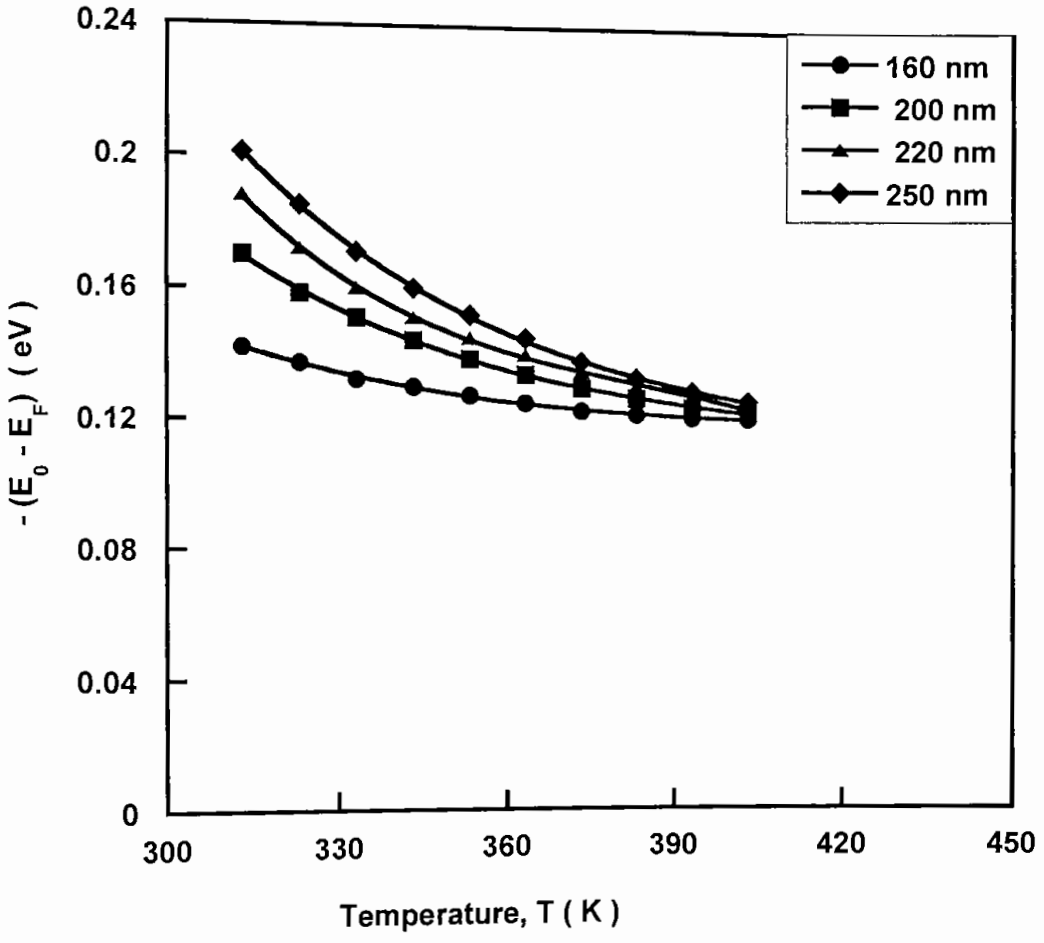

Figure 4.33: *The plot of Fermi level as a function of temperature of MnO_2 films of different thicknesses.*

From Figure 4.33 it is observed that $-(E_c - E_F)$ decrease with temperature so that in the brackets the 1st term of Equation 4.15 is positive. The second term is also positive because $(E_c - E_F)$ is negative and we have already ignored any

possible temperature variation of A as it corresponds to the higher temperature limit of thermo power. Thus the whole term in brackets is positive and hence $\frac{dQ}{dT}$ is negative, which suggests a decrease of thermopower with temperature. The minimum value of $-(E_c - E_F)$ as obtained from Figure 4.33 is 0.125 eV and is almost five times that of k_BT at room temperature. Thus our previous consideration of a non-degenerate model to explain the thermopower data is justified.

Thermopower in spray deposited non-stoichiometric $\mathbf{MnO_2}$ thin film shows a thickness as well as temperature dependence. The Fermi-levels are found to show a gradual pinning mode near the band edge with increasing temperature. An annealed as well as the as-deposited samples show negative thermopower, which indicates that the $\mathbf{MnO_2}$ are n-type semiconductor.

In general the transport properties in these samples are controlled mainly by the ionized impurity scattering process corresponding to a scattering index of -1.5 obtained from thermopower data. Film thicknesses also have a remarkable effect on the activation energy, E_0 and on the temperature coefficient of activation energy (γ). In the room temperature region, γ has strong thickness dependence while it is almost thickness independent in the high-temperature region.

4.16 OPTICAL STUDIES

The optical study is comprised of two variables namely dependence on deposition temperature as well as on film thickness.

Spectral transmittance T (λ) and near normal reflectance R (λ) were measured at wavelength ranges $0.3 < \lambda < 2.5$ μm using a "Perkin-Elmer lambda-19 double beam spectrophotometer". Figure 4.34 shows the spectral transmittance/reflectance versus wavelength spectra for a 200 nm annealed MnO_2 films of different deposition temperatures.

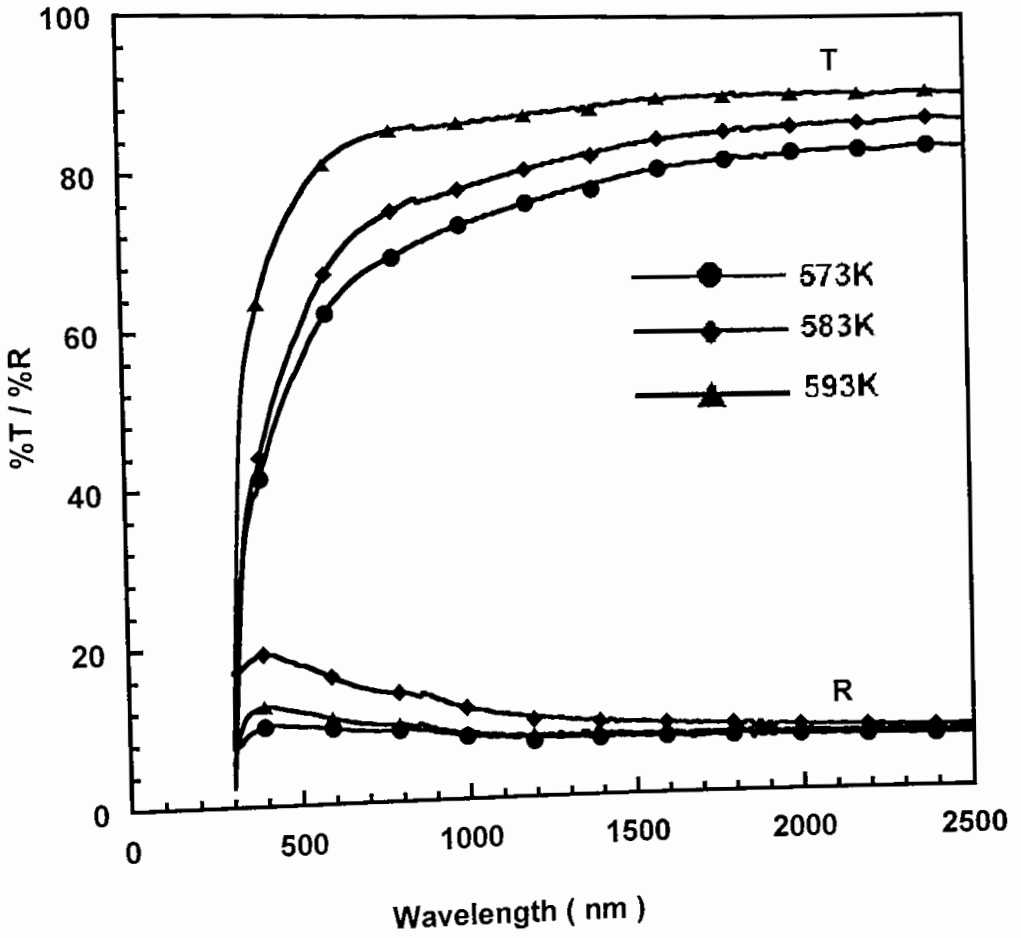

Figure 4.34: *Optical spectra of different deposition temperatures of MnO_2 thin films of thickness 200nm.*

It is seen that the transmittance curve exhibits a significant transmittance in the visible as well as in the infrared region. The reflectance spectrum, however, shows a low reflectance in the entire wavelength region. Among the three

transmittance plots it is seen that films deposited at T_s = 593K is the highest in transmittance value.

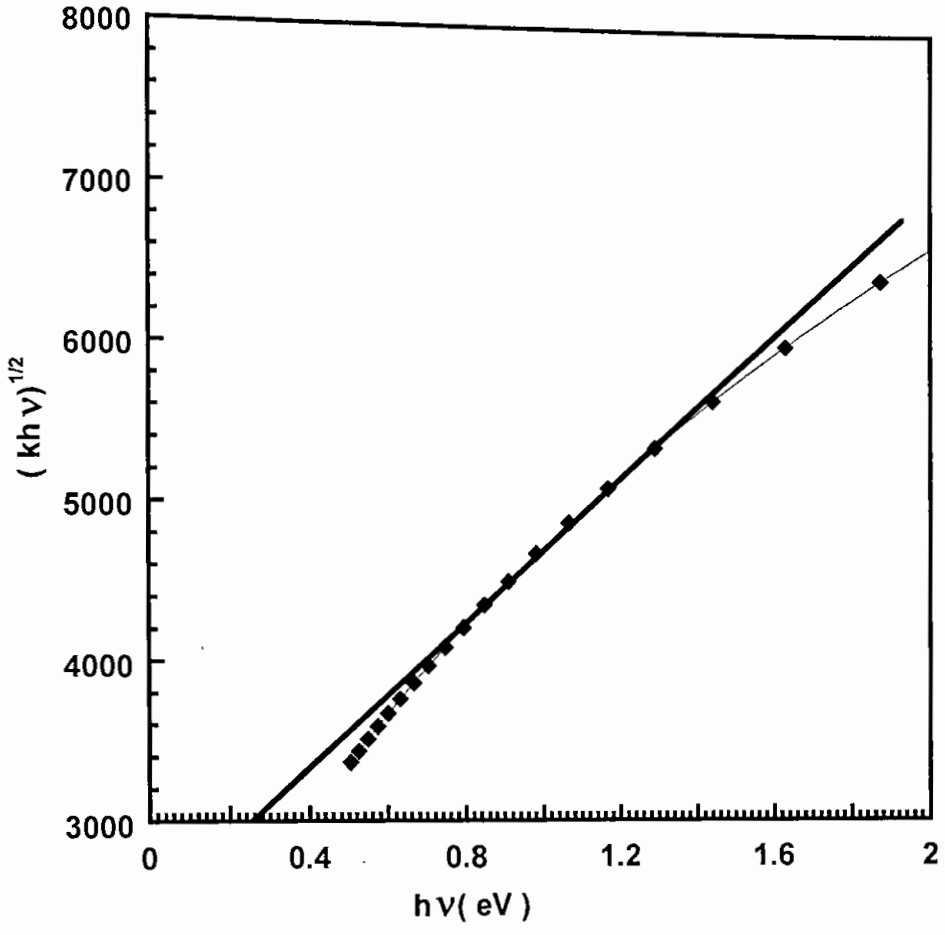

Figure 4.35: *$(kh\nu)^{1/2}$ vs. Photon Energy ($h\nu$) plot for a annealed MnO_2 film of thickness 200 nm deposited at 593K.*

From the above transmittance data, the optical band gap E_g is determined from the $(kh\nu)^{1/2}$ versus $h\nu$ plots as shown in Figure 4.35. This plot indicates that the transition is an allowed indirect type with a band gap at $E_g \approx 0.26$ eV.

Figure 4.36 shows the spectral transmittance/reflectance versus wavelength spectra for annealed **MnO_2** films of different thicknesses. It is observed that the transmittance curve exhibits a significant transmittance in the visible as well as in the infrared region. The reflectance spectrum, however, shows a low reflectance in the entire wavelength region. It is seen that the transmittance decreases with

increasing film thickness. On the other hand, the reflectance increases with increasing film thickness.

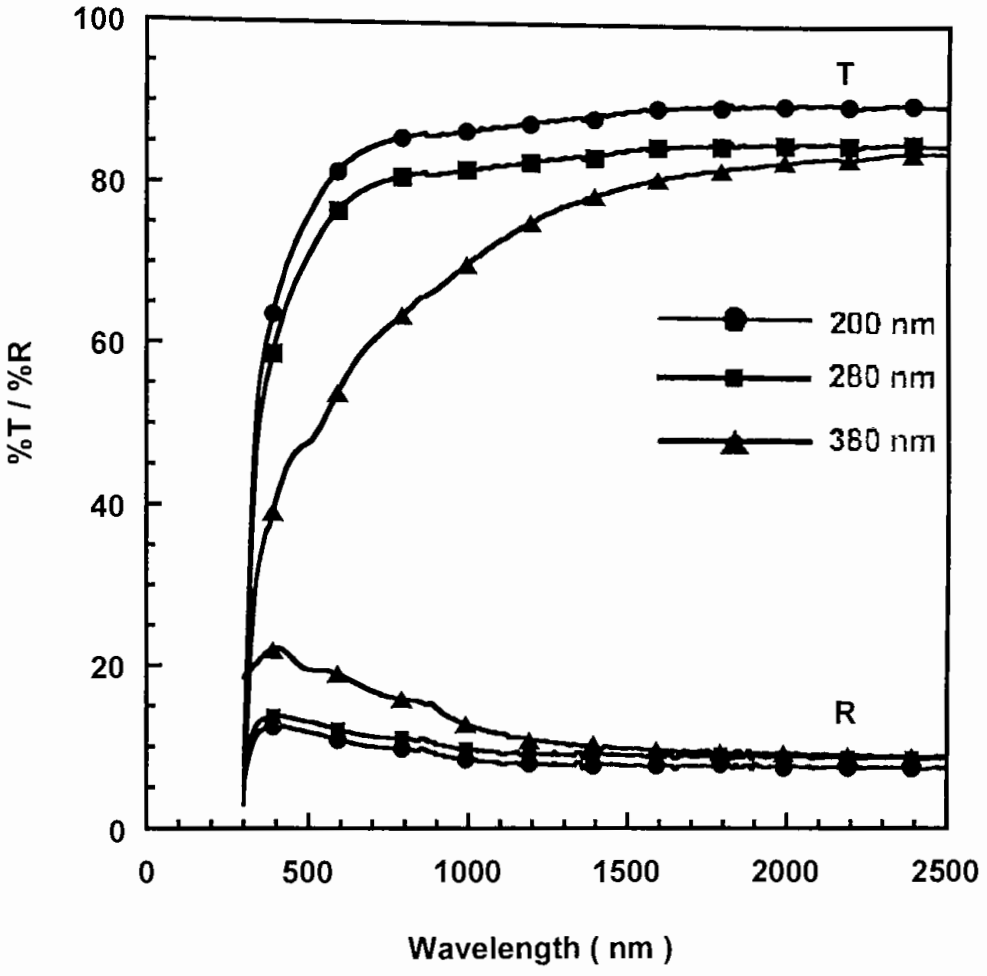

Figure 4.36: *Optical spectra of different thicknesses of MnO_2 thin films are deposited at 593K.*

From the above transmittance data, the optical band gap (E_g) is also determined from the $(khv)^{1/2}$ versus hv plots, which is shown in Figure 4.37. This plot also indicates that the transition is an allowed indirect type with a band gap at $E_g \approx 0.26$ eV.

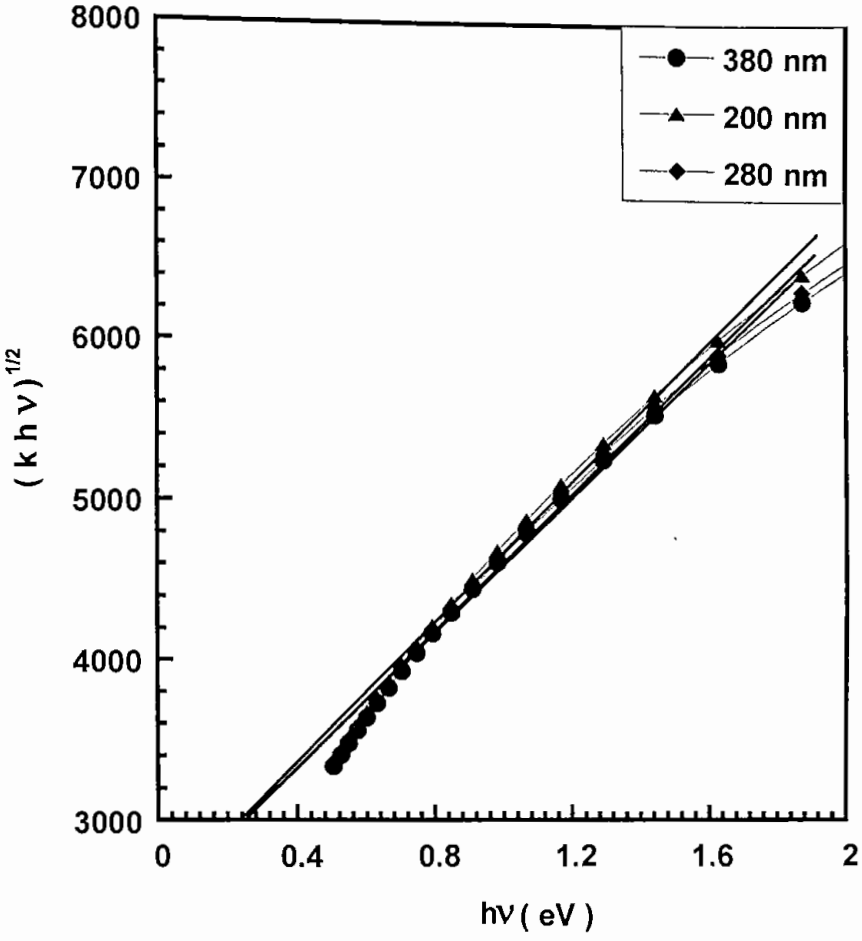

Figure 4.37: *$(kh\nu)^{1/2}$ vs. Photon Energy($h\nu$) plot for a annealed MnO_2 film of different thicknesses deposited at 593K.*

The value of band gap (E_g) in both electrical and optical method obtained by author's work is an excellent agreement with the reported value of band gap determined by other workers [11, 12, 28, 48, 157].

4.17 ELECTRON AFFINITY AND WORK FUNCTION CALCULATION FOR MnO_2

To obtain the highest performance from an electrode in electrochromic cell and photoelectrochromic cell, the conduction band discontinuity ($\Delta E_c = \chi_s - \chi_{os}$) should be zero [114], where χ_s and χ_{os} are the electron affinities of the base semiconductor and the oxide semiconductor, respectively. To get optimum device performance, the work function of the oxide semiconductor should be less than or equal to the electron affinity of the base semiconductor. Therefore to use $\mathbf{MnO_2}$ thin film as electrodes, its work function is to be known.

According to Sanderson electronegativity principle [115], when two or more atoms initially different in electronegativity combine chemically, they adjust to have the same intermediate electronegativity within the compound. This intermediate electronegativity is given by the geometric mean of the individual electronegativity of the component atoms. That is, the geometric mean of n numbers is obtained by multiplying all of the numbers together and taking the n^{th} root of the product. According to this principle, the electronegativity of $\mathbf{MnO_2}$ can be written as

$$\mathbf{E_n\,(MnO_2) = \left[E_{Mn} \times (E_O)^2\right]^{\frac{1}{3}} = \left[2.20 \times (3.65)^2\right]^{\frac{1}{3}} = 3.08\ eV,}$$

where $E_{Mn} = 2.20$ and $E_O = 3.65$ eV are the electrornegativities of manganese and oxygen atoms, respectively [115]. E_n is the electronegativity of $\mathbf{MnO_2}$.

Semiconductors are generally covalent in nature, but it is an established fact that no bond is purely covalent or purely ionic in character but always a mixture. From the electronegativity concept the percentage of the ionic character, **y** of the bond between manganese and oxygen can be obtained by using Sanderson's electronegativity values [115] in Pauling's empirical relation [116]

$$\textbf{\% ionic character(y)} = [1 - \exp(-0.25\{E_{Mn} - E_O\}^2)] \times 100\%$$

or, **% ionic character(y) = 40.88 %.**

The calculation of the electron affinity and work function are done in the polycrystalline $\mathbf{MnO_2}$ samples. It may be explained from the calculation that the bonds between manganese and oxygen are considered as the principal bond and

within the limits of native and foreign impurity content, $\mathbf{MnO_2}$ is more covalent than ionic.

Electron affinity and work function are defined respectively, as the energy required to remove an electron from the bottom of the conduction band E_c, and from the Fermi level E_F, to a position just outside the surface of the material (vacuum level). In the absence of straightforward method of determining the electron affinity of the bulk semiconductor, an indirect and empirical method [117] is used to determine the electronegativity of the atoms. In the case of semiconductor the relation between bulk electronegativity E_n corresponds to the intrinsic Fermi level E_F with respect to the vacuum level is [118]

$$\mathbf{E_F \approx E_n = \chi + E_g /2} \qquad (4.16)$$

where χ is the electron affinity and E_g is the optical band gap between the conduction band and valance band. The position of E_F in a bulk semiconductor is determined by the regular crystallographic structure of the intrinsic material. The electronegativity can therefore be assumed here to be a constant parameter and the effect of a change in the impurity contents possible in the bulk material can be accounted for by a net change in the electron affinity of the sample.

From the optical data of $\mathbf{MnO_2}$ thin film, the band gap (E_g) is obtained from the plot of $(khv)^{1/2}$ vs. hv. The position of the Fermi level (E_F) is obtained from the thermoelectric data for $\mathbf{MnO_2}$ thin film and the carrier concentration (n) is determined from the Hall effect experiment. Figure 4.38 shows the variation of E_g and E_F with the carrier concentration n. From curve (a) and taking E_n= 3.08 eV, the value of electron affinity χ of different MnO_2 samples is determined using Equation 4.16. The calculated values of electron affinity are tabulated in Table 4.9

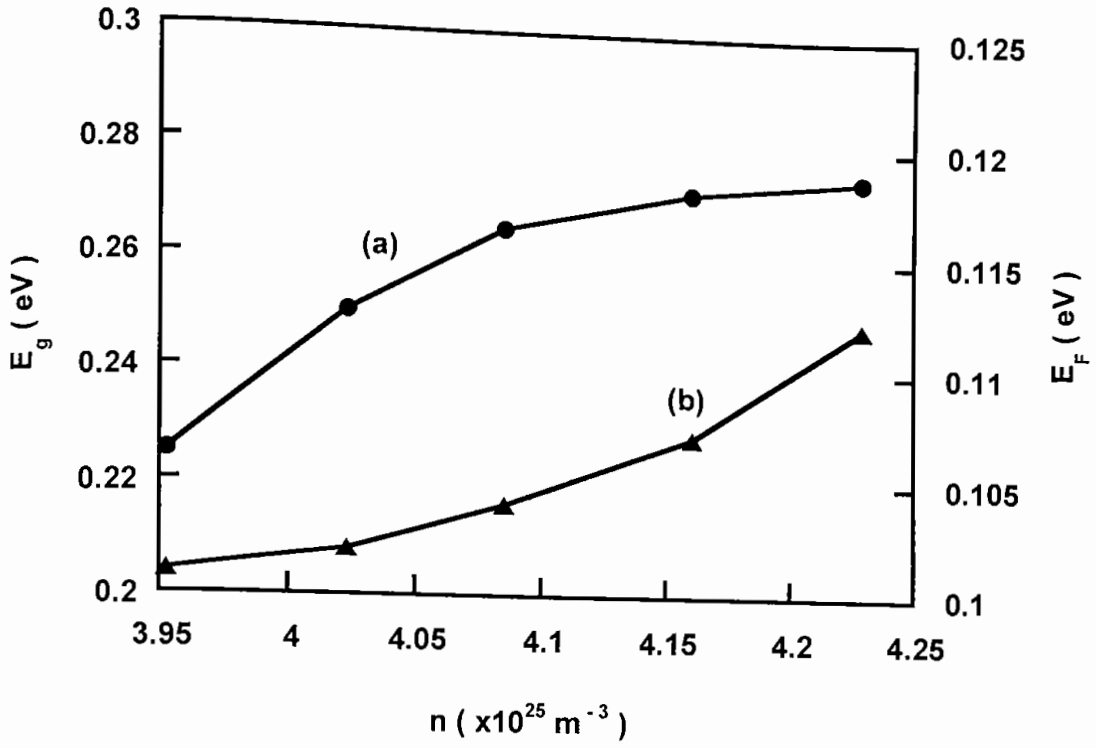

Figure 4.38: *The variation of (a) energy band gap (Eg) and (b) Fermi energy (E_F) with carrier concentration (n), respectively.*

Table 4.9

n (x 10^{25} m^{-3})	E_F eV	E_g eV	χ eV	W eV
3.952	0.101	0.225	2.968	2.867
4.023	0.102	0.250	2.955	2.853
4.085	0.104	0.265	2.948	2.844
4.160	0.107	0.272	2.944	2.837
4.229	0.112	0.275	2.943	2.830

Using the values of χ and taking values of E_F from the curve (b) of Figure 4.40, different values of the work function (W) are obtained using the following relation [118]

$$W = \chi - E_F. \tag{4.17}$$

The calculated values of electron affinity and work function of MnO_2 films are tabulated in Table 4.9. It is found that the work function (W) of the samples varies from 2.83 to 2.87eV. The values of χ are found to vary from 2.94 to 2.97eV

in the carrier concentration range $4.2x10^{25}$ to $3.9x10^{25}$ m^{-3}, respectively. The author's calculated electron affinity value is well agreed with the reported value of electron affinity by other workers [158, 159, 160].

4.18 SELECTIVE SURFACE STUDY

It is convenient to introduce integrated optical quantities, especially the luminous (lum) and (sol) properties. They can be obtained from

$$X_\rho = \frac{\int d\lambda \Phi_\rho X(\lambda)}{\int d\lambda \Phi_\rho(\lambda)}$$

where X denotes transmittance or reflectance. The luminous quantities were obtained by setting $\Phi_\rho = \Phi_{lum}$ equal to the standard luminous efficiency function for photooptic vision [124] as specified CIE (Commission International de l'Éclairage). For solar quantities, one can use $\Phi_\rho = \Phi_{sol}$, according to the tabulated AM2 irradiance spectrum [125]. This calculation was done for different substrate temperatures (T_s) as well as of different film thicknesses (t). The calculated $\%T_{sol}$, $\%R_{sol}$ and $\%T_{lum}$, $\%R_{lum}$ are tabulated in Table 4.10 and 4.11, respectively.

Table 4.10

Solar		
T_s K	T_{sol} %	R_{sol} %
573	66.27	8.981
583	70.91	9.01
593	82.46	9.992
603	72.90	9.69
613	65.17	7.98

Luminous		
T_s K	T_{lum} %	R_{lum} %
573	59.65	9.754
583	65.32	9.79
593	79.325	11.004
603	66.18	10.14
613	61.79	8.18

Table 4.11

Solar		
t nm	T_{sol} %	R_{sol} %
120	86.39	7.16
160	84.78	8.12
200	82.46	9.992
250	78.87	10.57
340	71.38	11.82

Luminous		
t nm	T_{lum} %	R_{lum} %
120	81.54	8.56
160	80.43	9.27
200	79.325	11.004
250	70.24	12.08
340	67.81	12.44

It is seen from Table 4.10 that the values of the integrated luminous and solar transmittance are increased up to 593K with deposition temperatures and then their values are decreased monotonously with deposition temperatures. Similar behavior is observed for the integrated luminous and solar reflectance as well. From Table 4.11 it is seen that the integrated luminous and solar transmittance are decreased with increasing film thicknesses, whereas their values for reflectance are increased with increasing film thicknesses. Higher order of the integrated values of luminous and solar transmittance and lower values of reflectance suggest that this material is a potential candidate for the application in selective surface devices.

Chapter 5

Conclusion

&

Suggestions for Future Work

5.1 CONCLUSIONS

The purpose of this chapter is to summarize the results obtained in this work. First, manganese dioxide thin films were prepared by a simple spray pyrolysis technique. Then its structural properties were studied. The electrical and optical properties were also measured. In the light of the structural, electrical, and optical studies of MnO_2 thin films, the following conclusions may be drawn:

A. Undoped manganese dioxide (MnO_2) thin films of thickness ranges 85 – 380 nm have been prepared onto glass substrate by a simple spray pyrolysis technique under various deposition conditions. The deposition rate is 6.7 nm/min. The effects of different deposition variables on structural, electrical and optical properties of the films have been studied in detail. These studies show that various deposition parameters have remarkable effects on spray deposited MnO_2 thin films.

B. X-ray diffraction studies show that spray deposited MnO_2 thin films are polycrystalline in structure.

C. Transmission Electron Microscopy analysis also indicates that the MnO_2 samples are homogeneous and polycrystalline in structure.

D. The virgin films are shown highly resistive whereas annealed films exhibit a reasonable conduction. Electrical conductivity has been measured as a function of temperature ranging from 303 to 413K and its conductivity exhibits an anomaly at a temperature 323K. The decrease in resistivity with increasing temperature indicates that the samples are semiconducting in nature.

E. The heat-treatment of the MnO_2 samples at different ambient have remarkable effects on the electrical transport properties. During annealing oxygen chemisorption-desorption mechanism is found to play an important role in controlling the electronic properties of the films.

F. A thickness effect of activation energy is observed in MnO_2 films. The effect shows that the activation energy above anomaly is inversely

proportional to the thickness whereas its value is directly proportional below the anomaly temperature.

G. Variation of electrical conductivity with thickness is observed in **MnO_2** films. It is observed that the conductivity increases with thickness and attains a constant value ≈ 6.5 Ω^{-1}-m^{-1} at 220 nm. Above this thickness value, the electrical conductivity is approximately thickness independent, which is agreed well with the Fuchs-Sondheimer theory.

H. Aging effect is studied for consecutive 15 days at various thicknesses MnO_2 films. This study shows that the conductivity decreases sharply with time and its fall in conductivity is more pronounced in films of lower thickness than the higher one.

I. Hall effect studies indicate that the **MnO_2** film is n-type semiconductor and its band gap is found approximately 0.27eV. The calculated donor levels are shallow and mainly due to the native defects, such as interstitial manganese and oxygen vacancies. The carrier concentration is increased with increasing temperature as well as with increasing thickness. The carrier concentrations of the sample are found in the range 4.7×10^{25} to 6.5×10^{25} m^{-3} and the Hall mobility is found in the range -0.97×10^{4} to -1.057×10^{4} $m^2V^{-1}S^{-1}$, respectively. This study shows that the Hall mobility is controlled by the grain boundary potential barrier heights, which are modulated by the heat-treatment effects. Fermi level lies near the donor level, but are at 1.8 to $2.6k_BT$ below the conduction band edge at room temperature, which indicates that the samples are non-degenerate. The Debye screening length and grain size calculation indicates that the grain boundary trapping model for the thermal activation of mobility is applicable.

J. Thermoelectric power (TEP) of **MnO_2** films has been measured from room temperature up to 403K with reference to pure lead (**Pb**). This study shows that **MnO_2** sample is an n-type semiconductor. The Fermi level is determined using a non-degenerate semiconducting model. The carrier scattering index, activation energy and temperature co-efficient of the activation energy have been calculated at different range of thickness as

well as of temperature. It is interesting to note that the Fermi level is found to be pinned near the conduction band edge with the increase of temperature. The calculated value of the scattering index is ≈ - 1.5, which indicates that ionized impurity scattering is dominant in the **MnO_2** films. Similar observation is observed form the Hall effect study. The minimum value of $-(E_c - E_F)$ is obtained as 0.125eV and is almost five times that of k_BT at room temperature, which is supported the consideration of a non-degenerate model to explain the thermopower data.

K. The optical study was carried out in the wavelength range $0.3 < \lambda < 2.5$ μm using Perkin-Elmer Lambda-19 double beam spectrophotometer at room temperature. This study shows a transition of indirect allowed type with a band gap of $E_g = 0.26$eV. A similar study of band gap in electrical measurements of **MnO_2** films does give a value of 0.27eV, which is an excellent agreement with the reported value of band gap by other workers. The refractive indices of these films in the visible range of wavelengths are found in the range 2.65 to 4.34 for **MnO_2** films.

L. The calculation of the electron affinity and work function are done in the polycrystalline **MnO_2** samples. This calculation indicates that the bonds between manganese and oxygen are considered as the principal bond and within the limits of native and foreign impurity content, **MnO_2** is more covalent than ionic.

M. Integrated luminous and solar transmittances as well as reflectance of **MnO_2** films are calculated from the optical data. It is observed that the values of the integrated luminous and solar transmittance are increased up to 593K with deposition temperatures and then their values are decreased monotonously. Similar behavior is also observed for the case of integrated luminous and solar reflectance. The integrated luminous and solar transmittances are decreased with increasing film thicknesses, whereas their values for reflectance are increased with increasing film thicknesses. Higher order of transmittance and lower values of reflectance suggest that this material is a potential candidate for the application in selective surface devices.

5.2 SUGGESTIONS FOR FUTURE WORK

Manganese dioxide is a low band gap, high optical constant semiconductor. In recent years manganese dioxide has a variety of applications, particularly as an electrode in electrochemical and electrochromic batteries, in fuel cells as well as in energy efficient devices applications. Hence to get better performance of this material prepared by spray pyrolysis technique, the following research works may be extended:

(i) Electrochemical study of spray deposited $\mathbf{MnO_2}$ may be carried out.

(ii) Electrochromic study of spray deposited $\mathbf{MnO_2}$ may be carried out.

Chapter 6
References

REFERENCES

[1] A.Kumar, Y.W.Chung, J.J. Moore and J.E. Smugeresky, in "Surface Engineering Science and Technology 1", The Minerals, Metals & Materials Society, Warrendale, 1999.

[2] D.A. Gloker and S.I. Shah, in "Hand Book of Thin Film Process Technology", Institute of Physics Publishing, Bristol and Philadelphia, 1998.

[3] A. Goswami in "Thin Film Fundamentals" New Age Int.(P) Ltd. Publishers, New Delhi, 1996.

[4] A.Kumar, Y.W.Chung, R.W.J. Chia, in "Hard Coatings", The Minerals, Metals & Materials Society, Warrendale, 1999.

[5] K.L. Chopra and S.R. Das, in "Thin Film Solar Cells" New Age Int. (P) Ltd. Publishers, New Delhi, 1983.

[6] C.G. Granqvist, in "HandBook of Inorganic Electrochromic Materials", Published by Elsevier, 1995.

[7] C.G. Granqvist and G. A. Niklasson in "Thin Film Technology", Gothenburg, Sweden.

[8] D.L. Smith, in "Thin Film Deposition", McGraw Hill Book Company, New York, 1995.

[9] K.L. Chopra, in "Thin Film Phenomena" Published by McGraw-Hill Book Company, New York, 1969.

[10] Web Elements Data Base, URL:"http://www.webelements.com/Mn/"

[11] V.G. Bhide and R.V. Damle. Physica Vol. **26**, 1960, p. 33-42.

[12] V.G. Bhide and R.H. Dani. Physica, Vol. **27**, 1961, p.821-826.

[13] K. Honda and T. Sone. Sci. Rep. Tohoku Univ. Vol. **3**, 1914, p.139.

[14] C.B. Sawer and C.H. Tower. Phys.Rev. Vol. **35**, 1930, p. 269.

[15] E. Blechstein. Physik.Z. Vol. **39**, 1938, p.212.

[16] A. Von Hippel. Rev. mod. Phys. Vol. **22**, 1950, p.221-237.

[17] E.J.W. Verwey in "Semiconducting materials", Butterworths, Scientific Publ. Ltd. London. 1951.

[18] J. Volger. Ibid., Vol. **98**, 1951, p.162-170.

[19] C.G. Koops. Phys. Rev. Vol. **83**, 1951, p.121-124.

[20] R. Mansfield and S.A. Salam. Proc. Phys. Soc. Vol. **B66**, 1953, p.377.

[21] F.S. Goucher and M.B. Prince. Phys. Rev. Vol. **89**, 1953, p.651

[22] K. Sasaki and K. Kojima. J. Electrochem. Soc. Japan Vol. **22**, 1954, p.564.

[23] A.B. Lidiard. Rep. Progr. Phys. Vol. **17**, 1954, p.201.

[24] R. Glicksman and C.K. Moorehouse. J. Electrochem. Soc. Vol. **103**, 1956, p.149

[25] H.D. Megaw in "Ferroelectricity in crystals", Methuen & Co. Ltd. London, 1957.

[26] J.N. Das. Z. Physik, Vol. **151**, 1958, p. 345.

[27] V.G. Bhide, R.V. Damle and R.H. Dani. Physica, Vol. **25**, 1959, p.579-580.

[28] J.P. Chevillot and J. Brenet. C.R. Acad. Sci.(Paris). Vol. **248**, No. 6, 1959, p. 776-8.

[29] J. Brenet, Schwiezer Archiv, A. Wiss. U. Tech., Vol. **26**, No1,1960, p. 10.

[30] W.C. Vosburgh and J.H. Delap. J. Electrochem. Soc. Vol. **107**, No.4, 1960, p.255.

[31] J.S. Wiley and H.T. Knight, J. Electrochem. Soc. Vol. **111**, 1964, p. 656.

[32] J.H. Cash, Jr., and R. Seet Clark. Paper Presented at the Cleveland Meeting of the Society, May 1966.

[33] R.M. Valletta, J.S. Makris and W.A. Pliskin. Proc. Elect. Comp. Conf., May 1966.

[34] R.M. Valletta and W.A. Pliskin. J. Electrochem. Soc. Vol. **114**, No .9, 1967, p. 944- 947.

[35] P.H. Klose. J. Electrochem. Soc. Vol. **117**, No. 7, 1970, p.854-858.

[36] A. Kozawa. J. Electrochem. Soc.(USA), Vol. **134**, No. 4, 1987 p. 780-791.

[37] S.I. Goncharov, M. Yu. Serbinovskii and V.G. Voloshchuk. Sov. Electr. Eng.(USA), Vol. **58**, No. 7, 1987, p. 109.

[28] M.W. Rophoul, N.S. Petro and L.B. Khalil. J. Power Sources (Switzerland), Vol. **22**, No. 2, 1988, p. 149-161.

[39] K. Kuwabara, K. Hanafusa and K. Sugiyama. J. Electrochem. Soc. (USA), Vol. **136**, No.2, 1989, p.319-23.

[40] H. Takahara. J. Am. Ceram. Soc. (USA), Vol. **72**, No. 8 (1989), p. 1532-5.

[41] N. Chiba, K. Yoshida, T. Miyashita and H. Miura. Denki KagaKu (Japan), Vol. **57**, No. 6, 1989, p. 456-8.

[42] T. Nohma, H. Watanabe, S. Narukawa, K. Teragi and T. Amazutzumi. Sanyo Tech. Rev. (Japan), Vol. **21** No.3, 1989, p. 114-22.

[43] I.A. Raj and K.I. Vasu. Int.J. Hydrog.Energy(UK). Vol. **15**, No. 10, 1990, p.751.

[44] L. Jarvis. J. Power Sources (Switzerland). Vol. **32**, No. 3, 1990, p. 271-6.

[45] S. Llompart, L.T. Yu, J.C. Mas, A. Mendiboure and R. Vignaud. J. Electrochem. Soc. (USA), Vol. **137**, No. 2, 1990, p. 371-7.

[46] I. Susana, T. de Torresi, A. Gorenstein. Proc. SPIE Vol. **1728**, p.92-102, 1992, Optical Materials Technology for Energy Efficiency and Solar Energy Conversion XI: for Smart Windows, Edited by A. Hugot-le Goff, C.G. Granqvist and C.M. Lampert.

[47] O. Erlandsson, N.T. Nguyen, V.H. Nguyen, N. D. Nguyen. Proc. SPIE Vol. **2017**, 1993, p.182-193, Energy Conversion XII Editors: C.M. Lampert.

[48] A.K. Mallick and K.A. Khan. Phys. Stat. Sol. (a) Vol. **142**, 1994, p. 409-414.

[49] P. Fau, J. P. Bonino and A. Rousset. Appl. Surface Sicence. Vol. **78**, No. 2, 1994, p 203.

[50] L.M. Gassa, H.T. Mishima, B.A. Lopez de Mishima and J.R. Vilech. Electrochimica. Acta. Vol. **42**, No. 11, 1997, p. 1717-1723.

[51] Y.Tanakaa and M. Tsujib. Materials Research Bulletin. Vol. **32**, No. 4, 1997, p.461.

[52] J.J. Xu, S. Passerini, B. Boone and W.H. Smyrl. Proceedings published as Vol. **548**, EE 3.72, of the Material Research Society, 1998.

[53] H.de F. Gorgulho. Proceedings published as Vol. **548**, EE 3.67, of the Material Research Society, 1998.

[54] C. Poinsignon. Proceedings published as Vol. **548**, EE 2.4, of the Material Research Society, 1998.

[55] A. Le Gal La Salle, S. Sarciaux, A. Verbaere, Y. Piffard, D. Guyomard. VISTA (Vietnam), Vol. **147**, No 3, 2000, p.945.

[56] Y. Lvov, B. Munge, O. Giraldo, I. Ichinose, S.L. Suib and J.F. Rusling. Langmuri, Vol. **16**, No. 23, 2000, p. 8850-8857.

[57] L.W. Guo, D.L. Peng, H. Makino, T. Hanada, S.K. Hong, K. Sumiyama, T. Yao and K. Inaba. J. App. Phy. Vol. **90**, 2001, p 351-354.

[58] J.W. Long, L.R. Qadir, R.M. Stroud and D.R. Rolison. J. Phy. Chem. B. Vol. **105**, No. 37, 2001, p. 8712-8717.

[59] M. Chigane, M. Ishikawa and M. Izsaki. J. Electrochem. Soc. Vol. **148**, No.7, 2001, p D96-D101.

[60] C.Julien, M. Massot, S. Rangan, M. Lemal and D. Guyomard. J. of Raman Spectroscopy. Vol. **33**, No. 4, 2001, p.223-228.

[61] X. wang and Y. Lie. J. AM. CHEM. Soc. Vol. **124**, No. 12 2002, p. 2880.

[62] H. Unuma, T. Kanehama, K. Yamamoto, K. Watanabe, T. Ogata and M. Sugawara. J. of Materials Sci, vol. **38**, no.2, 2003, p. 255-259.

[63] W. Mingdeng, Y. Konishi, H. Zhou, H. Sugihara and H. Arakawa. J. Nanotechnology. Vol. **16**, 2005, p. 245-249.

[64] W. Kern and K. K. Schuegraf, in "Handbook of Thin-Film Deposition Processes and Techniques", Noyes Publ., New York, 1988

[65] K.L. Chopra, R.C. Kainthla, D.K. Pandya and A.P. Thakoor. Phys. Thin Films, Vol. **12**, 1982, p.167.

[66] M.S. Tomar and F.J. Garcia. Prog. Crystal growth charact., Vol. **4**, 1981 p.221.

[67] J.C. Viguie and J. Spitz. J. Electrochem Soc., Vol. **122**,1975, p.585.

[68] W. Kern and V.S. Ban, "Thin film process", (Ed. J.L. Vossen and W. Kern, Academic Press, New York 1978).

[69] F.C. Eversteijn, Philips Res. Rept. Vol. **29**, 1974, p. 45.

[70] O. Almen and G. Bruce, Nucl. Instrum. Methods. Vol. **11**, 1961 p.257 & 279.

[71] S. Somekh. J. Vac. Sci. Technol. Vol. **13** 1976, p.1003.

[72] M. Ohring, in "The Materials Science of Thin films", Academic Press, New York, 1992.

[73] M. Volmer and A.Z. Weber. Phys. Chem. Vol. **119**, 1925, p.277.

[74] M.G. Ambia and M.N. Islam and M. O. Hakim. J. Mter. Sci. Vol. **28**, 1993, p. 2659.

[75] G.A. Bassett, J.W. Menter and D.W. Pashley, "Structure and Properties of Thin Films"(Ed. C.A. Neugebaure, J.B. Newkirk and D.A. Vermilyea, John Wiley and Sons Inc., 1959).

[76] R. Thun, "Physics of thin film", Ed. G. Hass, Academic Press Inc., New York, vol. **1**, 1964.

[77] R.B. Belser, J. Appl. Phys. Vol. **28**, 1957, p.109.

[78] O. Wiener. Wied. Ann. Vol. **31**, 1887, p.629.

[79] S. Tolansky in "Multiple Beam Interferometry of Surfaces and Films", Oxford University Press, 1948.

[80] J. G. Gottling and W.S. Nicol. J. Opt. Soc. Am., Vol. **56**, 1966, p. 1227.

[81] J. Guzman-Mendoza, M. Garcia-Hipolito, M. Aguilar- Fruties and C. Falcony- Guajardo. J. Phys.: Condens. Matter Vol. **13**, No. 50, 2001, L955-959.

[82] Van-der-Pauw. Philips Res. Rept., Vol. **13**, 1958, p.1.

[83] A. Goswami and R.H. Jog. Indian J. Pure Appl. Phys. Vol. **6**, 1966, p.416.

[84] A. Goswami and S.M. Ojha. Thin Solid Films, Vol. **16**, 1973, p.187.

[85] S. N. Ghosh and S. Dev, in "A Synopsis of Physics", The World Press Ltd., Calcutta, 1937.

[86] E.H. Hall. Phil. Vol. **11**, 1881, p.157.

[87] A. R. Smith. in "The Physical Principles of Thermodynamics", Chapman and Hall, New York, 1952.

[88] C. Kittel, in "Introduction to Solid State Physics", 7th Edn, John Wiley and Sons Inc., Singapur, 1995.

[89] N. F. Mott and E.A. Davis, in "Electronic Process in non-crystalline materials", 2nd Edn, Clarendon Press, Oxford, 1979.

[90] H. Harry, B. Kwok and R.H. Bube. J. Appl. Phys. Vol. **44**, 1973, p. 138.

[91] N. B. Hannay in "Semiconductors" Cambridge University Press, 1968.
[92] N.W. Ashcroft and N.D. Mermin in "Solid State Physics" Holt, Rinehart and Winston, New York, 1976, p. 573.
[93] N.W. Ashcroft and N.D. Mermin in "Solid State Physics" Holt, Rinehart and Winston, New York, 1976, p. 574.
[94] W. Shockley, in "Electrons and Holes in Semiconductors", D. van Nostrand, W. Inc. New York, 1950.
[95] N. F. Mott and H. Frolich. Proc. Roy. Soc. London, Vol. **A171**, 1939, p.496.
[96] D. J. Howarth and E. H. Sondheimer. Proc. Roy. Soc. London, Vol. **A219**, No. 53, 1953, p.496.
[97] T. D. Lee, F. E. Low and D. Pines. Phys. Rev. Vol. **90**, 1953, p.297.
[98] F. E. Low and D. Pines. Phys. Rev. Vol. **91**, 1953, p.193.
[99] K. Lark-Horovitz, A. E. Middleton, E. P. Miller and I. Wilerstein. Phys. Rev. Vol. **69**, 1946, p. 258.
[100] E. Conwell and V. F. Weisskoff. Phys. Rev. Vol. **77**, 1950, p. 388.
[101] N. B. Hanney, in "Semiconductors", Reinhold Publishing Corporation, New York, 1959.
[102] G.L. Pearson and J. Bardeen, Phys. Rev. Vol. **75**, 1949, p. 865.
[103] D. L. Dexter and F. Seitz. Phys. Rev. Vol. **86**, 1952, p. 964.
[104] J. Y. W. Seto. J. Appl. Phys. Vol. **46**, 1975, p. 5247.
[105] G. Baccarani, B. Ricco and G. Spadini. J. Appl. Phys. Vol. **49**, 1978, p. 5565.
[106] A. K. Ghosh, C. Fishman and T. Feng. J. Appl. Phys. Vol. **51**, 1980, p. 446.
[107] R. L. Petritz. Phys. Rev. Vol. **110**, 1958, p. 1254.
[108] A. Goswami and A. B. Mandale. Japanese J. Appl. Phys., Vol. **17**, 1978, p. 473.
[109] H. Brooks. in "Advance in Electronics and Electron Physics", Academic Press, New York, Vol.7, 1955.
[110] J. Bardeen, F. J. Blatt and L. H. Hall. Photoconductivity Conference (Ed. Wiley, New York), 1956.
[111] D. L. Dexter Phys. Rev. Vol. **101**, 1956, p.48.
[112] J. C. Manifacier, J. Gasiot and J. P. Fillard. J. Phys. E. Vol. **9**, 1967, p. 1002.
[113] G. Frank, E. Kauer and H. Kostlin. Thin Solid Films, Vol. **77**, 1981, p.107
[114] H. J. Hovel, in " Solar Cells, Semiconductors and Semimetals", Vol. **2**, Edited by R. K. Willardson and A.C. Beer, Academic., New York,1975.
[115] R. T. Sanderson. "Chemical Periodicity", Reinhold, New York, 1960.
[116] S. H. Maron and J. B. Lando. "Fundamentals of Physical Chemistry", Macmillan, New York, 1974.

[117] M. A. Butler and D. S. Ginley. J. Electrochem. Soc. Vol. **125**, 1978, p.228

[118] M.N. Islam and M.O. Hakim. J. Material Sci. letters, Vol. **5**, 1986, p.63-65.

[119] M. P. Thekaekara. in "Solar Energy Engineering", Edited by A. A. M. Sayigh, Academic Press, New York, 1977.

[120] Y. S. Touloukian, D. P. Dewitt and R. S. Hernicz. in "Thermophysical Properties Coatings", IFI/Plenum, New York, Washington, 1972.

[121] M. K. A. Khan. Ph.D. Thesis, University of Rajshahi, Rajshahi, Bangladesh, 1989.

[122] G. Wyszecki, in "Hand Book of Optics", Edited by W. G. Driscoll and W. Vaughan, Magraw –Hill , New York, 1978, Section 9.

[123] J. C. C. Fan and F. Bachner. J. Appl. Opt. Vol. **15**, 1976, p. 1012.

[124] G. Wyszecki and W.S. Stiles in "Color Science", 2nd Edt. Wiley & Sons, New York, 1982.

[125] P.J. Moon. Franklin Inst. Vol. **230**, 1940, p.583.

[126] J. C. Manifacier, M. De Murcia and J. P. Fillard. Mat. Res. Bull. Vol.**10**, 1975, p. 1215.

[127] B. K. Gupta and O. P. Agnihotric. Solid State Commun. Vol. **23**, 1977, p. 295.

[128] J. Aranovich, A. Ortiz and R. H. Bube. J. Vac. Sci. Technol. Vol. **16**, 1979, p. 994.

[129] E. Shanthi, V. Dutta, A. Banerjee and K. L. Chopra, J. Appl. Phys. Vol. **51**, 1980, p. 6243.

[130] S. Kulaszewicz. Thin Solid Films. Vol. **74**, 1980, p. 211.

[131] M. N. Islam and M.O. Hakim and H. Rahman J. Mater. Sic. Vol. **22**, 1984, p.1379.

[132] M. G. Ambia, M. N. Islam and M. O. Hakim. Solar Energy Materials and Solar Cells. Vol. **28**, 1992, p. 103.

[133] M. G. Ambia, M. N. Islam and M. O. Hakim. J. of Materials Sci. Vol. **27**, 1992, p. 5169.

[134] G. Blandenet, M. court and Y. Lagrade. Thin solid Films, Vo. **77**, 1981, p. 81.

[135] M. N. Islam and M.O. Hakim. J. Phys. Chem. Solids, Vol. **46**, No.3, 1985, p. 339.

[136] S. K. Som and S. G. Mukharjee. Acta Mech. Vol. **36**, No. 1-2, 1980.

[137] C. M. Lampkin. Prog. Cryst. Growth charact. Vol. **1**, 1979, p.405.

[138] R. Brown. in "Handbook of thin Film Tchenology", (Eds. L. I. Maissel and R. Glang, McGraw Hill Inc. 1970).

[139] V. D. Das and J. C. Mohanty. J. Appl. Phys. Vol. **54**, 1983, p.977.

[140] Dr. Yoshiyuki Yamamoto, Assistant Professor, Magnetic Materials Lab., School of Material Science, Japan Advanced Institute of Science and Technology,1-1 Asahidai, Tatsunokuchi, Ishikawa 923-1292, Japan.

[141] JCPDS Card# 24-0735, Joint Committee on Powder Diffraction Standards, Japan. 1969.

[142] K.L. Chopra, S. Major and D.K. Pandya. Thin Solid Films, Vol. **102**, 1983, p.1.

[143] S.K. Ghandhi, R.J. Field and J.R. Shealy. Appl. Phys. Lett. Vol. **37**, 1980, p.449.

[144] Y.Fujita and T.Kwan. J. Res. Inst. Catal. Vol. 7,1959, p.24.

[145] S. C. Chang, J. Vac. Sci. Technol. Vol. **17**, 1980, p.366.

[146] M.N. Islam and M.O. Hakim. J. Phys. D. Vol. **19**, 1986, p.615.

[147] L.V.Azaroff and J. J. Brophy. "Electronic process in materials", McGraw Hill Book Co. 1963.

[148] S. Major, A. Banerjee and K. L. Chopra in. Thin Solid films, Vol. **108**, 1983, p.333.

[149] Neugebauer CA. Physics of Thin Films (ed. Hass G. Thun, R.E., Academic Press, New York); 1970.

[150] K. Fuschs Electron transport phenomena in metal films. in, "Thin Flims Phenomena" K.L. Chopra, McGraw-Hill Publ. Co. New York 1969.

[151] E H. Sondhemier Adv. Phys. London, Oxford University Press; 1952.

[152] S. Major, A. Banerjee and K. L. Chopra. Thin Solid films Vol. **125**, 1984, p.179.

[153] M.O. Hakim. J. Mater. Sci. **Vol. 25,** 1990, p.1294.

[154] CRC HandBook of Chemistry & Physics, 82th Edn.,(2001-2002) (CRC Press, LCL).

[155] J. W. Orton and M.J. Powell. Rep. Progr. Phys. Vol. **43**, 1980, p.1263.

[156] L. L. Kazmerski. in "Polycrystalline and Amorphous Thin Films and Devices", Academic Press, New York, 1980.

[157] R. Druilhe and J. P. Suchet. Czech. J. Phys. B Vol. **17**, 1967, p. 337.

[158] E.B. Rudnyi, E.A. Kaibicheva and L.N. Sidorov, Rapid Commun. Mass Spectrom., Vol. 7, 1993, p.800.

[159] G.L.Gutsev, B.K. Rao, P. Jena, X. Li and L.S. Wang. J. Chem. Phys., Vol. **113**, 2000, p.1473.

[160] A. Pramann and K. Rademann. Int. J. Mass Spectrom., Vol. **187**, 1999, p.673.

PAPER

I

Available online at www.sciencedirect.com
SCIENCE DIRECT®
Renewable Energy xx (xxxx) 1–14
RENEWABLE ENERGY
www.elsevier.com/locate/renene

Technical note

Effects of deposition variables on spray-deposited MnO_2 thin films prepared from $Mn(C_2H_3O_2)_2 \cdot 4H_2O$

A.K.M. Farid Ul Islam, R. Islam, K.A. Khan*

Department of Applied Physics and Electronics, University of Rajshahi, Rajshahi 6205, Bangladesh

Received 16 July 2004; accepted 14 February 2005

Abstract

Undoped MnO_2 thin films have been prepared by a modified spray pyrolysis technique under various deposition conditions and the effects of different variables on electrical and optical properties have been studied in detail. It is found that substrate temperature, spray rate, solution concentration, carrier air pressure and post-deposition heat-treatment, spray outlet to substrate distance play important role in obtaining optimum films.

Electrical conductivity study shows an anomaly in conductivity at a temperature 323 K and its thickness dependent resistivity follows Fuchs–Sondheimer theory. The Hall effect and thermoelectric studies indicate that the deposited sample is an n-type semiconductor. Optical study in the entire wavelength 0.3–2.5 μm range exhibits a high transmittance in the visible as well as in the near infrared. Calculation from optical data, the sample exhibits a band gap at 0.28 eV, which also supports the value obtained from the Hall effect study. These studies may be of importance for the applications of this material in energy efficient surface coating devices.

Keywords: Preparation technique; Spray pyrolysis; MnO_2 films; Deposition variables; Anomaly in conductivity; Selective surface

1. Introduction

Research and development on thin films has led to the conclusion that different classes of materials are of particular interest for different applications. Manganese dioxide is of

* Corresponding author. Tel.: +880 721 750 254; fax: +880 721 750 064.
E-mail address: kakhan_ru@yahoo.ca (K.A. Khan).

0960-1481/$ - see front matter © 2005 Published by Elsevier Ltd.
doi:10.1016/j.renene.2005.02.010

particular interest because the material has in recent a variety of applications in electrochemical [1,2], electrochromic [2], and fuel cell [3,4] devices. Manganese dioxide is a low band gap, high optical constant semiconductor that exhibits ferroelectric properties [5,6].

Literature reports indicate that thin films of manganese dioxide have been produced by a number of techniques by many researchers. These include the reactive deposition [7], electrochemical and thermal deposition [2,8,9], plasma assisted molecular beam epitaxy [10], r.f. sputtering [11], thermal decomposition [12], and sol–gel [13,14] derived techniques. Most of the reports address themselves to the electrochromic, electrochemical and spectroscopic performance of the films, emphasizing the inter-relation between the substrate materials, film structure and their performance in catalytic and rechargeable battery oriented applications. Although there have been a number of investigation on the electrical, optical and electrochromic properties of the films [14–16], no systematic study appears to have been done on electrical and optical properties at varying deposition conditions. Moreover, there is a considerable lack of understanding [7,9,17], concerning the surface properties of the oxides in different applications oriented measuring techniques. Different microstructures caused by different deposition conditions could be the probable reasons for the lacks in understanding. Hence there is a need to study how varying deposition conditions affect the physical properties of manganese dioxide films to assess its usefulness in the energy efficient devices applications. In this paper, we present and discuss the effect of deposition variables in the production of manganese dioxide films by a simple spray pyrolysis technique and to study the physical properties of the films.

2. Experimental

Undoped MnO_2 thin films were prepared from a solution of $Mn_2(C_2H_3O_2)_2 \cdot 4H_2O$ onto glass substrates at various thicknesses by modified spray pyrolysis techniques, a technique which is similar to the production of tin oxide films in our laboratory [18]. It is a very simple, indigenous, low-cost technique, which has not been used before for the deposition of thin manganese dioxide films.

A mixture of manganese acetate [$Mn_2(C_2H_3O_2)_2 \cdot 4H_2O$] compound and deionized H_2O in the form of solution is taken in the pyrolysis flask as working solution for the formation of MnO_2. The basic reaction involved in the process is:

$$Mn(C_2H_3O_2)_2 \cdot 4H_2O + H_2O \leftrightarrow MnO_2 + 2CH_3COOH + 3H_2O + H_2 \quad (1)$$

2.1. Description of apparatus

Fig. 1 shows a schematic diagram of the experimental setup in our laboratory for the production of MnO_2 films. The left part of the above setup is designated as pyrolysis system and the right one is the reactor zone. Some of the special aspects of the aerosol production unit are: A, aerosol production nozzle in a flask; F, pyrex flask; P, compressed air inlet; C, conduit tube; E, stainless steel enclosure; S, substrate; H, heater; G, graphite block and Tc, the thermocouple to measure the substrate temperature.

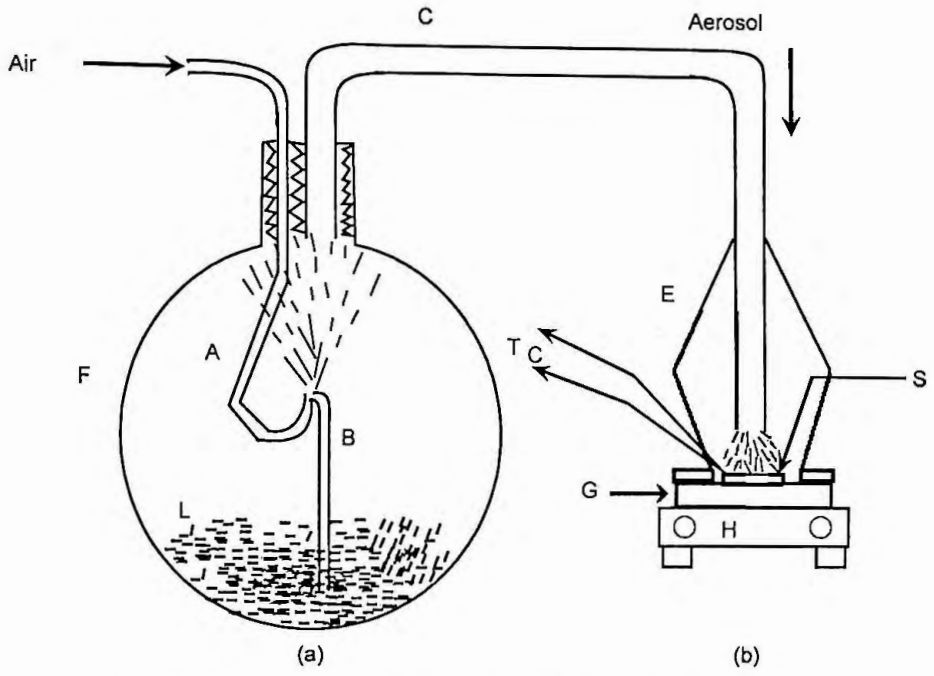

Fig. 1. Schematic diagram for perpetration of MnO_2 thin film by spray pyrolysis.

Before deposition, the whole setup was thoroughly cleaned. A clean substrate with suitable mask was placed on heat susceptor of the heater and a chromel–alumel thermocouple was put in contact to the substrate surface. To have a clean substrate, the substrate at first was immersed in lukewarm aqueous solution of sodium carbonate. It was then washed in a stream of cold water and again dipped into dilute nitric acid for several minutes. After that it was placed in a chromic acid solution for several days. Finally it was washed with deionized water and was dried by blowing hot air and then used for deposition.

Before supplying the compressed air, the heater was kept on for sometimes to attain the desired temperature. The air was then passed through the tube at a constant pressure. A fine aerosol in the form of cloud was produced in the flask. The aerosol was carried by the incoming air current to the reactor zone. On reaching the substrate surface, oxides of manganese were formed by the pyrolytic action on the surface of the substrate as deposits and the by-product gases were carried out by the exhausted fan.

Because of the reversibility in Eq. (1), the structure, composition, and thus the optical and electronic properties of MnO_2 films depend critically on many deposition parameters, i.e. temperature of the substrate, spray rate, deposition time, concentration of the solution, carrier air pressure, annealing temperature, spray outlet to substrate distances. In this present study, the effects on the film properties are investigated independently of sequence by changing one of these deposition variables while the others are kept unchanged. Moreover, the interdependency of the deposition variables on the properties of the films is also thoroughly investigated.

After setting the optimum deposition parameters, manganese dioxide films was deposited onto glass substrates. The as-deposited films did exhibit poor conductivity. To increase conduction, the films were heat-treated. Heat-treatments of these coatings changed the optical and electrical properties substantially. Heat-treatments were carried out in a vacuum at a constant temperature of 473 K for 2 h. The annealed films were then exhibited significant conductivity.

2.2. Measurement technique

Electrical conductivity σ was measured as a function of temperature in the 303–413 K ranges. The glass substrate was heated by a specially designed heater and the temperature was measured by a chromel–alumel thermocouple placed on the middle of the substrate. The conductivity was obtained by applying a d.c. 15 V bias across the film with lead contact and recording the current and voltage simultaneously by using a four-probe van-der-Pauw technique [19]. The thickness was measured by the Tolansky [20] interference method with an accuracy of ± 5 nm. Optical studies were carried out with Parkin–Elmar lambda-19, double beam spectrophotometer.

3. Results and discussion

3.1. Effect of substrate temperature

The substrate temperature T_s is the most important parameter in the pyrosol process. Fig. 2a and b show the dependency of thickness and resistivity, respectively, with substrate temperature T_s in the range of 563–623 K for a MnO_2 film prepared at a fixed spray rate 0.8 ml/min, solution concentration 0.8 M, and carrier air pressure 1.38×10^5 Pa. The deposition rate of the sample was 6.7 nm/min. It is noted in Fig. 2a that the film thickness increases to a peak value at $T_s = 593$ K and then its value slowly falls with T_s. The optimum thickness is obtained at a deposition of substrate temperature $T_s = 593$ K. Fig. 2b is a plot of resistivity vs. substrate temperature for a MnO_2 film of thickness 200 nm. It indicates the fall in resistivity with substrate temperature until it attains a minimum resistivity at $T_s = 593$ K and beyond this range its resistivity goes slowly up. It is, therefore, significant that substrate temperature plays a vital role in obtaining a conductive films at $T_s = 593$ K and the authors used $T_s = 593$ K in all deposition of MnO_2 films.

3.2. Effect of spray rate

In order to optimize the deposition parameters, a trial and error procedure was adopted in obtaining conductive and transparent films. In doing so, one of the variables was varied maintaining the others remained fixed. Fig. 3a and b show the variation of film thickness and resistivity with spray rate S_r, respectively, for a MnO_2 film which was deposited at a fixed deposition rate 6.7 nm/min, substrate temperature 593 K, solution concentration 0.8 M and carrier air pressure 1.38×10^5 Pa. It is noted that film thickness monotonously increases with S_r, and its value saturates at S_r of 0.8 ml/min. Fig. 3b is a plot of resistivity vs. spray rate for a MnO_2 film of thickness 200 nm. It is seen that the linear fall in

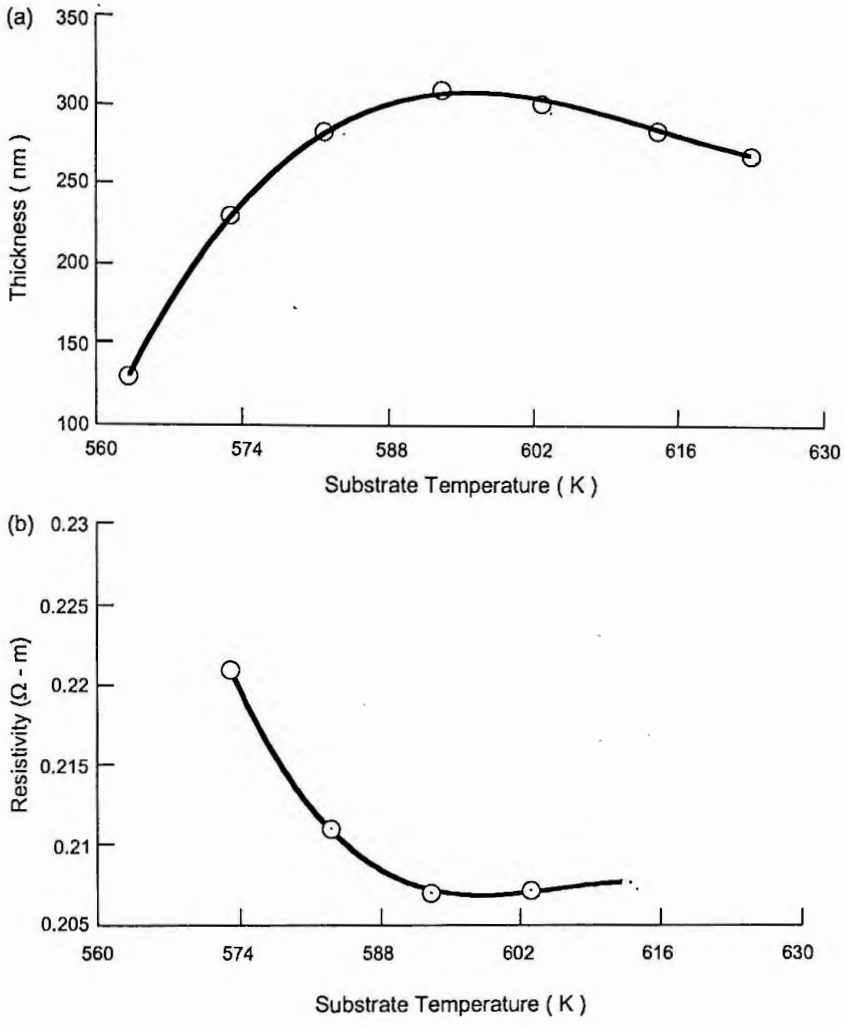

Fig. 2. Variation of (a) thickness, (b) resistivity vs. substrate temperature of MnO_2 films.

resistivity is observed up to a spray rate 0.8 ml/min after that its resistivity is increased with higher spray rate. So it indicates from the plots that minimum resistive film is obtained at a spray rate S_r of 0.8 ml/min. The film thickness increases with spray rate may be attributed to the structural characteristics of the films.

3.3. Effect of solution concentration

The variation of film thickness and resistivity of a MnO_2 film deposited at a fixed deposition rate 6.7 nm/min, the substrate temperature $T_s = 593$ K as a function of solution concentration are shown in Fig. 4a and b, respectively. Fig. 4a shows a monotonous increase of thickness with concentration and its saturation is attained within 0.7–0.9 M and the author used the concentration of 0.8 M in all depositions. This is quite natural, of

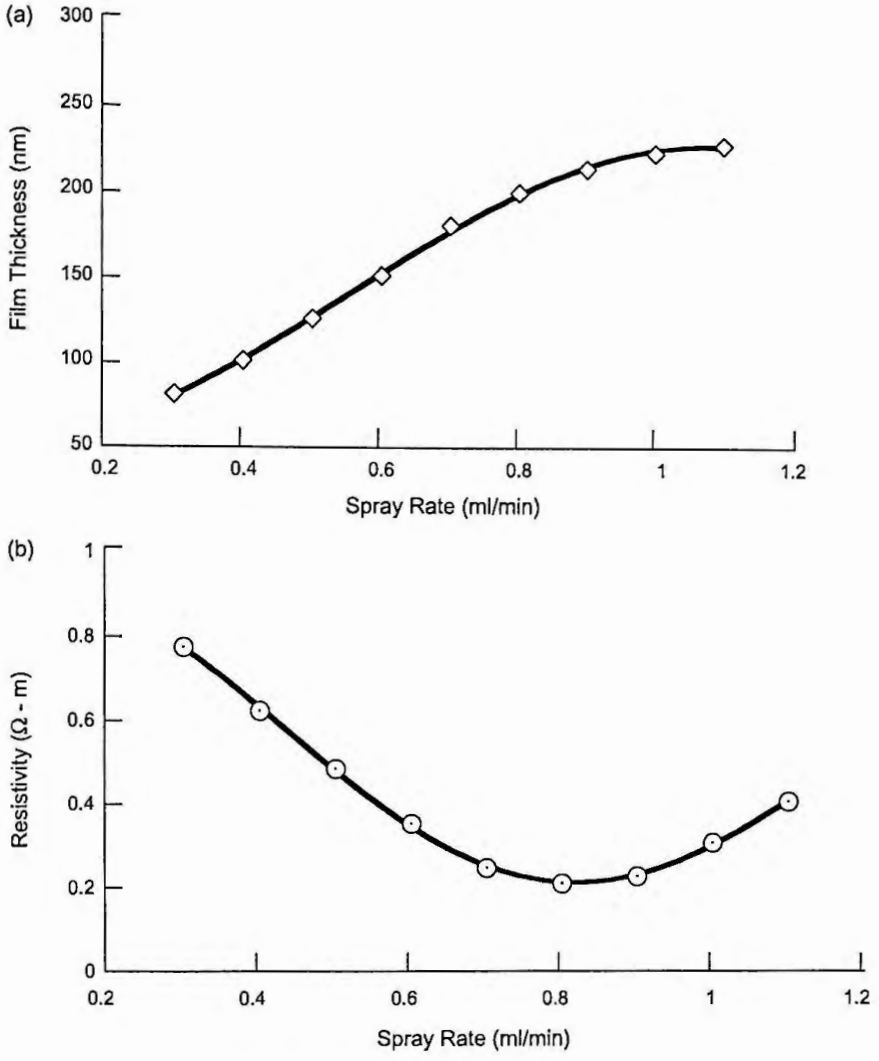

Fig. 3. Variation of (a) thickness, (b) resistivity vs. spray rate of MnO_2 films.

course up to a certain maximum limit, since an increasing supply of the reactant should increase the product accordingly. Fig. 4b represents a plot of resistivity vs. solution concentration for a MnO_2 film of thickness 200 nm. It indicates a fall in resistivity with increasing solution concentration and it attains a minimum resistivity at concentration of 0.8 M. Obviously, to optimize the deposition process, working solution concentration was maintained of 0.8 M in all deposition.

3.4. Effect of carrier air pressure

Compressed air was used as a carrier gas and maintaining its constant flow rate is very important. The dependency of film thickness and resistivity of the MnO_2 film prepared at

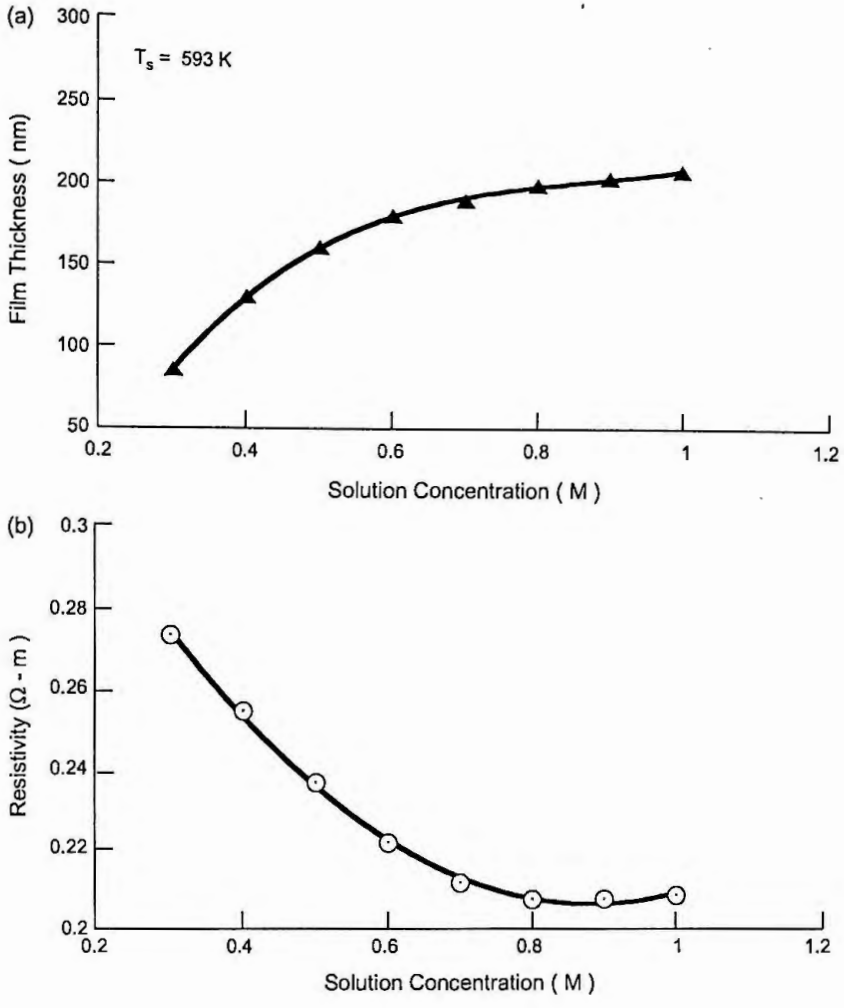

Fig. 4. Variation of (a) thickness, (b) resistivity vs. solution concentration of MnO_2 films.

$T_s = 593$ K, deposition rate 6.7 nm/min, spray rate 0.8 ml/min and solution concentration 0.8 M, as a function of carrier air pressure are shown in Fig. 5a and b, respectively. The decrease in resistivity with increasing carrier air pressure in Fig. 5b of a 200 nm MnO_2 film, shows a minimum resistivity at carrier air pressure 1.38×10^5 Pa, which also supports a saturation value of thickness in Fig. 5a of thickness vs. carrier air pressure plot. So the author used the 1.38×10^5 Pa pressure in all deposition of MnO_2 films.

3.5. Size effect

Variation of electrical conductivity σ with thickness t of MnO_2 films is shown in Fig. 6a. It is observed that the conductivity increases with thickness and attains a constant value of 6.5 $\Omega^{-1}\,m^{-1}$ at $t \approx 220$ nm. Since the conductivity does not depend on film

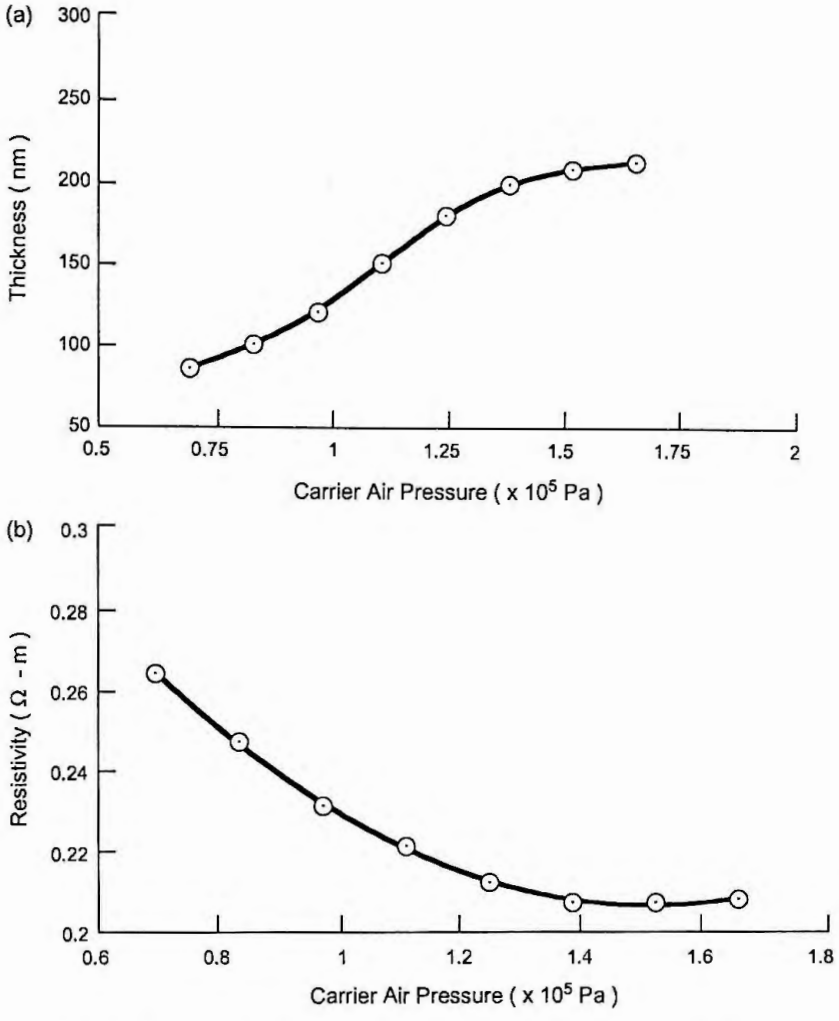

Fig. 5. Variation of (a) thickness, (b) resistivity vs. carrier air pressure of MnO_2 films.

thickness in the 220–320 nm, the current density should be uniform and therefore, the calculated values are considered to give the volume conductivity, but not the surface conductivity in this thickness range. The thickness dependence of conductivity is well in conformity with Fuchs–Sandheimer theory [21,22]. The conductivity decreases sharply below 160 nm, which is probably due to the discontinuous structure of the film.

3.6. Effect of heat-treatment

The as-deposited MnO_2 films show poor in electrical conduction and they were subjected to heat-treatment. After heat-treatment the films exhibit significant electrical conduction. Heat-treatment of the sample was carried out at four different temperatures. Fig. 6b shows the variation of resistivity ρ with annealing temperature T_a. It is seen from

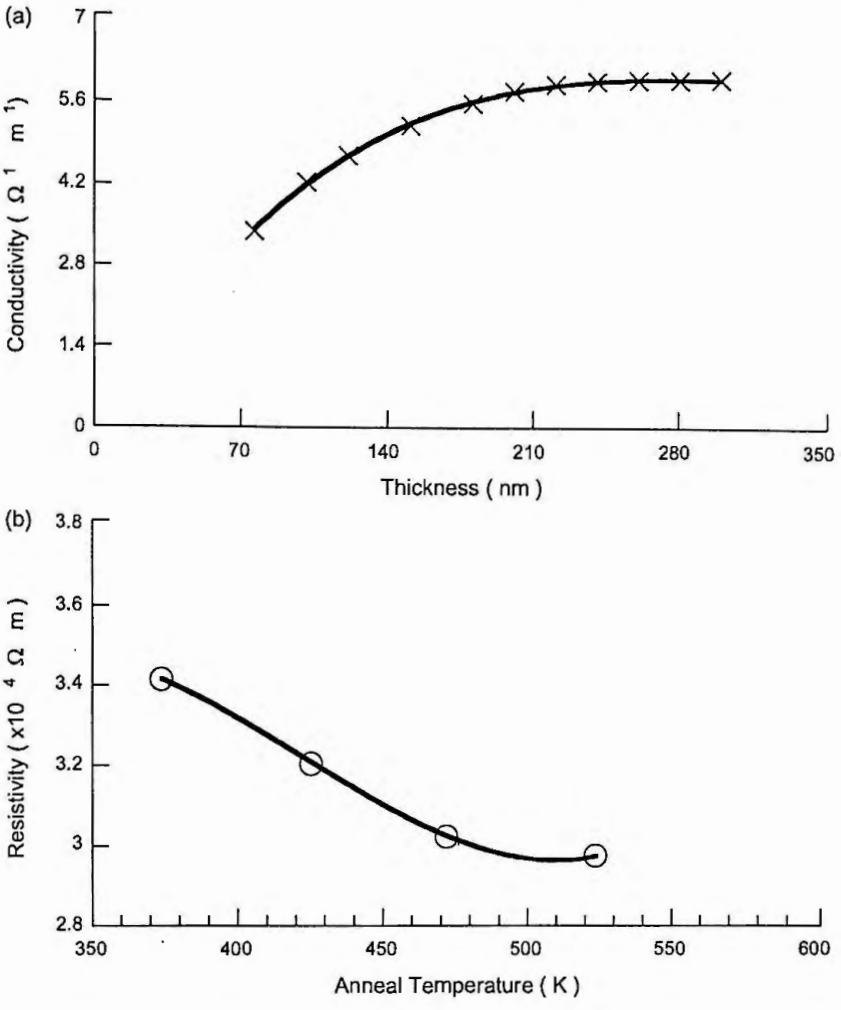

Fig. 6. Variation of (a) conductivity vs. thickness, (b) resistivity vs. annealed temperature of MnO_2 films.

the curve that resistivity decreases with the increase of annealing temperature up to $T_a = 523$ K and above this temperature, its resistivity remains constant. Therefore, all the MnO_2 films utilized in the study were annealed at $T_a = 473$ K.

3.7. Conductivity measurements

Fig. 7a reports the ln σ vs. $1/T$ curves for annealed MnO_2 films of thicknesses 100, 120, 160 and 200 nm, respectively. It is observed that the conductivity increases with temperature indicating semiconducting behavior. It is, however, interesting to point out that this behavior is not linear over the entire range of temperature. It is also seen that there is an anomaly in conductivity in the ln σ vs. $1/T$ curves at a particular temperature and this temperature is observed at 323 K. The anomaly in conductivity of author's work is noted

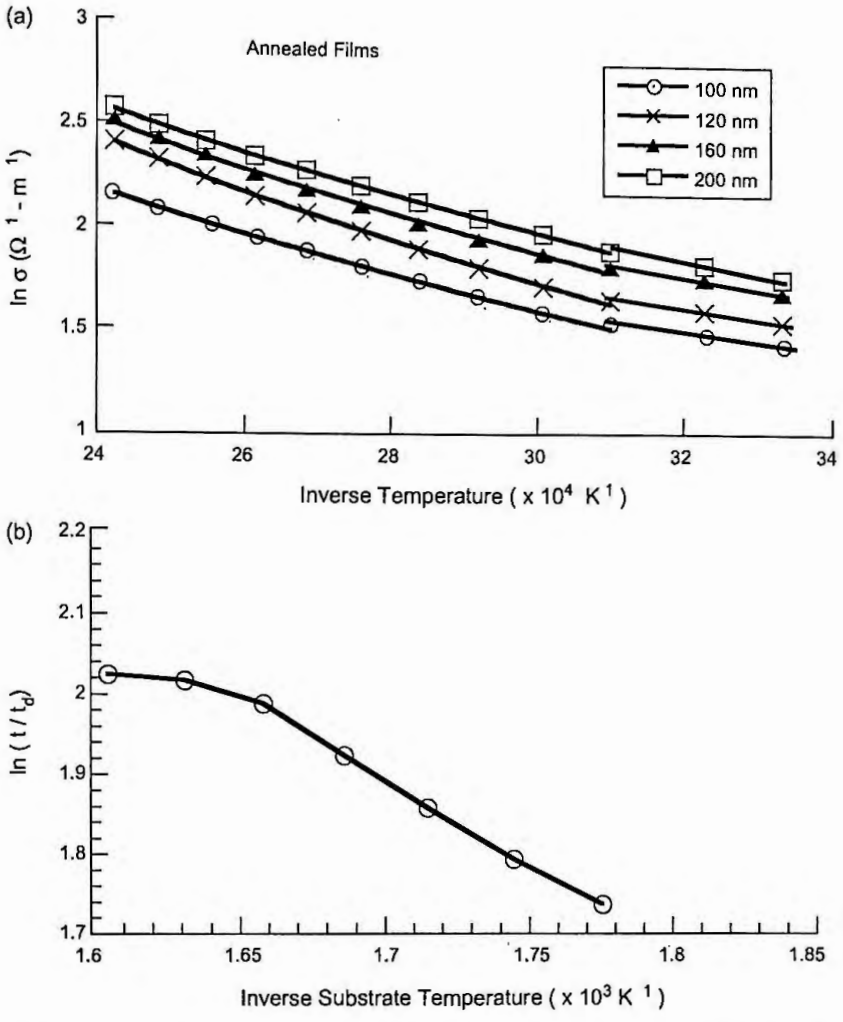

Fig. 7. (a) ln σ vs. inverse temperature curves for annealed MnO_2 films of different thicknesses, (b) ln (t/t_d) vs. inverse substrate temperature curve for as-deposited MnO_2 films.

both in as-deposited and annealed films, which is well agreed in reports of other workers [23–25]. This result suggests that MnO_2 becomes ferroelectric below the anomaly temperature. The evaluated value of the activation energy of the above four MnO_2 films in Fig. 7a is tabulated in Table 1.

It is seen that the activation energy for the four MnO_2 films are fairly low and is of the order of 0.14–0.27 eV. The increase of activation energy with decreasing film thickness above the anomaly temperature can be understood from island structure theory based on tunneling of charged carries between islands separated by a short distance [26].

The substrate temperature has a remarkable effect on the growth rate. The growth rate t/t_d, where t_d denotes the deposition time, a plot of the variation of growth rate ln (t/t_d) with inverse substrate temperature T_s is shown in Fig. 7b. The curve has a part of linear growth

Table 1
Activation energy evaluated for four annealed samples of MnO_2 films below and above anomaly temperature

Thickness (nm)	Activation energy below the anomaly (eV)	Activation energy above the anomaly (eV)
100	0.1390	0.2413
120	0.2510	0.2240
160	0.2612	0.2110
200	0.2711	0.2010

as well as a portion of flat growth region. The linear growth portion has a slope of activation energy of about 0.25 eV. The flat region indicates a temperature independent character at higher temperature. This phenomena indicates that in the lower temperature region the surface reaction in Eq. (1) is dominated by two factors, the temperature T_s and the rate of reactant supply, but at the higher temperature region the rate is so fast that the film growth rate becomes mostly dependent on the rate of reactant supply which was kept constant in the present study.

3.8. Thermoelectric power

The thermoelectric power measurement of MnO_2 films was carried out by the integral method [27] in the temperature range 300–450 K by taking pure metallic lead as reference metal. From the variation of thermoelectric power with inverse temperature, it is seen that the thermoelectric power increases linearly with the increase of temperature. The negative sign in the thermo e.m.f. measurements indicates that the carriers in the MnO_2 films are electrons and the films are n-type semiconductor.

3.9. Hall effect measurements

Hall effect studies were carried out by van-der-Pauw's [19] technique in the substrate temperature T_s of 573–613 K ranges. The Hall mobility μ and carrier concentration n with substrate temperature T_s of the heat-treated MnO_2 films of thickness 200 nm are 1.057 $cm^2\ V^{-1}\ S^{-1}$ and $4\times10^{19}\ cm^{-3}$, respectively [24]. It is seen that both μ and n have maximum at T_s of 593 K. All of the films studied for Hall effect measurements were found to show n-type conductivity. In as-deposited films, however, it was very difficult to observe any appreciable Hall voltage.

3.10. Optical studies

Spectral transmittance $T(\lambda)$ and near normal reflectance $R(\lambda)$ were measured at wavelength $0.3<\lambda<2.5$ μm using a Perkin–Elmer lambda-19 double beam spectrophotometer. Fig. 8a shows the spectral transmittance/reflectance vs. wavelength spectra for a 200 nm annealed MnO_2 film. It is seen that the transmittance curve exhibits a significant transmittance in the visible as well as in the infrared region. The reflectance spectrum, however, shows a low reflectance in the entire wavelength region.

From the above transmittance data, the optical band gap E_g has been graphically determined from the $(\eta h\nu)^n$ vs. $h\nu$ plots, where $(\eta h\nu)^n$ indicates optical absorption,

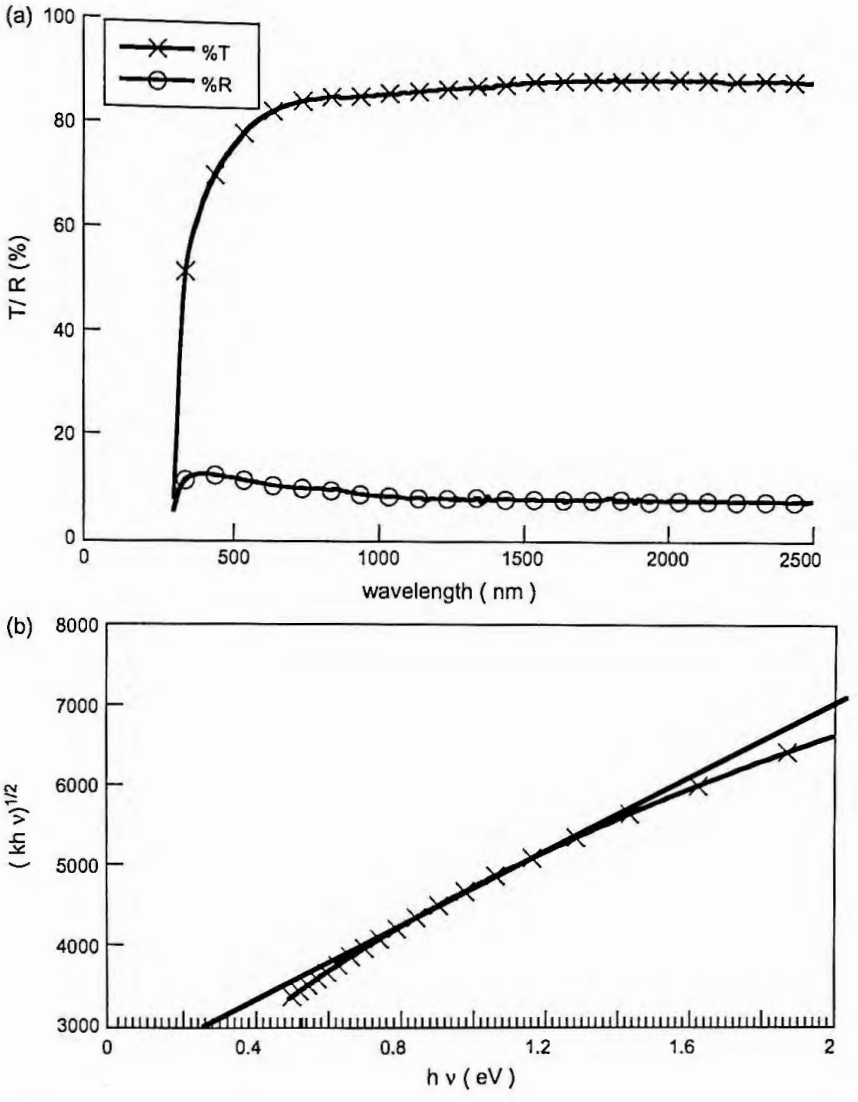

Fig. 8. (a) Optical spectra vs. wavelength, (b) $(khv)^{1/2}$ vs. photon energy plot for a annealed MnO_2 film of thickness 200 nm.

n represents the nature of transition. The plot indicates that the transition is an allowed indirect type with a band gap at $E_g = 0.26$ eV. To make a meaningful comparison of band gap, the authors did a similar calculation by Hall effect measurements. It is known that variation of Hall co-efficient R_H with temperature at various thicknesses of Hall samples are given a straight line. From the slope of ln R_H vs. T^{-1} plot, the band gap E_g was obtained at 0.26 eV for MnO_2 film of thickness 200 nm. The value of band gap E_g in both electrical and optical method obtained by author's work is an excellent agreement with the reported value of band gap by other works [23,24,28]. The high value of transmittance

coupled with low reflectance in the entire wavelength range of MnO_2 films may, therefore, be of importance of this material in particular selective surface application.

4. Conclusion

Various deposition parameters have remarkable effects on spray deposited MnO_2 thin film on glass substrate when prepared by the technique described in this article. Electrical conductivity measurements show an anomaly in conductivity at a temperature of 323 K, which agrees well with previous reports of other workers [23–25]. The thickness dependency of resistivity follows Fuchs–Sondheimer size effect theory [21,22]. The nature of the carrier as determined from thermoelectric measurement is in agreement with the Hall effect measurement and the film is a n-type semiconductor. Optical studies in the entire wavelength $0.3 < \lambda; < 2.5$ μm range exhibit high transmittance in the visible as well as in the infrared region. Author's study of band gap determination from optical and electrical data does agree well the value of band gap by other workers [23,24,28]. The low value of reflectance in the entire wavelength range is a potential advantage in using of this material in reflective coating applications.

Acknowledgements

One of us, A.K.M. Farid ul Islam is indebted to the Ministry of Education, Govt of Bangladesh for providing the study leave during this work. He is also grateful to UGC Bangladesh for providing fellowship during this period.

References

[1] Komaba S, Kumagai N, Baba M, Miura F, Fujita N, Groult H, et al. Preparation of Li–Mn–O thin films by r.f. sputtering method and its application to rechargeable batteries. J Appl Electrochem 2000;30(10): 1179–82.

[2] de Torresi Cordoba, Susana I, Gorenstein Annerre. Electrochromic properties of MnO_2 thin films. In: Hugot-Le Goff Anne, Granqvist Claes G, Lampert Carl M, editors. Proc SPIE. Optical materials technology for energy efficiency and solar energy conversion XI: chromogenics for smart windows, vol. 1728, 1992. p. 92–102.

[3] Kozawa A. Lithum–MnO_2 cells containing CF_x or C_2F in the cathode. J Electrochem Soc 1987;134(4): 780–91.

[4] Raj IA, Vane KI. Characterization of electrolytic MnO_2 based oxygen electrodes for alkaline water electro layer/fuel cell reactions. Int J Hydro Energy 1990;15(10):751–6.

[5] Bhide VG, Damle RV, Dani RH. Dielectric hysteresis in pyrolusite. Physica (Utrecht) 1959;25:579–80.

[6] Koops CG. On the dispersion of resistivity and dielectric constant of some semiconductors at audio frequencies. Phy Rev 1951;83(1):121–4.

[7] Rizzi GA, Zanoni R, Disiro S, Perrillo L, Granozzi G. Epitaxial growth of MnO nanoparticles on Pt(111) by reactive deposition of Mn-2 (CO)(10). Surf Sci 2000;462(1–3):187–94.

[8] Gassa LM, Mishima HT, Lopez de mishima BA, Vilche JR. An electrical impedance spectroscopy study of electrodeposited manganese oxide films in borate buffers. Electrochimica Acta 1997;42(11):1717–23.

[9] Chigane M, Ishikawa M, Izaki M. Prepration of manganese oxide thin films by electrolysis/chemical deposition and electrochromism. J Electrochem Soc 2001;148(7):D96–D101.
[10] Guo LW, Peng DL, Makino H, Hanada T, Hong SK, Sumiyama K, et al. Structural characteristics and magnetic properties of MnO_2 films grown by plasma-assisted molecular beam epitaxy. J Appl Phys 2001;90: 351–4.
[11] Fau P, Bonino JP, Rousset A. Electrical properties of sputtered MnO_2 thin films. Appl Surf Sci 1994;78(2): 203.
[12] Segal SR, Cao LX, Suib SL, Tang X, Satyapal S. Thermal decomposition of dimethyl methylphosphonate over manganese oxide catalysts. J Catal 2001;198(1):66–8.
[13] Long JW, Qadir LR, Stroud RM, Rolison DR. Spectroelectrochemical investigations of cation-insertion reactions at sol–gel derived nanostructured, mesoporous thin films of manganese oxide. J Phyl Chem B 2001;105(37):8712–7.
[14] Minami T, Shirai T, Nakatani T, Miyata T. Electroluminescent devices with Ga_2O_3: Mn thin films emitting layer prepared by sol–gel process. Jpn J Appl Phys, Part-2 Lett 2000;39(6A):L524–L6.
[15] Radhakrishnan R, Oyama ST, Chen JGG, Asakura K. Electron transfer effects in ozone decomposition on supported manganese oxide. J Phyl Chem B 2001;105(19):4245–53.
[16] Erlandsson O, Lindvall J, Ngoc T, Van H, Nang D. Electrochromic properties of manganese oxide (MnO_x) thin films made by electron beam deposition. Proc SPIE 1993;2017:182–93.
[17] Tang WP, Hanoh HT, Yang J, Ooi K. Preparation of plate-form manganese oxide by selective lithium extraction from monoclinic Li_2MnO_3 under hydrothermal conditions. Chem Mater 2000;12(11):3271–9.
[18] Islam MN, Hakim MO. A simple technique for the pyrosol process and deposition of tin oxide films. J Phys Chem Solids 1986;46:339–43.
[19] Chopra KL. Thickness measurement and analytical techniques. Thin films phenomena. New York: McGraw-Hill; 1969 p. 85.
[20] Tolnasky S. Multiple beam interferometry of surface and films. London: Oxford University Press; 1948.
[21] Fuschs K. Electron transport phenomena in metal films. In: Chopra KL, editor. Thin films phenomena. New York: McGraw-Hill; 1969. p. 346.
[22] Sondhemier EH. Adv Phys 1952.
[23] Rhide VG, Damle RV. Dielectric properties of manganese dioxide partI. Physica (Utrecht) 1960;26:33–42.
[24] Rhide VG, Dani RH. Electrical conductivity in oxides of manganese and related compounds. Physica (Utrecht) 1961;27:821–6.
[25] Mallick AK, Khan KA. Pressure effect on the electrical properties of manganese dioxide thin films. Phys Stat Sol(a) 1994;142:409.
[26] Neugebauer CA. In: Hass G, Thun RE, editors. Physics of thin films, vol. 2. New York: Academic Press; 1970. p. 1.
[27] Das VD, Mohanty JC. Size and temperature effects on thermoelectric power of β-tin thin films. J Appl Phys 1983;54(2):977–81.
[28] Chevillot JP, Brenet J. Influence of foreign ions on the semiconductivity of dioxide of manganese. CR Acad Sic (Paris) 1959;248(6):776–8.

PAPER

II

JOURNAL OF MATERIALS SCIENCE: MATERIALS IN ELECTRONICS 16 (2005) 203–207

Studies on the thermoelectric effect in semiconducting MnO_2 thin films

A. K. M. FARID UL ISLAM, R. ISLAM, K. A. KHAN*
Department of Applied Physics and Electronics, University of Rajshahi, Rajshahi-6205, Bangladesh
E-mail: kakhan_ru@yahoo.ca

The thermoelectric power of MnO_2 thin films prepared by pyrolytic technique has been measured from room temperature up to 423 K with reference to pure lead. The thickness and temperature dependence of its related parameters have been studied. The Fermi levels were determined using a non-degenerate semiconducting model. The carrier scattering index, activation energy and temperature coefficient of activation energy have all been obtained at different ranges of thickness and temperature. All the samples were optically transparent and polycrystalline in structure.

1. Introduction

Manganese dioxide is a low band gap, high optical constant semiconductor that exhibits ferroelectric properties [1, 2]. This material has in recent years had a variety of applications, particularly as an electrode, in electrochemical and electrochromic batteries, in fuel cells as well as in energy efficient device applications [3–5]. Like most of the pure oxide crystals, undoped MnO_2 is normally an electrical insulator. But its electrical conductivity as practically observed is due to the presence of many crystal defects such as a stoichiometric excess or deficiency of vacancies introduced in the sample during the process of sample preparation [6]. Usually MnO_2 is a transparent semiconductor with an *n*-type carrier in conduction.

Thermoelectric power (TEP) is the most sensitive quantity to any change or distortion of the Fermi-surface in the material; a measurement of TEP would be a useful option for investigating the electronic conduction process in such a sample. Reports in literature indicate that manganese dioxide thin films have been produced by a number of techniques by many researchers [3–5, 7]. It also has a report on manganese nitrate based pyrolysed bulk MnO_2 materials [8]. In this study we used the modified spray pyrolysis process [9] to deposit MnO_2 films of desired thickness and discuss some of the results of the measurement of TEP in MnO_2 thin films. Although there have been a number of investigation on the electrical, optical and electrochromic properties of the films, no systematic study appears to have been done on the thermoelectric properties of MnO_2 films by spray pyrolysis technique at varying deposition condition which stimulates the authors to study the TEP properties of the material.

2. Experimental

With 0.8 M aqueous solution of manganese acetate, $Mn(C_2H_3O_2)_2 \cdot 4H_2O$, in Pyrex flask, an aerosol is prepared using a pneumatic spray gun and compressed air. The aerosol is then carried to the pyrolysis section by the same in-flowing air. In this section, a heater is situated, over which a substrate is placed on a thick stainless steel platform. When the reacting aerosol reaches the substrate surface, pyrolysis of the manganese acetate takes place and MnO_2 is formed as a thin film on the glass substrate. The probable reactions include:

$$Mn(C_2H_3O_2)_2 \cdot 4H_2O + H_2O \xrightarrow{heat} MnO_2 + 2CH_3COOH + 3H_2O + H_2 \quad (1)$$

The substrate temperature was ~593 K and was kept constant for the present set of samples. Details of the film deposition process were reported for ZnO films [10].

All the samples were then annealed at a constant temperature at 473 K for 2 hr before using for any measurements. The annealing was necessary because the as-deposited samples were of high order of resistivity. For TEP measurements pure lead was used as reference metal and a thick lead film was deposited on the substrate by thermal evaporation of metallic lead, which is shown in Fig. 1. During pyrolysis two films were prepared in a single run, one for thickness, conductivity and Hall effect studies, and the other for TEP measurement. An appropriate masking arrangement gives the proper shape of the experimental sample. The film thickness was determined by the Tolansky interferometric method [11]. These films were non-stoichiometric and were highly transparent onto glass

* Author to whom all correspondence should be addressed.

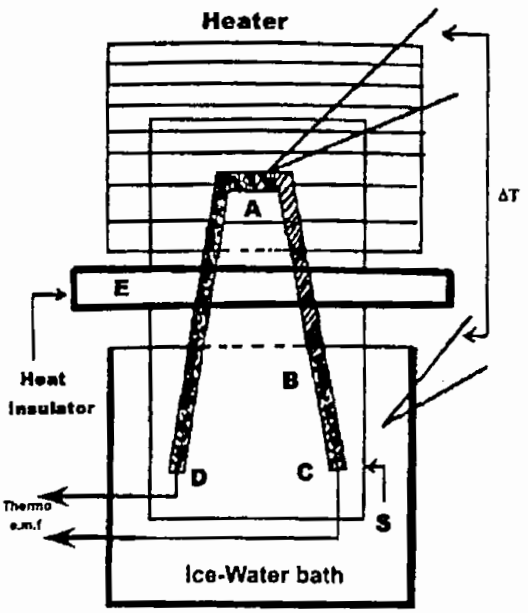

Figure 1 Schematic diagram of thermopower measuring apparatus: AB, MnO_2 film; DA and BC, lead films; S, substrate; E, heat insulating barrier; ΔT is the temperature difference between hot and cold ends.

substrates. Films were of 160 to 250 nm in thicknesses. The electrical conductivity and Hall effect study were done by van der Pauw method [11]. Measurement of TEP was carried out by the integral method [12], in which junction A was heated by a flat nichrome strip heater with regulated power supply to keep it at different temperature. The other junction B, was immersed in an ice-water bath of constant (273 K) temperature. The temperature of the hot junction was measured using a chromel-alumel thermocouple attached to the sample. The generated thermo e.m.f. was recorded using a 614 Keithley digital electrometer. The hot and cold junctions were kept thermally isolated by inserting an insulated barrier between the junctions. The immersed portion of the film was kept electrically insulated to remove any leakage of e.m.f. between D and C due to contact with the ice-water. The whole apparatus was kept in a suitable enclosure to minimize any air current disturbances. The temperature of the hot junction was raised slowly from room temperature, with a regular interval of 10 K. The thermo e.m.f. was noted up to the highest temperature of 423 K.

3. Results and discussion

Fig. 2 shows the value of thermo e.m.f. at different temperatures for four samples of thickness 160, 200, 220 and 250 nm, respectively. It is observed that the thermo e.m.f. is negative with respect to lead. The plots indicate a linear decrease in thermo e.m.f. with increasing temperature. Fig. 3 shows the variation of the corresponding thermoelectric power, Q, with inverse temperature, $1/T$. It is observed from this figure that the thermoelectric power decreases continuously with increasing temperature and saturates at higher temperature region. The rate of change of Q with temperature is higher for

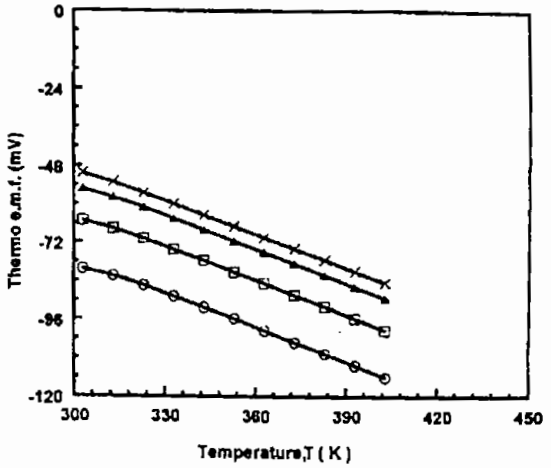

Figure 2 Variation of thermo e.m.f. with temperature of MnO_2 films of different thickness: (○) 160 nm, (□) 200 nm, (▲) 220 nm, (×) 250 nm.

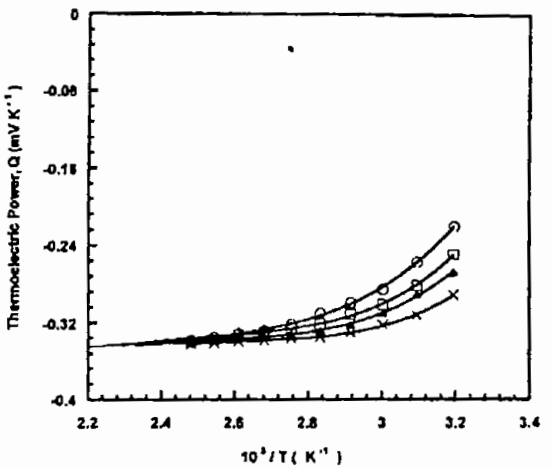

Figure 3 The plot of thermopower, Q, vs. inverse of temperature, $1/T$, of MnO_2 films of various thicknesses: (○) 160 nm, (□) 200 nm, (▲) 220 nm, (×) 250 nm.

films of higher thickness than that of lower ones. At a fixed temperature the variation of thermo power with film thickness is shown in Fig. 4. This figure represents the variation of thermo power of MnO_2 films as a function of thickness at three different temperatures of 313, 333 and 413 K, respectively. It indicates that at lower temperature it has thickness dependence while it is thickness independent in higher temperature.

The author's sample of Hall effect measurement yields the carrier concentration, n, of MnO_2 films of the order of 4.7×10^{25} to 8.4×10^{25} m^{-3} and it is of n-type carrier. So, it is logical to employ a nondegenerate model to analyze the thermoelectric power data. For a nondegenerate n type crystalline semiconductor with spherical constant energy surface under thermal equilibrium, the thermoelectric power is given by [13]

$$Q = -\frac{k_B}{e}\left(\frac{E_c - E_F}{k_B T} + A\right) \qquad (2)$$

where K_B is the Boltzmann constant and E_c is the energy of conduction band edge; A is a constant that

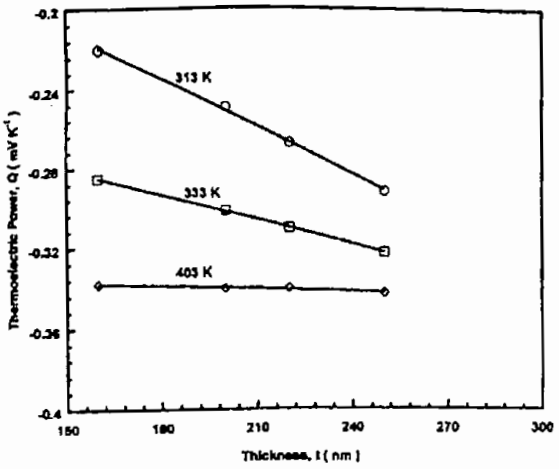

Figure 4 The variation of thermopower of MnO_2 film as a function of thickness, t, at three different temperatures. (○) 313 K, (□) 333 K, (▲) 403 K.

depends on the nature of the scattering process. Normally, for a material like a Fermi glass, A runs between 2 and 4. If energy is measured with respect to the bottom of the conduction band, then Equation 2 reduces to

$$Q = -\frac{k_B}{e}\left(A - \frac{E_F}{k_B T}\right) \tag{3}$$

where E_F is the position of Fermi level in the band gap. Harry *et al.* [14] have pointed out that $A = (5/2) - r$, where r corresponds to the scattering index and is equal to -0.5 for piezoelectric scattering and -1.5 for ionized impurity scattering. Thus $A = 3$ for piezoelectric scattering and 4 for ionized impurity scattering. From Equation 2 it is clear that A corresponds to a value of the thermopower at infinite temperature limit.

From Fig. 3 the extrapolated tangent curves at the higher temperature (above 350 K) region give a common intercept at the ordinate $Q = 0.345$ mV/K. Putting this value of Q in Equation 3 the value of A has been obtained as 4.003. This value corresponds to the scattering index ≈ -1.5 and is an indication that ionized impurity scattering is dominant in these MnO_2 films. This is a signature of ionized impurity scattering, which is well verified by other workers [8].

In all of the author's samples it has been found that $E_c - E_F$ varies with temperature, T, and it can be assumed that for a limited temperature range [13]:

$$E_c - E_F = E_0 - \gamma T \tag{4}$$

where E_0 is the low -temperature limit of $E_c - E_F$ and corresponds to the activation energy equivalent to the band gap, γ is the temperature coefficient of activation energy. Putting Equation 4 into Equation 2

$$Q = -\frac{E_0}{eT} + \left(\frac{\gamma}{e} - \frac{Ak_B}{e}\right). \tag{5}$$

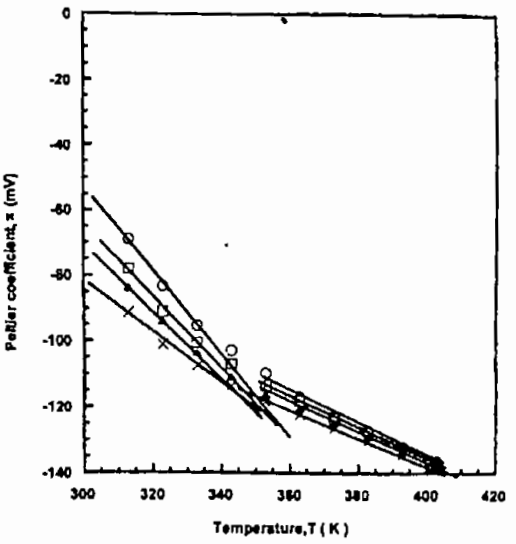

Figure 5 The plot of Peltier coefficient, π, versus temperature, T, of MnO_2 films of various thicknesses. (○) 160 nm, (□) 200 nm, (▲) 220 nm, (×) 250 nm.

Now, the Peltier coefficient $\pi = QT$, is given by

$$\pi = -\frac{E_0}{e} + \left(\frac{\gamma}{e} - \frac{Ak_B}{e}\right)T. \tag{6}$$

This equation shows that a π versus T plot should yield a straight line and the value of γ can be obtained from its slope. Fig. 5 shows such plots and it is observed that the slopes at room and at high temperature (above 350 K), regions are different. Both slopes have been determined and using $A = 4.0$, various values of γ were calculated for films of different thickness. These values of γ are plotted as a function of thickness in Fig. 6. It shows that at the higher temperatures (above 350 K), γ is almost thickness independent, while in the room-temperature limit; it shows strong thickness dependence.

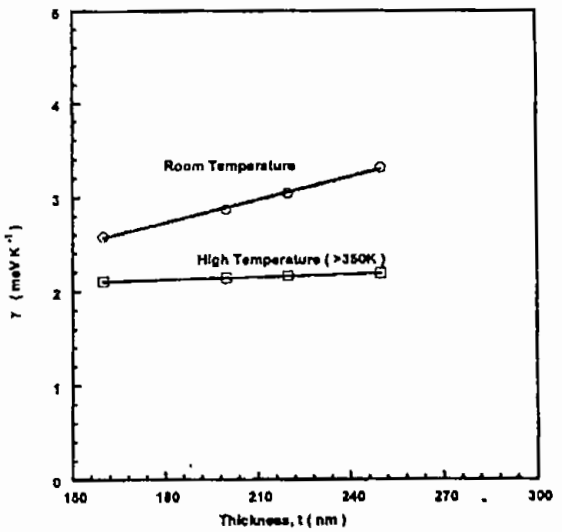

Figure 6 The variation of temperature coefficient of activation energy, γ, as a function of thickness, t, of MnO_2 thin films at room temperature and at high temperature (above 350 K).

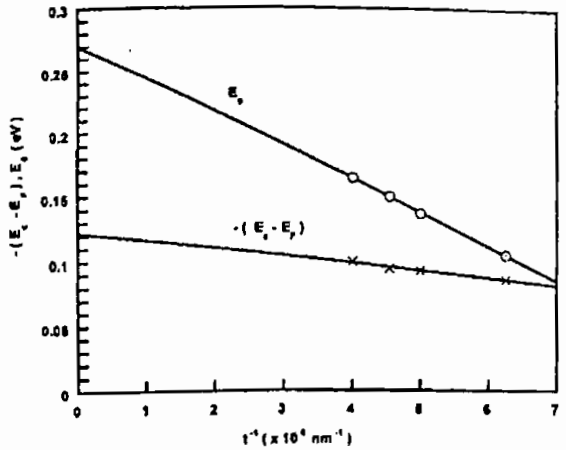

Figure 7 The variation of E_0 and $-(E_C - E_F)$ with inverse thickness, $1/t$, of MnO_2 thin films.

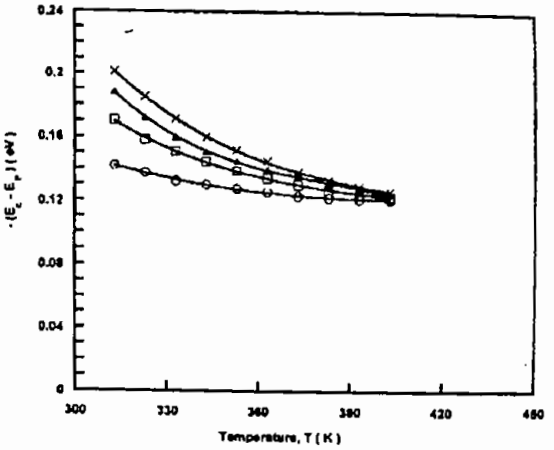

Figure 8 The plot of Fermi-level as a function of temperature of MnO_2 films of different thicknesses: (○) 160 nm, (□) 200 nm, (▲) 220 nm, (×) 250 nm.

Using these values of γ at room temperature, the values of E_0 for the different film thickness may be calculated from Equation 6 and the values of $E_c - E_F$ from Equation 4. The variation of E_0 and of $E_c - E_F$ at room temperature as a function of inverse film thickness, $1/t$, is shown in Fig. 7. In this figure it is observed that E_0 has fair thickness dependence and its bulk value corresponding to $1/t = 0$, is 0.27 eV. This value agrees well with the band gap of MnO_2 crystal (0.28 and 0.26 eV, respectively) as reported previously [15, 16]. In extrinsic samples, the variation of E_0 with film thickness is obvious. E_0, which is calculated from Equation 4, is some type of thermal activation energy and depends on the detailed variations of the pattern of conduction and valence edges with the structure of the film, including various defects. This is not necessarily a vertical transition. But the optical band gap, E_g corresponds to the optical absorption at some frequency and involves mostly vertical transitions between the bands. Thus the variation of E_g with thickness is not so straightforward as for E_0. In this case, of course, carrier concentration plays an important role.

In the high-temperature region, the thermo power saturates for all the samples (Figs. 3 and 4), it suggests that the Fermi-levels in these films are pinned near the band edge at higher temperature. This is now shown in Fig. 8 where this pinning can be clearly observed. The gradual decrease of thermo power with temperature also is shown in Fig. 3. In thin film samples when the material behaves like a Fermi-glass, this type of variation is usual [13]. We obtain some idea about this variation by differentiating Equation 2 with respect to temperature, which yields,

$$\frac{dQ}{dT} = -\frac{k_B}{e}\left[\frac{d(E_c - E_F)}{k_B T dT} - \left(\frac{E_c - E_F}{k_B T^2}\right) + \frac{dA}{dT}\right] \tag{7}$$

From Fig. 8 it is observed that $-(E_c - E_F)$ decrease with temperature so that in the brackets the 1st term of Equation 7 is positive. The second term is also positive because $(E_c - E_F)$ is negative and we have already ignored any possible temperature variation of A as it corresponds to the higher temperature limit of thermo power. Thus the whole term in brackets is positive and hence $\frac{dQ}{dT}$ is negative, which suggests a decrease of thermopower with temperature. The minimum value of $-(E_c - E_F)$ as obtained from Fig. 8 is 0.125 eV and is almost five times that of $k_B T$ at room temperature. Thus our previous consideration of a non-degenerate model to explain the thermopower data is justified.

4. Conclusion

Thermopower in spray-deposited non-stoichiometric MnO_2 thin films shows a thickness as well as temperature dependence. The Fermi-levels are found to show a gradual pinning mode near the band edge with increasing temperature. An annealed as well as the as-deposited samples shows an *n*-type thermopower which supports also in Hall effect data.

In general the transport properties in these samples are controlled mainly by the ionized impurity scattering process corresponding to a scattering index of -1.5 obtained from thermopower data. Film thicknesses also have a remarkable effect on the activation energy, E_0 and on the temperature coefficient of activation energy, γ. In the room temperature region, γ has strong thickness dependence while it is almost thickness independent in the high-temperature region.

Acknowledgement

One of us A.K.M. Farid ul Islam is indebted to the Ministry of Education, Govt. of Bangladesh for providing the study leave during this work. He is also grateful to U.G.C. Dhaka, Bangladesh for providing fellowship during this period.

References

1. V. G. BHIDE, R. V. DAMLE and R. H. DANI, *Physica (Utrecht)* 25 (1959) 579.
2. C. G. KOOPS, *Phy. Rev.* 83 (1951) 121.
3. C. DE TORRESI, I. SUSANA and A. GORENSTEIN, *Proc SPIE.* 92 (1992) 1728," Optical Materials Technology for

Energy Efficient and Solar Energy Conversion XI, Chromagenics for Smart Windows," edited by A. Hugot- le Goff, C.G. Granqvist and C.M. Lampert.
4. S. KOMABA, N. KUMAGAI, M. BABA, F. MIURA, N. FUJITA, H. GROULT, D. DEVILLIERS and B. KAPLAN, *J. Appl. Electrochem.* 30 (2000) 1179.
5. M. CHIGANE, M. ISHIKAWA and M. IZSAKI *ibid* 1481 (2001) 96.
6. R. M. VALLETTA and W. A. PLISKIN, *N. J. Electrochem. Soc.* 114 (1967) 944.
7. A. K. MALLICK and K. A. KHAN, *Phys. Stat. Soli. (a)* 142 (1994) 409.
8. P. H. KLOSE, *J. Electochem. Soc.* 117 (1970) 854.
9. M. N. ISLAM and M. O. HAKIM, *J. Phys. Chem. Solids* 46 (1986) 339.
10. *Idem*, *J. Mater. Sci.* 22 (1987) 1379.
11. K. L. CHOPRA, in "Thin Films Phenomena" (McGraw-Hill Publ. Co. New York 1969) p. 83.
12. V. D. DAS and J. C. MOHANTY, *J. Appl. Phys.* 54 (1983) 977.
13. N. F. MOTT and E. A. DAVIS, in "Electronic Process in Non-Crystalline Materials," 2nd edn. (Clarendon Press, Oxford, 1979).
14. H. HARRY, B. KWOK and R. H. BUBE, *J. Appl. Phys.* 44 (1973) 138.
15. R. DRUILHE and J. P. SUCHET, *Czech. J. Phys. B* 17 (1967) 337.
16. J. P. CHEVILLOT and J. BRENET, *C.R. Acad. Sci (Paris).* 248 (1959) 776.

Received 8 July
and accepted 21 November 2004

PAPER III

THE 9th ASIA PACIFIC PHYSICS CONFERENCE

9th APPC

Hanoi, October 25-31, 2004

9thAPPC
Hanoi-2004

AAPPS
Association of Asia Pacific Physical Societies

MOST
Ministry of Science and Technology

VAST
Vietnamese Academy of Science and Technology

and

VPS
Vietnam Physical Society

Website: www.ims.ac.vn/appc03

Effects of Deposition Variables on Spary-Deposited MnO_2 Thin Films Prepared from $Mn(C_2 H_3 O_2)_2$ for Applications in Selective Surface.

A.K.M. Farid ul Islam R. Islam and K.A. Khan*

Department of Applied Physics and Electronics.
University of Rajshahi. Rajshahi-6205, Bangladesh.

* Corresponding Address: Tel. 880-721-750254(Res.)
Fax: 880-721-750064 Email: kakhan_ru@yahoo.ca

Abstract- Undoped MnO_2 thin films have been prepared by a modified spray pyrolysis technique under various deposition conditions and the effects of different variables on electrical and optical properties have been studied in detail. It is found that substrate temperature, spray rate, solution concentration, carrier air pressure and post deposition heat-treatment, spray outlet to substrate distance play important role in obtaining optimum films.

Electrical conductivity study shows an anomaly in conductivity at a temperature 323K and its thickness dependent resistivity follows Fuchs-Sondheimer theory. The Hall effect and thermoelectric studies indicate that the deposited sample is an n-type semiconductor. Optical study in the entire wavelength 0.3 – 2.5μm range exhibits a high transmittance in the visible as well as in the near infrared. Calculation from optical data, the sample exhibits a band gap at 0.26eV, which also supports the value obtained from the Hall effect study. These studies may be of importance for the applications of this material in energy efficient surface coating devices.

1. Introduction

Literature reports indicate that thin films of manganese dioxide have been produced by a number of techniques by many researchers[1,2]. Although there have been a number of investigation on the electrical, optical and electrochromic properties of the films [1,2], no systematic study appears to have been done on electrical and optical properties at varying deposition conditions. In this paper, we present and discuss the effect of deposition variables in the production of manganese dioxide films by a simple spray pyrolysis technique and to study the physical properties of the films.

2.Experimental

Undoped MnO_2 thin films were prepared from a solution of $Mn_2(C_2H_3O_2)_2.4H_2O$ onto glass substrates at various thicknesses by modified spray pyrolysis techniques. The basic reaction involved in the process is:

$$Mn(C_2H_3O_2)_2.4H_2O + H_2O \leftrightarrow MnO_2 + 2CH_3COOH + 3H_2O + H_2$$

The optimum deposition parameters are the followings:

(a) Substrate temperature T_s =593K
(b) Spray rate S_r = 0.8 ml/min
(c) Solution concentration C = 0.8M
(d) Carrier air pressure $P_a = 1.38 \times 10^5$ Pa
(e) Substrate to spray outlet distance d_s = 0.05 m
(f) Anneal temperature T_a = 473K

3.Result and Discussion

3.1. *Size effect*

Variation of electrical conductivity σ with thickness t of MnO_2 films is shown in Figure 1. It is observed that the conductivity increases with thickness and attains a constant value of 6.5 Ω^{-1}-m^{-1} at t ≈ 220 nm. The thickness dependence of conductivity is well in conformity with Fuchs-Sandheimer theory [3, 4]. The conductivity decreases sharply below 160 nm, which is probably due to the discontinuous structure of the film.

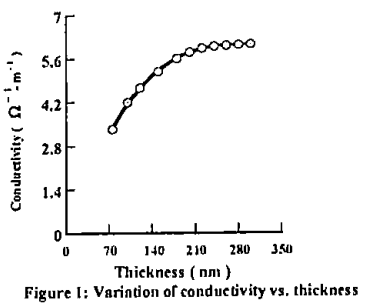

Figure 1: Variation of conductivity vs. thickness

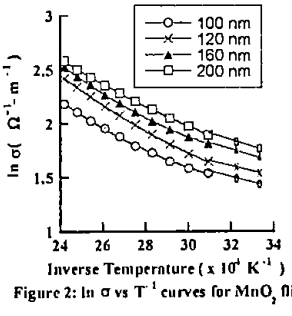

Figure 2: ln σ vs T^{-1} curves for MnO_2 films.

3.2. *Conductivity measurements*

Figure 2 reports the lnσ versus 1/T curves for annealed MnO_2 films of thickness 100, 120, 160 and 200nm, respectively. It

is observed that the conductivity increases with temperature indicating semiconducting behavior. It is, however, interesting to point out that this behavior is not linear over the entire range of temperature. It is also seen that there is an anomaly in conductivity in the ln σ versus 1/T curves at a particular temperature and this temperature is observed at 323 K. The anomaly in conductivity of author's work is noted both in as-deposited and annealed films, which is well agreed in reports of other workers [5,6]. This result suggests that MnO_2 becomes ferroelectrics below the anomaly temperature.

3.3 *Optical studies*

Figure 3 shows the spectral transmittance/reflectance versus wavelength curves for a 200 nm annealed MnO_2 film. It is seen that the transmittance curve exhibits a significant transmittance in the visible as well as in the infrared region. The reflectance spectrum, however, shows a low reflectance in the entire wavelength region.

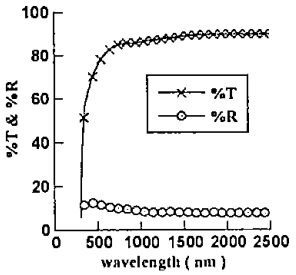

Figure 3: Optical spectra vs. wavelength for an annealed MnO_2 films of thickness 200 nm.

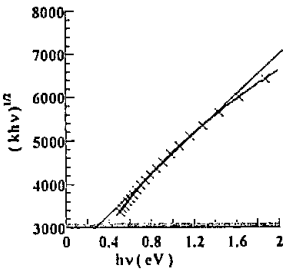

Figure 4: $(khν)^{1/2}$ vs hν curve for an annealed MnO_2 films of thickness 200 nm.

From the above transmittance data, the optical band gap E_g has been graphically determined from the $(khν)^n$ versus hν plots, where $(khν)^n$ indicates optical absorption, n represents the nature of transition. The plot in Figure 4 suggests that the transition is an allowed indirect type with a band gap at E_g = 0.26eV. To make a meaningful comparison of band gap, the authors did a similar calculation by Hall effect measurements. It is known that variations of Hall co-efficient R_H with temperature at various thicknesses of samples are given a straight line. From the slope of ln R_H vs. T^{-1} plot, the band gap E_g was also obtained at 0.26 eV for MnO_2 film of thickness 200 nm. The value of band gap E_g in both electrical

and optical method obtained by author's work is an excellent agreement with the reported value of band gap by other works [5, 7]. The author also calculated the luminous and solar integrated optical properties from the optical spectra and it suggests that the MnO_2 films may, therefore, be of importance for selective surface applications.

4. Conclusion

Various deposition parameters have remarkable effects on spray deposited MnO_2 thin film on glass substrate when prepared by the technique described in this article. Electrical conductivity measurements show an anomaly in conductivity at a temperature of 323K, which agrees well with previous reports of other workers [5, 6]. The thickness dependent of resistivity follows Fuchs-Sondheimer size effect theory [3, 4]. The nature of the carrier as determined from thermoelectric measurement is in agreement with the Hall effect measurement and the film is an n-type semiconductor. Optical studies in the entire wavelength $0.3 < \lambda < 2.5$ μm range exhibit high transmittance in the visible as well as in the infrared region. Author's study of band gap determination from optical and electrical data does agree well the value of band gap by other workers [5, 6, 7]. The low value of reflectance in the entire wavelength range is a potential advantage in using of this material in reflective coating applications.

References

[1] Cordoba de Torresi, Susana I, Gorenstein Annerre. Proc SPIE 1992; 1728: 92-102 Optical Materials Technology for Energy Efficiency and Solar Energy Conversion XI: Chromogenics for Smart Windows, Anne Hugot-Le Goff, Claes G. Granqvist; Carl M. Lampert; Eds..
[2] Minami T, Shirai T, Nakatani T, Miyata T. Jp J Appl Phys, Part- 2 letters 2000; 39(6A): L524-26.
[3] Fuschs K. Electron transport phenomena in metal films. In: Chopra KL,Thin Flims Phenomena, McGraw-Hill Publ. Co. New York 1969, p.346.
[4] Sondhemier E H. Adv. Phys. London, Oxford University Press; 1952.
[5] Rhide VG, Dani RH.. Physica (Utrecht) 1961; 27: 821-26.
[6] Mallick A K, Khan KA. Phys Stat Sol(a) 1994; 142: 409.
[7] Chevillot JP, Brenet J. CR Acad Sic (Paris) 1959; 248(6):776-8.